Development of Portable Diffuse Optical Spectroscopic Systems For Treatment Monitoring

Christopher J. Fong

Submitted in partial fulfillment of the
requirements for the degree of
Doctor of Philosophy
in the Graduate School of Arts and Sciences

COLUMBIA UNIVERSITY

2017

ABSTRACT

Development of Portable Diffuse Optical Spectroscopic Systems For Treatment Monitoring

Christopher J. Fong

The goal of this dissertation is to demonstrate the utility of portable, small-scale diffuse optical spectroscopic (DOS) systems for the diagnosis and treatment monitoring of various diseases. These systems employ near-infrared light (wavelength range of 650nm to 950nm) to probe human tissue and are sensitive to changes in scattering and absorption properties of tissues. The absorption is mainly influenced by the components of blood, namely oxy- and deoxy-hemoglobin (HbO_2 and Hb) and parameters that can be derived from them (e.g. total hemoglobin concentration [THb] and oxygen saturation, StO_2). Therefore, I focused on diseases in which these parameters change, which includes vascular diseases such as Peripheral Atrial Disease (PAD) and Infantile Hemangiomas (IH) as well as musculoskeletal autoimmune diseases such as Rheumatoid Arthritis (RA). In each of these specific diseases, current monitoring techniques are limited by their sensitivity to disease progression or simply do not exist as a quantitative metric.

As part of this project, I first designed and built a wireless handheld DOS device (WHDD) that can perform DOS measurements at various tissue depths. This device was used in a 15-patient pilot study for infantile hemangiomas (IH) to differentiate diseased skin from normal skin and monitor the vascular changes during intervention. In another study, I compare the ultra-small form-factor WHDD's ability to monitor synovitis and disease progression during a patient's treatment of RA against the capabilities of a proven frequency domain optical tomographic (FDOT) system that has shown to differentiate patients with and without RA. Learning from clinical utility of the

WHDD from these two studies, I adapted the WHDD technology to develop a compact multi-channel DOS measurement system to monitor perfusion changes in the lower extremities before and after surgical intervention for patients with peripheral artery disease (PAD). Using this multi-channel system, which we called the vascular optical spectroscopic measurement (VOSM) system, our group conducted a 20-subject pilot study to quantify its ability to monitor blood perfusion before and after revascularization of stenotic arteries in the lower extremities. This proof-of-concept study demonstrated how DOS may help vascular surgeons perform revascularization procedures in the operating room and assists in post-operative treatment monitoring of vascular diseases.

Table of Contents

List of Figures

List of Tables

List of Acronyms

Acronym	Definition
2D	Two-Dimensional
3D	Three-Dimensional
ABI	Ankle-Brachial Index
AC	Alternating Current
BMI	Body Mass Index
CAD	Computer-Aided Design
CC	Correlaiton Coefficient
CT	X-Ray Computer Tomography
CV	Coefficient Of Variation
CW	Continuous-Wave
DAQ	Data Acquisition Card
DC	Direct Current
DOT	Diffuse Optical Tomography
DSP	Digital Signal Processer
ERT	Equation Of Radiative Transfer
FD	Frequency-Domain
Hb	Deoxy-Hemoglobin
HbO2	Oxy-Hemoglobin
HbT	Total Hemoglobin
I&Q	In-Phase And Quadrature
ICCD	Intensified Charge Coupled Device
IH	Infantile Hemangioma
LD	Laser Diode
LPF	Low-Pass Filter
MRI	Magnetic Resonance Imaging
OTI	Optical Tomographic Imaging
PAD	Peripheral Artery Disease
PCA	Prgrammable Gain Amplifier
PD	Photodiode
PDW	Pulse Density Wave
PVR	Pulse Volume Recording
RA	Rheumatoid Arthritis
RF	Radio Frequency
ROI	Region Of Interest
rSQP	Reduced Hessian Sequential Quadratic Programming
SiPD	Silicon Photodiode
SNR	Signal-To-Noise Ratio
TD	Time-Domain

TIA	Trans-Impedance Amplifier
UART	Universal Asynchronous Receiver/Transmitter
US	Ultrasound
μa	Absorption Coefficient
μs'	Reduced Scattering Coefficient

Dedication

For Aunt Linda

1 Background and Motivation

1.1 Overall Goal and Thesis Outline

The overall goal of the dissertation is to demonstrate the clinical utility of portable, small-scale diffuse optical spectroscopy (DOS) systems for the diagnosis and treatment monitoring of various diseases. DOS is an optical imaging technique that uses infrared laser light to investigate functional changes (i.e. oxygenation and metabolism) in the body. The physical principles of DOS allows this by having the near-infrared (NIR) light penetrate biological tissue such as skin, fat, and underlying muscle and is absorbed and scattered within the tissue. The attenuation of NIR light in tissue is due to chromophores such as oxy- and deoxy-hemoglobin, or by light scattering from cellular structures. Since these chromophores are biological markers that can be affected during the progression of various diseases, it provides an opportunity to use DOS to diagnose and monitor diseases. Unfortunately, many investigational DOS systems lack the portability and ease of use to be implemented in a clinical setting.

Development of a low-cost wireless handheld DOS device (WHDD) with a small form factor, portable enough to be utilized in various clinical settings offers a solution to these shortcomings

with its ability to measure hemodynamic and optical changes without ionizing radiation or contrast injection. To test this hypothesis, I pursued the following four specific aims:

SPECIFIC AIM 1: Design a wireless handheld DOS device (WHDD) to perform optical measurements on patients with medical condition that lead to a change in tissue optical properties.

SPECIFIC AIM 2: Use the WHDD in a longitudinal pilot study to assess optical changes during treatment and natural history of infantile hemangiomas (IH), to determine the clinical utility of the WHDD.

SPECIFIC AIM 3: Compare the sensitivity of optical measurements of the WHDD to the proven capabilities of a frequency domain optical tomographic (FDOT) system for a clinical study monitoring the affects of treatments for patients with RA.

SPECIFIC AIM 4: Based on the findings and experiences in clinical studies performed under specific aims 2 and 3, design, build, and verify within a clinical study a compact multi-channel DOS system to monitor perfusion changes in leg extremities before and after intraoperative intervention for patients with peripheral artery disease (PAD).

Current diffuse optical imaging systems are mostly large scale, making them difficult to transport and use in exam and operating rooms. The new technology presented in this thesis demonstrates the potential of how use-of-use DOS systems can provide sensitive measurements for monitor and diagnosis to various diseases without the use of contrast agents or ionizing radiation. Furthermore, the evaluation of this technology to monitor multiple diseases demonstrates the breadth of this technology.

The dissertation is organized as follows: In Chapter 1, I provide an overview of DOS technology and its use to measure tissue chromophores such as oxy- and deoxy-hemoglobin along with other functional blood parameters. I also explain the signal detection techniques that were implemented

within the instrumentation of my thesis work. Lastly within this chapter, I provide a short introduction of three medical applications that are currently studied with DOS technology to provide a foundation of the work in this thesis.

In Chapter 2, I introduce the previous work of a WHDD that was built for verification of a DOS reconstruction algorithm to compute hemodynamic parameters such as oxy- and deoxy-hemoglobin (HbO2 and Hb). I will then discuss the design of an updated WHDD that can easily and reliably be used in a clinical setting. I will also describe the how I verified the WHDD ability to reconstruct optical properties with phantom measurement as well as its ability to make repeatable measurements.

In Chapter 3, I describe how the updated WHDD has the potential to be used to help physicians manage treatment of infantile hemangiomas (IHs) in a 15-subject longitudinal pilot study. This will include study population, cohort selection and imaging imaging protocol. I explain the statistical analysis for evaluating WHDD ability to track IH progression within its treatment and natural history. Finally, I describe how the two-layer discrimination of optical properties can be applied to this application. I will describe a new reconstruction algorithm that has the ability to compute optical properties in two layers and I demonstrate its ability by presenting a numerical simulation study in which I evaluate the accuracy of the algorithm with dozens of different simulations. A two-layer phantom study is also presented to show the ability of the algorithm with physical experiments.

In Chapter 4, I compare the sensitivity of the DOS-WHDD probe in monitoring the treatment efficacy in patients with rheumatoid arthritis (RA) to that of a more proven method in frequency-domain optical tomographic (fDOT) imaging. I will describe an fDOT system and it's capabilities that our lab has used in a previous study and how the fDOT and the WHDD probe was used in a

20-subject longitudinal study. This will include the study protocol, which includes several different clinical modalities for comparison, along with the optical imaging protocol. With only a single patient enrolled over a 4-year recruitment period, I will present a case study and demonstrate how fDOT and WHDD optical measures performed compared to that of the other clinical modalities.

In Chapter 5, I discuss the expansion of the WHDD design into a new multi-channel DOS system, which we call Using this multi-channel system, which we called the vascular optical spectroscopic measurement (VOSM) system, that can be used to monitor revascularization treatments for patients with PAD. I will explain the design details of VOSM and how the multiple channels interface to the measurement subject's foot. I will describe how the system was characterized by presenting results from noise and repeatability experiments. In addition, I will describe the initial results of a 100-patient clinical study that uses VOSM to monitor perfusion in patients before and after their revascularization treatment. Furthermore, I describe the methods for handling the data sets as well as feature extraction and analysis techniques. I explain the statistical analysis for evaluating VOSM ability to monitor and assess severity as well as localize PAD in the foot using angiosome theory.

Finally, I will conclude my thesis by addressing future directions for my thesis work within the three of the clinical studies to improve the efficacy and other limitations that were observed in my work. I will introduce current research that is being done to improve the instrumentation and

methods on how to improve the instrumentations use in clinical settings and improvements that could be made on interfacing to the subject.

1.2 Diffuse Optical Spectroscopy and Tomography

1.2.1 Introduction

When light interacts with tissue it can be absorbed and scattered. The amount of absorption and scattering is dependent on the tissue's optical properties. These properties are represented by the wavelength-dependent absorption coefficient (μ_a), scattering coefficient (μ_s) and anisotorpy factor (g). The μ_a represents the probability of a photon being absorbed per unit length. It is proportional to the number of chromophores that absorb the light as it propagates through the tissue. The μ_s represents the probability of a photon being scattered per unit length and the anisotropy factor represents the direction at which light scatters within the medium. The value of g ranges between positive and negative one. A value of g=-1 implies a completely backward scattering medium, g=0 an isotropic medium and g=1 is a completely forward scattering. Most biological tissues are highly forward scattering with a $g > 0.9$. Also widely used is the term reduced scattering coefficient, which is defined as $\mu_s' = \mu_s(1-g)$.

In diffuse optical spectroscopy (DOS) red and near-infrared light ($650nm < \lambda < 900nm$) are used to probe biological tissues. This wavelength range is used because light absorption is relatively low, enabling the light to penetrate deep into the tissue. The absorption coefficient increases rapidly as the wavelength of light deviates from the NIR as can be observed in Figure 1.1.

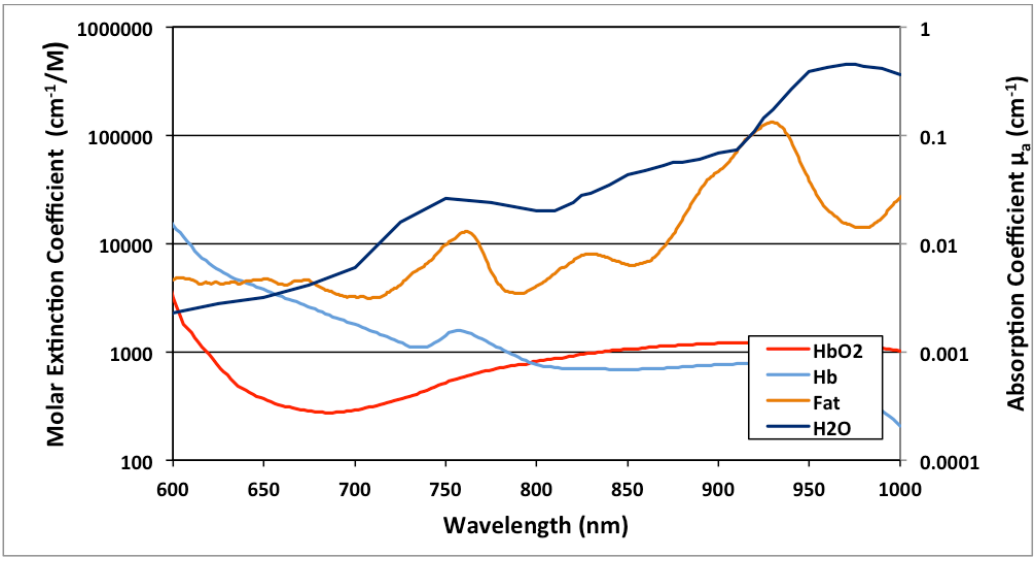

Figure 1.1 This image shows the absorption spectrum of major intrinsic chromophores in tissue, within the NIR wavelength range.

In DOS, non-radiative energy (~1 to 2.5 eV) is delivered to one or more locations on the surface of the body part under investigation and back-reflected light intensities are measured at distances up to 10 cm. Using multiple wavelengths, we are able to extract the effect of certain chromophores within the body. Of special interest are the blood constituents oxy-hemoglobin (HbO2) and deoxy-hemoglobin (Hb), which have distinctly different absorption spectra in the visible and near-infrared wavelengths (Fig. 1.1). By performing measurements at multiple wavelengths, concentration of these chromophores as well as derived parameters such as total hemoglobin ([HbT] = [HbO2] + [Hb]) and oxygen saturation ([HbO2]/[HbT]) can be obtained [1]. By gathering data at different wavelengths and using multi-wavelength reconstruction codes, measurements of these parameters can be generated.

Using a reflectance geometry between the source and the detector, a banana-shaped curve describes the most-likely path of photons between the source and detector (Figure 1.2); therefore, the effective path length is greater than the geometric distance between the source and a detector. It is generally accepted that, for a source-detector separation of 3 cm, the region of maximum

brain/muscle sensitivity will be found between the source and detector fiber tip location, and roughly 1.5 cm below the surface of the skin, though a banana-shaped region of sensitivity extends both above and below this depth [2]. For our studies, we have assumed that our light penetration is about d/2 for a d source-detector distance.

In diffuse optical tomography (DOT), the NIR light is also delivered to one or more locations on the surface of the body part under investigation and transmitted and/or back- reflected light intensities are measured [3-6], just as in DOS. If the spatial geometry of the imaging medium is know, illuminating the tissue from various spatially distributed source positions and measuring the transmitted and reflected light at a number of detector positions surrounding the sample, DOT generates 3D spatial maps of the absorption (ua, typically 0.01-1 cm-1) and scattering (us', typically 10-100cm-1) of tissue back onto the 2D or 3D volume that is known.

This makes DOT similar to X-ray computed tomography in terms of using electromagnetic radiation for generating imaging contrast, but they are different in several aspects. First, X-ray uses shorter wavelengths with higher ionizing energy (~5 to 150 keV), whereas DOT uses longer wavelengths with lower, non-ionizing energy (approximately 1 to 2.5 eV). As a result, DOT imaging, and its counterpart DOS, can be used more safely than X-ray imaging in applications and longitudinal studies. Secondly, while X-ray uses Beer-Lambert law and the inverse radon transform for the image reconstruction, direct inversion schemes cannot be used in DOT imaging. Unlike X-ray imaging DOT has to deal with multiple scattering events by cellular and sub-cellular tissue structures. Such scattering effects inside the tissue are taken into account by employing

appropriate light propagation model [7-11]. The reconstructed images of optical properties are obtained by solving the associated inverse problems.

By gathering data at different wavelengths and using multi-wavelength image reconstruction codes, 2 and 3-dimensional maps of these and other parameters, such as blood volume, can be generated [12-20]. The DOT imagers in this thesis will be referred to as frequency-domain optical tomography (fDOT) imaging system that is used in Chapter 4 to study RA and DOS systems in this thesis will be referred to as wireless handheld DOS device (WHDD) and the vascular optical spectroscopy measurement (VOSM) system.

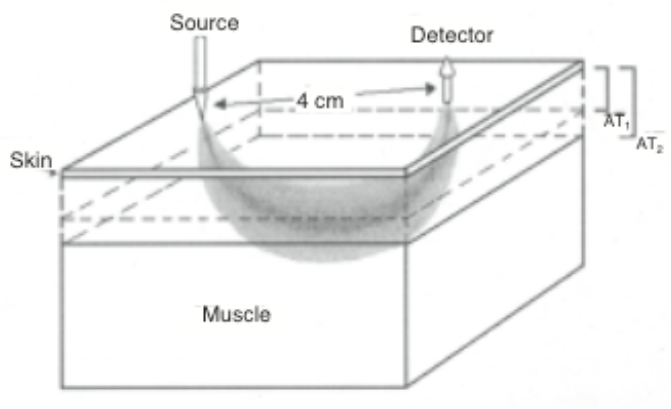

Figure 1.2 Penetration depth of NIR light depends on adipose tissue thickness. In particular, the light goes deeper in the muscle tissue in the case of low subcutaneous fat (AT1) and reaches the shallow region of the muscle tissue in the case of high subcutaneous fat (AT2).

1.2.2 Signal Detection Techniques for Differentiating Optical Properties

While spectroscopy measures optical properties of within one- or two-dimensions, tomography makes the same measurements two- or three-dimensional space with a known spatial geometry. Thus, in optical tomography, anatomic shaped images of optical maps are produced, providing information of absorption and scattering properties within tissue. As with spectroscopy, when

multiple wavelengths are used for illumination, chromophore concentrations of Hb and HbO2 can be computed.

There are several methods in which to perform optical imaging through tissue. Generally, the instrumentation operates in one of three possible modes: steady-state domain also known as continuous wave (CW) domain, frequency domain (FD), or time domain (TD) (Figure 1.1). The CW mode uses a constant intensity light as a source and solely measures the attenuation of light intensity passing through tissues. This attenuation is usually wavelength dependent. This approach allows for simple low-cost instrumentation with high signal-to-noise-ratio (SNR) and faster data acquisition for dynamic signal detection. The disadvantage of this signal detection technique is that relatively low information can be derived from the detected signal, which makes it difficult to differentiate between the absorption and the scattering effects in tissues [21]. The Wireless Handheld DOS device (WHDD) that will be presented in Chapter 1 and the Vascular Optical Spectroscopic Measurement (VOSM) system in Chapter 5 both operate in CW mode, in which the light impinges on the tissue surface with a constant intensity and the intensity of the light transmitted through different sections of the tissue is detected.

In TD systems, pico-second light pulses illuminate tissues and high speed detectors record temporal profiles of light (Temporal Point Spread Function (TPSP)) at different photon arrival times [22]. This approach yields much more information and helps to differentiate absorption and scattering properties in tissues. As a result, the TD mode can improve spatial resolution and sensitivity compared with the CW imaging mode. However, due to the very short time-gated detection, SNR is low and long data acquisition times are required. These characteristics also prevent the use of TD systems for studying sub-second hemodynamic effects. In addition, these

systems are rather expensive compared to CW and FD imaging modes, because of the fast time-gated detection technology and high-speed pulse laser components that are required for imaging.

FD systems constitute a compromise between CW and TD systems [23-25]. In FD mode, the incident light is modulated in the megahertz to gigahertz range, which causes so-called “photon density waves” (PDWs) to be generated and travel through the tissue [24]. Detection of amplitude and phase of those PDWs provides information about the damping and the time delay of the wave. The intensity attenuation and the phase shift of PDWs can be measured. FD systems are less expensive and offer higher SNR than TD system. In addition, FD systems can differentiate absorption and scattering more precisely and show better spatial resolution than the CW system.

However, the FD system is somewhat more expensive and has lower SNR than the CW system [26]. The FD mode of imaging is used in the fDOT finger imaging system discussed in Chapter 4.

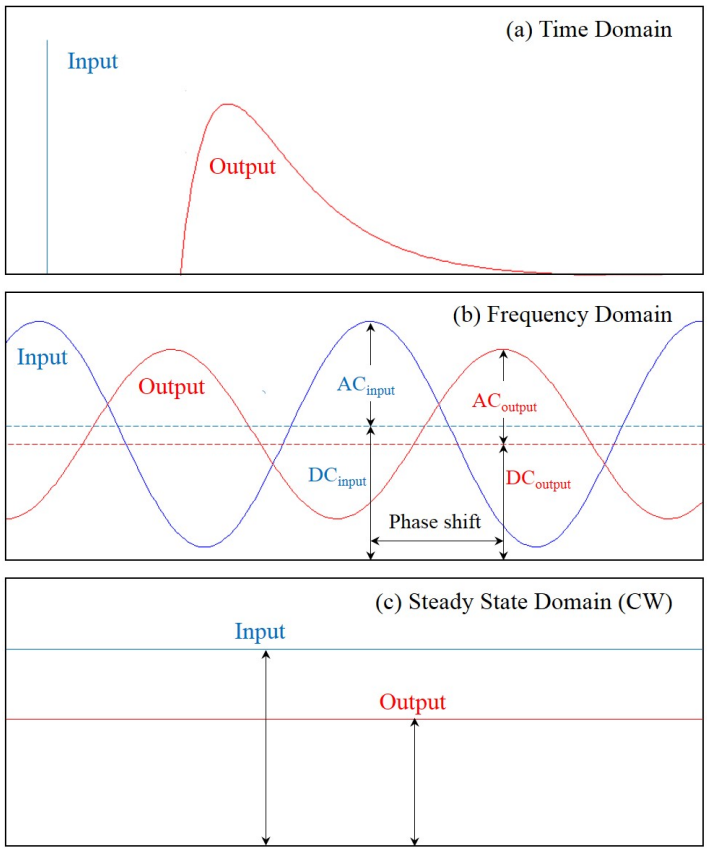

Figure 1.3 Diagram representing signal detection modes (a) time domain (TD), (b) frequency domain (FD), and (c) continuous wave (CW) modes

Going from steady-state domain over frequency domain to time domain, the imaging systems become increasingly complex and, hence, the cost for these systems increases. However, with increasing complexity the amount of information available increases too. For example, absorption

and scattering properties can be better separated using frequency-domain data when compare to CW data.

1.2.3 Applications of Diffuse Optical Imaging

Diffuse optical imaging (DOI), which includes DOS and DOT, has various applications due to its high sensitivity to blood-dependent parameters. Medical problems that involve changes in the blood-related parameters could benefit from the use of DOI. Especially, cancerous tumors often exhibit higher vascularity and higher blood volume than normal tissues; blood oxygenation levels are often used to monitor the status of tumor progression. Currently, DOI imaging for cancer detection has been primarily focused on breast imaging. DOI is a safe, noninvasive and inexpensive imaging method compared to traditional X-ray mammography and MRI [27-30]. In many research studies, high total hemoglobin concentrations (THb) and oxygen saturation level have been used for diagnosis and monitoring the efficacy of cancer treatments [31, 32].

The ability to monitor blood parameters such as [Hb] and [HbO2] in cancerous tumors also makes DOI a research tool to analyze vascular skin diseases such as melanoma [33-35]. Current studies examine hypoxia, hemoglobin absorption, and the spectral features in the NIR range. Current studies have found success in classifying between malignant and benign tumors using spectral features and separation in oxygenation levels between melanoma and normal skin. This research in melanoma makes the study of IH with DOS a good extension of vascular skin diseases, such as infantile hemangioma (IH).

DOI has also been used to study exercise physiology by examining oxygenation of calf muscles before, during, and after exercise [36-38]. Exercise studies have provided insight to how oxidative metabolism increases and decrease during plantar flexion and exercise. These studies have also

provided information about the regional changes in oxygen availability during dynamic exercise. Such studies provide a foundation to study perfusion in the lower extremities for diseases such as peripheral artery disease (PAD).

Another application is joint disease monitoring. Scattering coefficient changes are observed in the synovial fluid of joints affected by arthritis and inside the bones of patients with osteoarthritis. Hence several groups have focused their efforts on developing DOI systems for joint and bone imaging [39, 40].

1.3 Review of Existing Portable Diffuse Optical Imaging Systems

With the emergence of high-tech wearable devices over the past several, medical device technology has also miniaturized, including in the field of biomedical optics. Portable and wireless optical imaging platforms have recently been developed for wearable technologies [41-45], endoscopy [46, 47], and breast cancer [48-50]. In addition, cell phone based technologies have been employed for general hemodynamic or spectrometer measurements [51-53].

A wearable patch-like device designed by Muehlemann et al. uses 4 CW sources and 4 detectors with 2 wavelengths [45]. Similarly, a larger, but still portable wearable brain-imaging system developed by Atsumori et al. [44] uses 8 CW sources and 8 detectors with 2 wavelengths for imaging the frontal cortex. Along with a portable pack that attaches to the subject's waist, the wireless system allows the subject to move around during imaging. Both of these systems focus on differential imaging and use the modified Beer-Lambert law to look at relative changes in the concentration of [HbO2] and [Hb]. A flexible printed circuit board holds the illumination, detection, and wireless transmission electronics. A wearable fNIRS system was developed by Piper et al uses 8 dual wavelength LEDs and 8 SiPDs that are embedded onto a stretch fabric cap. Ribbon cables sending and receiving signals for acquisition connect to the components on the cap

and the system electronics. The system electronics and a notebook used for acquisition are placed in a backpack, which the user carries during acquisition. Functional brain measurements are made while the user is on a bicycle.

A miniature Bluetooth enabled NIRS system with 2 LEDs with separate wavelengths and 2 SiPD used to measure hemoglobin changes in the brain of rats was designed by Kuo et al [42]. The probe has LEDs and PDs in direct contact with the rat's head with source-detector distances of 16mm to measure oxygenation changes while subjected to a traumatic brain injury.

An ambulatory diffuse optical tomographic and multimodality physiological monitoring system was designed by Hu et al [54]. This handheld system is capable of recording 64-channels of NIRS imaging data, as well as EMG or ECG data. The "NINscan-M" contains 8 laser diode sources and 8 photodetectors that can be employed on a limb, head, or abdomen for NIRS scanning while the EMG/ECG module contains 8 channels. The device can sample at 250Hz and runs on 2 AA batteries. Data is either stored on flash memory or can be streamed a smartphone via Bluetooth.

Portable and wireless tissue oxygenation monitoring systems were produced by Watanabe et al [51]. for the use of analyzing brain hemodynamics and sports medicine. The PocketNIRS Duo consists of 2 channels, with each channel consisting of 3 NIR LEDs and a single photodiode. This device is controlled by a smartphone or a PC with Bluetooth communication. In addition, the group developed the PocketNIRS HM specifically for brain oxygenation, where the device is embedded in a plastic helmet. Evaluation of these devices were done with a solid phantom, an arm cuff occlusion test related to exercise monitoring, and a breath-hold test for brain oxygenation monitoring.

Within breast cancer research, Jung et al. developed a compact wide-field NIR scanner has been developed towards contact as well as no-contact based real-time imaging in both reflectance and

transmission mode for the use of breast cancer imaging and functional brain mapping [48]. Phantom experiments have been conducted to estimate the feasibility of diffuse optical imaging by using Indian-Ink as absorption-based contrast agents and preliminary in-vivo studies demonstrated the feasibility of real-time monitoring of blood flow changes. The use of this device was continued by Rodriguez et al. as a potential use of breast cancer screening [49]. In this study, 10 healthy females were scanned with an India ink marker on the breast to mimic a region of increased absorption.

An ultra-compact wireless NIRS imaging system for breast tumor detection was implemented by Cheng et al., where an image reconstruction algorithm was implemented of a custom-made system-on-chip (SoC) using VLSI technology [50]. Transmission of data is performed via Bluetooth to a tablet or PC.

In endoscopy, capsule-like wireless devices have been designed for spectral, fluorescent, and bright field imaging of the gastrointestinal tract [46, 47]. These devices use small complementary metal-oxide semiconductor (CMOS) or charged couple device (CCD) sensors to perform qualitative imaging for identifying suspicious regions at the surface of the tissue.

Incorporations of NIR imaging to smartphones have also emerged in various designs. A smartphone-based spectrometer was designed by Das et al to carry out measurements in a range of studies in the optics field [52]. The device has a dedicated app interface on the smartphone to communicate, receive, plot and analyze spectral data. Validations of the device were carried out by demonstrating non-destructive ripeness testing in fruit samples.

Smith et al. developed a microscope attached to a smartphone that transformed the phone's integrated lens to a 350um microscope and visible-light spectrometer [53]. The microscope has a

resolution of 1.5 um and a usable FOV of 150 x 150 um without image processing and approximately 350 x 350 um with post-processing.

Despite this progress, there are currently no wireless optical imaging devices that perform diffuse optical tissue measurements with absolute reconstruction of the concentrations of tissue chromophores, including the contribution of tissue scattering, as a complete system.

2 Hardware Design for a Diffuse Optical Spectroscopy Device

2.1 Device Background

A first prototype of a portable wireless handheld DOS device (WHDD) was previously developed [55] in our biophotonics and optical radiology laboratory for the purpose of breast cancers hemodynamic measurements. The original WHDD was a Bluetooth enabled device that contained four near-infrared lasers and two photodetectors that operate in continuous-wave mode. The light passes through the sample and is absorbed and scattered as it travels to two detectors configured in reflectance geometry and located 1.8–2.4 cm and 2.7–3.3 cm away from the sources. The laser power was modulated at 3-5kHz and uses digital detection techniques to perform measurements at 2.3 Hz. The average laser power was 5mW. The device is enclosed by a plastic case measuring 11.5 cm × 16 cm × 2.5 cm. A Labview program on a laptop computer was created to acquire data. Using a multispectral evolution algorithm for chromophore reconstruction, the device can measure absolute oxygenated and deoxygenated hemoglobin concentration as well as scattering in tissue.

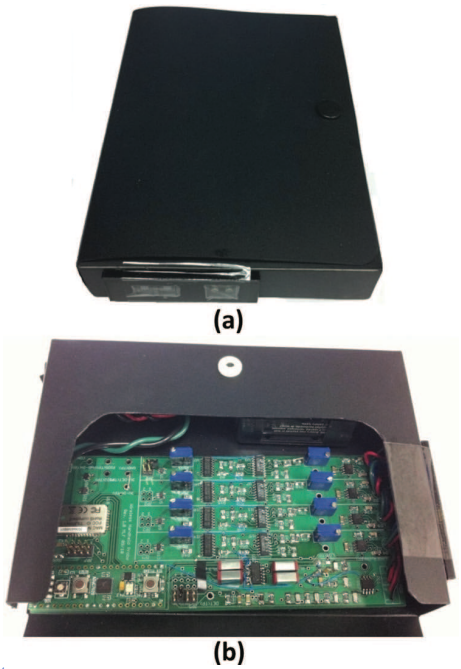

Figure 2.1 Photograph of (a) the 1st iteration of the WHDD device and (b) with the enclosure opened to expose the electronics.

This first prototype was used as a proof-of-concept and its performance was evaluated using a series of liquid phantoms comprised of Intralipid, ink, and other dyes. While these tests on tissue phantoms were successful, its use in clinical settings was problematic as the device was not as robust as required in a demanding clinical situation. For example, upon turning on, the device would begin its acquisition, before pairing with a host device (Labview). This makes it dangerous in a clinical setting as the lasers could illuminate at the subject's eye if not careful. This method of acquisition also is wasteful for the battery. The plastic case was also unstable, as it was made of a soft plastic, with the electronics inside was Velcro'd to the plastic casing. This made it difficult to make repeatable measurements as the lasing interface and electronics would slide or move depending on the pressure put on the casing. Additionally, the hardware acquisition performance suffered, as features such as laser modulation and signal conditioning had to be physically set on board manually. Because of these limitations, the development of second-generation portable WHDD was pursued. This chapter discusses the instrument design and improvements made to the first-generation device.

2.2 Design and Creation of a Second-Generation WHDD

The new design is a similar DOS system configured in reflectance geometry that is similar to the previous design. The new WHDD is composed of four near-infrared wavelengths of light to illuminate tissue. The light passes through the tissue and is absorbed and scattered as it travels to two detectors configured in reflectance geometry. At this separation, the effective light depth will be about 40% of the source detector distance [56], or 2-10mm. The light is detected by a silicon photodiode where the signal is conditioned by a 16-bit analogue-digital converter (ADC) controlled by a microcontroller. The new WHDD contains a more powerful microcontroller that

demodulates the signal and passes the result back to the host controller via Bluetooth® or through USB if a wired connection is needed.

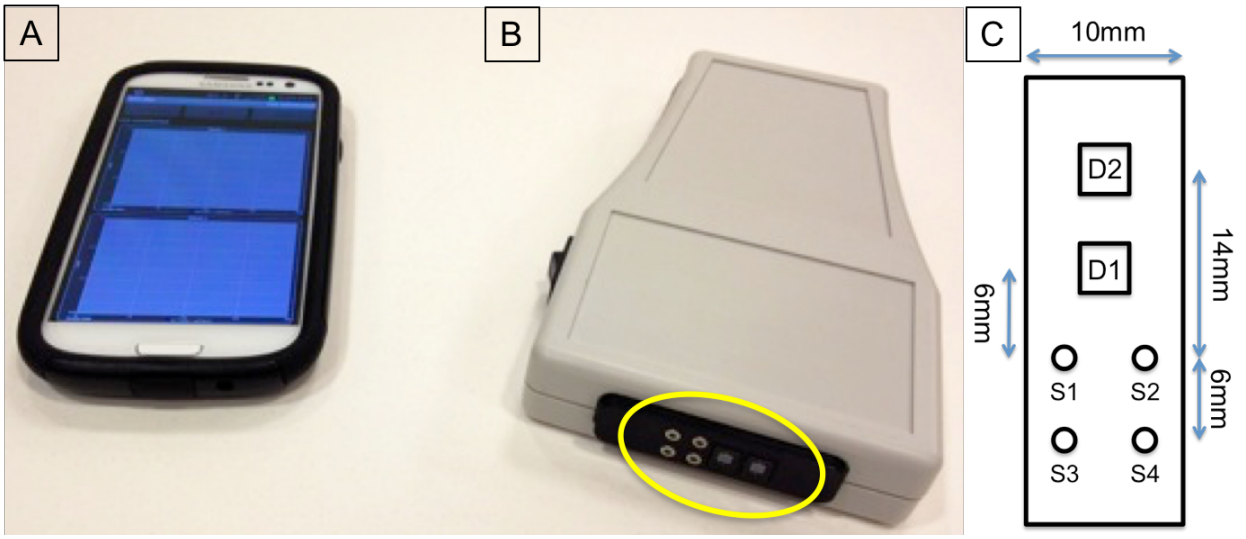

Figure 2.2 System for performing DOS measurements for infantile hemangiomas. (A) Smartphone with a custom-built phone application for system control. (B) Wireless handheld diffuse optical spectroscopy (WHDD) device with measurement head circled in yellow. (C) Diagram of measurement head with dimensions. S1-S4 represents light sources at 780, 905, 850, and 808nm. D1 and D2 represent the two detectors with a sensing area of 5.7mm2 used to capture back-reflected light from skin tissue.

Use of haywires and breadboards from the previous design were replaced by a two-part 4-layer PCB design that consisted of a main board that consisted of backend and digital components and an imaging head where laser and detector components are placed. Multiple PCB designs of the imaging head were made to not only be optimized of superficial imaging, but deeper tissue imaging for applications such as breast cancer and peripheral arterial disease. These imaging heads can be easily swapped out for another by use of a sliding connector. For each imaging head design, components were accurately positioned on the PCB. The board corners were filed to fit the enclosure of the device. The laser and detector components that protrude out were fit into a cover

slip that was made from laser cut Delrin pieces so that both the components and cover would be flush with the sample. The imaging head was re-designed and optimized for infantile hemangiomas (IHs) because the tissue medium require more superficial measurements. For the application of imaging IHs, the detectors are located 0.6-1.4 cm and 1.25–2.0 cm away from the sources as shown in Figure 2.2C.

In this section, the design of the probe will be described. A block diagram of the device is shown in Figure 2.3.

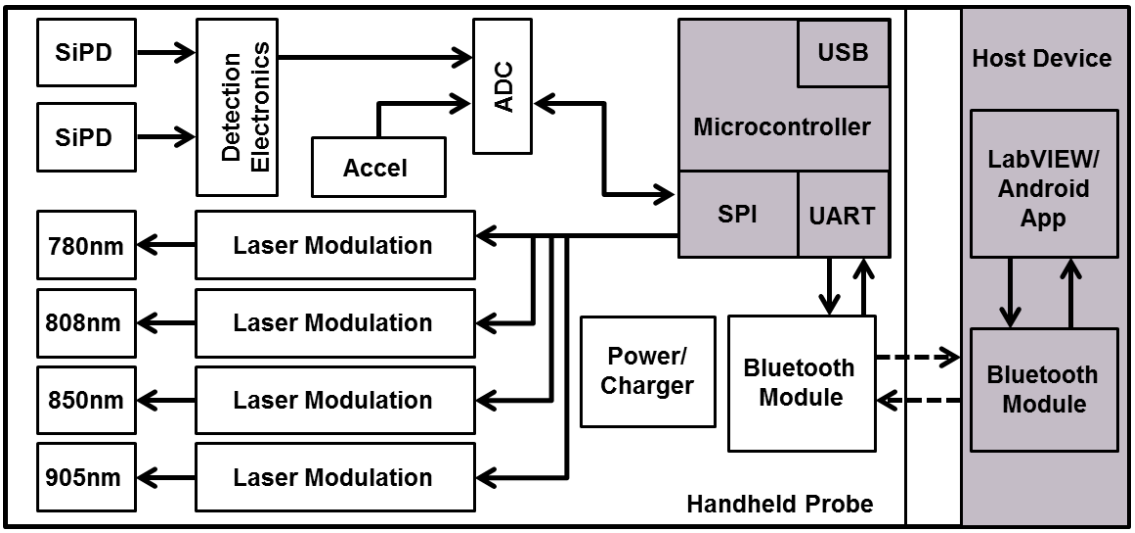

Figure 2.3 System block diagram for the handheld wireless device.

2.2.1 Light Illumination

The input light is generated by 5 mW 5.6 mm-diameter laser diodes at wavelengths λ of 780 nm, 808 nm, 850 nm, and 904 nm (L780P010, L808P010, L850P010, L904P005, Thorlabs). The wavelengths are selected to provide a range of spectral information to reconstruct μ_a, μ_s', and the concentrations of oxygenated hemoglobin ([HbO2]), and deoxygenated hemoglobin ([Hb]).

The laser source for each wavelength is modulated programmatically using a combination of a 1 kHz–33 MHz Oscillator (LTC69034, Linear Technology), a binary counter (M74HC4820,

STMicroelectronics) and a low-pass filter (LTC1067, Linear Technology). This constitutes and improvement over the previous system where the modulation frequency was set by a potentiometer. The potentiometer had to be carefully set and was susceptible to changes when the device was subject to vibrations. The modulation of the input light provides several advantages including superior noise rejection (including ambient light) as well as the ability to illuminate the tissue simultaneously with multiple wavelengths.

The laser diodes are driven by the 15 V Laser Diode Driver (iC-WKN, iC Haus). The power of the laser diode can be controlled using a 20kOhm potentiometer that regulates the current to the laser driver. The modulation of the input light provides several advantages including superior noise rejection (including ambient light) as well as the ability to illuminate the tissue simultaneously with multiple wavelengths.

2.2.2 Light Detection

The light is absorbed and scattered as light passes through the sample to two silicon photodiodes (SiPD) (Hamamatsu S1337-33BR) on an interface adapter board configured 0.6-1.4 cm and 1.25–2.0 cm away from the sources. Current from the two SiPD is converted to voltage using a transimpedance amplifier that utilizes a bandwidth-extension technique previously implemented in [57]. Unlike in the first prototype, the transimpedance amplifier (TIA) no longer uses jumpers to manually change the gain settings and instead uses carefully laid out components to minimize noise. Additionally, a 3-bit programmable gain amplifier (PGA) stage is used to optimize the signal to the scale range of the ADC (LTC6910, Linear Technology). Filtering of the signal prior to the ADC has been upgraded from a first-order passive low-pass filter to a 10th order programmable filter stage (LTC1569-7, Linear Technology). This stage improves the signal remarkably as demodulation of the signal can be noise dependent. Gain control of the PGA are digitally set using

I/O pins from the microcontroller. The cutoff frequency of the filter stage is set via the microcontroller by its pulse-width modulation module (PWM) which can create clock speeds up to 20MHz. For our purpose, the cutoff frequency was set to 7kHz by creating a 224kHz clock from the PWM to the LTC1569-7 chip. Their values can be adjusted through the user interface settings. The result is an increase in SNR by 30dB from the previous hardware revision. Once the signals on both channels are well conditioned, they are multiplexed into a level shifter and quantized using a 16-bit ADC (LTC1865, Linear Technology) that provides speeds up to 150kps.

2.2.3 Processing and Communication

At the heart of the design improvements is a 32-bit pic microcontroller (PIC32MX695F512H, Microchip Technologies) that provides USB connectivity and DSP functionality. This upgrade gives the device complete digital control of the source and detector stages as well as the addition peripherals. Additionally, this controller provides high speed and increased memory that addresses the issues as mentioned in [55]. As before, the signals are demodulated using our digital lock-in detection scheme [58] by the microcontroller. The microcontroller has the ability to demodulate all four wavelengths in one imaging cycle, providing the ability to illuminate at source lasers at once. This dramatically increases the scan rate of the system. As previously reported, the scan rate of the previous system is 2.3Hz, with no combined source laser illumination provided. With the speed and DSP functionality of the new microcontroller, the speed of the system is increased to ~12Hz for no combination of illumination, ~18Hz for two combined wavelengths, and ~24Hz when all sources are illuminated. Once demodulated, the resulting data is then passes the result back via Bluetooth or USB to the host controller.

2.2.4 Firmware

The firmware of the WHDD commands the system to perform tasks requested by the user. The PIC32 microcontroller firmware was developed using the Microchip MPLAB 8 IDE with additional bug fixes done in MPLAB X IDE and the C32X compiler. The configuration bits for the chip were hardcoded such that the PIC32 was computing from the internal oscillator, with the speed set to SYSCLK=80MHz and PBCLK=40MHz.

The device then performed initialization of the controller modules and the peripheral chips. These modules include the timer, interrupts, Universal asynchronous receiver/transmitter (UART), Serial Peripheral Interface (SPI) Bus, and the Output Compare (OC) modules. After the initialization of the modules, the following peripherals are setup:

1. The I/O pins shut off the lasers, set gain settings to –inf dB, disable MUX leading to the ADC
2. Initialize the Bluetooth chip via the UART module
3. Initialize the ADC via the SPI module
4. The modulation frequencies of the laser sources are set to the SPI controlled oscillator chips.
5. The cutoff frequency of the anti-aliasing filter is set by creating a square wave with a computed frequency based on the filter chip

After the system setup is completed, the firmware will go into its imaging subroutine, where the device waits on an instruction from the user. When a command is sent to the device from the user,

the UART interrupt is initiated and a task to performed. The flow chart in Figure 2.4 provides details of the firmware processing.

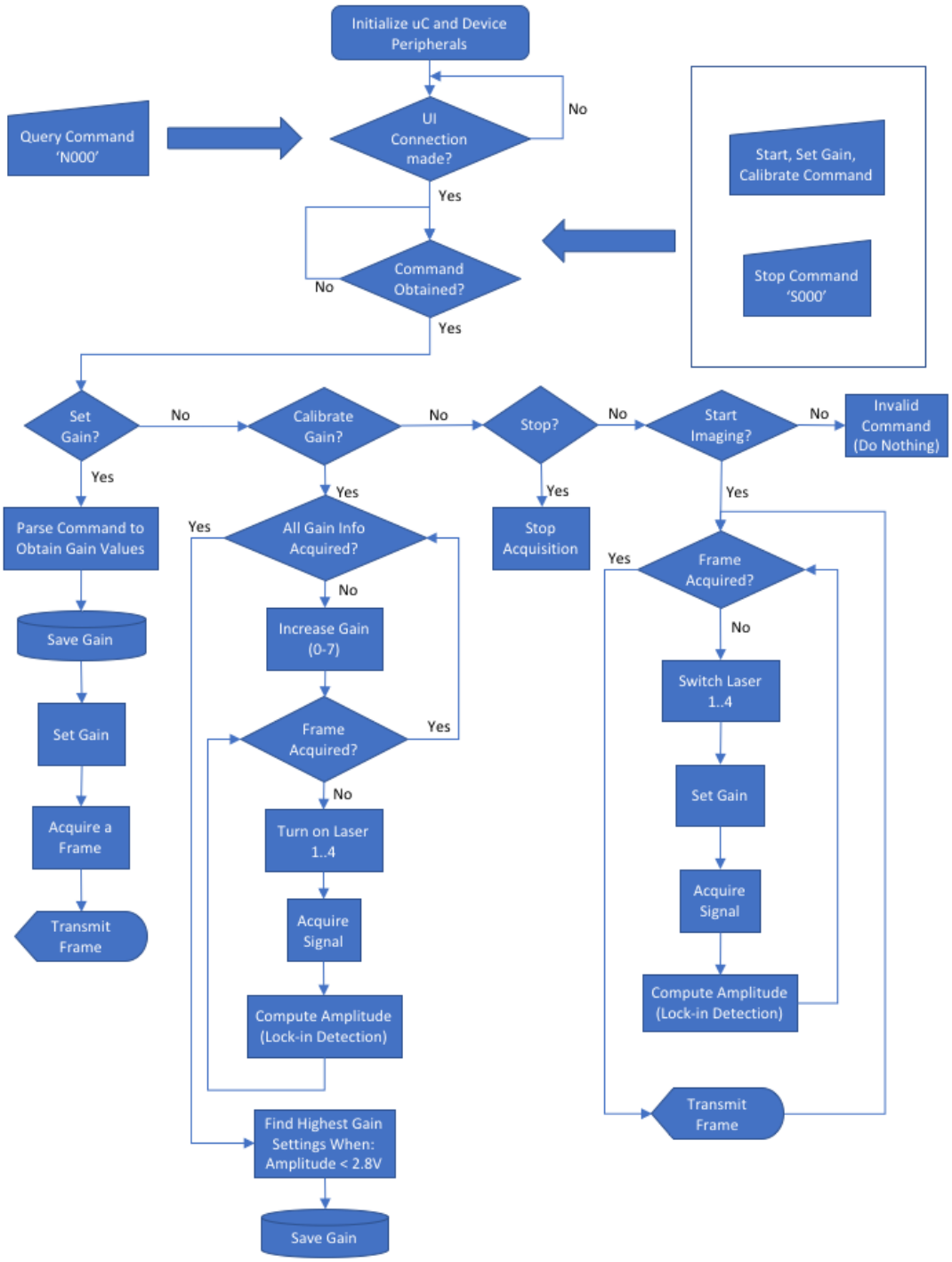

Figure 2.4 Flow chart of WHDD firmware processing to set gain, calibrate gain, start, and stop acquisition.

The commands from the user are strings of ASCII code that is parsed by the device. For most commands, only the first ASCII character is needed for the command. Only the gain settings contain a payload more the 0. Table 2.1 shows the header command structure needed for the device to perform tasks.

Command	Header Command	Payload	Example
Start	Y	0	'Y000'
Stop	S	0	'S000'
Calibrate Gain Settings	C	0	'C000'
Configure Gain	G	(# of SD pairs) * 2	'G020 1 2 3 4 5 6 7 7'
Initialize Device	N	0	'N000'

Table 2.1 Commands excepted by the WHDD to perform imaging and control tasks.

2.2.5 Gain Optimization and Calibration

A firmware routine in the device measures the optimal gain setting for the PGA for a given sample. While the probe is at the sample, the gain optimization routine illuminates all of the lasers at all of the gain settings. The best gain is chosen for each source detector pair by computing the highest amplitude of the signal that does not exceed the threshold set by the user. Although the threshold is user controllable, the threshold is nominally set at 2.8V. This is because the ADC can only sample voltages from 0-3.3V and 2.8V provides a 15% buffer from the maximum computable amplitude.

Once in the calibration routine, the device acquires frames and computes the amplitude for all gain settings. This creates a matrix with size (# of gain settings) by (# of SD pairs). The best gain selection is determined by picking the gain setting where the corresponding amplitude is the largest gain setting under the threshold. The best combination of gain settings is loaded to the device and the single frame of data is acquired and is sent back to the user interface.

2.2.6 Reconstruction Algorithm

A brief description of the reconstruction algorithm previously described is presented here [55]. The algorithm computes the special distributions of μ_a, μ_s', and the concentrations of oxygenated hemoglobin ([HbO2]), and deoxygenated hemoglobin ([Hb]). The diffuse spectroscopic technique is based on the reflectance measured at multiple locations on the surface of the medium, where the diffuse reflectance depends solely on the absorption coefficient μ_a and the reduced scattering coefficient μ'_s and the source- detector separation d. Under the assumption of a semi-infinite homogeneous medium, the closed-form analytic solution for the spatially resolved reflectance is given by Farrell et al. [59] as

$$R(d)_{dc} = \frac{1}{4\pi\mu_t'}\left[\left(\mu_{eff} + \frac{1}{r_1^2}\right)\frac{exp\left(-\mu_{eff}r_1\right)}{r_1^2} + \left(\frac{4}{3}A + 1\right)\left(\mu_{eff} + \frac{1}{r_2}\right)\frac{exp\left(-\mu_{eff}r_2\right)}{r_2^2}\right] \tag{2.1}$$

where,

$$r_1 = \sqrt{\left(\frac{1}{\mu_t'}\right)^2 + d^2}, \qquad r_2 = \sqrt{\left(\frac{\frac{3}{4}A + 1}{\mu_t'}\right)^2 + d^2} \tag{2.2}$$

Here μ_{eff} is the effective attenuation coefficient $\mu_{eff} = \sqrt{3\mu_a\mu_s'}$, $\mu't$ is the total transport coefficient ($\mu'_t = \mu_a + \mu'_s$) and A is the internal reflection parameter [60] that takes into account the refractive index mismatch at air-tissue interface.

We employed a multispectral direct method that exploits the following relations that describe the tissue absorption, chromophore concentration, and scattering as

$$\mu_a(\lambda) = \sum_{i=1}^{N_c} \varepsilon_i(\lambda) C_i \tag{2.3}$$

and,

$$\mu_s' = A\lambda^{-b} \tag{2.4}$$

where $\varepsilon_i(\lambda)$ and C_i are the absorption extinction coefficient and the concentration for the ith chromophore in tissue. Nc is the number of tissue chromophores that contribute to the absorption at wavelength λ. The scattering parameters A and b are the scattering amplitude and the scattering power, respectively. The multispectral direct method reconstructs Ci, A. The scattering power, b, is kept constant and is set by the user. The scattering power should be decided by the medium of the measurement. For example, phantom measurements typically assume a flat scattering across the NIR range, but muscle or fat will have a scattering profile that is more linear, and decreases with the increase in wavelength [61].

The SRS problem with the direct approach can be formulated as the following inverse problem where the optimal solution can be found by minimizing the misfit between predictions R_d and measurements z_d of the reflectance on the tissue surface

$$F(x) = \sum_{\lambda,d} \left(R_d^{\lambda} - z_d^{\lambda}\right)^2 \tag{2.5}$$

where x is the vector of all unknowns, e.g., x = (C_j, A). Although this algorithm can solve many several different variables at once, the algorithm developed will only reconstruct chromophores [HbO2] and [Hb], alongside the scattering amplitude A. To minimize this equation, an evolution strategy algorithm was implemented.

The general structure of the ES algorithm used here can be described as follows. Consider a population of individuals $P_k = (x_1, ..., x_n)_k$ at iteration k, where each individual x_j represents a potential solution to the inverse problem under investigation. Each individual x_j is evaluated using the objective function (Eq. (4)). Next individuals are randomly recombined and mutated to give more than n individuals and then each individual is evaluated again with the objective function, and the n fittest individuals are selected to generate the new population $P_{k+1} = (x_1, ..., x_n)_{k+1}$. This process is repeated until the fittest individual is selected. Table 2.2 shows the pseudo-code of the ES algorithm.

1	Set $k = 0$
2	Initialize $P_k = (x_1,...,x_n)$ with $x_j = (C_{HbO2}, C_{Hb}, A, b)_j$
3	Evaluate P_k
4	Repeat while (not converged)
a	Recombine $\tilde{P}_k = (\tilde{x}_1,...,\tilde{x}_m)(m>n)$
b	Mutate $P_k = \tilde{P}_k + Z_k$
c	Evaluate P_k
d	Select n best individuals
e	$k = k + 1$
5	End

Table 2.2 Pseudo-code of the evolution strategy algorithm.

2.2.7 User Interfaces

The host controllers we have developed include a MATLAB interface and an Android mobile application. The WHDD mobile application we developed controls the hardware and receives and

stores the transmitted data. Currently, the most popular operating environments on mobile devices are Android and iOS. However, with the iOS environment having significant limitations on the Bluetooth standard and protocols, we decided to develop the application for the Android operating system so that we could utilize the Bluetooth 2.1+EDR standard with the RFCOMM protocol. The Android SDK provided the tools and API's necessary to communicate with the hardware via Bluetooth. The application was developed based off the open-source application BlueTerm, which is a terminal emulator for communicating with devices using a Bluetooth serial adapter. Our application allows the user to control the hardware (initialize or connect to the device, calibrate gain settings, start recording, and stop recording) using buttons in the interface that send unique commands to the device (Figure 2.5). The application also allows the user to connect and disconnect to a paired Bluetooth device through a menu. In separate threads, the data is parsed, stored on the devices removable SD storage, and plotted in real-time to on-screen graphs. Once acquisition is complete, the acquired data can be uploaded to our data servers via the Dropbox

phone application which is also stored on the Android phone. The phone used for data acquisition is a Samsung Galaxy SIII.

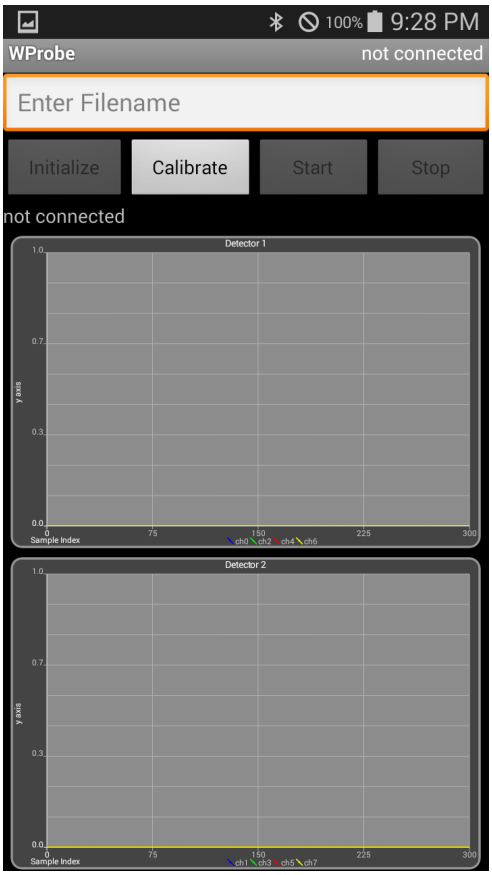

Figure 2.5 Screenshot of the user interface from the Android application to control and collect data from the wireless handheld probe.

A MATLAB Graphical User Interface (GUI) (Figure 2.6) was developed as a tool where long experimentation times make USB connectivity more suitable. The GUI can connect to the probing device using a virtual COM port, making connectivity to both Bluetooth and USB available. The GUI was developed using MATLABs Graphical User Interface Design Environment (GUIDE). The GUIDE module allows the user to create point-and-click control of software applications, eliminating the need to learn a language or type commands in order to run the application. It integrates the two primary tasks of app building—laying out the visual components and

programming app behavior—and allows you to quickly move between visual design in the canvas and code development in an integrated version of the MATLAB Editor.

The GUI that was created has the ability to control the WHDD probe, save the data to a specified location, load previous gain settings, and display incoming data from the WHDD in real time. The GUI controls the device using the same command signals as the Android application and can control the device with functions: connect, stop, start, and calibration of gain. The data received by the GUI is saved to a text file at a user specified location. The interface also has the ability to manually adjust and send individual gain settings to the device using sliders for each source detector pair by pressing the "Send Configuration" button. With 4 sources and 2 detectors, there are a total of 8 source-detector pairs that can have their gain adjusted.

The user can load previous gain information by clicking on the "Browse" button on the "Open Config. File" section and selecting a "*_config.txt" file and pressing the "Load" button. Once loaded, the sliders for the gain configuration will update accordingly. The user must then press the "Send Configuration" button to send the loaded gain settings to the device.

Once the gain configuration is sent, the user can press the "Start" button to begin acquiring data. The start data will send a command to the device to begin imaging. Once the imaging is initiated, the WHDD will continually collect frames of SD pair data. Each frame of data is sent in a packet via USB or Bluetooth. Each packet contains a header with the packet size, the SD pair data with an adjustable size of significant digits of raw (voltage) data, and the gain of the SD pair. For each frame, the GUI parses the packet by computing the size of the packet from the header. The GUI then separates the data from the packet and writes the frame to the text file. In addition, the frame of data is displayed on the GUI screen for real-time visualization of the data acquisition. The displayed data is a rotating buffer of incoming data, with up to 500 frames allowed to be viewed

at once. This rotating buffer scheme was used to improve the performance of the acquisition since displaying data is computationally taxing.

If the computer used for data acquisition is Bluetooth enabled, a virtualized COM port can be created for it to be used as a connection pathway to acquire data instead of using USB. Although this GUI can be natively used with a Windows PC, this GUI has the ability to be used with the Mac OSx operating system as well with the installation of the Prolific PL2303 USB to RS232 driver (PL2303_MacOSX_1.6.1_20160309.pkg).

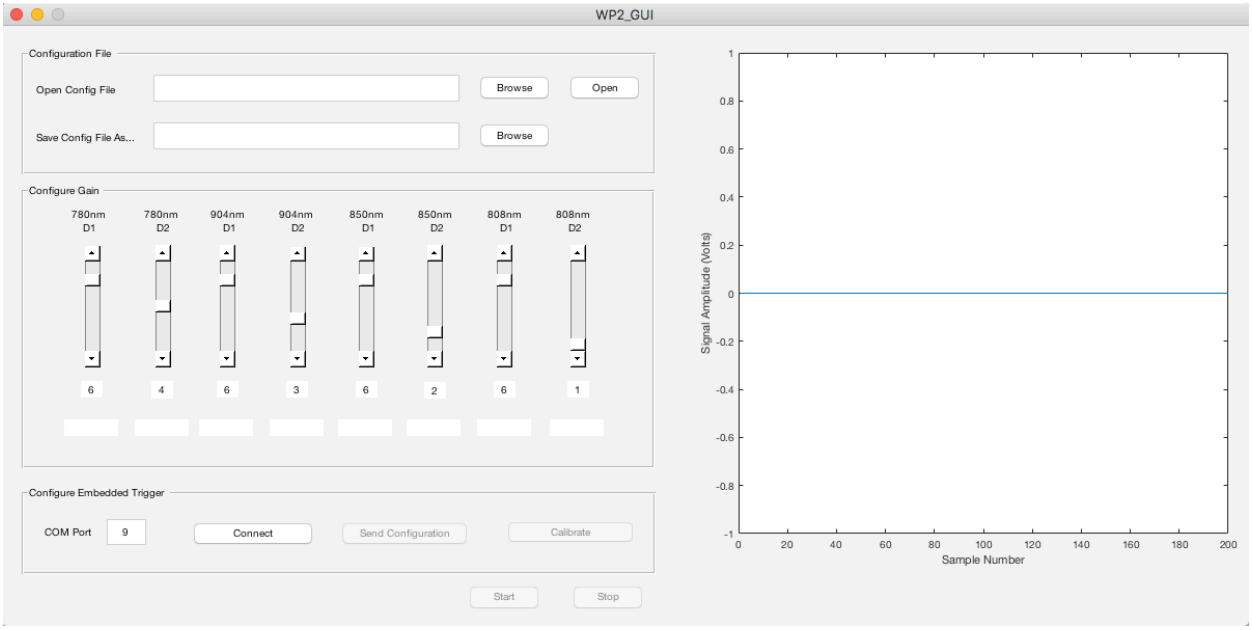

Figure 2.6 Screenshot of the user interface from the MATLAB to control and collect data from the wireless handheld probe.

2.3 System Characterization

For monitoring applications where the location of the diseased tissue is known, the WHDD may provide a simplified diagnostic solution for easier clinical use. In ensure that the system can be used appropriately for a given application, characterization of the device capabilities must be

performed. Here we discuss the characterization of the system with the following parameters: Speed, Sensitivity and Dynamic Range, Linearity, Stability, Size.

2.3.1 Speed

The speed of acquisition is an essential parameter for making point measurements where motion artifacts may play a role during acquisition. The temporal response of the WHDD system is limited by the digital lock-in detection scheme applied in microcontroller of the acquisition board. However, the method of performing the digital lock-in detection can be adjusted to performing the task with 1, 2 or all 4 lasing wavelengths at a time. As previously reported, the scan rate of the previous system is 2.3Hz, with no combined source laser illumination provided. With the speed and DSP functionality of the new microcontroller, the speed of the system is increased to ~12Hz for no combination of illumination, ~18Hz for two combined wavelengths, and ~24Hz when all sources are illuminated.

2.3.2 Sensitivity and Dynamic Range

The dark noise represents the smallest measurement that can be reliably performed with the system, occurring when no incident light is present while measuring. Figure 2.7 shows the average dark noise measured for each gain setting with the error bars representing the standard deviation across wavelength measurements. By increasing amplification in the PGA stage, we see an increase of noise, with a large increase in noise at gain 64x (101uV). However, at the gain stages 1-16, we see noise levels below 75 μV. Although the highest gain settings results in a much higher dark noise measurement compared to the lowest, the RMS dark noise only results in a noise of less

the 1% of the optimal return for a foot measurement, which is 2.7V. That is 101uV/2.7V = 0.004%, or 88dB of SNR.

The largest light signal that can be detected uses the full detector range for the lowest gain setting, which in this case is to detect a 3V peak-to-peak voltage on the 20kV/V gain setting. Using these values, we can calculate the dynamic range of the system to be 89.5 dB.

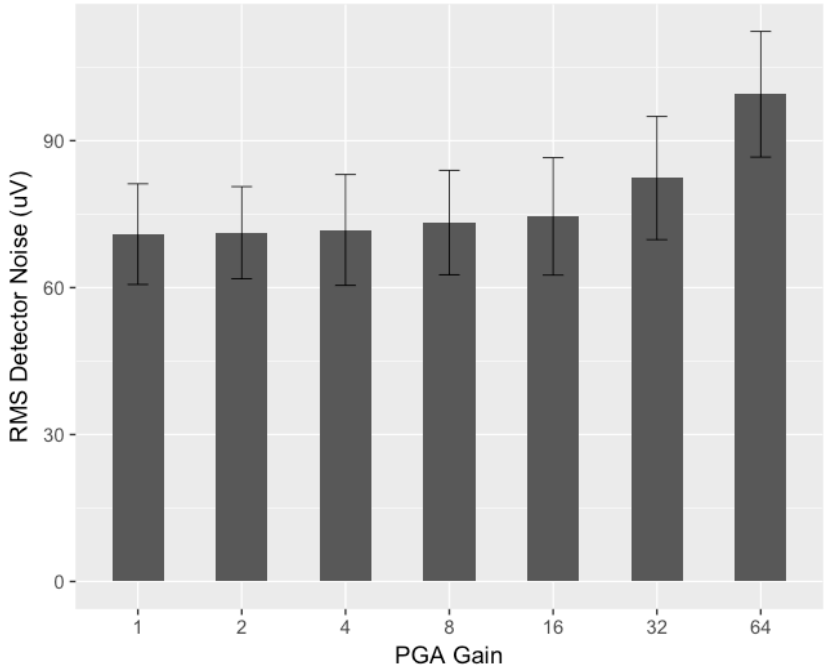

Figure 2.7 Plot of the root mean squared (RMS) dark noise for each detector gain setting. Error bars represent the standard deviation of all detectors.

2.3.3 Linearity

System linearity was examined by measuring the detected voltage from the solid block phantom across all possible PGA chip gain settings (LTC6910-2, Linear Technology). The PGA chip used in the detector channels are 3-bit controlled with gain settings (0, -1, -2, -4, -8, -16, -32, -64V/V). The results are plotted in Figure 2.8, where it is demonstrated that a linear relationship across the

gain settings is generally maintained. For the curves below, linearity with R-squared measures of R=0.975.

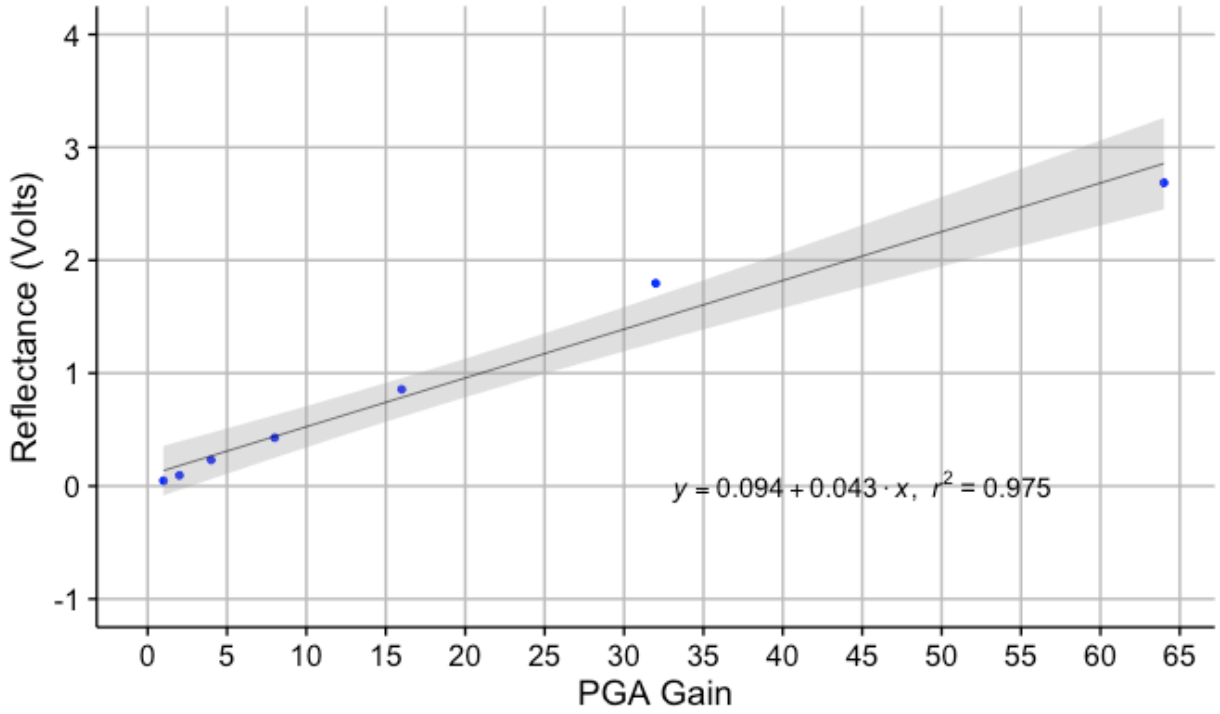

Figure 2.8 Linearity across all gain settings measured with the INO phantom block.

2.3.4 Repeatability

Repeatability measurements tests were performed to ensure that the device can be reliably be used for repeated measurements, such as in a longitudinal study. In order to quantify the repeatability of the WHDD, two types of experiments were performed. The first test was to use the WHDD to scan a solid phantom with a homogeneous medium as shown in Figure 2.9. The solid phantom is a Biomimic Optical Phantom (INO, Canada) which has optical properties shown in Table 2.3. The optical properties requested by our group is the requested values, and the measured values are the

values from the characteristic report supplied by INO. The optical properties of the phantom made by INO are advertised to have a flat spectrum and have a reliable reduced scattering coefficient.

	Optical Properties of Solid Phantom			
WL (nm)	670	780	808	850
Predicted (ua)	0.15	0.15	0.15	0.15
Predicted (us')	8.5	8.5	8.5	8.5
Measured (ua)	0.214	0.179	0.173	0.168
Measured (us')	9.31	8.93	8.97	8.72

Table 2.3 Optical properties of solid phantom used for repeatability study.

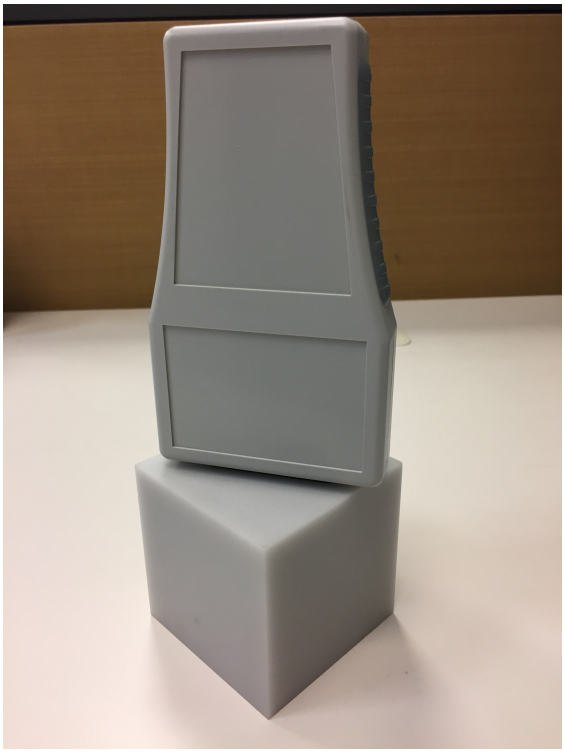

Figure 2.9 The Wireless Handheld DOS Device imaging the INO solid phantom block.

The protocol of the repeatability measure on the phantom was to scan the solid phantom on one location at two different orientations, such that the WHDD interface is rotated 180 degrees. This measurement was repeated another two times, in 1 hour intervals, totaling in 6 measurements. A

Bland-Altman diagram was created to demonstrate repeatability (Figure 2.10). This figure demonstrates that the percent change in reflectance between repeated measures is achievable to 99.7% accuracy with a standard deviation of 1.00%

In addition, a repeated-measure ANOVA was performed to compare the repeated scans of the phantom. Using this method, it was found that the mean temperature difference between the repeated measures were not significant (P = 0.475). Because repeatability requires that measurements not change between trials, accepting the null hypothesis is desired.

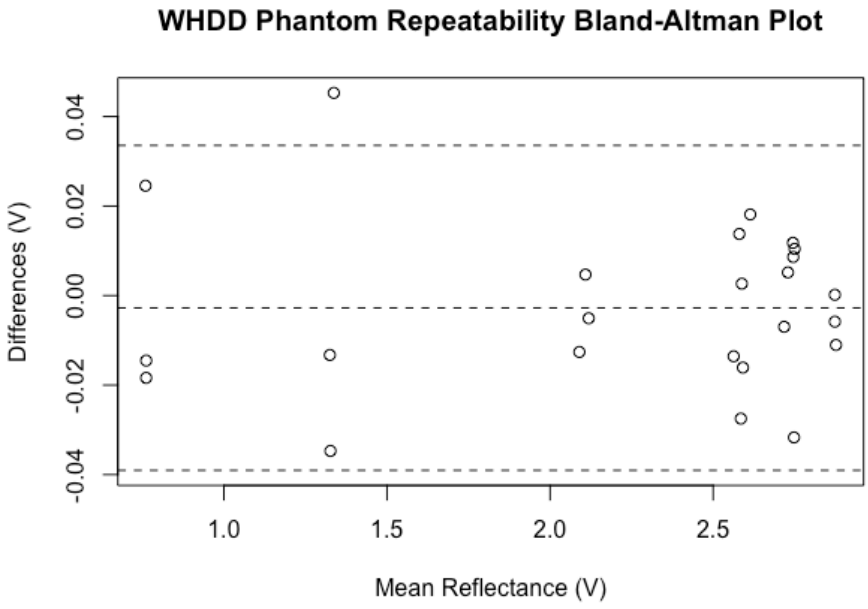

Figure 2.10 Bland-Altman plot demonstrating repeatability on a phantom block. A total of 3 independent tests were performed from WHDD's 8 source-detector pairs.

A similar protocol was also repeated on human skin. For this repeatability test, the wrist of 5 subjects were scanned with the WHDD with 2 repeated measurements. For each repeated measurement, the probe was placed onto the wrist for 5 seconds, released from skin contact for 5 seconds, and then placed back onto the wrist for another 5 seconds. A Bland-Altman plot was created for all subjects and source-detector pairs (Figure 2.11). The mean percentage change

between these measurements was 4.35% with a standard deviation of 5.05%. It is important to note that repeatability accuracy increases when the reflectance measurements increases. For example, reflectance measurements above 2.1V result in a repeatability change of 1.8% with a standard deviation of 2.1%. In addition, a repeated-measure ANOVA was performed to compare the means of the initial scan and the repeated scan of the wrists of subjects and differences between these scans were not significant (P = 0.429).

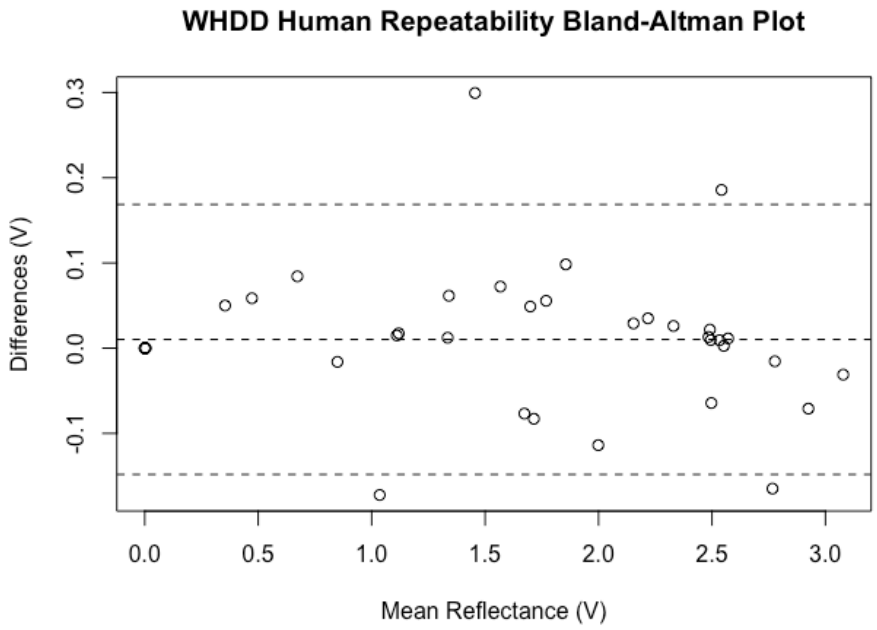

Figure 2.11 Bland-Altman plot demonstrating repeatability on human subjects. Measurements were taken from the wrists of 5 subjects with the WHDD's 8 available source-detector pairs.

2.4 System Summary

We have presented a new hand-held wireless device for diffuse optical tissue spectroscopy. The prototype was created for less than $500 and presents an inexpensive, portable, and user-friendly device for clinical optical measurements. The size of the device is currently suited for hand-held operation, but could be further scaled down in size to a device pen sized, by selecting smaller component footprints, a smaller battery, and denser board layout. Table 2.4**Error! Reference**

source not found. presents a comparison between the new wireless handheld DOS device and the previous version presented by Flexman et al. [55]. The most important difference between the WHDD system described in this thesis and previous version lies in the digital control of peripheral signal processing of illumination and detection. This results in a 10-fold increase in system speed, from 2.4 to 24 Hz. In addition, the detection section has more gain control that is can be more easily manipulated by the user. This gain feature allows for a great dynamic range, allowing for a wider range of absorbing and scattering tissues than the previous hardware version. Finally, although the gain of the system has higher control, the system dark noise is similar to the previous version (<50μV for most gain settings). This is due to the fact that the front end of the detection circuit has the same transimpedance topology as before.

Features	First Generation	Second Generation
Scanrate	2.4Hz	24Hz
Laser modulation	Potentiometer Adjustable	Digitally Programmable
Detection Gain	Manual Jumpers	Digitally Programmable
Accelerometer	No	Yes
USB Option	No	Yes
Rechargeable	No	Yes
DSP Functionality	No	Yes
Sampling	12-bit MCU	16-bit ADC

Table 2.4 Comparison of 1st and 2nd generation handheld wireless DOS probe

This device can facilitate future clinical studies exploring the optical signatures of various medical applications such as vascular anomalies, skin cancers, as well as subcutaneous cancers such as breast cancer. Indeed, this device provides a fast and easy way to make static and dynamic measurements on many other tissues, including, for example, brain, limbs, and breast, without the need for specific interfaces for each application. The ease of use, portability, and low cost of this

device will complement many existing clinical optical studies by providing real-time measurements, and will create opportunities for new clinical applications.

3 Diffuse Optical Spectroscopic Assessment of Infantile Hemangiomas

3.1 Infantile Hemangiomas

Infantile hemangiomas (IHs) are the most common benign vascular neoplasms in infants, affecting ~5% of all infants born [62, 63]. Females are more likely to develop IH with a sex ratio ranging from 3:1 to 5:1 and even until 9:1 in case of PHACES syndrome. (PHACE Syndrome is the association between large infantile hemangiomas, usually of the face, and birth defects of the brain, heart, eyes, skin and/or arteries. It is an acronym that stands for the medical names of the parts of the body it often impacts.) Other identified risk factors are: race (Caucasian), prematurity, and low birth weight (less than 1500 g) [64].

The natural history of these lesions, with initial rapid proliferation followed by gradual involution and regression, has not been completely elucidated. At birth the lesions are either absent or barely evident. It has been suggested that the onset of IH is caused by hypoxic stress [62, 65]. The proliferative stage involves the proliferation of benign endothelial cells and mast cells in the first few weeks to months of life. This results in an increase of blood vessels and vasculature within the area. After 5 to 10 months, the growth curve flattens, followed by an involution phase over several months to years [62-64, 66]. Within this involution stage, histological examination reveals a diminishing endothelial cellularity and an increase in fibrofatty tissue [62, 64, 65, 67]. At the age of 5 years, 50 percent of the hemangiomas have involuted, and at the age of 9 years 90 percent have [67].

Their clinical presentation can vary significantly, from nodular lesions several millimeters in diameter to plaque-like tumors covering the entire face or a quadrant of the body [67]. Larger tumors can interfere with vital organ function and/or cause permanent disfigurement. Complications include ulceration, threat to vision, airway obstruction, and congestive heart failure

[68]. Fig. 2.1 shows a mixed hemangioma that contains a superficial feature and a subcutaneous feature.

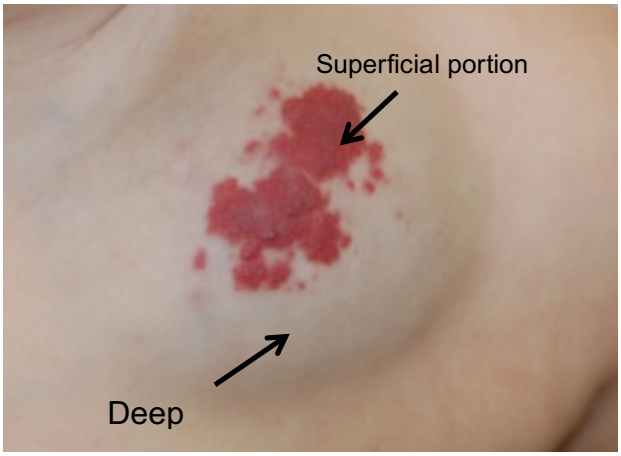

Figure 2.3.1. An example of infantile hemangioma. This particular hemangioma has a deep component that can be seen as a large bulge, and a red, blotchy superficial component

3.2 Clinical Measures

IH progression is documented using relatively subjective techniques relying upon physical examination findings, visual analog scale (VAS), and review of photographs [69-75]. Subjective clinical diagnostics typically include a visual assessment of the hemangiomas by photography of the lesions to analyze size, color, and anatomical distortion [70, 72, 73, 75]. Measurements of lesion are also taken to determine area and volume of the lesion [75]. These assessments give insight of which stage the lesions are in and whether treatment or its natural course is effective in its involution. Although it has been common practice to use subjective assessments to determine the status of the lesions, it has been of interest to validate and exercise necessary means for evidence based diagnostics [63, 76, 77]. It has also been noted that there has been a lack of objective evaluation in treatment monitoring in clinical studies [78], and their growth

characteristics can be hard to predict early in infancy, as they are not present as fully formed tumors at birth [75].

Surgical biopsies are performed in atypical cases and are done if the history, physical examination, and imaging studies do not clearly define the pathologic process. It is suggested that invasive measures are not to be used otherwise [64].

3.3 Imaging Techniques

Current evaluation consists of diagnostic imaging of the IH lesions by means of Doppler ultrasound (US), MRI, CT, and in rare cases angiography [64]. Doppler US is a non-invasive tool to measure IH thickness, as well as blood flow and vessel density to follow IH regression [79-81]. However, everyday clinical use is further limited by the need for an experienced ultrasonographer and operator variability. MRI is a noninvasive effective tool for imaging and classification of vascular malformations based on the presence of lobulated masses, signal voids, and hemodynamic flow characteristics. MRI also provides details about anatomic extent of the lesion, proximity to vital structures, and involvement of multiple tissue planes [82]. CT scan images examine for density before contrast medium enhancement, the presence of calcification(s), the limits of the lesion, the fat stranding and the type of enhancement [83]. Although these imaging techniques are well suited to measure hemangiomas in three dimensions, they are not immediately available and costly, and in the case of CT or MR, may require sedation or general anesthesia in young infants [75]. Additionally in the case of US, there are limitations by its small field-of-view, restricted penetration and operator dependency [82]. Moreover, imaging is reserved to evaluate the depth and extent of the lesion, usually underestimated by physical examination especially for symptomatic lesions when treatment is contemplated [82]. These methods make it unviable for early detection and diagnosis, where proliferation is barely evident. The temperature difference

between IH and surrounding or contralateral skin commonly observed makes infrared thermography (IRT) a viable solution for monitoring IH [84]. However, results showed that IRT observed a much faster months to zero-temperature difference between the deep IH and the contralateral normal skin site than that of the mixed or superficial IH subtypes. This shows that IRT is less sensitive to deep IH because deep IH have a much longer involution stage than superficial IH, but due to the lack of heat from the more subcutaneous deep IH, the temperature difference is closer to that of normal skin. False temperature elevations may also result from ulcerated IH by use of IRT.

Optical imaging techniques have shown the potential to monitor treatment and give an early diagnosis to vascular skin lesions, most notably melanoma. Studies of this nature have been reported previously [85-88]. Kuzmina, et. al. reported results using diffuse reflectance spectroscopy (DRS) and a multi-spectral imaging (MSI) analysis to image various vascular skin lesions in adults, before and after laser treatment [86]. Their results showed that the optical density spectrum, color parameters, and the spectral ratio of diseased and healthy skin changed before, immediately after, and 2-3 weeks after laser treatment. Kokolakis et al. presented an optical computed tomography (optical-CT) system as a tool for three-dimensional (3-D) imaging of biopsy samples of melanocytic lesions and its ability to discriminate benign from malignant melanocytic lesions while simultaneously determining the thickness of invasive melanoma [87]. In a less invasive approach, Konig et al. used two OCT modalities and dermoscopy to image various dermatological disorders. It was concluded that the combination of the three could be a useful tool in early skin cancer diagnostic and the evaluation of treatment [85]. However, these presented modalities consist of a several large components and control cables where the size and

weight complicate the handling in demanding environments. This makes it difficult to image lesions on all locations of the body or to image multiple localized lesions that may be evident.

3.4 Assess Optical Changes in IH During Treatment and Natural History

Recently, it has been suggested that IHs are brought on by hypoxic stress of local skin tissue [62, 65]. However, the lack of objective and quantifiable tools to measure IH biology and severity can hamper understanding of pathophysiological processes, such as hypoxia or other mechanisms that may contribute to risk for ulceration, that may be involved [63, 66], and make it difficult to quantify and compare efficacies of different treatments. Thus, it is of great interest to clinicians to develop and validate means for evidence based diagnostics [76, 77].

One appropriate solution for measuring vascular and hypoxic changes in human tissue is by diffuse optical imaging, whether by DOS or DOT. Optical imaging has been widely utilized for diagnostic imaging for brain oxygenation in newborn infants suffering from cerebral hypoxic-ischemic injury [89-92]. In addition, DOS has also been utilized to measure chromophore concentrations of the skin, as well as vascular lesions [93-99]. For example, work performed by Lim et al [93] showed that Raman spectroscopy was the best imaging modality for discriminating Melanoma from non-Melanoma lesions. A study was performed by Tsang et al in which chromophore concentrations of human skin was measured in-vivo from absorption and scattering coefficients. These results suggested that diffuse reflectance techniques with the visible and near infrared light sources can be employed to investigate the hemodynamics and optical properties of upper dermis and lower dermis. Although DOS has been shown to be a viable tool for skin and vascular lesion measurements, the technology has not been utilized to measure infantile hemangiomas. Given the extensive background in imaging oxygenation in tissue, a small form factor DOS measurement

device could provide clinicians with a tool that can be easy to use and non-intimidating for children and parents while being used in a clinical setting.

To address this clinical need, we employed our WHDD system in a longitudinal pilot study to evaluate its utility in IH vascularity assessment. We monitored changes in [THb] and StO_2 over several time-points up to 18 months in patients that were untreated or treated with propranolol or topical timolol. The DOS characteristics of IH in different stages (proliferation, plateau and involuting) and IH receiving treatment was correlated with clinical features.

3.4.1 Clinical Examination

IRB approval was obtained from Columbia University Medical Center (CUMC) Investigational Review Board (Protocol# IRB-AAAJ1201), and patients were recruited from the Pediatric Dermatology practices at CUMC. Infants were eligible if they were younger than 9 months at the time of initial visit and had at least one cutaneous IH greater than 2 cm in diameter in an area accessible by our probe's 3x1cm measurement head. Frontal facial lesions were excluded. Patient's eyes were shielded from the light using an NIR light absorbing material. Infants were scheduled to be assessed with the WHDD at the initial visit, at 2-4 months, and at 1 to 2 year follow-up visits. Parents of eligible patients were informed of the investigational nature of the study protocol and were required to read, agree to, and sign a statement of informed consent prior to participation.

Patients were assigned to the "natural history" cohort if no medical intervention was clinically indicated. Patients were enrolled in a "treatment" cohort when medical intervention was indicated with either oral propranolol or topical timolol. Prior to DOS measurements, subjects underwent clinical examination and photographic documentation. IH staging (proliferating, plateau, or involuting) and classification, in which the IH lesion is deep (subcutaneous), superficial, or mixed

(both) was determined based on parental history of IH appearance Figure 3.2, clinical and parental photos, patient age, and IH characteristics (e.g. color, texture) on physical exam at the time of assessment. The assessments were made at routine clinic visits by the same treating physician for continuity.

Figure 3.2 Examples of different IH classification. Left: Superficial IH. Center: Deep IH. Right: Mixed deep and superficial IH.

3.4.2 Study Device

All patients were scanned with our enhanced WHDD system (Figure 3.3A,B), which is an optimized version of a previously presented device (11). The WHDD (Figure 3.3C) is composed of four near-infrared wavelengths of light to illuminate tissue to provide a range of spectral

information to determine the concentrations of [HbO2], [Hb], [THb], and StO2. The measurement probe was controlled via Bluetooth by a custom designed Android phone application.

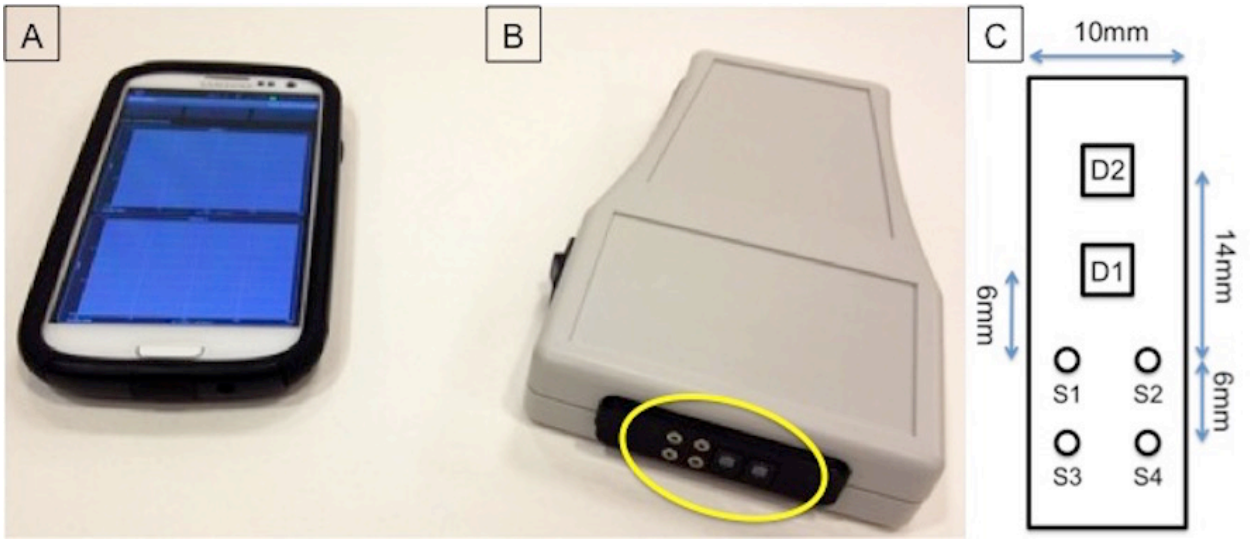

Figure 3.3 System for performing DOS measurements for infantile hemangiomas. (A) Smartphone with a custom-built phone application for system control. (B) Wireless handheld diffuse optical spectroscopy (WHDD) device with measurement head circled in yellow. (C) Diagram of measurement head with dimensions. S1-S4 represents light sources at 780, 905, 850, and 808nm. D1 and D2 represent the two detectors with a sensing area of 5.7mm2 used to capture back-reflected light from skin tissue.

The WHDD probe head was placed on top of the IH or contralateral normal skin for measurements. If the IH lay in the center of the body, a normal skin measurement would be performed a minimum of 5cm above or below the IH. Multiple measurements at different probe orientations were taken to ensure consistency of the measurement area. Individual measurements take only seconds; and the entire measurement procedure, including placement of the probe at multiple sites, can be performed in less than a minute. Once the infant had been scanned, the detected light intensities

were entered into a reconstruction algorithm (11) to compute [HbO2], [Hb], [THb] and StO2. These functional parameters from the multiple measurements were averaged prior to analysis.

3.4.3 Data Analysis

Since [THb] and StO_2 may differ at different skin sites around the body, each IH measurement was normalized to the measurement performed at the contralateral normal tissue site to produce [THb] and $\%StO_2$ ratios:

$$rTHb = \frac{[THb_{IH}]}{[THb_{Normal}]}, \qquad rStO_2 = \frac{\%StO_{2_{IH}}}{\%StO_{2_{Normal}}} \quad . \tag{3.1}$$

The ratio *rTHb* provides a metric for volume measurement based on overall vascularity observed. For example, in bulkier, deep IHs compared to superficial IHs, one would expect higher values of rTHb. The ratio $rStO_2$ provides a relative measure of the oxygen supply within the microvasculature between involved and uninvolved tissue.

The *rTHb* and *rStO2* features may vary greatly depending on the subtype and staging, which could make it difficult to interpret the overall state of the IH. To quantify the overall state of the IH, we derived a third index that combines the two features with equal weight, which we call the Normalized Hypoxia Fraction (NHF):

$$NHF = \frac{rTHb + \frac{1}{rStO_2}}{2} \tag{3.2}$$

This unitless index equally combines information about [THb] and StO_2 into one number, since *rTHb* and $rStO_2$ may change independently over time. This index, as we found, provides the best distinction between the proliferation, plateau, and involuting stages. As the IH evolves through

these stages, *rTHb* and $rStO_2$ will trend towards 1— suggesting that the vascular properties of the IH site is equivalent to that of the normal skin site. The three DOS derived parameters (*rTHb*, $rStO_2$, and NHF) were correlated to the results of the clinical examination.

3.4.4 Statistical Analysis

Comparisons between patients in different stages of IH were made using a one-way analysis of variance (ANOVA). The Holm-Sidak t-test was used to determine individual inter-group significance. Boxplots were generated for visualization of the range, shape, and skewness of data. Scatterplots showing normalization of NHF over time were produced. Repeatability of the system measurements was computed by measuring the coefficient of variance of [THb] and StO_2 for each patient.

3.4.5 Study Demographics

Thirteen infants with fifteen hemangiomas were enrolled. All subjects were female. A summary of the enrolled patients is found in Table 3.1.

	Age (Months)	Classification			Location		
		Superficial	Deep	Mixed	Trunk	Extremities	Head
All IH (N=15)	5.8 ± 2	N=8	2	5	10	3	2
Untreated IH (N=11)	6 ± 1.9	5	2	4	8	1	2
Treated IH (N=4)		3	0	1	2	2	0

Table 3.1 Demographic features and clinical classifications for all subjects.

3.4.6 Untreated Infants with IH

We performed a total of 23 measurements on 13 untreated IHs including two pre-treatment measurements from two of the four treated infants for our analysis of untreated patients. Three IHs were scanned three times, five were scanned twice, and four were scanned once. At time of measurements, the IHs were classified as being in the proliferation (N=6), plateau (N=12), or

involuting stage (N=5) and correlated with patient age: the mean (SD) ages of subjects were 5.1 (±2.2), 9.1 (±2.3), and 14.0 (±7.9) months respectively.

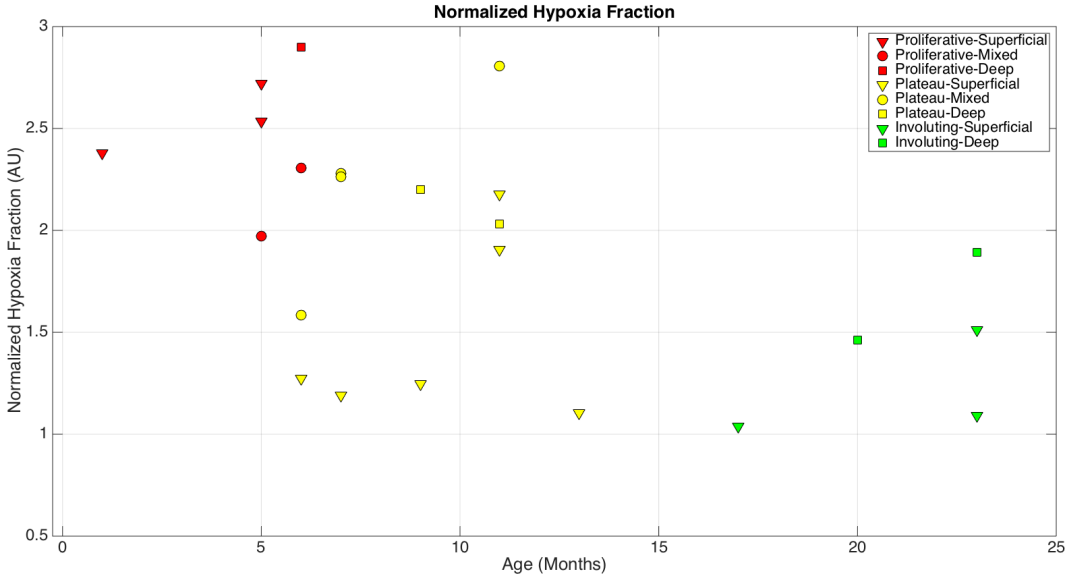

Table 3.2 Scatterplot of Normalized Hypoxia Fraction measurements of untreated subjects

The NHF index peaked at 6 months of age (±2.9) (Figure 2). NHF index decreased and trended towards normal skin over time. IHs with a deep component (deep or mixed IH) reached a minimum value of 1.46, while the superficial IH reached a minimum value of 1.03, showing that no deep or mixed IH was fully involuted before the age of 23 months.

Overall, mean NHF indices decreased significantly as IHs progressed from proliferative to involuting (Figure 3, ANOVA, $p = 0.002$). Using the Holm-Sidak t-test, the NHF index during the proliferative stage was significantly higher than during the plateau and involuting stages ($p=0.020$, $p=0.001$ respectively). There was no significant difference in the NHF index between plateau and involuting stage IHs ($p=0.121$). A summary of the statistical results can be found in Table 3.3,

which shows that NHF yields a better distinction than the measures of vascularity or oxygenation by themselves.

Feature	Comparison (p-value)		
	Proliferative vs. Plateau	Plateau vs. Involuting	Proliferative vs. Involuting
rTHb	0.0236*	0.3355	0.0027*
$rStO_2$	0.9343	0.0001*	0.0010*
NHF	0.0204*	0.1206	0.0005*

Table 3.3 P-values of features comparing the three stages of IH (Proliferative, Plateau, and Involuting).

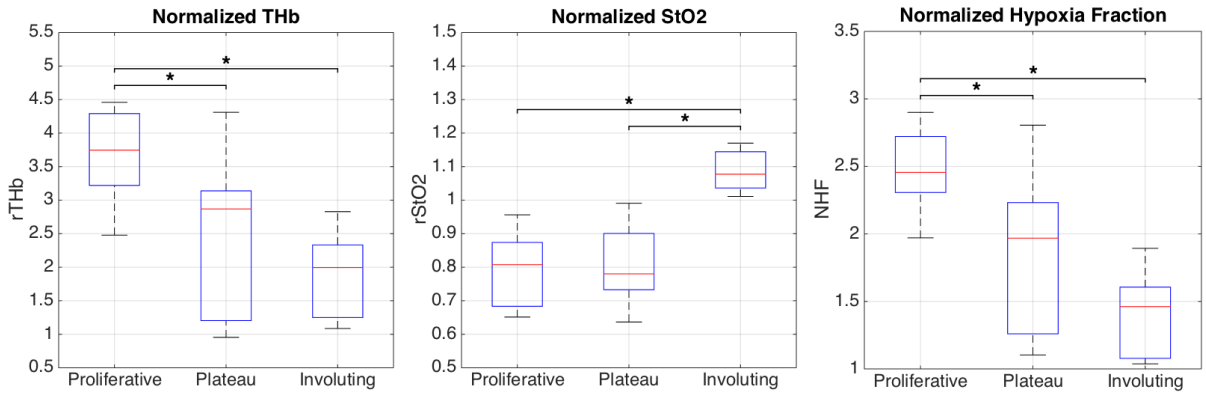

Figure 3.4 Boxplots show the distribution of NHF measurements according to the stage classification: Proliferation (N=6), Plateau (N=12), and Involuting (N=5). One star (*) indicates statistical significance based on the Holm-Sidak t-test.

3.4.7 Treated Infants with IH

Within the treatment subjects (N=4), 3 IHs were classified superficial and 1 as mixed. All subjects demonstrated response to propranolol treatment according to clinical criteria or size, volume, and

color. Of the four infants, two did not have complete measurement data and were omitted from the analysis. From the remaining two subjects, one showed an improvement in NHF by 39.2% over a 3-month span of treatment with topical timolol.

The final subject (Figure 3.5) presented at 1 month of age with a large segmental superficial proliferative IH of the left lower extremity and was started on oral propranolol. Pre-treatment (1 month) and post-treatment (3 and 13 months) measurements were obtained from the IH and the contralateral, unaffected leg.

Figure 3.5 Photographs of a subject classified with a large segmental superficial IH. Top, subject at 1 month of age, just prior to treatment. Middle, subject after 2 months of treatment. Bottom, subject after 12 months of treatment.

The baseline DOS measurements demonstrated hypoxia in the IH (NHF 2.38), which normalized to normal skin oxygenation (NHF 0.96) after 2 months of propranolol treatment. This correlated to clinical observations of decreased red discoloration and papules (Figure 3.5, Table 3.4). After propranolol discontinuation at 13 months, NHF continued to be normal (0.97). These parameters suggest that total hemoglobin content was reduced while oxygen saturation in the IH increased towards normal skin values during propranolol treatment.

Response to Propranolol: DOS Measurements			
	1 month	3 months	13 months
rTHb	3.22	0.85	0.98

$rStO_2$	0.65	0.94	1.04
NHF	2.38	0.96	0.97

Table 3.4 Normalized [THb] StO2 and NHF results from the treated case subject. Measurements were made at 1 month of age just prior to treatment, and at 3 month and 13 months of age where propranolol was administered.

3.4.8 Study Discussion

IHs are the most common tumor of infancy and have phenotypic heterogeneity that can complicate management decisions and objective monitoring for natural progression or response to treatment. Accepted standards use subjective visual assessments of the IHs such as clinical examination, visual analog scale (VAS), and photography to analyze size, color, and anatomical distortion [70, 72, 73, 75]. Methods to measure IHs to determine area and volume of the lesion have been proposed [70, 72, 75]. Haggstrom, et. al. developed a comprehensive severity score that that attempts to account for size, complications, and location, and disfigurement [71]. Although the results are promising, the scale does not provide information with regard to IH volume and extent, and subjective measures integrated in the calculation made is operator- dependent. In summary, assessments are largely subjective and operator-dependent thus may not be easily replicable and compared.

Furthermore, the lack of objective and quantifiable tools to measure IH biology and severity can hamper understanding of pathophysiological processes, such as hypoxia, that may be involved [63, 80], and make it difficult to quantify and compare efficacies of different treatment modalities. Thus, it is of great interest to clinicians to develop and validate means for evidence based diagnostics [63, 76, 77].

We have developed a WHDD device that provides an objective, reproducible, non-ionizing, non-invasive and portable tool to measure hemoglobin content and oxygen saturation in IHs of all stages without the need for sedation. By using these measures, DOS can tell us more about IH in

its different stages and how the vascular information could be applicable towards understanding the pathophysiology.

Employing the WHDD, we have defined NHF as a measure of tissue hypoxia and vascularity that correlates well to clinical appearances and stages of IHs. NHF peaks at 6 months of age, correlating with the end of the most active proliferative period. By 13 months of age, a period of plateau phase, the NHF is steadily decreasing. This demonstrates the IH become more like normal skin as they mature and become less hypoxic. This might explain why IH become more likely to ulcerate during rapid growth periods [100]. Furthermore, propranolol treatment normalized NHF at time points earlier than untreated IHs, suggesting that propranolol may target IHs in part by correction of the hypoxic state. This demonstrates that with successful treatment of IH, DOS may be able to track accelerating involution or movement towards normalization.

There are limits to this study. Although this system can be used for facial IH, we decided to take a conservative approach for ease of recruiting subjects given that greater ocular protection would be required to use the device on lesions closer to the eye. Use of protective goggles caused infants to become more active, and a result, repeatability measures faltered for these measurements. We did not use a formal visual analog scale (VAS) to assess patients at time points. US was only performed as clinically indicated and we do not have data for all patients. In cases in which US was performed the clinical classification (superficial versus having a deeper component) correlated with our clinical impression. Ulcerated IHs were excluded because the WH-DOS interface requires contact with the skin. Future versions of the WH-DOS could have a non-contact interface for measuring ulcerated lesions and improving repeatability.

In conclusion, we demonstrate that DOS has the potential to aid in monitoring IH growth and involuting stages, which may aid in management decision and quantify treatment efficacy. The

high variability in the size and classification of IHs require more subjects for a more complete analysis. The treatment cohort was small and anecdotal and our findings need to be confirmed in a larger study. Future studies are required to evaluate DOS in relation to other objective measures of IH growth such as VAS and US, as well as to assess its applicability in complicated IHs.

3.5 Two-Layer Discrimination of Optical Properties

Using the reconstruction technique described in section 2.2.6, a semi-infinite target medium is assumed of our measurement area. Thus, the optical properties of that medium are assumed to be uniform throughout the medium. For infantile hemangiomas (IH), the lesion is largely cutaneous and the normal tissue lies underneath. Because of this, our DOS measurements is largely an integration of the IH and normal tissue, depending on the depth of the IH and the distance of the source-detector (SD) pair. For example, if the SD distance is 20mm, as is the case with two of the pairs from the WHDD system, the measured tissue within a 10mm depth will be integrated as one semi-infinite medium with the light prorogation model described in section 2.2.6. Therefore, it would be advantageous to have the ability to discriminate the optical properties of the IH and the normal skin underneath. For example, an IH that is located on the scalp will not have the optical properties of the skull or brain integrated into the reconstruction. This not only provides a more accurate depiction of the optical properties of the IH, but also allows the IH to be measured without interference of the various tissue types that the IH may be located.

The end objective for the use of two-layer discrimination of optical properties is to use the data obtained during the clinical trial and the calculated depth from Ultrasound images against the two-layer model to estimate the optical properties of the IH and the normal tissue layer beneath it. Unfortunately, US was only performed as clinically indicated and we do not have data for all

patients. In addition, US imaging was taken place weeks before or after the DOS measurements, and therefore cannot be combine in this research.

In this section, work towards discriminating the IH and normal tissue layers are presented. To discriminate the optical properties of the two tissue types, a two-layer reconstruction was developed that can more accurately compute the optical properties of the two different layers (Figure 3.6). To test the two-layer reconstruction, several numerical simulations were performed to test the theoretical viability of the algorithm. Optical properties of the two layers will be computed with the developed two-layer reconstruction model while varying the number of variables the algorithm can compute. For example, results with and without the depth information will be compared, as well reconstructing the scattering parameter, or setting the scattering parameter to a fixed value. To test the algorithm experimentally, a two-layer liquid phantom model was created.

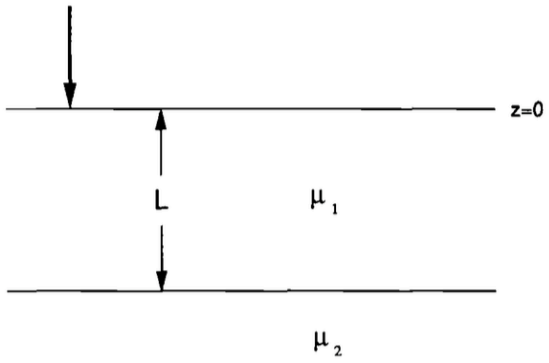

Figure 3.6 A schematic drawing of a two-layer system with a semi-infinite bulk medium. The parameter z is taken in the vertical direction and the interface is at z=0. The parameter L is the depth of the first layer, which will represent the IH lesion. Parameters u1 and u2 are the absorption coefficients in the respective layers.

3.5.1 Ultrasound Guided Optical Imaging

Optical imaging based on diffusive near-infrared NIR light has the great potential to differentiate tumors from normal tissues through determination of tissue parameters, such as blood volume, blood O2 saturation, tissue light scattering, and water concentration. As a potential diagnostic tool, however, NIR diffusive light imaging suffers from low spatial resolution and lesion location uncertainties because of intense light scattering in tissue.

Reconstruction of tissue optical properties in general is underdetermined and ill-posed because the total number of unknown optical properties always exceeds the number of measurements, and the perturbations produced by the heterogeneities are much smaller than the background signals. In addition, the inversion reconstruction algorithms are sensitive to measurement noise and model errors. Current instruments can distinguish simple structures approximately 1 cm in size, but sharp edges are typically blurred by a few millimeters.

Other groups have developed hybrid imaging methods that combines ultrasound and NIR diffusive light imaging [101-103]. The hybrid imaging obtains coregistered ultrasound and NIR diffusive light images through simultaneous deployment of an ultrasound array and NIR source–detector fibers on the same probe. Coregistration permits joint evaluation of acoustic and optical properties of different tissue types (i.e. tumor and normal tissue) and enables use of lesion morphology provided by high-resolution ultrasound to improve the lesion optical property estimate. With the a priori knowledge of lesion location and shape provided by coregistered ultrasound, NIR imaging reconstruction can be localized within specified regions. As a result, the reconstruction is overdetermined because the total number of unknown optical properties is reduced significantly.

For our application, the two-layer reconstruction of optical properties between the IH and normal skin can be better resolved if the number of unknown are reduced, particularly if the depth information is known in order to only obtain the optical properties. To this point, it is possible to

use Doppler ultrasound as a high spatial resolution imaging modality to compute the depth of the IH as a priori information that can be used in the two-layer optical reconstruction algorithm.

3.5.2 Reconstruction Algorithm

Many different parts of the human body exhibit a layered structure, e.g., skin layer, the head or the extremities. Specifically for IH, a highly vascular diseased layer of tissue overlays a much thicker normal layer of tissue. To this end, the semi-infinite reconstruction algorithm described in section 2.2.6 is expanded such that he SRS equation is solved for the 2-layered turbid media in the steady-state. With the semi-infinite model, there were three unknown variables to solve for using the ES optimization technique (HbO_2, Hb, reduced scattering, μ_s'). For the two-layer model, the number of variables have increased to seven variables. These consist of the previous three, (HbO_2, Hb, μ_s'), but both are independent for the two layers, in which case there is HbO_{2top}, Ho_p, $\mu_s'_{top,}$ $HbO_{2bottom}$, Hb_{bottom}, $\mu_s'_{bottom}$. The seventh variable is the thickness of the top layer, L (Figure 3.6). If more chromophores are within the tissue medium, then any additional variables must be added to the model.

The solutions were derived for a semi-infinite layered and for a finite layered geometry, i.e., the bottom layer has an infinite and finite thickness, respectively. For simplicity of presentation, only two spatial dimensions are considered. Hereafter, z denotes depth and x the transverse spatial variable. For simplicity, we assume index-matched boundaries. The optical properties in one layer may be different from the other layer. To acknowledge this difference, we denote the optical

properties in the top layer by (HbO_{2top}, Hb_{top}, μ_{s1}') and those in the lower layer by ($HbO_{2bottom}$, Hb_{bottom}, μ_{s2}'), as shown in Figure 3.7.

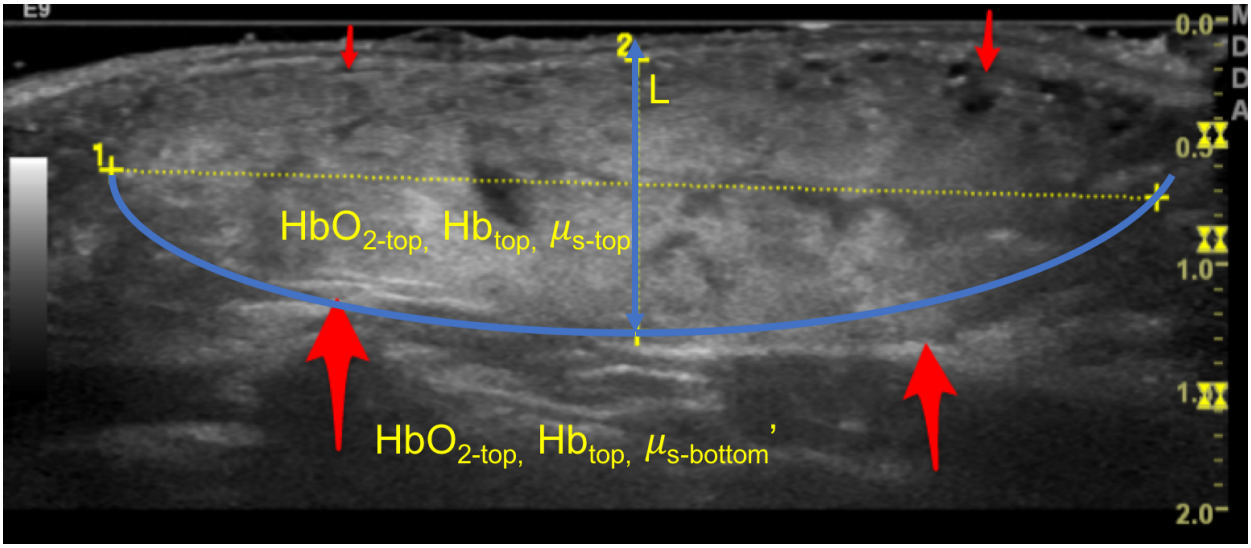

Figure 3.7 Ultrasound image of a deep IH from a patient in our IH-DOS measurement clinical study. Radiologist measurements of the length and depth (L) are in dotted yellow. Labels show how the two-layer model separates the optical properties of the IH and the underlying layer.

3.5.3 Numerical Simulations

Numerical simulation experiments were conducted to evaluate the capabilities of the reconstruction algorithm to accurately measure the different absorbers in a two-layer medium. This algorithm is capable of reconstructing optical properties of human tissue, specifically chromophores of [Hb], [HbO2], lipid, and water concentrations. In addition, the algorithm can also reconstruct optical properties for phantom experiments, namely ink and water concentrations. For purposes of characterizing the algorithm's capabilities, numerical simulations were done for both cases of human tissue and phantom measurements.

The numerical simulation experiments are done in two parts. First, simulated data must be created by the reconstruction's forward model, and second, using the simulated data, reconstructions of the tissue or phantom's medium properties are computed. In order to create simulated data, a

forward calculation is made with known properties of the simulated two-layer medium. These forward calculations provide the theoretical reflectance data acquired at the detector of the experimental setup. This simulated reflectance data sets were then used in the two-layer reconstruction algorithm to compute the optical properties of the two layers.

To simplify the numerical simulation experiments, parameters were either assumed to be known or assumed to be equal between the two layers. Specifically, the depth (L) was assumed to be known, since the depth of an IH lesion is commonly computed using US imaging, particularly with IH that can affect the functionality of surrounding organs. In addition, the scattering amplitude and power is assumed to be equal between the two layers. This is due to the limitation of continuous wave DOS imaging, which makes it difficult to accurately separate scattering from absorption coefficients when reconstructing optical properties. It is expected that the number of potential unknowns (N=7) is too great for the number of source-detector pairs (N=8) and that not enough information is provided for the reconstruction algorithm making the problem largely ill-posed compared the semi-infinite based model.

When reconstructing the optical properties of the simulated two-layer medium, an initial guess of the optical properties of the medium must be provided to be used as a starting point for the algorithm to reconstruct the actual properties. If the starting point is the exact properties of the medium, then obviously, the reconstruction algorithm will immediately reconstruct the medium with accurate results. Because of this, the initial guess made for each unknown parameter was randomly made with a starting point within the mean of the provided range for the particular

chromophore. For example, if the range for reconstructing [Hb] is from 5 to 250uM, then the initial guess for the chromophore is 127.5uM.

For numerical simulations based on simulating different IH lesions with different depths and optical properties for the "top", or IH layer, while keeping the "bottom", or normal tissue layer constant for different experiments. Because IH lesions will have a much higher absorption than the bottom layer, due to the higher concentration of HbO2 and Hb in the lesion, the parameters will be such that the total hemoglobin concentration ([HbT]) will always be higher than that of the normal, "bottom", layer. In addition, the IH lesions are proposed to be hypoxic compare to the normal tissue, and as such the concentrations of [HbO2] and [Hb] will vary such that the %Sto2 will be lower than that of the bottom layer. The SNR of the reconstructions were set to 20 to simulate noise acquired during acquisition. Table 3.5 contains the values of the simulated tissue properties [HbT] and %StO2 and Figure 3.8 shows the error results of the reconstructions.

Tissue Simulation	HbT ([uM])	StO2%
IH Layer (Proliferative)	450	44
IH Layer (Plateau)	250	60
IH Layer (Involuting)	100	75
Normal Tissue Layer	65	77

Table 3.5 Values for simulated properties of IH diseased and normal tissue layers.

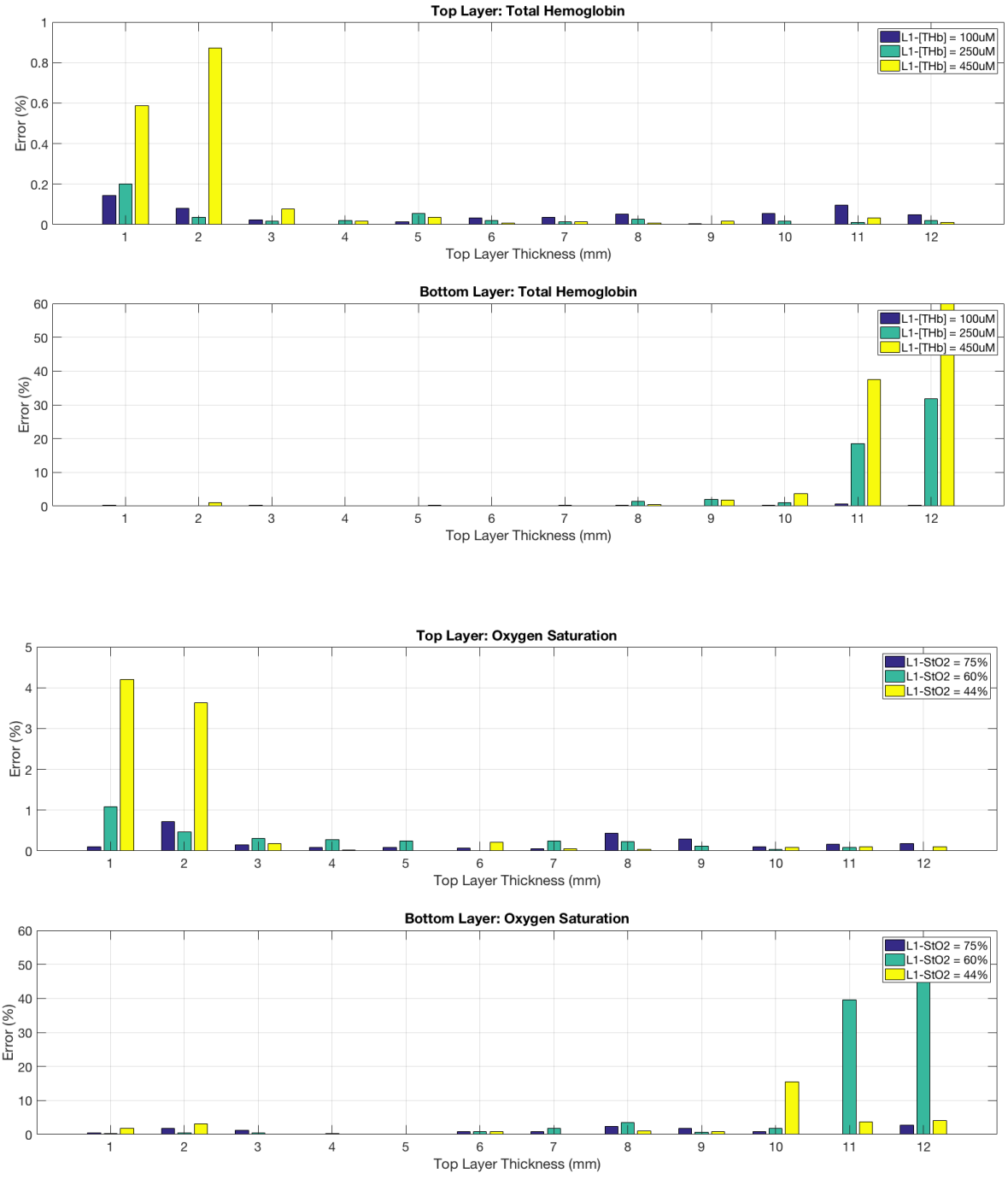

Figure 3.8 Computed error of reconstruction results that simulate IH diseased and normal tissue layers. (TOP): shows the total hemoglobin concentration error for top layers, given 3 different simulations. The bar graphs on the bottom layer show the accuracy of the properties of the bottom layer provided the depth and the concentration of the top layer. L1 denotes "layer 1" or top layer. (BOTTOM): error of the reconstructions of StO2%. This demonstrates the algorithms ability to discriminate different chromophores.

The optical and physical parameters chosen for the numerical study was derived from the results of our clinical study, based on the semi-infinite medium based reconstruction algorithm. Our clinical results showed IH depths of 0.1cm to 1.5cm and a range of THb from 120 to 400uM for the first layer. The simulations created had a linear profile of depth to THb concentrations. The StO2 was also varied for each THb and depth profile. The StO2 in these simulations were 30%, 60% and 70%. This simulates a highly hypoxic, moderately hypoxic, and non-hypoxic tissue. The second layer, simulating normal tissue, assumed a THb of 65uM and a StO2 of 77%. Scattering power was assumed to be equal in both layers. To evaluate the improvement in accuracy using a priori or assumed information, experiments were done using a known depth. This would simulate the use of a high spatial resolution imaging such as US to determine the depth of the lesion.

The results for the first layer show that the reconstructions fall within 5% of the actual value of HbT and StO2. The measured results of the optical properties from the second layer is not as accurate as the top layer and the accuracy varies greatly for different first layer depths. This is due to the fact that the larger the depth of the top or diseased tissue, the less amount of light is penetrated to the bottom layer, and consequently, the amount of light reflected back to the detector is even lower. This makes for an inaccurate measurement for the bottom layer, but fortunately, the optical properties of the top or diseased layer are most important and it may be assumed that for a certain thickness of IH tissue, the medium can to modelled as semi-infinite. Results from the second layer show that the properties are accurate within 5% up to depths to 10mm. Beyond 10mm, the properties of the bottom layer reconstruct with an error up to 52%.

In addition to simulating optical properties of tissue, I evaluated the algorithms ability to reconstruct simulated phantom data. Simulating phantom data was done to help design a physical phantom study. This way, the actual phantom results can be compared to the theoretical results. In

this simulation, I created two profiles for a two-layer phantom. The first profile consists of a high absorbing top layer, simulating the high absorption of an IH lesion. The second profile is a lower absorbing layer than the first, simulating an IH lesion that is in its plateau or involuting stage. The second bottom layer has a lower absorption than the top layers two profiles. The scattering coefficient for this simulation is equal for all layers. Table 3.6 contains the absorption and reduced scattering coefficients for the simulated phantom, and Figure 3.9 shows the error of the reconstructed values against the actual values.

Phantom Layer	"Top" Layer (Low)	"Top" Layer (High)	"Bottom" Layer (Solid phantom)
Absorption (cm^-1)	0.537	0.895	0.179
Scattering (cm^-1)	8.93	8.93	8.93

Table 3.6 Optical properties of a simulated phantom design. Two profiles are shown: a lower absorbing top layer profile and a higher absorbing top layer profile. The bottom layer properties are the same for both profiles.

Results of this phantom simulations show that the lower absorbing profile can be accurately resolved even at depths of 12mm for both top and bottom layers. However, for the higher absorbing profile, the results are only accurate within 99% for the top layer. For the bottom layer of the higher absorbing profile, the accuracy is within 99% up until a top layer depth of 9mm, at which point the optical properties of the bottom layer cannot be accurately resolved. In the next two sections, I will describe a physical phantom and report experimental results based on the two profiles simulated in this section.

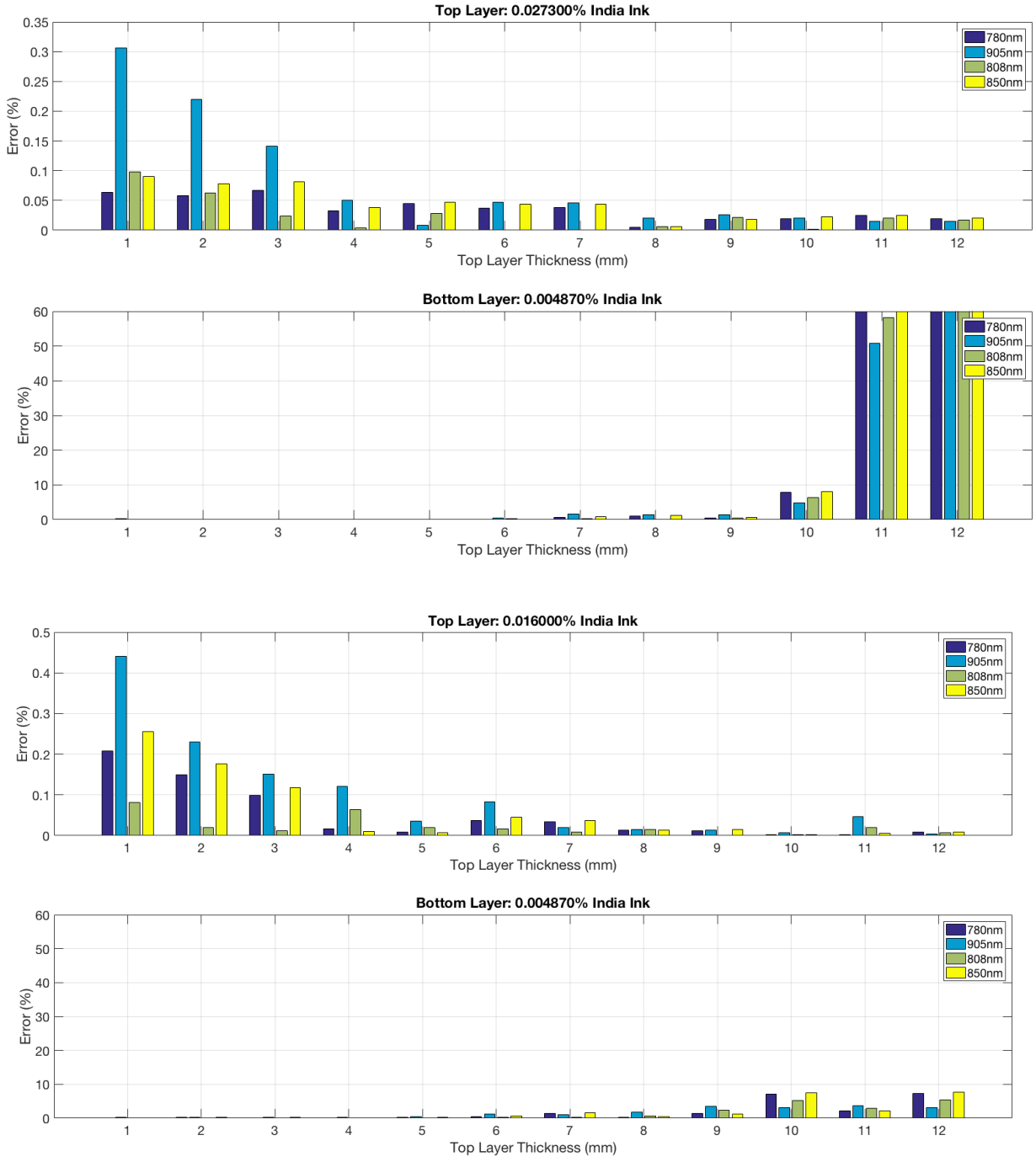

Figure 3.9 Reconstruction results of simulated phantom data. (TOP): This figure shows the error of the reconstruction for the higher absorbing profile, in which the top layer absorption coefficient is ua=0.895(cm^{-1}). (BOTTOM): This figure shows the results for the lower absorbing profile, which demonstrates that the properties can be accurately resolved at this lower absorbing coefficient of ua=0.537(cm^{-1}).

3.5.4 Two-layer Phantom Design

To verify the use of the two-layer algorithm experimentally and to demonstrate the viability of the reconstruction algorithm, the numerical study was translated into phantom experiments to simulate real tissue. Various groups have created two layer optical phantoms to simulate skin and skin lesions such as melanoma [104-108]. Although there were several designs to utilize as a baseline for a two-layer phantom, I choose the design from Bianco et. al., in which a phantom was produced that used U-shaped spacers of different thicknesses and mylar sheets as a clear separator to create multiple wells to hold liquid solutions to simulate multiple layers of tissues with different optical properties [109]. Since this design was the most applicable for simulating an IH lesion while using liquid solutions to simulate tissue, I used this design as the backbone for my phantom design.

Implementation of the design however was not a robust solution for reproducibility, and the making of a two-layer phantom while using liquid solutions took many iterations of design for a successful phantom design. The initial two-layer phantom design that was be created was a two-well box that can hold liquid solutions that simulate optical properties of that of human tissue. As with Bianco et al, I used U-shaped spacers that were made from laser cut acrylic that were 4mm thick. The spacers were stacked to make up the proper volume of the two wells, which was 1 to 15mm thick for the "top" or IH diseased layer and 100mm for the "bottom" or normal tissue layer. The large depth of the second well is due to the assumption that the second layer is a semi-infinite medium. The two wells will be separated by mylar film that is only 20um thick. This mylar film also is used as a window to the outer box so that the WHDD can make as close a contact to the liquid solution as possible. Each layer of spacer and mylar window separator were sealed using RTV silicone to prevent leaking. In order to hold the phantom wells together and to prevent leaking, seven 15cm long socket caps are pushed through the entire phantom with wing nuts

screwed into the other end to secure all phantom parts together. A photo of the design is shown in Figure 3.10.

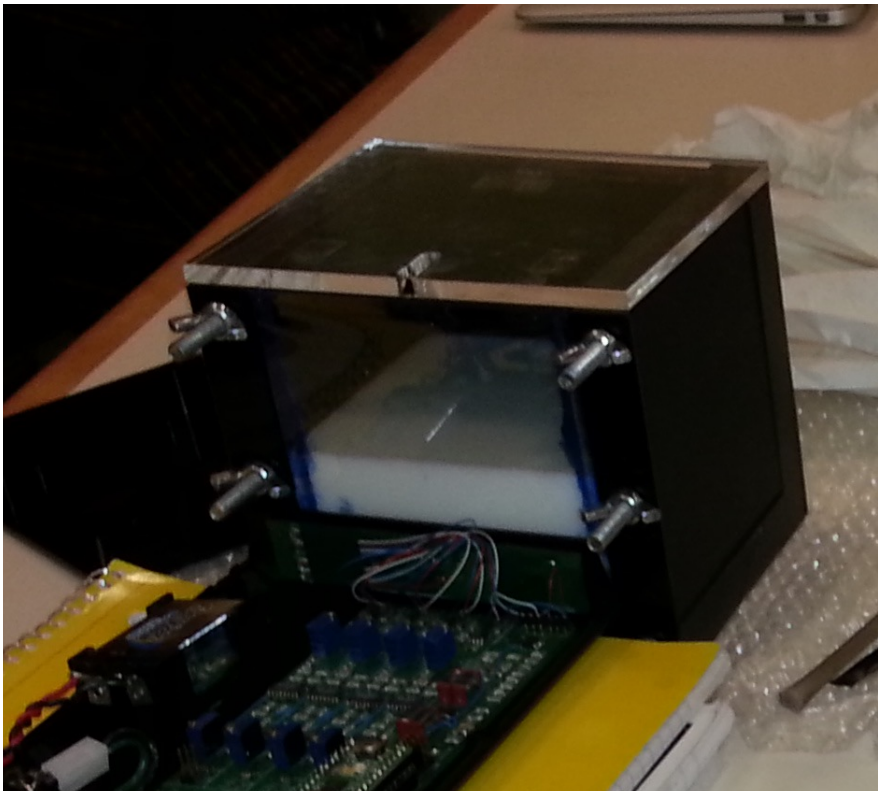

Figure 3.10 Photo of the first two layer phantom design. A prototype of the WHDD is shown imaging the phantom at the mylar window.

Two major issues with the design of the phantoms was securing a leak-free enclosure for the liquid phantom solutions and designing the wells such that inserting and removing the liquid solution. With two different absorbing and scattering solutions, it was important that the solutions do not interact with each other. In addition, leaks from individual wells was also an issue, as the liquid solution is costly and difficult to make. As such it was important for us to preserve the solution.

To solved the problem of leaking and repeated use, silicone spacers were used instead of using the combination of acrylic spacers and RTV silicone. These silicone spacers were designed similarly to the acrylic spacers but was implemented differently. In order to create the spacers, an aluminum

sheet of 30mm thickness was milled to create moldings for the two-part silicone mixture (Dragon Skin 20). Four moldings with different depths (1, 3, 6, and 10mm) were milled into the aluminium sheet (Figure 3.11).

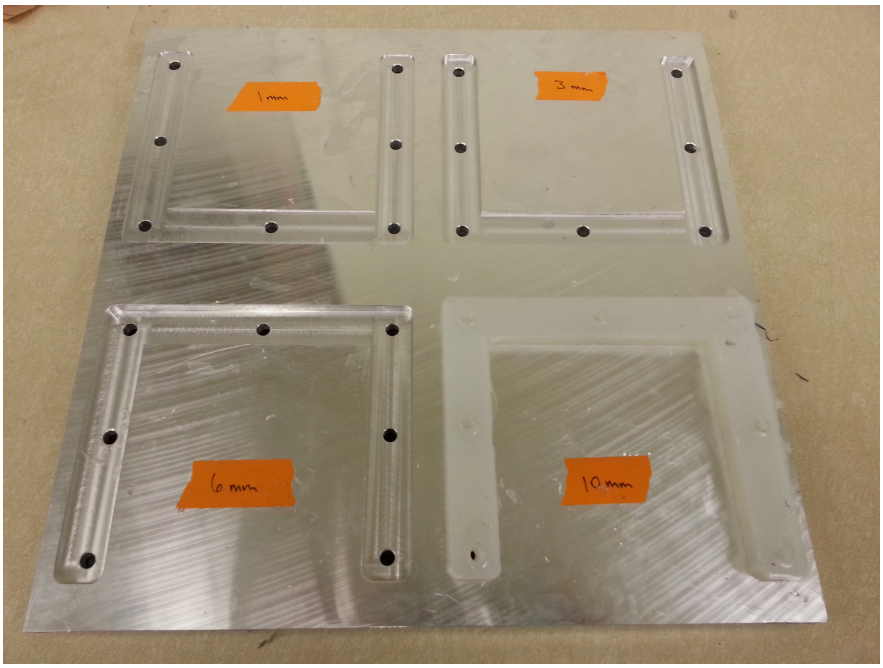

Figure 3.11 This aluminum sheet was milled to create a molding for the silicone spacers.

Once the silicone mixture cured (About 24hr cure time), the spacers were stacked in the same way as the acrylic spacers. Mylar sheets were used to separate the wells, and screws were used to tighten and hold the phantom in place (). This design of using silicone made the spacers double as a spacer for the well and a gasket to prevent leaking. The silicone design also was easier to use and reuse, as RTV silicone did not have to be replaced when modifying the phantom for a different well thickness. Unfortunately, the use of silicone spacers with the screw tightening caused the silicone

to compress much more than expected, and with the use of the mylar windows, the thickness of the "top" layer well could not be accurately measured.

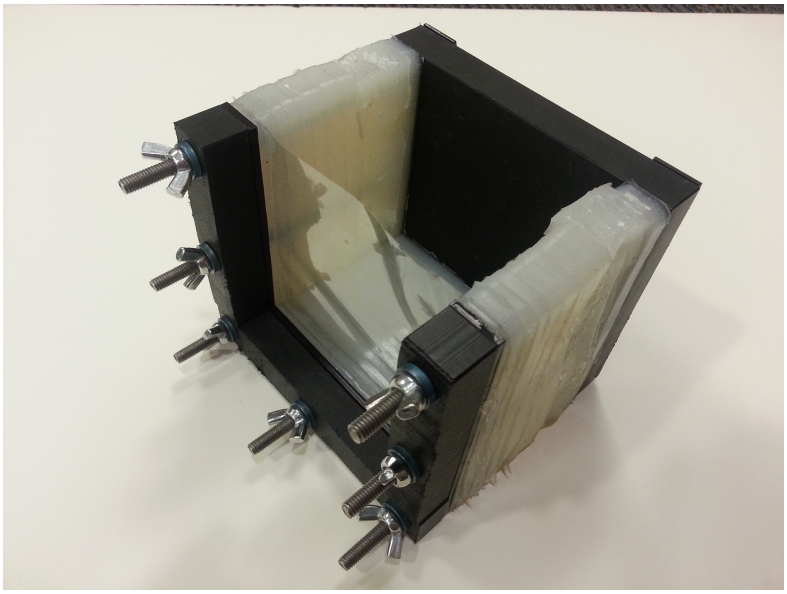

Figure 3.12 Phantom design with silicone spacers. The silicone in this design made a tight seal to prevent leaks but was not rigid enough to accurately measure the thickness of the "top" well.

Due to the difficulty of using liquid solutions for a multi-layer phantom, a half solid, half liquid solution phantom design was implemented. In this final design, a single well with dimensions of 10cm x 10cm by 12cm was created, where a 10x10x10cm solid phantom (Biomimic, INO Québec, Canada) was used as the lower absorbing bottom layer and a high absorbing liquid solution was used as the top layer. The properties of the solid phantom are shown in Table 3.7. A clear Mylar window at one end was used so that the DOS probe could be placed and the phantom could be imaged with minimal interference from the clear window. A Solidworks image of the design, as shown in Figure 3.13 shows the single well phantom for two-layer measurements.

	INO Phantom Block Optical Properties (1/cm)			
WL (nm)	670	780	808	850
Predicted (ua)	0.15	0.15	0.15	0.15
Predicted (us')	8.5	8.5	8.5	8.5
Measured (ua)	0.214	0.179	0.173	0.168

Measured (us')	9.31	8.93	8.97	8.72

Table 3.7 Optical properties of the INO solid phantom block. Predicted values are the values submitted to INO. Measure values are the actual optical properties.

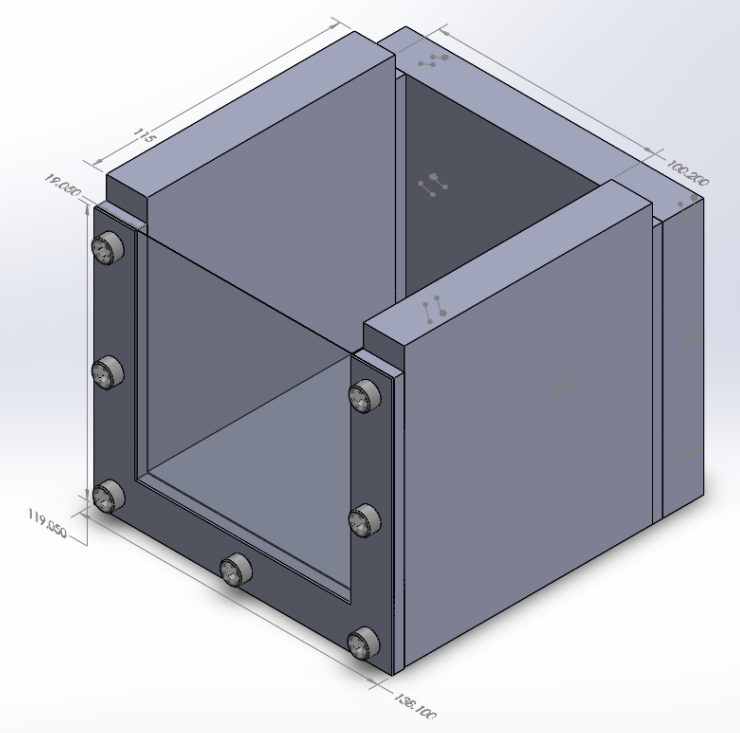

Figure 3.13 Solidworks design of a two-layer phantom mold that contains two wells to hold tissue-simulating solutions for optical spectroscopic measurements. The front well will simulate the IH lesion while the larger second well will simulate normal tissue. The spacers can be changed and adjusted by unscrewing the container.

In this design, the solid phantom was wrapped tightly with one layer of Saran wrap and placed into the well such that there was 1 to 15mm of space between the solid phantom block. In the space between the solid phantom block and the mylar window, the liquid solution that consisted of water, ink and Intralipid was inserted. To adjust the depth of the layer of liquid solution, the solid phantom block could be place back and forth to a set distance from the mylar window. A small metric ruler

was placed onto the edge of the phantom well to accurately adjust the depth of the first layer. A photo of the final phantom design is shown in Figure 3.14.

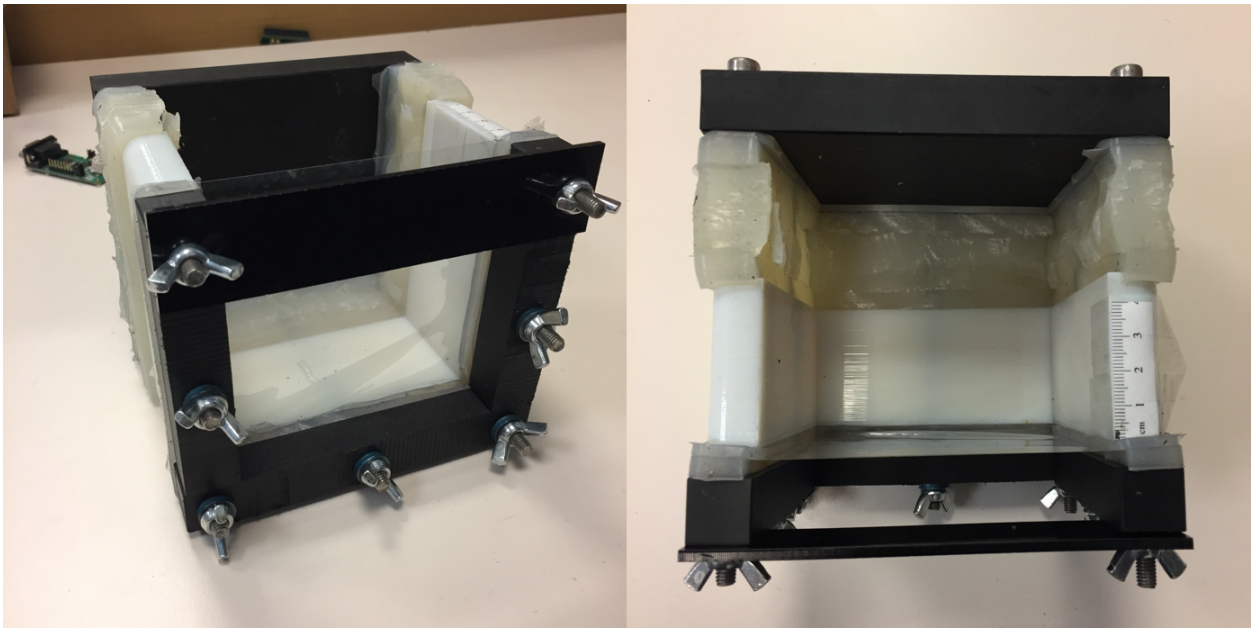

Figure 3.14 Photos of phantom well with modified front window with increased tension for more accurate two-layer measurements.

3.5.5 Discussion

Infantile hemangiomas (IH) are vascular plaques that proliferate during early stages of life. Its presentation consists of a nodular tumor of varying classification (Deep, superficial, mixed) with normal tissue surrounding it. In section 3.4, I describe a clinical study in which IH optical properties were measured using a reconstruction algorithm that assumes a semi-infinite medium. Although the results were promising, a two-layer model better represents the IH overlaying normal tissue. To this end a two-layer reconstruction model was developed. The reconstruction algorithm was characterized using various numerical simulations that varied the absorption of the "top" IH layer while keeping the absorption from the "bottom" layer constant. The scattering coefficient was assumed to be constant and equal for both tissue layers. The depth of the top layer was assumed to be known, corresponding to the use of Ultrasound imaging to determine the thickness and size of the IH. The theoretical experiments modelled both tissue and phantom based mediums

accurately within 95% for most cases. It was observed that at “top” layer depths of 9mm and greater, the error of the reconstructions exceeded 10% and reached as high as 50%.

To characterize the two-layer model even further, the numerical simulations were translated into a phantom study, in which a large phantom well that contained a solid phantom with well characterized optical properties and a liquid solution that was optically absorbing and scattering were used simulate the two-layer IH-normal tissue layers.

Future work would consist of imaging IH subjects on the same day as the Ultrasound imaging to ensure that the depth of the lesion is accurate to the measurements time of DOS. US was only performed as clinically indicated and we do not have data for all patients. Unfortunately, US was never perform on the same day of the DOS measurements. To expand on the two-layer measurement study, it will be important that US and DOS imaging be done at the same time. In addition, there are groups that have implemented a US-DOS probe to perform the measurement simultaneously [110-112]. A system as such would be beneficial to hemodynamic research of IH lesions as it can provide accurate a prioi data for DOS reconstructions.

4 Optical Imaging Techniques for Monitoring Treatment of Rheumatoid Arthritis

The content for this chapter focuses on the effort towards achieving Aim 3 of this dissertation, where the objective is to compare the sensitivity of optical measurements of the WHDD to the proven capabilities of a frequency domain optical tomographic (fDOT) system for a clinical study monitoring the effects of treatments for patients with RA. In this chapter, I will first provide an overview of RA and its prevalence, the current treatment strategy, and the clinical and radiological imaging measures used to characterize the severity of the disease. Next, I will describe the current optical imaging techniques used for imaging RA and the outcomes. This will include the previous work from our research lab. I will also describe the system and techniques used by our lab's fDOT imaging system used to diagnose RA. Finally, I will describe a longitudinal treatment study for patients suffering from RA. I will provide fDOT and WHDD results and compare them both to each other as well as the clinical measures.

4.1 Rheumatoid Arthritis

Rheumatoid arthritis (RA) is a systemic, chronic, inflammatory autoimmune disorder that causes chronic inflammation of the synovial membrane of small and large joints [113, 114]. RA is characterized by the persistent synovial inflammation and damage to the associated articular cartilage and underlying bone, typically in the peripheral joints and their surrounding tendons and ligaments [115]. While RA can be mild, it can also be severe and can be associated with significant pain and disability, with studies showing that up to 10% of individuals suffering from RA can experience total disability [116].

RA affects 1% of the population worldwide, with approximately 1.3-2.1 million people in the US [117-119]. The disease also leads to 5–50 per 100,000 new cases annually [120] and leads to 9

million physician visits per year in the US [121]. Women are about three to four times as likely as men to develop RA [120]. RA can occur at any age, although it is more likely to occur among those aged 40-70 years and its incidence rate increases with age. Fifty percent of the risk for development of rheumatoid arthritis is attributable to genetic factors. Smoking is the main environmental risk.

Subjects with RA can suffer from severe pain, joint stiffness, swelling of multiple joints, and lack of joint mobility. Symptoms primarily affect the peripheral joints, with common joints being the wrists, proximal interphalangeal (PIP), and the metatarsophalangeal joints [115, 121]. Uncontrolled, the symptoms can lead to self-limiting arthritis or rapidly progressing multi-system inflammation with significant morbidity and mortality (including cardiac, neurological, and hematological complications) [115]. These symptoms can eventually lead to severe disabilities and loss in quality of life. The severity of RA has been classified by different authors have providing classifications of the disease progression into different stages [118, 122].

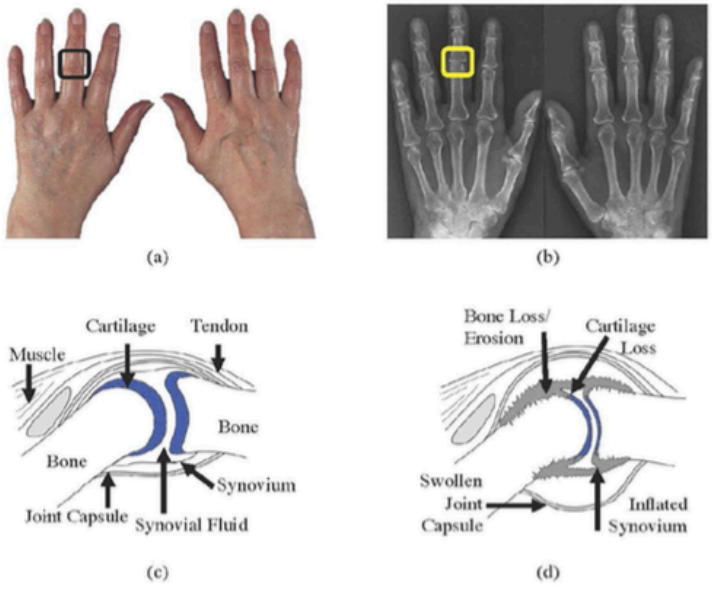

Figure 4.1 (a) Example of symmetric synovitis affecting the hands, highlighting the location of a PIP joint. (b) X-ray images with radiographic evidence of RA, highlighting the location of a PIP joint. (c) Illustration of a typical healthy joint. (d) Illustration of a typical joint exhibiting symptoms of RA. (c,d) Schematic of a typical synovial joint.

The pathophysiology of RA is not completely known, but in the past 10 years there has been several key advances into the pathophysiology of RA [123, 124]. At its onset, the synovium sublining undergoes alterations, resulting in prominent infiltration of mononuclear cells such as T-cells, B-cells, macrophages, and plasma cells. Overproduction and over-expression of TNF is one of several key inflammatory forces in RA, and is known to drive synovial inflammation (Synovitis) and joint destruction [115]. The handicaps associated with RA can result in large financial costs due to health care expenses and loss of productivity at work. Despite recent advances in therapeutic intervention including biological therapies, there is currently no cure for RA. Early treatment of RA, however, has been shown to significantly improve clinical outcome and management of the disease. It is, therefore, important to diagnose a subject with RA as early as possible.

4.2 Treatment of RA

There is currently no cure for RA [124]. Disease-modifying anti-rheumatic drugs (DMARDs), the key therapeutic agents, reduce synovitis and systemic inflammation and improve function. The leading DMARD is methotrexate, which can be combined with other drugs of this type, such as hydroxychloroquine, or sulfasalazine. Because of the poor prognosis of RA and the effectiveness of early treatment, it has become important to diagnose RA as early as possible [121].

Many pro-inflammatory cytokines, chemokines and growth factors are expressed in diseased joints, and the recognition of the key role of TNF led to the development of highly effective new therapies. It was shown that anti-TNF agents may inhibit joint damage. Recent pharmacological advances saw the introduction of the first set of biological agents that target TNF and are approved for use by subjects with RA. These agents include etanercept (Enbrel), infliximab (Remicade), and adalimumab (Humira). However, approximately only 50% of patients treated with the most commonly used non-biologic DMARD (methotrexate) adequately respond to treatment. Among

patients not responding to treatment with methotrexate or another type non-biologic DMARD, up to 20% are eventually placed on therapy with biologic therapy, typically a TNF inhibitor.

4.3 Clinical Measures

4.3.1 Laboratory Measures

Laboratory tests are commonly used in helping diagnose RA, however, they are not specific to RA. The presence of biological markers, such as rheumatoid factor (RF) and anti-cyclic citrullinated peptide (anti-CCP) antibodies, are used in diagnosis of RA. The presence of elevated titers of RF has been associated with a more severe disease course [125]. The erythrocyte sedimentation rate (ESR), a measure of the rate at which red blood cells settle, is generally a useful measure for following the course of inflammatory activity in an individual subject. Concentration levels of the C-reactive protein (CRP), an acute-phase reactant, may also be used to monitor the level of inflammation.

4.3.2 Clinical Imaging

Frequently, rheumatologists seek imaging evaluation of the joints in order to further support a decision to advance treatment or monitor response to treatment. Numerous imaging modalities are available to evaluate joint involvement in RA. Radiography (X-ray) can document bone damage (erosion) that results from RA and visualize the narrowing of cartilage spaces. Although effective, X-rays use ionizing radiation to generate images in the body that can potentially cause damage to DNA. In addition, although X-ray is a standard diagnostic tool for RA, it has long been recognized that x-ray imaging is insensitive to the early manifestations of RA, namely effusion and hypertrophy of the synovial membrane. To evaluate X-ray images, the Sharp method is a well-established and used widely in many studies. In this method, erosions and joint space narrowing

are scored in 17 and 18 areas in each hand respectively. The maximum score per single joint for erosions is 5, and for joint space narrow, 4 [126, 127].

Magnetic resonance imaging (MRI) is a highly sensitive and accurate imaging technique that does not require radiation and can evaluate synovial inflammation, as well as damage to non-bony articular structures. MRI is most useful in assessing soft tissue problems, avascular necrosis, degree of cartilage erosion, osteonecrosis and carpal tunnel syndrome [128-131]. Cumbersome use, large costs, and the need for contrast agents (e.g. gadolinium to detect increase blood volume caused by neovascularization in the hypertrophic synovial membrane) have prevented MRI from becoming a widely used imaging modality for detection of RA. Scoring of synovitis and erosions will be performed according to the EULAR OMERACT criteria using a semi-quantitative scoring system as previously described by Schirmer [132].

Ultrasound is used for the detection of synovial changes in RA and has been validated as a measure of hyperemia in RA inflammation. Previous studies have shown that Doppler US can detect synovitis in the small joints [133-135], and a quantitative estimate of the degree of inflammation can be obtained. The degree of joint effusion and hypertrophy will be evaluated and classified on a 4-grade semi-quantitative ultrasound examination score (USS) according to Szkudlarek et al. [136].

4.3.3 Clinical Assessment

Disease activity in RA is estimated using tools that take into account swollen and tender joint counts, patient assessment of pain, patient and evaluator global assessment of disease activity, measurement of acute phase reactants and evaluation of functionality. These assessments help the

clinician decide how to adjust the medication regimen making it essential to managing the disease. The following are three commonly used scoring indices.

Clinical Disease Activity Index (CDAI): The calculation of CDAI is based on four measures. The first two summates the number of swollen and tender joints (swollen joint count [SJC] and tender joint count [TJC]) using a 28-joint count (Scored 0-28). Next, a patient global assessment (PTGA) score is made and finally, a provider global assessment (PRGA) score is made. The final score for CDAI is given by the equation CDAI = SJC + TJC + PTGA + PRGA. As part of the joint count assessment, basic lab results such as RA related antibodies and levels of inflammatory markers will be collected if they have been obtained for the participants as part of their routine care [137].

Health Assessment Questionnaire (HAQ): The HAQ is a generic measure of functional disability and is the most widely used measure of functional disability in RA. This self-assessment questionnaire comprises a functional disability index (DI), a visual analogue scale (VAS) that measures pain, and a patient global VAS [138].

Short Form 36 (SF-36): The SF-36 is a self-assessment questionnaire designed for use in clinical practice and research, health policy evaluations, and general population surveys. The SF-36 includes one multi-item scale that assesses eight health concepts for both physical and psychological distress [139]. Table 4.1 Interpretation and scoring ranges for the five non-imaging clinical scores. provides an interpretation for the various scoring methods.

	Disease Activity Range			
Measure	Remission	Low	Moderate	High
CDAI	< 2.8	2.8 - 10.0	10.0 - 22.0	22.0 - 76.0
CRP	< 3.0	> 3.0 can suggest inflammatory disease		
ESR	< 15-30	> normal can suggest inflammatory disease		
SF-36	Scored 0-100, with 0 being severe RA			
HAQ-DI	Scored 0-3 with 3 being severe RA			

Table 4.1 Interpretation and scoring ranges for the five non-imaging clinical scores.

4.4 History of Diffuse Optical Imaging for RA Diagnostics and Motivation for Utilizing the Wireless Handheld DOS Device

Optical techniques for imaging peripheral joints for the purpose of diagnosing the presence of RA occurred as a result of studies in the 1990s, when researchers first reported on differences in optical properties between finger joints with and without rheumatic disorders [140]. It was found that in the early stages of RA, changes in the optical properties could be expected in the synovium and the synovial fluid.

The number of leukocytes, or white blood cells, increases from 100/mL to 200/mL in healthy joints to 1,000/mL to 100,000/mL during stages 1 and 2, respectively. This is particularly important for optical techniques, as leukocytes have a diameter of approximately 7-21um and therefore have a considerable effect on the scattering coefficient. In regards to optical imaging of finger joints, the differences in optical signals between healthy joints and joints of subjects affected by RA were strongest at wavelengths between 600 and 700 nm [141].

These indications lead to the development of several optical imaging systems and some pilot studies [140, 142]. In these studies, light from one or more wavelengths were focused onto the back of the finger and transillumination intensity profiles were recorded by a CCD camera. Some of the limitations of pure transillumination imaging of finger joints were overcome with DOT imaging studies. Our research team has focused in the past on application of DOT imaging for detecting and characterizing inflammation in RA. Our research team has focused in the past on application of DOT imaging for detecting and characterizing inflammation in RA. Analysis of reconstructed DOT images of absorption and scattering coefficients in the proximal

interphalangeal (PIP) joints 2-4 has allowed classification of PIP joints with and without RA with sensitivity and specificity of 78% and 76%, respectively [143, 144].

Our research team's most recent work involved a 56 subject clinical study in which we used fDOT to image finger joints 36 RA affected and 20 healthy volunteers in an effort to detect RA [145]. This is accomplished by deriving multiple optical parameters from the optical tomographic images and combining them for the statistical analysis. Parameters derived from the scattering coefficient perform slightly better than absorption derived parameters. Furthermore, it was found that data obtained at 600 MHz leads to better classification results than data obtained at 0 or 300 MHz. Using fDOT techniques we showed that sensitivities and specificities of 0.85 and higher can be achieved in detecting RA when comparing to healthy volunteers without RA. The features that provided that best classification between healthy and RA affected joints were max us', and stdev ua. Other features that provided a good classification between healthy subjects and those affected with RA are stdev us' and max ua. The fDOT imaging in this study was performed using a custom built system used for finger imaging [146].

Interpretation of features stdev us' and max ua has not been fully established. It is known through our previous work that a large stdev (ua, us') from the ROI likely demonstrates that the patient does not have synovitis in that joint. It is my hypothesis that while synovitis will create an accumulation of white blood cells, which is highly absorbing and scattering, optical properties are similar to that of the cartilage on the bone, making the optical properties uniform across of the joint. In addition, a large max (ua, us') may show that bone edema and erosion is not present at

articular cartilage or bone ends. In a longitudinal study, we can expect that these two features will change according to the drug response of the patient.

Furthermore, the use of fluorescence contrast imaging has also been shown to provide a good diagnostic measure of RA inflammation and disease progression [20, 147-150]. For example, Werner er al. [147] utilized indocyanine green (ICG)-enhanced fluorescence optical imaging (FOI) to assess inflammation in RA patients and found that FOI correlated significantly with Disease Activity Score 28, US, and the Rheumatoid Arthritis MRI Score while showing normal results in 97.8% of joints of controls.

Continuous wave DOT has been employed in a previous study [151], where a dual-wavelength tomographic imaging system DOT was used to measure hemodynamic differences in normal and RA affected joints. Based on 8 RA cases studies and 6 healthy volunteers, differences in the vascular reactivity exist between affected and unaffected joints. Analysis of the images have shown an enhanced vascular supply feeding the rheumatoid joint. Additionally, the dynamic hemoglobin characteristics support existing works that show a rise in oxygen consumption and metabolic activity in RA.

Unfortunately, the current optical imaging instrumentation used for RA research thus far contains large components that are difficult to transport, which may prevent it use in a clinical exam setting, or is not feasible for screening purposes. Similar instrumentation scaled to have a smaller form factor of the technology used in these studies may provide diagnostic capabilities appropriate for screening use, or treatment monitoring. To test this hypothesis, the WHDD was employed alongside the fDOT in a clinical study monitoring the treatment efficacy for RA patients. It is

predicted that the use of the WHDD would provide information of rheumatically affected joints compared to non-affected or normal joints.

4.5 fDOT Instrumentation and Imaging Protocol for Monitoring the Treatment of RA

To evaluate RA progression under treatment, I will compare two optical imaging modalities, diffuse optical spectroscopy (DOS) and frequency-domain diffuse optical tomography (FDOT). As explained in section 1.2.2, frequency-domain (FD) optical tomography provides more accurate information about mediums optical properties than continuous-wave (CW) methods. With a sensitivity and specificity about 0.85 from the fDOT system used by our research group in our diagnostic study [145], we employed this system as a study device in the longitudinal study attempting to reliably detect optical changes from synovitis in the PIP finger joints to determine the efficacy of the drug therapy. In addition, the WHDD presented in Chapter 1 will be used to determine if the sensitivity of the device can concurrently detect the same optical changes as the fDOT system.

4.5.1 fDOT System for Imaging RA

The fDOT imaging system that will be used as a benchmark for optical changes in the finger joints has been described in previous literature [40, 146]. The system is made up of two units: a tomographic unit that performs FD based transillumination measurements and a topographic scanning unit, that is used to create 3D renderings of the finger joints that will be imaged. The two units together provide transillumination and structural information that is required to reconstruct 3D absorption and scattering mappings of finger joints.

The tomographic system employed is a frequency-domain system that allows for source-modulation frequencies up to 1 GHz. As described in section 1.2.2, incident light that is modulated in the megahertz to gigahertz range, causes photon density waves (PDWs) to travel through the

finger [152]. Detection of amplitude and phase of those PDWs provides information about the damping and the time delay of the wave, which is valuable information for reconstructing the absorption and scattering properties of the finger imaged. The light source is a thermoelectric controlled laser diode (LDH-M-C-670, PicoQuant GmbH, Germany) with an average optical power of 8mW at the wavelength = 670 nm. The transillumination from the incident light is captured using an ultrafast gateable ICCD camera that provides RF modulated light amplification up to 1 GHz (PicoStar HR12, LaVision GmbH, Germany). Specific directions on how to operate the tomographic imaging unit can be found in "Operation Instructions 3D-TopoScan 2010-06-02.pdf" and "Operation Instructions TomoScan 2010-11-01.pdf".

In addition to the transmission measurements, accurate surface coordinates of the finger can be generated by a topographic laser scanner unit. Using this unit, the finger is scanned by two red laser lines at the back and the palm. The shapes of the deformed laser lines on the finger surface are imaged with a fast video camera (SPC 900 NC, Philips, The Netherlands), which is controlled by the DAVID laser-scanner software (ver. 1.6b, TU-Braunschweig, Germany). Using a combination of the DAVID laser scanning software, a custom-made program for mesh fusion, and FEM filtering software (MeshLab) a surface mesh of the finger is acquired. Finally, the surface mesh is used to generate a volumetric discretization of the surface encapsulated by the surface mesh, often referred to as a finite-element method (FEM) mesh.

Specific directions on how to operate the topographic imaging unit, including information on how to fuse the mesh data, can be found in "Operation Instructions 3D-TopoScan 2010-06-02.pdf" A

surface mesh of the scanned part of the finger can be created and a 3D finite volume mesh can be generated using GMsh software (v2.16 http://gmsh.info/).

4.5.2 fDOT Imaging Protocol

Before fDOT imaging, each finger is marked with a small black dot on the dorsal surface of the finger, 17 mm distal from the PIP joint. This mark is used to position the finger identically in both the fDOT imager and in the laser scanner unit. Then, the finger is place inside the FDOT scanner using the hand rest to hold the hand. The laser beam is then moved to the marked position. The finger axis (along the length of the finger) aligns with the scanning plane of the laser. Finally, scanning begins by moving the laser to the first source position, located approximately 10 mm distal from the PIP joint. The laser is then scanned over a range of 20 mm, from proximal to distal end of the finger (Figure 4.2). Each position represents a unique "source."

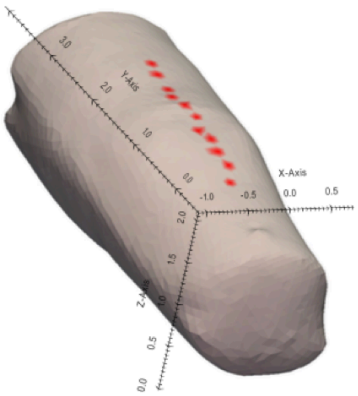

Figure 4.2 Positions of 11 laser sources on the dorsal side of the finger.

Transillumination (on the palmar surface) is recorded for each source position with the intensified CCD camera. The scan is performed twice, first in the forward direction with modulation frequency of 600 MHz, and then in the reverse direction at 300 MHz. Two examples of

transillumination obtained from a single surface source, as captured by the ICCD-based detector system, on the posterior (or palmar) surface of the finger are presented in Figure 4.3.

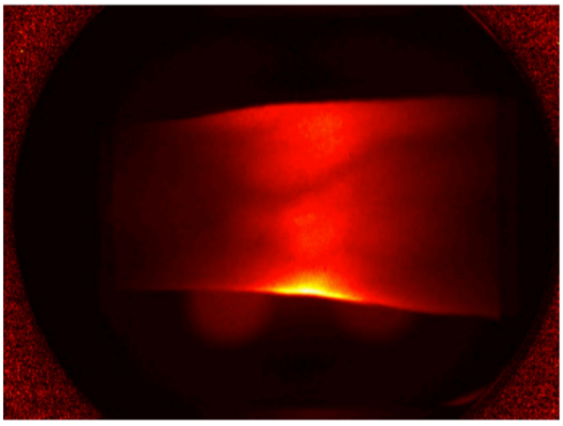

Figure 4.3 Transillumination captured by the ICCD detector unit on the palmar surface of a PIP joint from a subject with RA

Three fingers were scanned from the predominant hand of each subjects with RA and on both hands of control subjects; the index, middle, and the ring finger (PIP 2 to PIP 4). To avoid movement artifacts in the image reconstruction, the examiner controls the correct position of the finger again after the tomographic scan is finished. The complete tomographic scanning time needed for six fingers and two modulation frequencies was about 15 minutes, or about 7 minutes when using only one frequency.

4.5.3 Processing Prior to Reconstruction

As mentioned in the previous chapter, prior to imaging the finger joints, each finger is marked with a small black dot on the dorsal surface of the finger, 17 mm distal from the PIP joint. This mark is used to position the finger identically in both the fDOT imager and in the laser scanner unit. Although this solution is can be feasible for imaging patients, it can also be time consuming, as even subtle shifts left and right may occur and can go unnoticed until after the imaging procedure is complete. In addition, patients suffering with RA may have significant structural damage to the joint, which may cause the patient unable to straighten the PIP joint. This prevents

the tomo- and topo-scans from aligning correctly. That is, when source and positions are selected on the finger mesh, the corresponding pixel location of the CCD could be in another location due to the misalignment. To correct for these potential inconsistencies, an effort was put into place to programmatically align the joints utilizing the CCD camera images to locate the center of the joint and to be able to map the joint center of the CCD image to the finger mesh. In this section I will explain how X and Y axis offsets is computed to improve the mapping of the source and detector positions and pixel selection from the CCD images.

The acquisition of the CCD images produce the amplitude and phase of the laser transillumination from the finger. During the tomoscan, there are 11 positions along the sagittal plane of the finger that is illuminated for which the CCD acquires images (Figure 4.2). Along these 11 positions, it is expected that the source positions over the phalanx bones will have less light transmitted through the finger compared to the finger joint. From visual inspection from Figure 4.4, it is observed that the part of the finger with the highest amplitude also has the laser source directly over that location.

Once all 11 CCD images are acquired, the mean of these images is computed to create one image that produces the entire transillumination profile of the finger (Figure 4.5a).

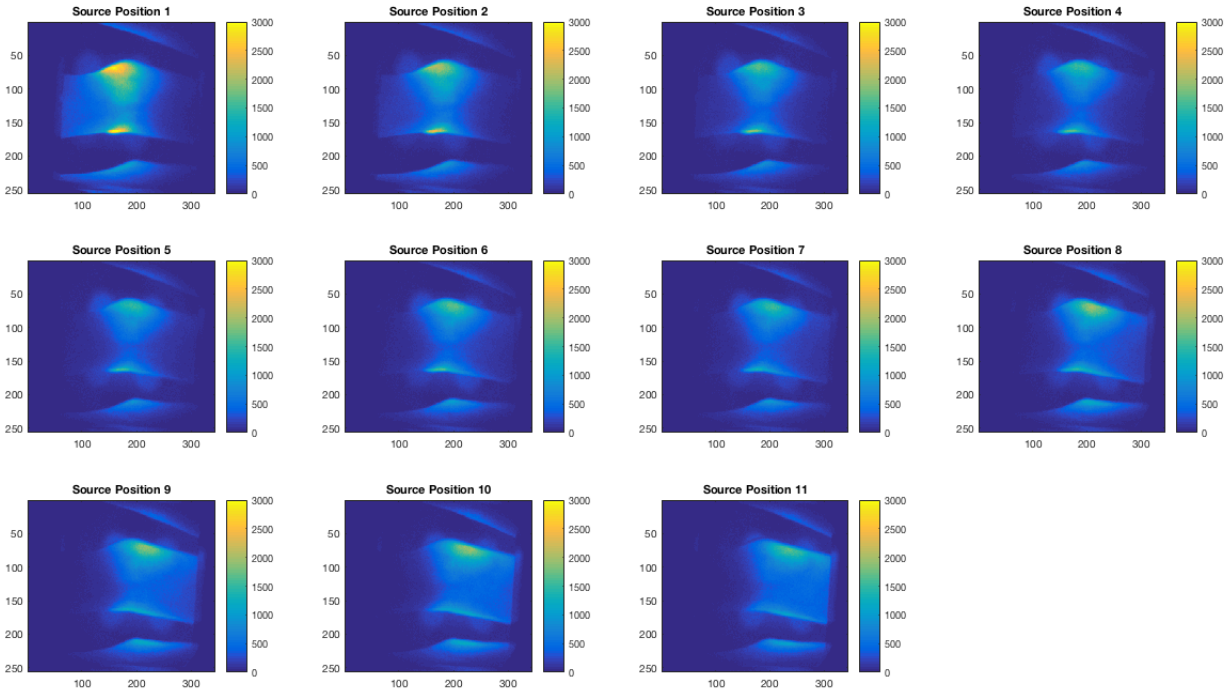

Figure 4.4 Amplitude measurements from the transillumination CCD images. Each subplot represents the amplitude image from the 11 source positions. From visual inspection, it is observed that the part of the finger with the highest amplitude also has the laser source directly over that location.

In addition to utilizing the amplitude images, the phase of the CCD images is used to locate the edges of the finger joint. Here, the phase conveniently creates a pseudo-mask in which the finger joint is distinguishable from the background of the CCD image (Figure 4.4b). Then, by using edge detection and median filters, a mask of the joint from the CCD image is created (Figure 4.5c). To account for images that may be noisy, a user input function is used so that the user can crop the

image before applying the edge and mask filters. Because user input can be a long and tedious task for multiple fingers and subjects, the CCD finger mask data is saved for later use.

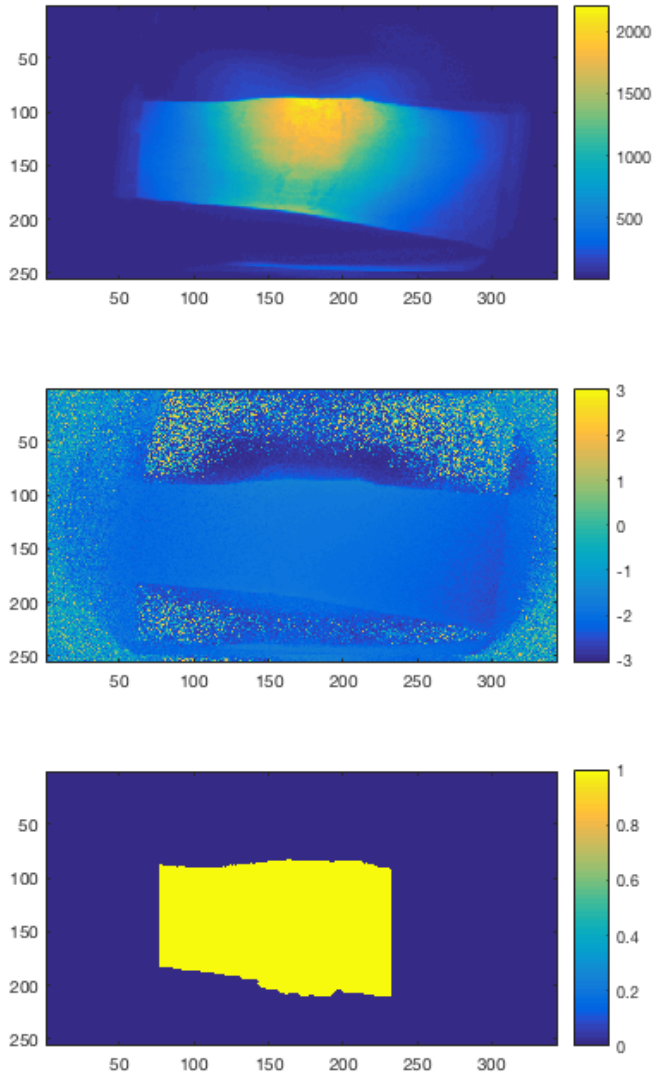

Figure 4.5 Using the CCD camera images of the finger joint to create a mask for the joint of the CCD image. (TOP) the average of the amplitude from 11 source positions. (MIDDLE) the median of the phase from the 11 source positions. (BOTTOM) a mask used to extract the detector positions from the CCD images.

With the amplitude profile and finger mask used to separate the finger from the CCD, the amplitude line profile in the X direction can be computed. The line profile can be represented as a second order Gaussian (guass2 in Matlab), and along with the amplitude line profile, the fitting for the profile is computed (Figure 4.6). This profile is used to determine the location of the center of

the joint. The center of the joint in the sagittal plane can be determined by computing the location of the pixel where the peak of the fitting is located. The pixel position where the peak is located is assumed to be the center of the finger joint. Using the finger mesh to determine the position of the center of the joint, the X offset can be determined.

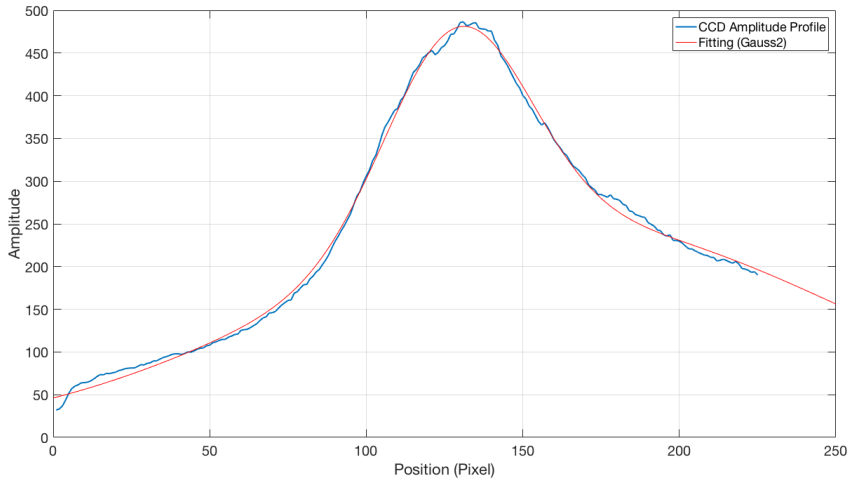

Figure 4.6 Amplitude profile across the sagittal plane of the finger. (Blue) The actual amplitude profile of the finger joint. (Red) The fitting of the CCD amplitude profile using a second-order Gaussian fitting.

To compute the offset in the Y direction for the CCD images, a combination of the CCD finger mask and the laser spot location is used. First, the laser spot location is predetermined prior to imaging. The position of the laser spot of the CCD images is determined by acquiring images without a finger or any object in the scanner. With a ND filter to reduce the laser intensity, the beam spot can be acquired without saturating the camera. The positions of the beam spots determine where the center of the finger (Y-axis) should ideally be located. Second, the mask of the finger from the CCD phase image can determine the actual center of the finger. The y-offset is

then computed by subtracting the y-axis location of the laser spot by the y-position of the center of the finger (Figure 4.7).

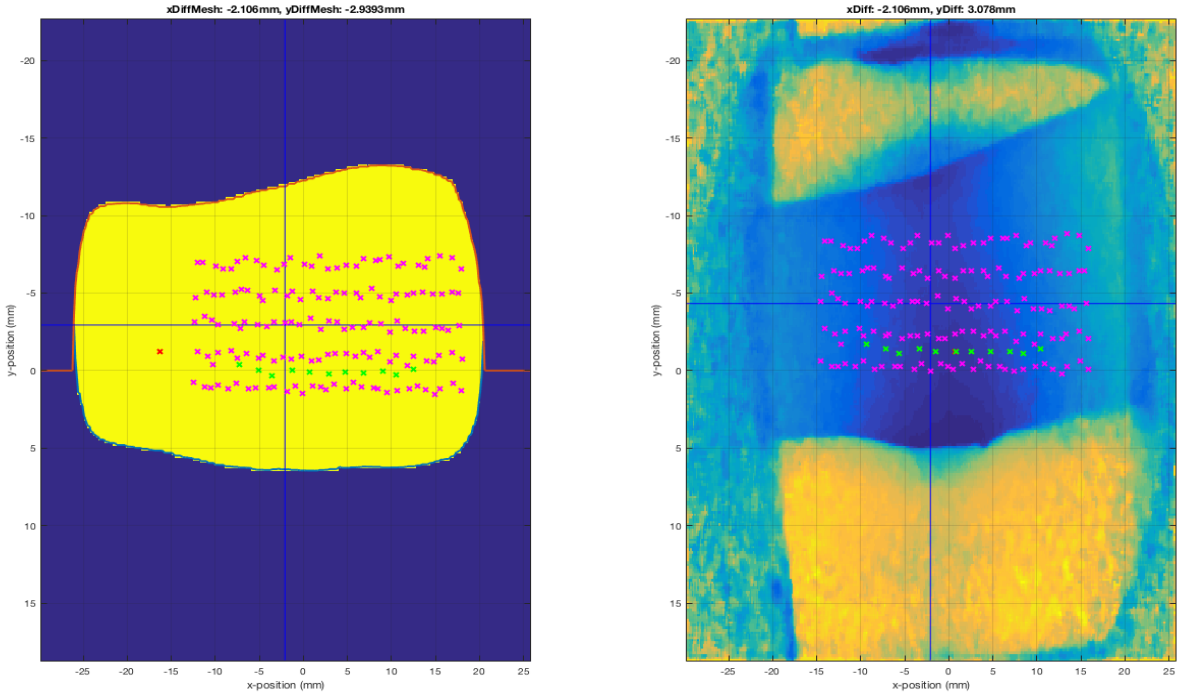

Figure 4.7 Alignment correction for mapping source positions and detector locations from the CCD image (Right) and the mesh projection on a 2D plane (Left). The blue crossing denotes the actual center of the joint as determined on the mesh projection and the CCD image. The green crosses in both images show the laser source positions and the magenta cross show the detector positions.

With the X and Y offsets determined, the mapping of the detector positions from the CCD to the source and detector positions on the mesh can simply be determined.

4.5.4 3D Reconstructions of Optical Properties from fDOT

Finally, 3D image reconstructions of absorption and scattering maps can be performed using the PDE-constrained reduced-Hessian SQP method [153], that solves the forward and inverse problems simultaneously. As a forward model, this code employs the frequency-domain equation

of radiative transfer [154, 155]. To be able to consider the refractive index mismatch at air-tissue interface [156], we implemented a partially-reflective boundary condition.

Given the spatial distribution of optical properties inside the medium, we solve the radiative transfer equation with a discrete ordinates method [156], which provides the prediction of measurements obtained on the surface of the medium. While reconstructing, the algorithm runs through multiple iterations to improve the estimate of the optical properties. For a given estimate of forward and inverse variables, the rSQP scheme makes the new iterate for both forward and inverse variables. Typically, the total reconstruction time was approximately 2-3 hours on a MacPro tower with an Intel Xeon 3.3 GHz processor.

4.5.5 Data Processing to Obtain 3D Reconstructions

Instructions on how to properly create FEM meshes from the toposcan, coregistering the toposcan to the tomoscan, and reconstruction of the finger data can be found in Appendix A.

4.6 Pilot Study to Evaluate Optical Imaging Techniques in Assessment of Joint Inflammation and Its Response to Treatment in Patients with Rheumatoid Arthritis

In this section, I will describe a clinical pilot study we employed to evaluate optical imaging techniques for the assessment of joint inflammation and response to treatment with patients with RA. From the previous results from our research group's diagnostic study on differentiating patients with and without RA, I used the same optical parameters that distinguished healthy and RA affect patients to characterize the effects of drug therapy during a 36-week longitudinal study. From our previous work, it was found that the features that provided that best classification between healthy and RA affected joints were max us', and stdev ua.

In investigating fDOT in this longitudinal study, I hypothesize that we can differentiate the severely affected from the non- or marginally affected joints at baseline. In addition, I predict that

a response to treatment will observe a higher standard deviation of ua and higher max us' over time in affected joints. Finally, I hypothesize that non- or marginally affected joints will not respond as highly to treatment than severely affected joints. To evaluate these hypotheses, I will compare optical trends to that of the clinical information provided. This will include self-assessment questionnaires, standard laboratory tests, and radiographic imaging.

4.6.1 Study Design

IRB approval was obtained from Columbia University Medical Center (CUMC) Investigational Review Board (Protocol# IRB-AAAI0501), and patients were to be recruited from the rheumatology practices at CUMC. A pilot study was employed in which patients with active disease were to be evaluated using optical imaging techniques of fDOT and DOS using the WHDD probe to study and track treatment response for RA patients. PIP joints 2-4 were measured (Figure 4.8) using these two optical imaging techniques to provide an assessment of the progression of RA throughout the trial.

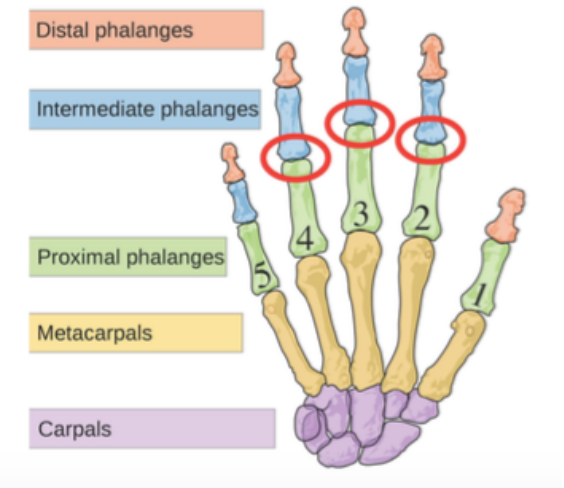

Figure 4.8 Bones of the human hand, highlighting in red the PIP joints 2-4 that were measured using fDOT and DOS using the WHDD probe. The PIP 1 joint denotes the thumb.

No investigational agents were tested as study participants received only FDA-approved therapies for RA following the current standard of care, with all treatment choices and/or changes made by

the subject's primary rheumatologist. RA adult patients with active disease (defined by CDAI >10) despite current methotrexate therapy who were being considered for treatment escalation were eligible for participation in this study. According to standard of care for patients with active disease despite methotrexate, study participant received either a second non-biologic DMARD (Disease-modifying anti-rheumatic drug) versus a biologic such as Humira in addition to methotrexate.

To assess and monitor disease progression while under therapy, several clinical scoring criteria were used at baseline (before initiation of treatment, or additional treatment) and at subsequently regular intervals of 2, 6, 12, 24, and 36 weeks. A list of the criteria is shown in Table 4.2. Under this criterion, patients were to be evaluated with optical imaging techniques, undergo a clinical assessment of their disease activity, and complete questionnaires regarding functional status. First, we compared changes in optical measures to changes in three clinical outcome measures: CDAI, SF36 and HAQ. Next, imaging modalities MRI, X-Ray and Ultrasound was used to assess the involvement of individual joints. Because MRI and X-ray are either expensive, time consuming, or radiative, these two imaging modalities were only used at baseline and at the end of the study, at 36 weeks. Ultrasound imaging was performed at all time points. Scoring guidelines from radiographic images as described in section **Error! Reference source not found.**. Finally, as part f their clinical assessment, standard of care laboratory studies such as RA related antibodies (anti-CCP, RF) and levels of inflammatory markers (CRP, ESR) would be collected if they have been

obtained for the participants as part of their routine care. In addition, we will also collect information from the subject regarding their RA and medication history.

visit study week	Visit 0 0	Visit 1 2	Visit 2 6	Visit 3 12	Visit 4 24	Visit 5 36
case History	+	-	-	-	-	-
demographic assessment	+	-	-	-	-	-
clinical evaluation	+	+	+	+	+	+
medication assessment	+	+	+	+	+	+
vital signs	+	+	+	+	+	+
CDAI	+	+	+	+	+	+
HAQ Score	+	+	+	+	+	+
SF36	+	+	+	+	+	+
Side effects	-	+	+	+	+	+
X-rays of hand joints	+	-	-	-	-	+
MRI of hand joints	+	-	-	-	-	+
Ultras. of hand joints	+	+	+	+	+	+
FDOT	+	+	+	+	+	+

Table 4.2 Timeline and criteria for monitoring progression of RA during drug therapy.

The aim of this study was to show that the tomographic algorithms and instrumentation developed are capable of detecting changes in optical imaging parameters in the finger joints with treatment. To this end, the results of the optical measurements were compared with changes in clinical disease activity measures of RA.

4.6.2 Study Subject

Over a three-year recruitment period, only one RA patient was enrolled into this study. Although we initially intended to enroll up to 20 subjects for this study, I will present the results as a case study for this work. Table 4.3 shows a clinical profile for our subject.

Clinical Profile	
Sex:	Female
Age:	42
Weight:	119 lbs
Height:	5'8''
Smoker:	No
Alcohol:	0 Drinks/Week

Drug Therapy at Baseline - 20mg Methotrexate once a week
Drug Treatment After Baseline - 20mg Methotrexate once a week - 2000mg Sulfasalazine seven days a week - 400mg Hydroxychloroquine once a week

Table 4.3 Clinical profile for this case study for RA treatment monitoring

This subject, a 42-year-old female, non-smoker, initially was taking 20mg Methotrexate once a week for treatment of RA. At enrolment, the subject was given additional treatment of 2000mg Sulfasalazine seven days a week, and 400mg of Hydroxychlorquine once a week. Both Sulfasalazine and Hydroxychloroquine are DMARDs that has shown to slow the progression of erosion, and have shown to inhibit TNF antibodies [113, 157-159]. Studies have also shown that the combination of Methotrexate, Sulfasalazine, and Hydroxychlorquine perform better together than each taken alone [160-162].

4.6.3 Non-Imaging Clinical Results

To assess and monitor disease progression while under therapy, several clinical scoring criteria were used, as mentioned in section 4.6.1. Within this criterion, there were several non-imaging clinical assessment scores, as presented in Table 2.1.

	Measure
Non-Imaging Clinical Scores	Clinical Disease Activity Index (CDAI)
	C-Reactive Protein (CRP)
	Erythrocyte sedimentation rate (ESR)
Self-Assessment Measures	Health Assessment Questionnaire (HAQ)
	Short Form 36 (SF-36)

Table 4.4 Table of non-imaging clinical scores and self-assessment measurement tool to assess the progression of RA.

Within the non-imaging clinical scores, the CRP and ESR are measures derived from standard laboratory blood tests. The scores for these tests will decrease if the progression of RA improves for the patient. Conversely, the CDAI measure, which is derived from a combination of a joint count assessment and self-assessment from the patient, will have it score increase if the progression of RA improves.

Figure 4.9 shows the results from the non-imaging clinical score measures. The CRP and ESR measures show that there was an overall improvement in the progression of RA. However, at weeks 6, 12, and 24, there was a fluctuation in the scores, suggesting that RA continued to progressed negatively. There was no data available at two weeks.

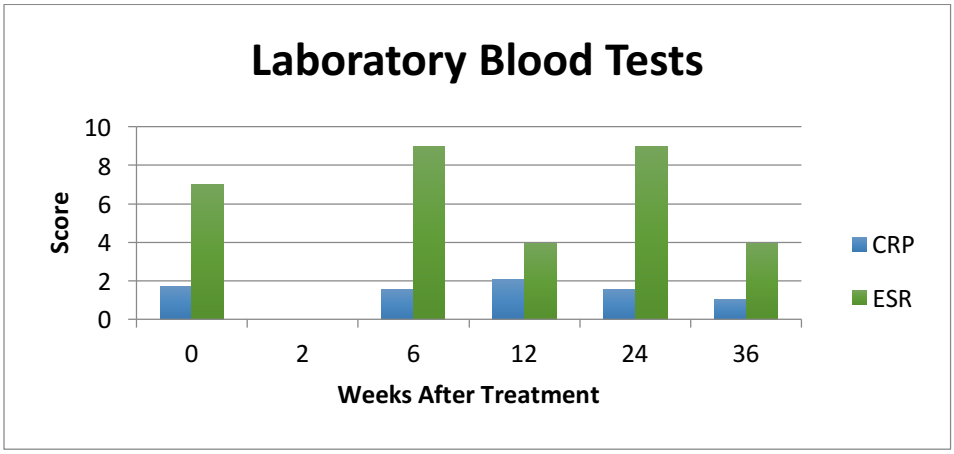

Figure 4.9 Laboratory blood test results for our case study.

While assessing joint count information using the CDAI scoring measure (Figure 4.10), the results showed an overall improvement of RA progression. As with the case with the blood test measures, there was fluctuation in the CDAI score over the course of the 36-week period. At the 2-week mark, CDAI score results more than doubled, which suggests that the subject had high disease activity just 2 weeks after the new treatment was administered. At 6 weeks however, the results dropped dramatically to its lowest point during the entire trial, but increased slowly for the remaining 30 weeks, to a moderate disease activity range. This suggests that according to the

CDAI, the medication took weeks to become effective. The CDAI score at 6 weeks suggested a low disease activity.

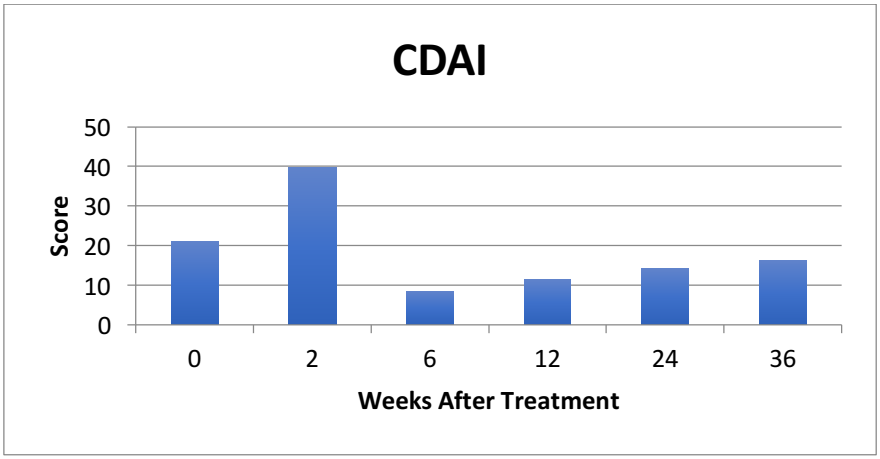

Figure 4.10 Results from the Clinical Disease Activity Index (CDAI)

Self-assessment questionnaires were used to evaluate the subjects' ability to do everyday activities such as opening a door and difficulty getting up in the morning. In addition, the questionnaires provide an assessment of mental health, since it is possible that even though the pathology and radiological scores of monitoring RA is not improving, the feeling of pain may subside. Figure 4.11 shows the results of the SF-36 self-assessment scores. The SF-36 results imply that the subject showed good improvement throughout the trial. This is evident especially at 6 weeks, where the

score nearly doubled from 2 weeks and held steady until the end of the trial. This jump at 6 weeks suggests that the therapy was most effective at this timepoint.

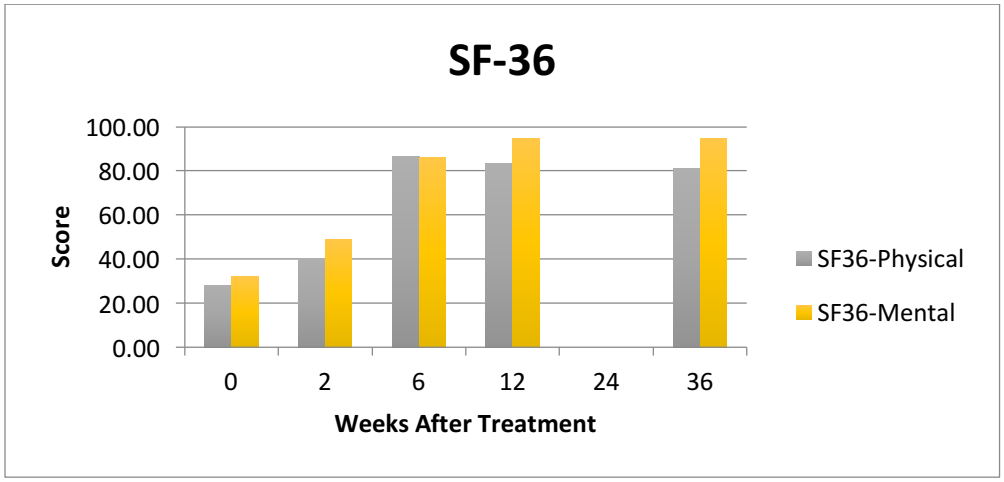

Figure 4.11 Results from the short form 36 (SF-36) assessment tests. Scores are out of 100, with a larger score corresponding to improvement to RA progression.

Finally, the Health Assessment Questionnaire – Disability Index (HAQ-DI), is a questionnaire to measure functional disability and is the most widely used measure of functional disability in RA (Figure 4.12). The HAQ-DI is a measure that decreases as RA reaches closer to remission. These results show that the drug therapy made a strong improvement to the disease activity at 2 weeks and stayed steady throughout the trial.

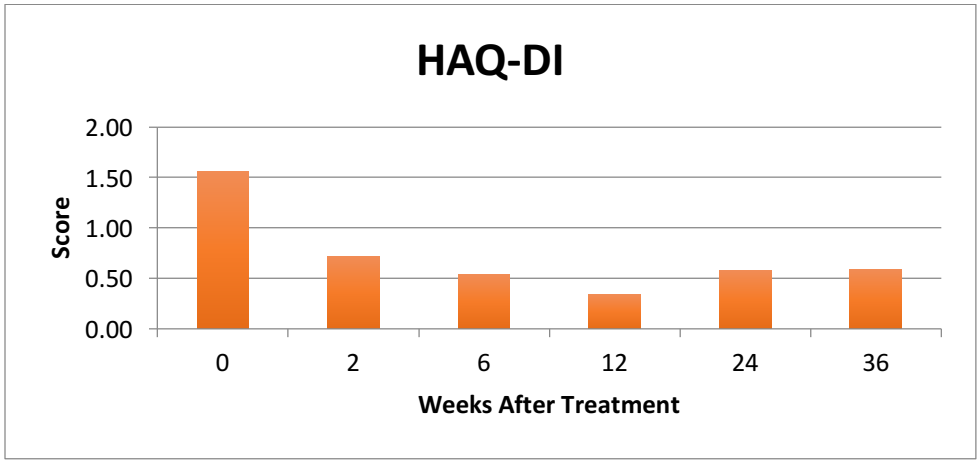

Figure 4.12 Results of the Health Assessment Questionnaire – Disability Index (HAQ-DI). Results suggest a decrease in disease activity over time.

Although there were fluctuations within the non-imaging clinical scores, all scores suggested that there was a reduction in the disease activity, showing that the drug therapy was improving the state of RA. Table 4.5 Summary of the non-imaging clinical results. provides a summary of these scores.

Measure	Result
CDAI	High disease activity after 2 weeks, reached low activity at 6 weeks but slowly worsened after
CRP	Worsened by 12 weeks but then improved by 36 weeks
ESR	Highly fluctuated. Overall showed improvement after 36 weeks
SF-36	Both mental and physical tests improved, with an increase of 100% at 6 weeks
HAQ-DI	Continual improvement up to 12 weeks, slightly higher disease activity thereafter

Table 4.5 Summary of the non-imaging clinical results.

4.6.4 Radiological Imaging Results

In addition to using self-assessment questionnaires, joint assessment, and laboratory measures, RA severity assessments to monitor disease progression while under therapy using radiological imaging scoring methods, as mentioned in section 4.3.2. These imaging modalities include X-Ray, MRI, and Doppler Ultrasound (US). Within each of these imaging modalities has multiple scoring criterion to assess structural damage and fluid assessment. A list of all of the imaging scores can be found in **Error! Reference source not found.**.

X-Ray Imaging: Traditional radiological imaging is used in RA to assess the structural changes that RA manifests to a subject. For this study, X-Ray's were only performed at 0 and 36 weeks. The two measures from X-Ray imaging are joint space narrowing and erosion (Figure 4.13). The x-ray results indicate that the right PIP 3 and left PIP 4 are the most affected joints that were scored. These joints did not exhibit a change during the 36 weeks. The joints that did observe a change are

the right PIP 2 and 4. During the course of the study, the joint space narrowing improved while the erosion in those same fingers worsened.

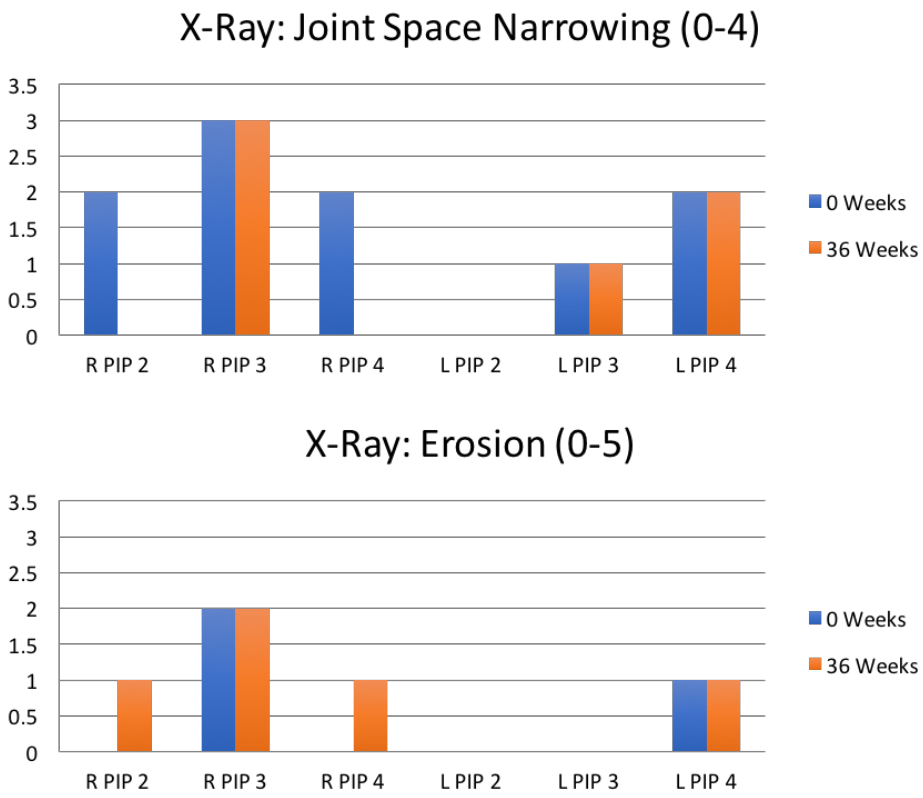

Figure 4.13 Quantitative scores for X-Ray imaging performed on our subject. (TOP): Joint space narrowing. (BOTTOM): Joint erosion from cartilage damage.

MRI Imaging: Imaging performed by MRI produces high resolution images which can provide detailed information of the soft tissues that may be affected by RA. MRI imaging is expensive, and requires long acquisition times. Because of these reasons, we only used MRI at 0 and 36 weeks. In addition, only the dominate hand (left hand) was imaged. The MRI scoring criterion include synovitis, erosion, and bone marrow (BM) edema (Figure 4.14). Results for MRI scoring present that left PIP 2 and 3 had marginal changes over the 36-week period for synovitis and BM edema. However, it was shown that erosion did not change in score. The joint with the highest severity of RA in the left hand was left PIP 4. Although joints left PIP 2 and 3 did observe a

worsening in severity, both joints were marginally worse and were not shown to be affected at baseline. The severity level of left PIP 4 corresponds to the severity level observed in the X-Ray scores.

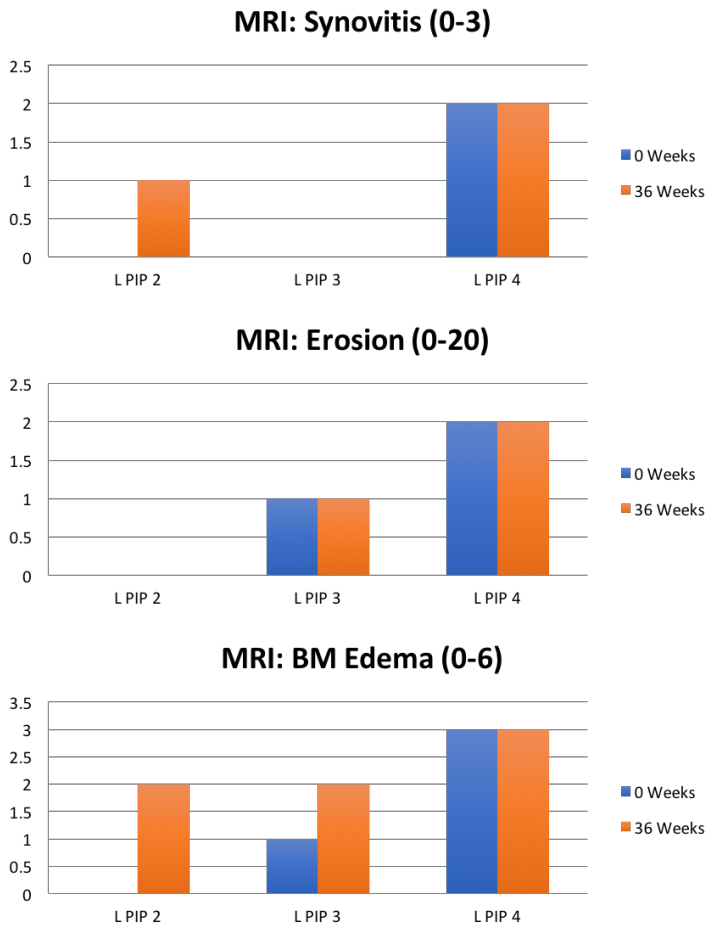

Figure 4.14 Quantitative scores for MRI imaging performed on our subject. (TOP): Synovitis score. (MIDDLE): Joint erosion from cartilage damage. (BOTTOM): Bone Marrow Edema.

Doppler Ultrasound Imaging: Doppler Ultrasound (US) was performed on the 6 PIP joints at all timepoints over the 36-week trial. Within the US scoring criterion, there are four measures: Joint effusion, synovitis, joint changes (erosion), and power doppler (vessel flow). A summary of the US results is shown in Figure 4.15. Most PIP joints analyzed showed that joint effusion worsened, with left PIP 2 initial showing improvement before worsening. Bone changes, or erosions largely remained constant at 1, with exceptions to left PIP 3 (improved 2 to 1). Synovial thickening largely

varied, with improvements in left and right PIP 3, worsening in right PIP 2, and constant at severity score 1 or 2 in all others PIP joints.

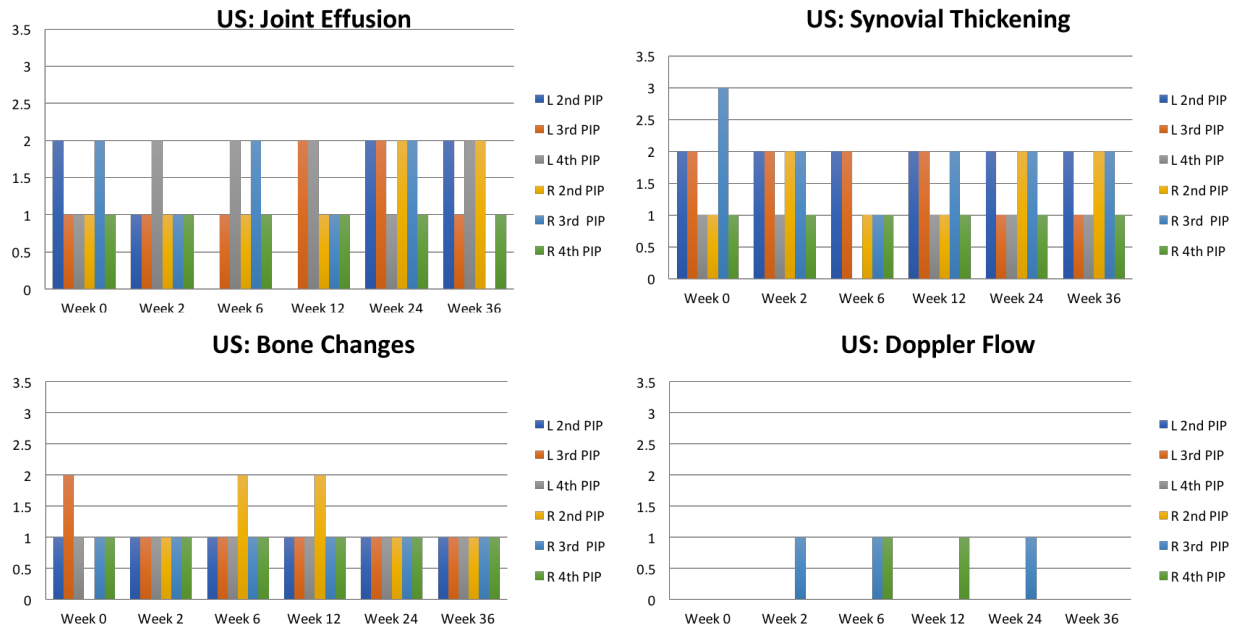

Figure 4.15 Quantitative scores for Doppler ultrasound imaging performed on our subject. (TOP LEFT): Joint Effusion. (TOP RIGHT): Synovitis score. (BOTTOM LEFT): Joint erosion from cartilage damage. (BOTTOM RIGHT): Doppler (vessel) flow.

As a global assessment of the US scoring, it was found that the right PIP 3 joint exhibited that most severity out of the six joints. Right PIP 4 and left PIP 4 showed the least severity, which for left PIP 4, counters the MRI and X-ray scores that left PIP 4 is one of the more severe cases. The fluctuations for US imaging scores being between 1 and 2 shows that the severity is mild but was difficult to strongly classify.

Combining Imaging Scores: With a large number of scoring criteria from three different imaging modalities, it may be difficult to determine treatment success. For this reason, I have simplified the nine imaging scores into three scores, one for each imaging modality. For this analysis, I have taken the summation of each subcategory for each imaging method. The purpose of performing this analysis is to demonstrate which fingers are the most affected by RA at baseline, which fingers

are not or marginally affected, and which fingers observed the most improvement from the new treatment therapy.

X-Ray Total Score: By combining the X-Ray subcategory scores, the scoring range is 0 to 9, with highly affected joints receiving a 9. The combined scoring for X-Ray produced findings that the left PIP 4 and right PIP 3 joints observed the highest severity of RA (Figure 4.16). In addition, the results also showed the left PIP 2 was not affected, and that the remaining joints were mildly affected. Right PIP 2 and 4 observed a reduction in severity by 1.

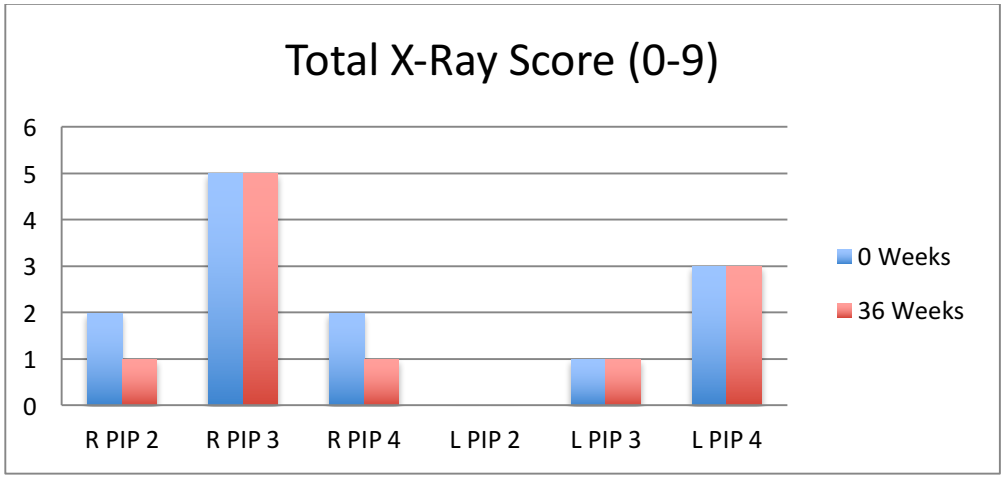

Figure 4.16 Total severity score for X-Ray, combining erosion and joint space narrowing.

MRI Total Score: The MRI subcategory scores were combined into one total score, with the score ranging from 0 to 29, with highly affected joints receiving a 29. The combined scoring for MRI produced findings that the left PIP 4 had the highest severity of RA for the left hand. At 36 weeks, the left PIP 2 and 3 joints had a score more than half of that of the left PIP 4 joint. This total score coincides with the trends of the individual scoring categories, in which the left PIP 4 showed to be

the highest affected joint in the left hand (Figure 4.17). The high severity score of the left PIP 4 also coincides with the x-ray total scoring results.

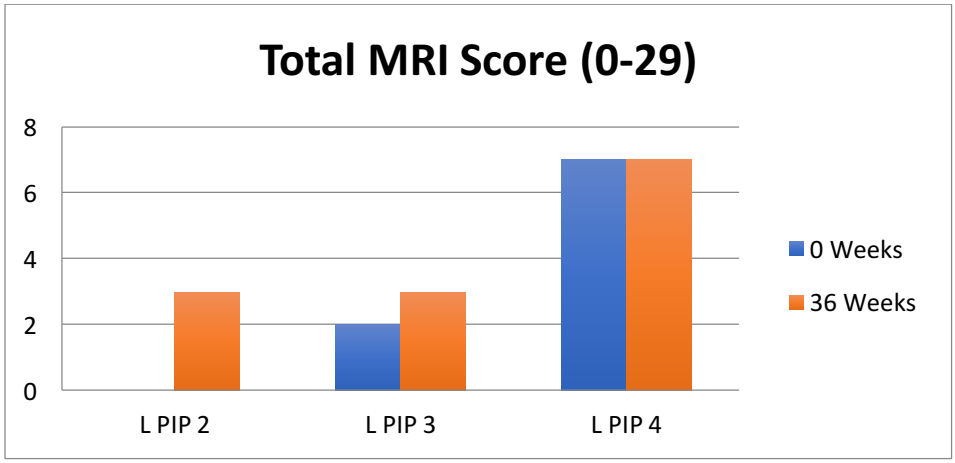

Figure 4.17 Total severity score for MRI, combining synovitis, erosion, and bone marrow edema. The MRI total severity score ranges from 0 to 29.

Doppler Ultrasound Total Score: Finally, the Doppler US subcategory scores were combines to have a total range of 0-12. These subcategories include joint effusion, synovitis thickening, bone changes, and Doppler flow. The combined scoring for US demonstrated that the right PIP 3 joint exhibited the highest severity of RA amongst the six joints analyzed at baseline (Figure 4.18). At 36 weeks, the right PIP 3 joint showed a dramatic improvement, decreasing from a score of 6 to 3. Conversely, right PIP 2 demonstrated an increase in RA severity over the trial. For this joint, the severity increased from 2 to 5. It was also shown from the total US score that the right PIP 4 was the least affected joint of the six. During the 36 weeks, this joint did not change in severity.

The PIP joints from the left hand were unchanged during the trial, except left PIP 3, which observed a drop in severity from 5 to 3.

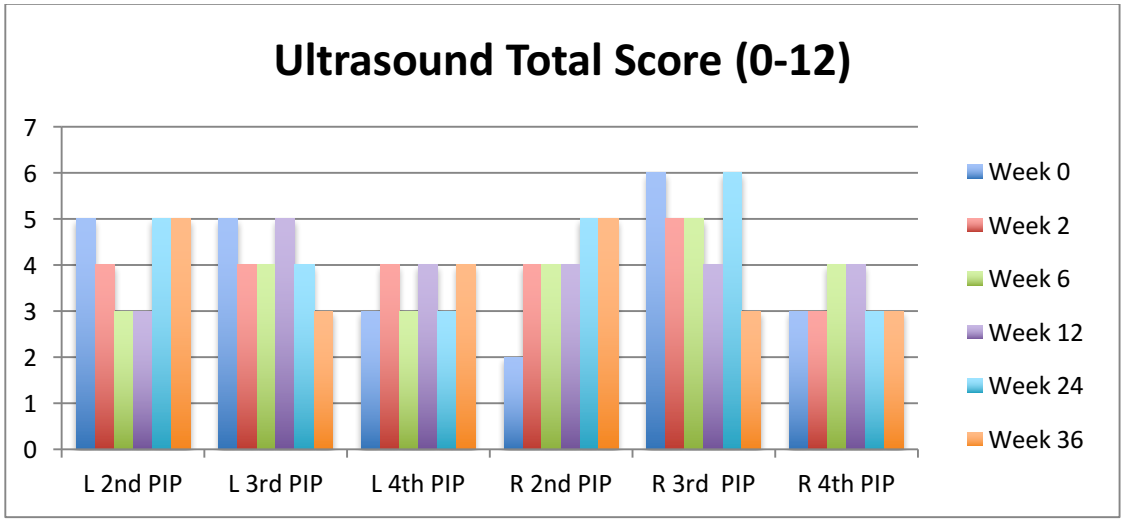

Figure 4.18 Total severity score for Doppler ultrasound, combining scores for joint effusion, synovitis score, joint erosion, Doppler (vessel) flow. The summation of the subcategories created a scoring range from 0-12.

Summary of Clinical Imaging Scores: In summary, all three imaging modalities demonstrated that the right PIP 3 joint was the most affected joint with RA. Only from the US total score did the right PIP 3 show improvement over the trial as oppose to x-ray, which showed that there was no change during that period. The left PIP 4 joint also showed a high severity of RA in MRI and x-ray, but not in the scoring in US. Conversely, the right PIP 4 joint demonstrated the lowest RA severity across x-ray and US. With these imaging modalities, the right PIP 4 did not change during this trial.

Assessment of US was found to largely have a contradictory score from the x-ray and MRI. The scores for the left PIP joints under US scoring found to have a similar score to that of the most severe joint, the right PIP 3. In this case, left PIP 2 and 3 observed a score of 5 during multiple imaging sessions, while the highest observed score for right PIP 3 was 6. This is contradictory to the MRI and X-ray scores, which observed severity scores of 1 or 2, which was the lowest scores

out of the analyzed joints. Based on all of the imaging scoring criterion, Table 4.6 provides a summary of RA joint progression.

Joint	Severity	Progression
Right PIP 2	Mild	Mostly worsened
Right PIP 3	High	Marginal Improvement
Right PIP 4	Mild	No Improvement
Left PIP 2	Mild	Worsened or No Improvement
Left PIP 3	Mild	Marginal Improvement
Left PIP 4	Moderate	No Improvement

Table 4.6 Summary of PIP joint severity and the overall progression over the course of the trial

4.6.5 FDOT Reconstruction Results

We start our optical results by showing example of two-dimensional cross-sections through the three-dimensional tomographic reconstructions of optical properties from the fDOT imaging

system. Figure 4.19 shows the transverse slices from the absorption coefficient while **Error! Reference source not found.** shows the transverse slices from the reduced scattering coefficient.

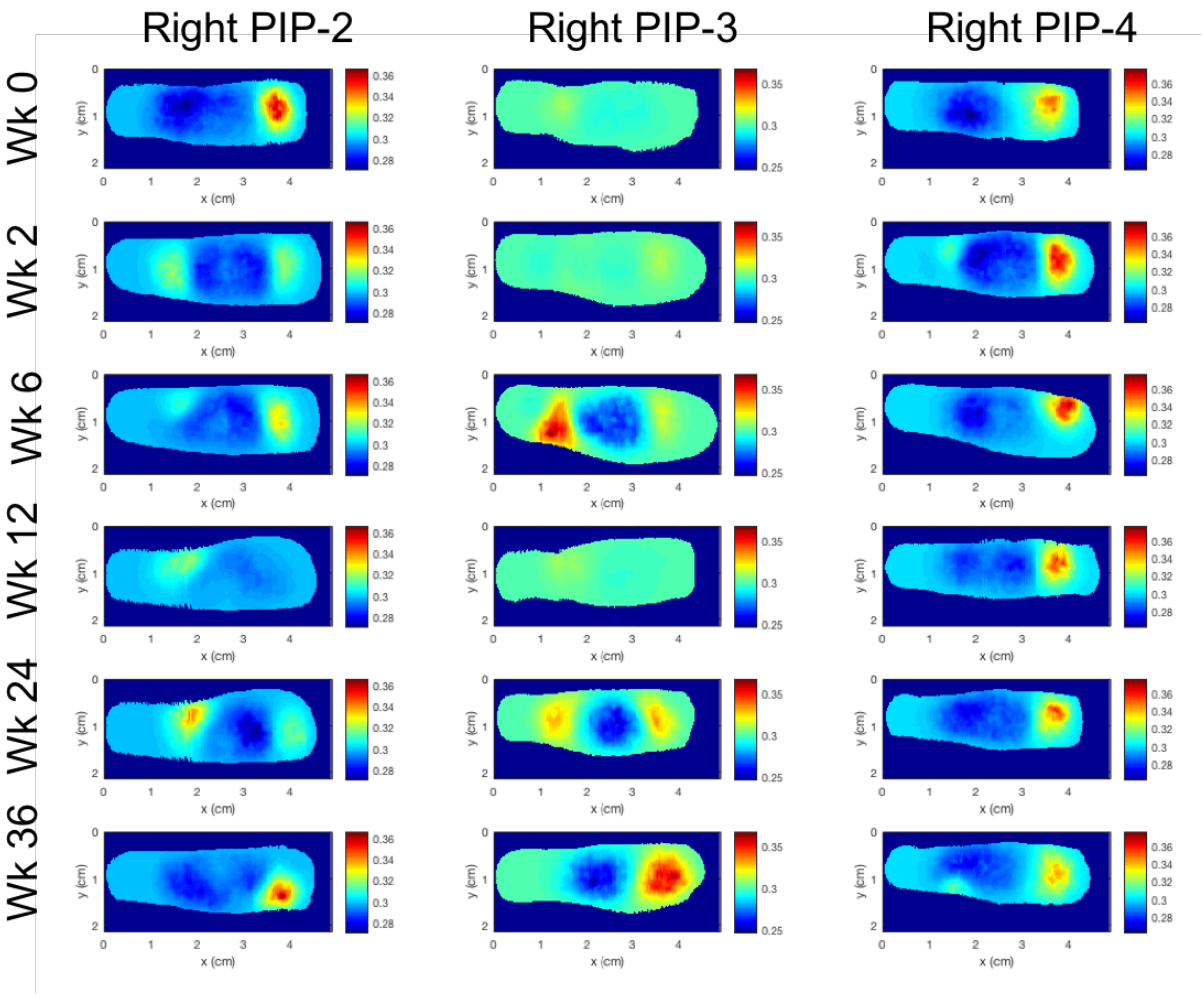

Figure 4.19 Transverse slices from the absorption coefficient of the fDOT reconstruction images. The column of images are from the 3 RIGHT PIP joints imaged, while the rows of images represent the timepoints in which these joints were imaged (0, 2, 6, 12, 24, and 36 weeks).

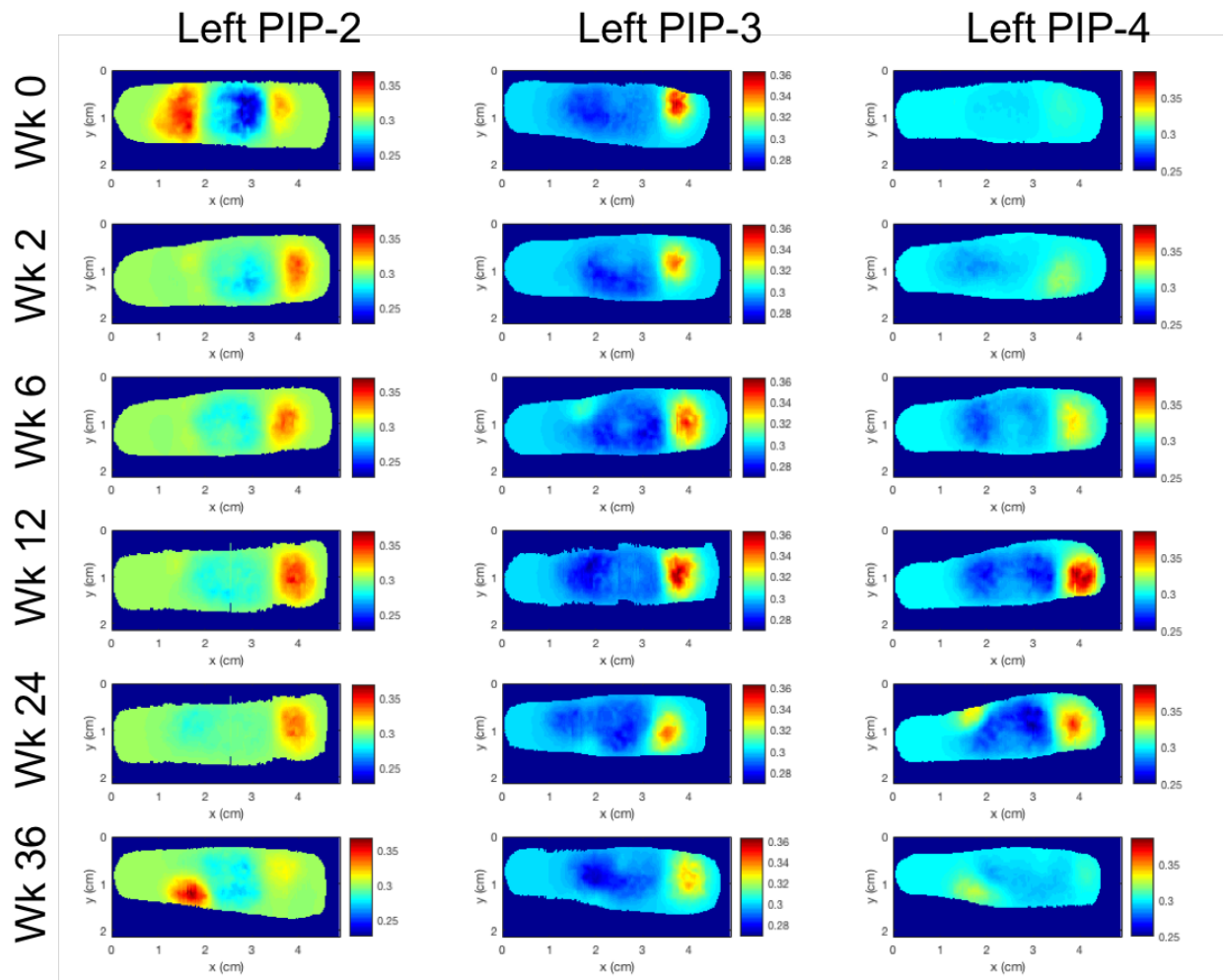

Figure 4.20 Transverse slices from the absorption coefficient of the fDOT reconstruction images. The column of images are from the 3 LEFT PIP joints imaged, while the rows of images represent the timepoints in which these joints were imaged (0, 2, 6, 12, 24, and 36 weeks).

The most pronounced differences between joints of subjects affected by RA and of subjects not affected by RA occur at the center of the images, where the joint cavity is located. For a subject responding to treatment, it is expected that both ua and us' would lower in the joint cavity region as the effects of the treatment begins to take shape. It has been shown in our research groups previous work that a lower ua and us' of the synovial fluid that fills the joint cavity and a higher ua and us' in the surrounding tissues (Cartilage, bone marrow). This profile of low absorbing/scattering of the joint cavity, and a high absorption/scattering in the surrounding areas

is indicative of a healthy joint [20, 40, 143, 145, 163, 164]. Joints affected by RA typically do not show a strong drop in optical properties in these regions.

However, diagnosis on the basis of visual inspection alone may mislead false positive or missed diagnose. In the following section, I explore feature extraction to assist in quantifying the accuracy of monitoring treatment.

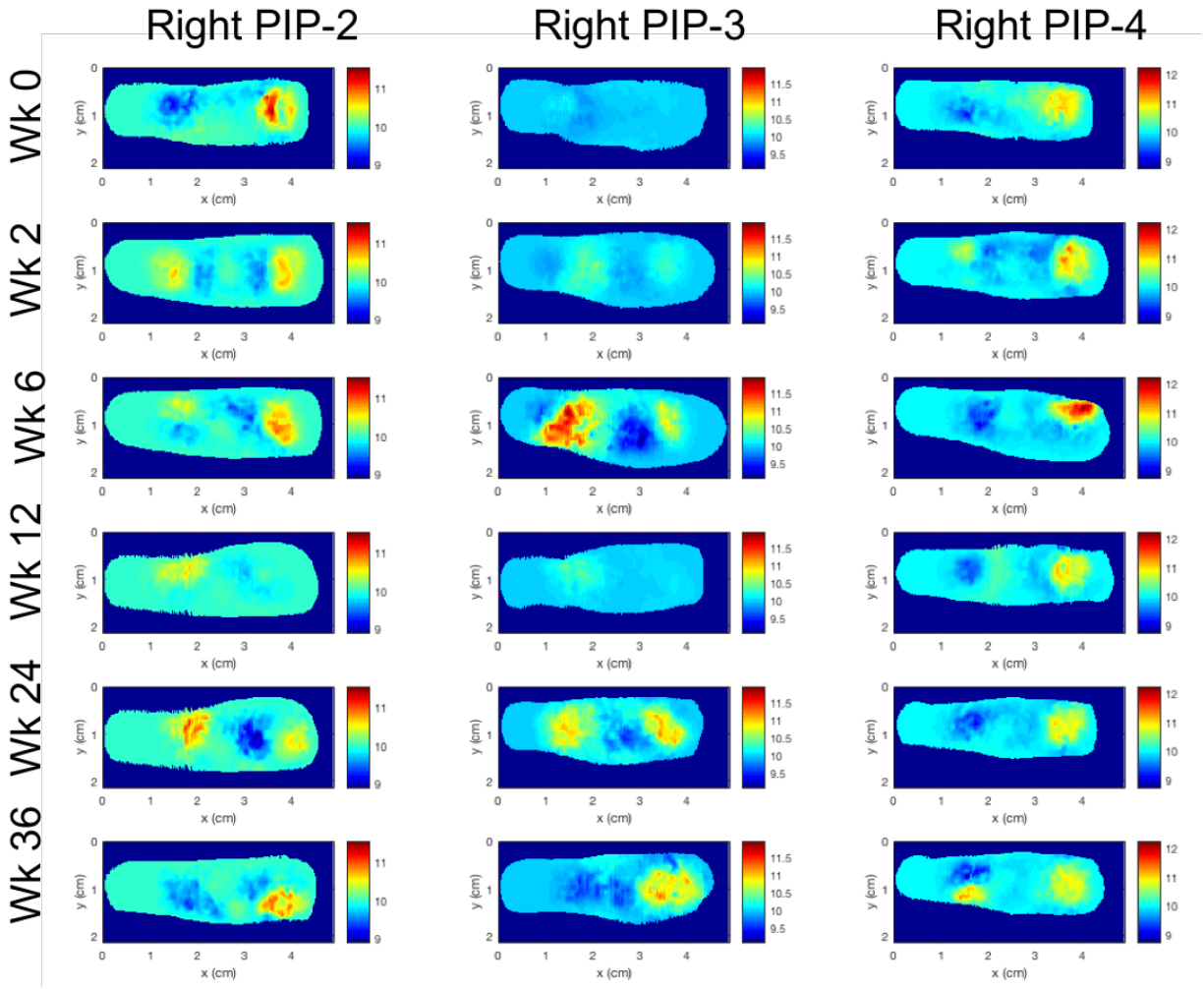

Figure 4.21 Transverse slices from the reduced scattering coefficient of the fDOT reconstruction images. The column of images is from the 3 RIGHT PIP joints imaged, while the rows of images represent the timepoints in which these joints were imaged (0, 2, 6, 12, 24, and 36 weeks).

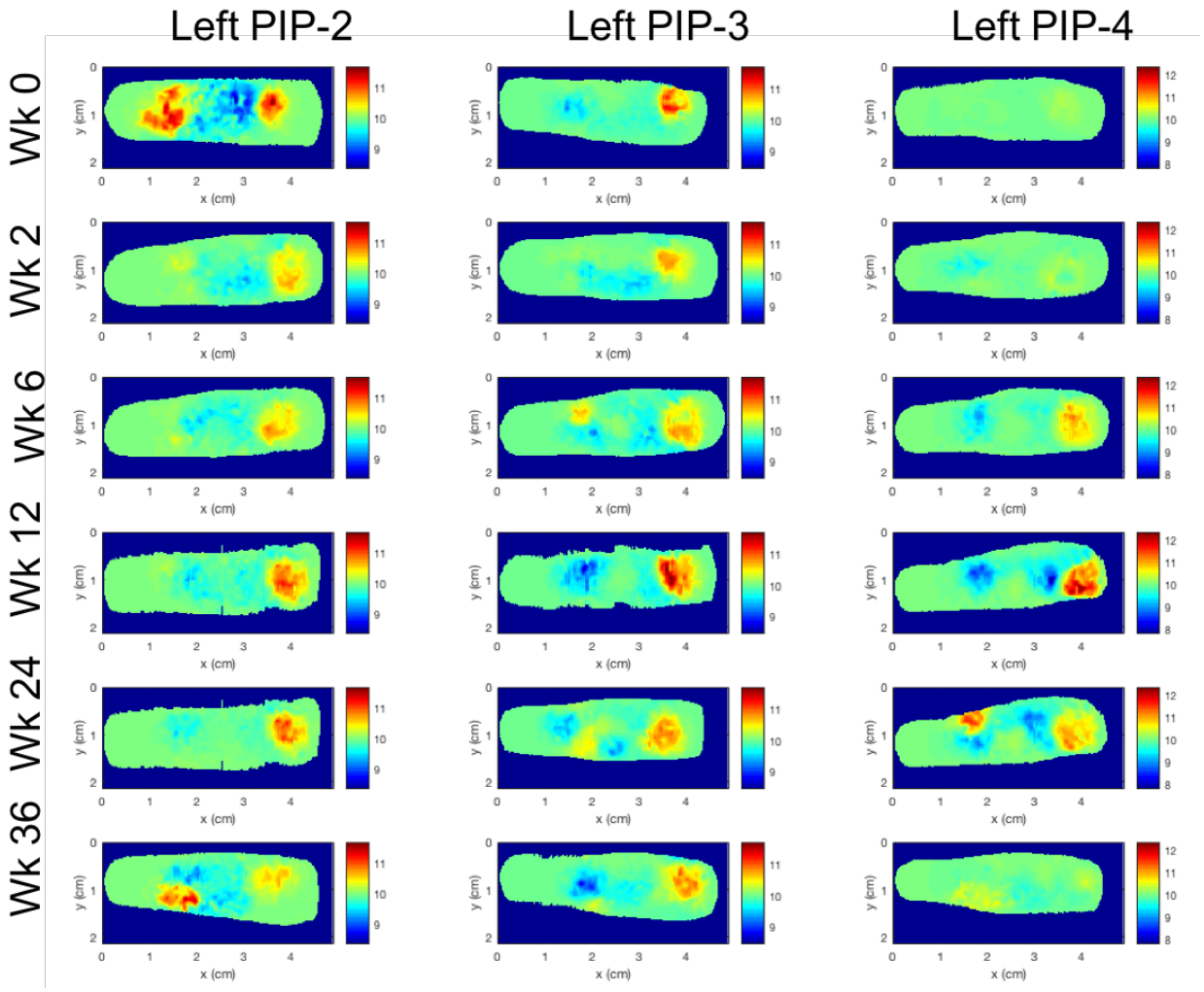

Figure 4.22 Transverse slices from the reduced scattering coefficient of the fDOT reconstruction images. The column of images is from the 3 LEFT PIP joints imaged, while the rows of images represent the timepoints in which these joints were imaged (0, 2, 6, 12, 24, and 36 weeks).

4.6.6 FDOT Feature Extraction

Each 3D reconstruction of the finger joints is unique, even for the same finger measured longitudinally, making it impossible to compare joints using all reconstruction data for two reasons. First, each mesh is unique to each joint, and as such, comparisons between joints on a pixel by pixel basis in not feasible. The same joint measured at multiple timepoints under treatment therapy may change structurally, as the treatment may improve range and decrease pain. In this scenario, extracting the structural information to create a finger mesh would make the fitting to the

previous time point difficult. The second reason is that the number of feature would be extracted if each pixel is considered a feature would larger than the number of unique samples. This would lead to over-fitting problems for data analysis.

To this end we consider only a small number of image features that can be computed from all reconstruction images. After reconstruction of the 3D spatial distribution of ua and us', a 3D region of interest (ROI) is determined for each finger. The mesh points used in the ROI is a center slice composed of voxels equidistant to the upper and lower bounds of the finger mesh. However, the mesh itself is an unstructured mesh, making the equidistant slice unique and ununiformed along the length of the finger. The ROI is created with the following steps. First, the unstructured mesh must be converted to a structured mesh using a custom built conversion algorithm [165]. Next, the center pixel position is computed according to the range of the upper to lower bounds of the finger while cycling through the finger length-wise, or sagittally (Figure 4.23). For each center pixel position found length-wise, a matrix of pixels is then extracted from the transverse plane of the finger. The pixels just above and below the center slice are extracted, and the top, center, and bottom pixels are averaged, creating a vector of pixels obtained from the transverse plane. Once all of the center pixel positions are cycled through and transverse vectors are extracted, the ROI then becomes a non-planer 2D slice of the transverse center of the finger. Finally, the 2D slice is cropped such that only mesh points that are at least 2mm away from the finger mesh boundary are removed. This helps eliminate any reconstruction boundary artifacts from being included in the

feature extraction process. The final ROI obtained produces a slice of the finger at the center of the finger joint, providing the best representation of the optical properties in the joint cavity [164]. With the ROI extracted, visual inspection of the reconstruction results and the associated ROI may mislead false positive or missed diagnose. Instead, it is best to explore feature extraction and classification to quantify the state of the finger.

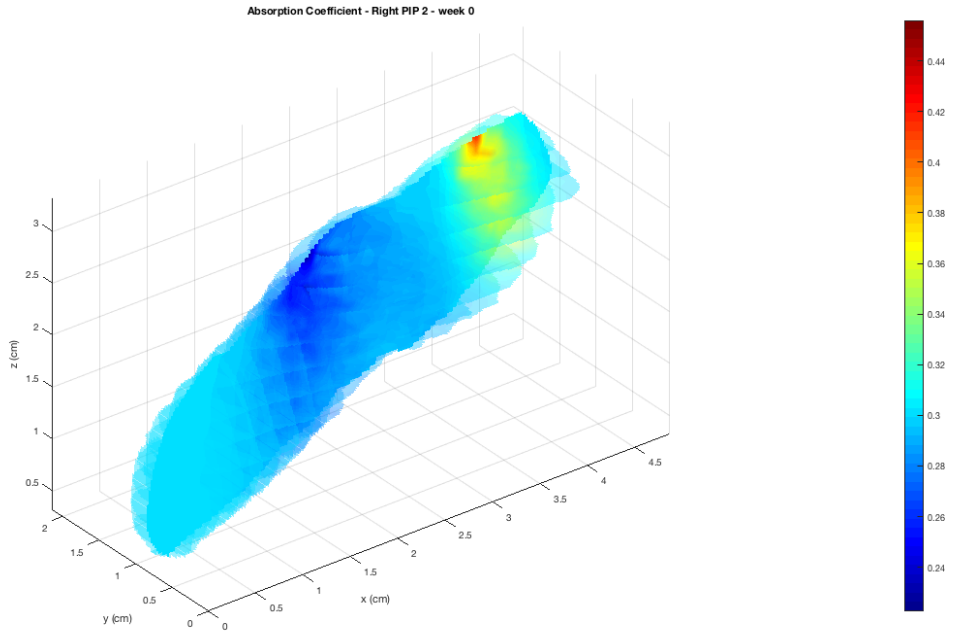

Figure 4.23 A 3D rendering of the absorption coefficient from a finger joint. The center sagittal slice is shown with multiple transverse and coronal slices shown at a lower opacity. The center coronal slice is created by computing the midpoint of the central sagittal slice at all of the coronal positions.

Features are extracted separately from the ua and us' of the ROI that were produced from the 3D reconstruction images. Then the maximum, minimum, mean, variance, and the ratio of the minimum to maximum of each data set are calculated as features. Therefore 10 features in total are obtained for each finger. Although all features were evaluated, multiple features produced promising results for our one case study. In our research group's previous studies, it has been shown that that the standard deviation of ua and the maximum us' (stdev ua, max us') are the two

most commonly significant features [40, 163, 164]. Because there are numerous clinical measures along with 10 optical features, the dimensionality of the feature comparison of this analysis requires a large number of subjects. Since we were only able to enroll one subject in this study, these two features were the only features analyzed in this work.

4.6.7 Evaluating FDOT for Monitoring RA

The features extracted from the finger reconstructions for our single subject over all time points were analyzed. From the clinical measurements, it was determined that the right PIP 2 and left PIP 4 joints were the only joint severely affected by RA, while the remaining four joints were either moderately affected (Right PIP 2, Left PIP 2 and 3), or marginally affected (Right PIP 4).

To test our first hypotheses, which was to differentiate the several affected joints from the moderate and mildly affected joints, the absolute values of our two features were analyzed. From previous work, it was shown that the lowest the value of these features, the higher the severity of RA. In **Error! Reference source not found.**, the absolute values of the standard deviation of ua and max s' are shown. Without any context of the values from the features to distinguish the severity of RA, the difference in the optical features at baseline show that right PIP 3 and left PIP 4 has the lowest standard deviation of the ua (Standard deviation of ~0.002 for both) and the lowest maximum us' (Max us' = 10.2 and 10.4 respectively). These results suggest that these two finger joints are the most affected by RA compared to the other PIP joints measured prior to the enhanced treatment. This finding correlates with the clinical scores, that suggested that these two finger joints were also the most affected by RA. Alternatively, the left PIP 2 joint showed the highest values from the two features, suggesting that this joint was the least affected by RA at baseline. This does not correspond with the clinical findings, in which the right PIP 4 as the least affected joint. Unfortunately, without any knowledge of the severity scale for the optical features, it is

difficult to postulate whether the four joints should be classified as moderate or mild. However, to examine the fDOT optical features even further between the two joints that were clinically determined to be severely affected and the remaining four joints, the mean and standard deviations of the optical features at baseline were computed (Figure 4.25). This figure demonstrates the difference of optical features of the joints are, and provides insight as to which joints may observed the highest effect to treatment over time.

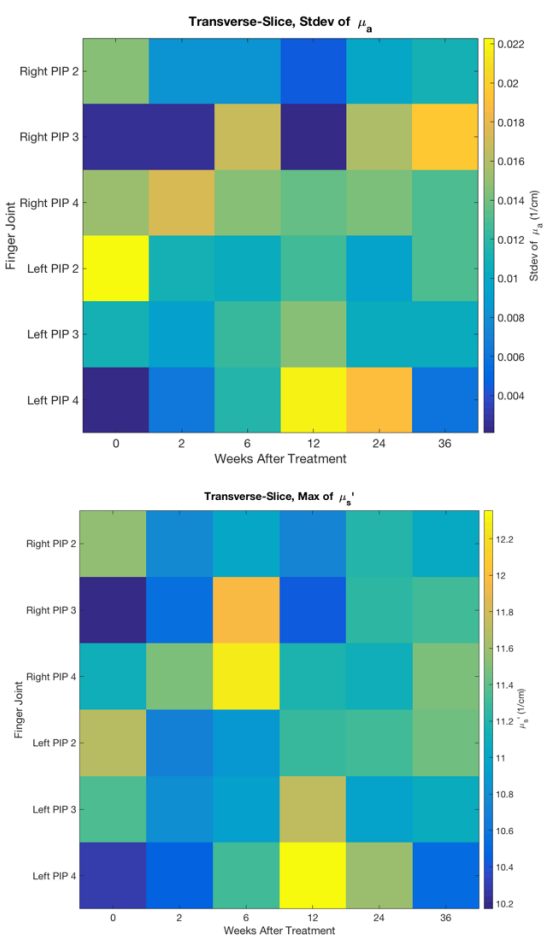

Figure 4.24 Graphical representation of feature results of stdev ua (TOP) and max us' (BOTTOM).

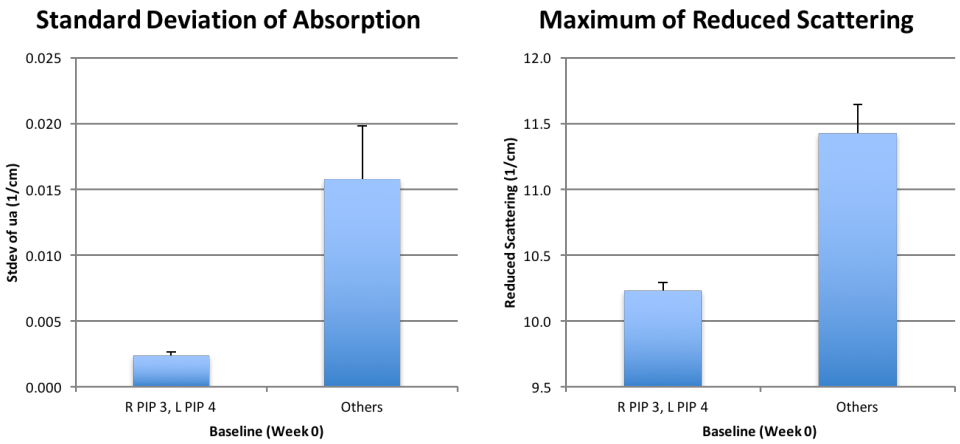

Figure 4.25 Comparison of fDOT optical features between the two severely affected joints and the remaining four joints. Features of standard deviation of the ua (Left) and the maximum of the us' (Right) are shown.

To evaluate our second hypothesis, in which we expect a patient that will respond to treatment will observe a higher standard deviation of ua and higher max us' over time in affected joints, the

interpretation is best delineated when the features are normalized to the baseline measures (Figure 4.26).

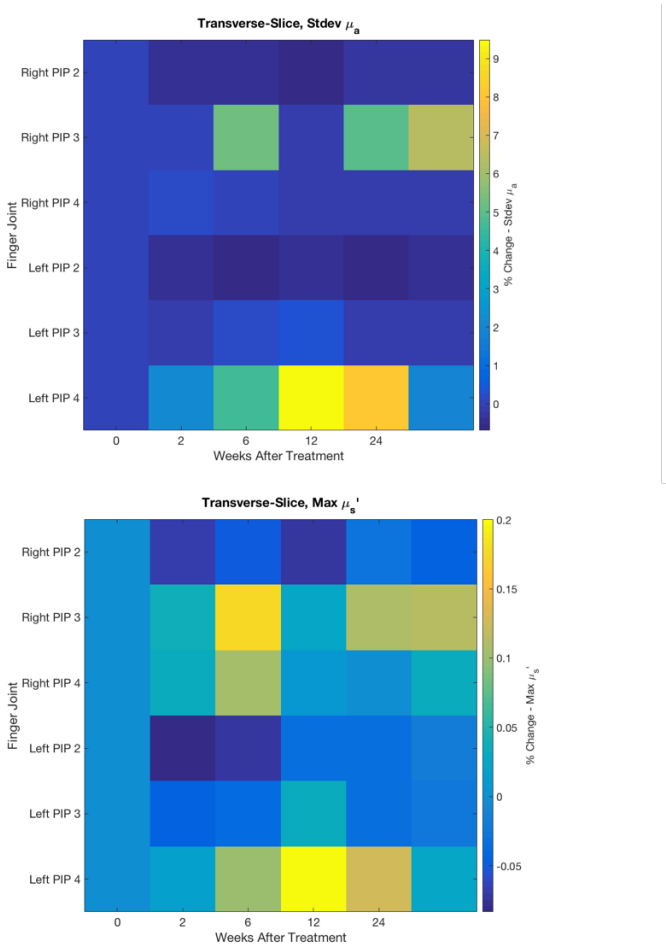

Figure 4.26 Graphical representation of normalized feature results of stdev ua (TOP) and max us' (BOTTOM). Results shown are normalized to the baseline measurement, at week 0. The values in this column are 0.

Here it is shown that although there are fluctuations in the optical features, the joints that showed an increase in the features over time were the most severely affected fingers. It may be deduced that the reason that the most severely affected joints showed the most improvement is because these joints had the most room for improvement compared to the other joints. In contrast, the relative changes in optical properties from the remaining four joints either had a marginal difference over time or worsened. Most notably, the right PIP 2 joint showed a 1% decrease in the standard deviation in ua and a 0.03% decrease in the max of us'. To examine the changes in optical

features over time even further, I have taken the mean and standard deviation of the two severely affected joints as well as the remaining four joints presumed to be moderately or mildly affected and displayed this calculation over time (Figure 4.27). This figure also validates our third hypothesis, which is that the mild or marginally affected joints will not observe any, or margin changes under treatment than the severely affected joints.

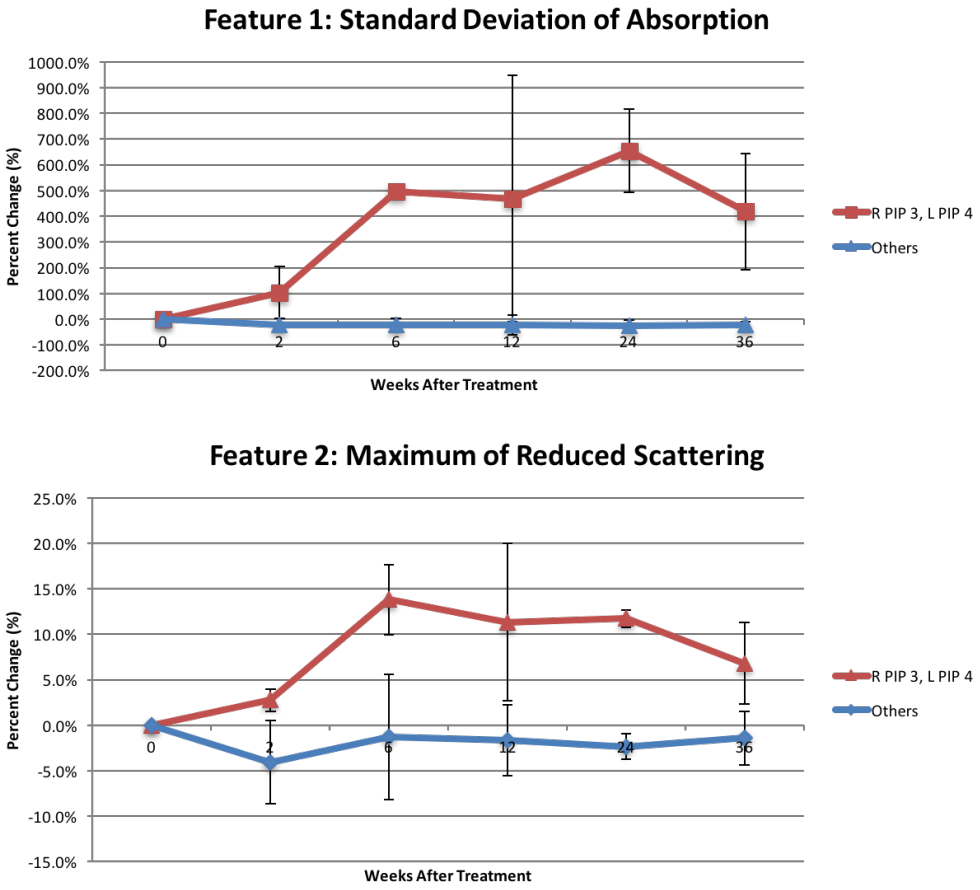

Figure 4.27 Relative changes in optical features between the two severely affected joints (Red) and moderate or mildly affected joints (Blue) observed over time. The standard deviation of ua (TOP), and the maximum us' (BOTTOM) both show that the severely affected joints had the most improvement during the clinical trial for this patient.

4.6.8 Evaluating DOS Using the WHDD for Monitoring RA

Although the fDOT system has shown its potential in discriminating healthy from RA affected joints [40], and has shown ability in monitoring treatment in our RA patient case study as shown

in the previous section, the system is large and is not easily transportable which makes its usability inside a typical exam room difficult. For example, the fDOT system had to be used in a small selection of available exam rooms at CUMC during our pilot study because the system simply could not fit in other exam rooms. Because of this, it was our goal to compare the already capable fDOT system to that of smaller scale version system. Thus, in addition to using the fDOT system to characterize the optical properties from finger joints, the wireless handheld DOS device (WHDD) was also used to assess RA progression in the PIP joints. In this section, I will compare the clinical imaging results from our RA patient to that of the WHDD. The WHDD hardware, along with the reconstruction algorithm, is a system that is designed to make point measurements of [Hb] and [HbO2] from human tissue.

Although the PIP finger joint has vascularity from the synovial membrane, the primary composition of the finger joint is low vascular cartilage and ligaments, as well as the proteins, water, and monocytes from the synovial fluid. The synovial membrane, which a dense net of small blood vessels that provide nutrients not only for synovium but also for cartilage, becomes inflamed for people suffering from RA [166]. This phenomenon of increased thickness of the synovial membrane, and the subsequent invasion by the pannus of cartilage and bone, is caused by an increase in the vascular supply to the synovium to cope with the increased requirement for oxygen and nutrients. This formation of new blood vessels, or angiogenesis, is a key event in the formation and maintenance of the pannus in RA.

Monitoring of increased vascularity due to angiogenesis has been monitored with power Doppler ultrasound is studies [167, 168]. Fukae et al discovered that the change of vascularity in response to DMARDs, defined as the percentage change in vascularity by the eighth week from baseline, was inversely correlated with radiographic progression in each MCP joint. Extending their work,

they also found that smouldering inflammation reflected by positive synovial vascularity under low disease activity was linked to joint damage. The damage progressed irrespective of the severity of positive synovial vascularity. Their work concluded that using vascularity as a guide to consider a therapeutic approach would have benefits for patients with active RA. Although this group used power Doppler ultrasound to measure vascular flow to assess the overall vascularity of the joint, optical techniques such as DOS can also be used to quantify the level of vascularity in the finger joint.

Figure 4.28 Example of the WHDD probe being placed on the palmer side of the second PIP joint.

Using DOS with the WHDD system, it was our hypothesis that DOS will have similar outcome to the of the fDOT system. Specifically, we first hypothesize that vascularity due to angiogenesis in severely affected RA joints can be differentiated from the non- or marginally affected joints at baseline. Second, a patient responding to treatment will observe a lower HbT and a higher %StO2

over the course of the study in severely affected joints. Finally, our last hypothesis is that non- or marginally affected joints will not respond as highly to treatment than severely affected joints.

To test these hypotheses, we employed the WHDD to scan the PIP finger joints at the palmar side of the hand to make point measurements of vascularity at the finger joint. Figure 4.28 shows an example of how the WHDD was placed on the joint. After measurements were taken from the finger joints, the probe was calibrated to a solid phantom cylinder with known optical properties (Table 4.7). Reconstructions of HbT and $\%StO_2$ were computed based on the calibration measurements, similar to the done in chapters 2 and 3.

	INO Phantom Cylinder Optical Properties (1/cm)			Linear Fit from Actual Properties			
WL (nm)	575	661	757	780	905	850	808
Measured (ua)	0.0693	0.0606	0.0512	0.0484	0.0359	0.0414	0.0456
Measured (us')	9.3200	9.2100	8.7800	8.6760	8.2885	8.4590	8.5892

Table 4.7 Optical properties of phantom cylinder used to calibrate the WHDD during the RA clinical study. A linear fit was made for wavelengths used in the WHDD. The wavelengths chosen for actual optical properties were based on fluorescence tomography calibration, and thus uses lower wavelengths.

The WHDD reconstruction results of total hemoglobin (HbT), and oxygen saturation (%StO2) from this case study is shown in Figure 4.6. From the absolute results, it can be interpreted that all finger joints had a low concentration of HbT prior to treatment which is expected of healthy finger joints, since normal joints have a small amount of vascularity. However, the joints observed an increase in HbT over the course of the treatment. As it was observed that the patient improved after treatment as measured by other imaging modalities, these results go against that trend.

The %StO2 measurements at baseline were well below what is considered normal (normal>70%), suggesting that the joints were hypoxic during baseline measurements. Unfortunately, the StO2 results during the course of the trial fluctuated negatively, which does not correlate with the results from the clinical and fDOT measures. The trends over time show that the right PIP 3 has the highest average HbT during the trial, which does correlate with what the severity of that joint observed.

The HbT results also suggest that the right PIP 2 joint worsened the most over time. The StO2 measurements over the trial largely jumped between 20 and 70%, which is unreasonable in regards to consistency. However, the right PIP 3 and left PIP 2 demonstrated a more monotonic change, in which right PIP 3 showed that most improvement. This finding correlates with clinical and fDOT measurements.

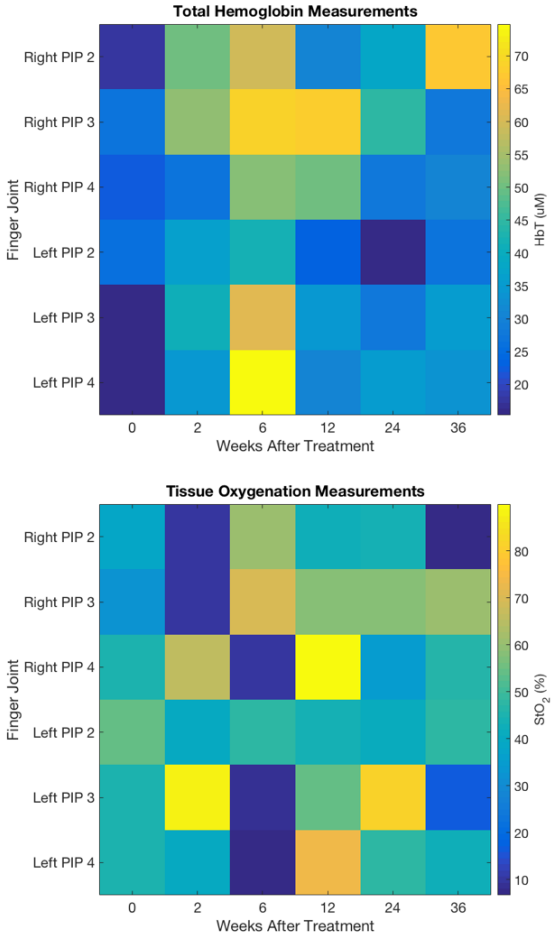

Figure 4.29 Absolute reconstruction results of total hemoglobin (TOP), and tissue oxygen saturation (BOT). The columns represent the number of weeks the patient has been under treatment and the rows represent the finger joints that were measured with the WHDD to make DOS measurements.

With the absolute results largely inconsistent with the clinical and fDOT measurements, we examine this further by analyzing the percent change from baseline of the HbT and StO2

measurements (Figure 4.30). Here, it is clear that all joints observed an increase in HbT during the trial, which would correspond to increase vascularity due to angiogenesis. This also suggests that by an increase in vascularity, that the joints are worsening in severity of RA. Conversely while analysing the percent change from baseline of StO2, most joints either decreased in StO2 (Right PIP 2, Left PIP 3), or showed a marginal decrease (Left PIP 2, Left PIP 4). For these four joints, the changes in function parameters was not monotonic and would jump as much as -80% to +80% from baseline. Alternatively, the right PIP 3 did show consistent improvement in StO2 over the

trial, which correlates with clinical and fDOT findings. In addition, the left PIP 2 joint only observed a marginal percent change in %StO2 (+/- 6.5%) during the trial.

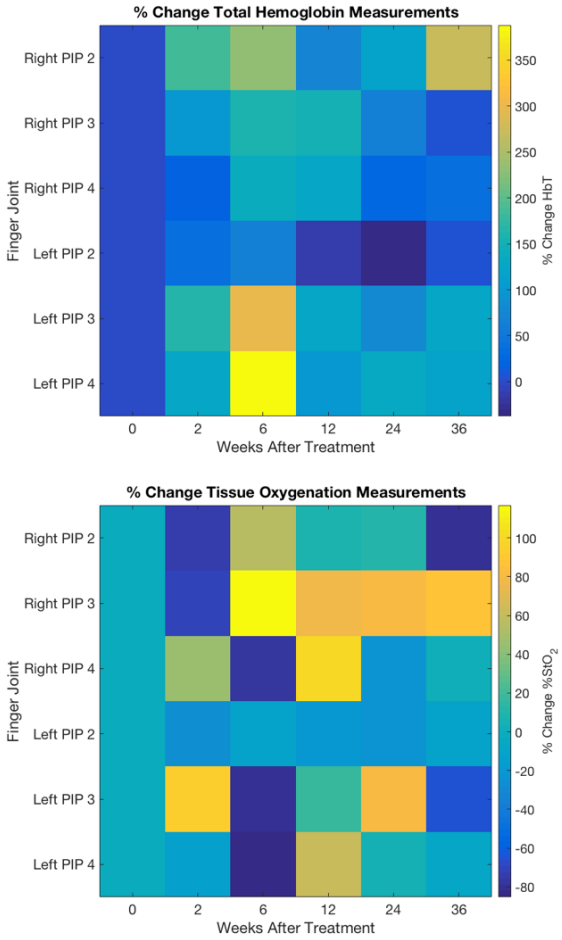

Figure 4.30 Relative reconstruction results of total hemoglobin (TOP), and tissue oxygen saturation (BOT). The columns represent the number of weeks the patient has been under treatment and the rows represent the finger joints that were measured with the WHDD to make DOS measurements.

4.6.9 Discussion Comparing DOS and FDOT

The optical imaging modalities DOS and fDOT were used to monitor the progression of RA in our single patient study. The fDOT system used is a highly sensitive tool to make localized measurements of absorption and reduced scattering coefficients at 660nm. The system size however makes it difficult to use in the exam room, as it was seen in our study, it could only fit in a select number of exam rooms. It was our secondary objective then to make additional

measurements using a handheld, transportable WHDD probe that uses continuous wave (CW) DOS imaging technology to make point measurements of total hemoglobin and tissue oxygen saturation.

Comparing the two NIR optical imaging modalities, it was expected that the optical trends between the two would show similarities for individual finger joints, or demonstrate a difference in severity between the PIP joints. Unfortunately, the WHDD measurements did not demonstrate either, disproving our hypotheses relating to the use of the WHDD for this case study. In this section I will discuss the potential shortcomings of using the WHDD to monitor the treatment of RA.

The WHDD may have not produced similar results to that of fDOT based on three observations. First, making good contact with the finger joint was difficult, especially for finger joints that had severe structural damage. The WHDD, although is handheld, the device can be too wide for making point measurement on PIP joints. In addition, WHDD measurements are easier to make when the finger is extended, which is painful or not possible for RA patients with significant structural damage.

The second potential reason for the shortcoming of the WHDD results is due to the configuration of the source-detector pairs. The WHDD uses a reflectance based configuration in which laser light is emitted at the tissue surface, light is then scattered and absorbed, and only reflected photons are acquired and measured. This configuration may be problematic because both the light illumination or detectors positions are not directly over the joint. Therefore, the scanning medium may be too small and heterogeneous to be measured accurately.

The third potential reason for why there may have been a shortcoming using the WHDD is the use of the CW imaging modality over fDOT to make static measurements. The fDOT system, as well as fDOT technology has been shown to separate the absorption and reduced scattering coefficients

better than CW. Therefore, chromophore reconstructions of HbT and StO2 with CW may not be as effective compared to fDOT. This, along with the previous two issues, may be the reasons why the DOS measurements showed very little similarity with the fDOT results.

For future considerations, I suggest that the interface of the WHDD be modified to a transmission based configuration, such that transillumination measurements can be made similar to that of the fDOT system. This will allow for laser illumination and measurements to be made directly above and below the finger joint, reducing the risk of not reaching the proper imaging medium. In addition, a physical finger clip placed at the joint can make the imaging procedure more comfortable for the patient. For this interface, the patient would be able to have their hand in a relaxed position, reducing the amount of pain that may be associated with the imaging procedure. Finally, in addition to making static measurements using CW, the imaging procedure can be modified to induce a venous or arterial occlusion at the upper arm, similar to using a blood pressure cuff for blood pressure measurements. Dynamic measurements using diffuse optical imaging such as DOS and DOT has been used in other projects [6, 169-171], and for RA imaging studies [151]. For dynamic measurements, the outcome results may be the rate of hemodynamic change, the rise time of the absorption measurements, or the change in the oxygen saturation over the time of the cuff occlusion. Additional design work towards a new interface is needed to explore these considerations.

4.6.10 Study Discussion

Rheumatoid arthritis is an inflammatory autoimmune disorder that causes chronic inflammation of the synovial membrane of small and large joints in 1% of the world's population. The severity of RA can be associated with significant pain and disability. There is currently no cure for RA, but disease-modifying anti-rheumatic drugs (DMARDs), the key therapeutic agents, reduce synovitis

and systemic inflammation and improve function. In addition, biologics such as Humira and Enbrel target pro-inflammatory cytokines, chemokines and growth factors such as TNF have been used more in the past decade to further reduce RA progression. However, these biological agents may have considerable toxic effects, and infections and high costs restrict prescription of them. Therefore, it is vital for RA remission that the patient treat and determine the efficacy of the treatment early.

Expanding on this group's previous studies in which RA can differentiated from normal joints, we developed a protocol to monitor the progression, or remission of RA under treatment. Using a fDOT system specifically designed to make highly sensitive measurements of optical absorption and reduced scattering, we monitored the efficacy of treatment in a single-subject case study. We compared the fDOT technology, in which we created 3D absorption and scattering maps of PIP joints 2-4, to that of standard clinical and imaging measures, in which we used quantitative scoring methods to objectively determine which joints were most severely affected by RA, and which joints showed a positive response to treatment. Although the fDOT system can reliably make accurate measurements of absorption and reduced scattering, the system is large and can be difficult to access in a clinical setting. To address this problem, we incorporated the use of the WHDD probe to make point measurements of total hemoglobin and oxygen saturation at the palmer side of the PIP joints. The vascular measurements taken by the WHDD were intended to monitor to the level of angiogenesis associated with RA. Potentially, DOS from the WHDD could measure the severity of RA and provide a better understanding of the pathophysiology of RA.

By using the fDOT and DOS techniques on a single patient case study, we have evaluated the capabilities of both methods and their abilities to accurately differentiate severity between joints and monitor RA progression as described by our gold standards of clinical examinations and

radiological imaging. Using features of standard deviation of ua and the maximum value of us' within the 3D spatial maps of the optical properties, the fDOT modality demonstrated that the right PIP 3 and left PIP 4 were the most affected joints while the other joints were observed to be moderately or mildly affected by RA. In addition, fDOT was able to show these two joints improved over the 36-week study under additional DMARD treatment.

Employing the WHDD, however, the vascular results from this modality exhibited inconsistent results from that of the fDOT and clinical measures. Since the clinical results showed an improvement from the treatment therapy, and with the fDOT results corresponding to same outcome, it was expected that the DOS measurements using the WHDD probe would show an increase in tissue oxygen saturation from a possible hypoxic state, as well as a decrease in the total hemoglobin concentration from the reduced amount of vascularity that stemmed from angiogenesis of the synovial membrane. Unfortunately, the trends that were hypothesized for the WHDD measurements were largely unobserved. Instead, the HbT measurements were shown to be at normal levels at baseline, suggesting that the joints were healthy. Over time, most joints observed an increase in HbT, suggesting that there was more vascularity in the joint. The %StO2 also observed similar trends. However, the right PIP 3, which is clearly the most severely affected joint of the six measured, did observe an increase in %StO2 of 80% from baseline. This suggested that this joint did improve over the trial. This singular observation was the only positive correlation from the WHDD measurements.

The potential limits of the use of the WHDD for monitoring RA may have been due to the reflectance geometry configuration used, in which transillumination measurements could not be performed as was done with the fDOT imaging system. In addition, interfacing issues with the finger joint may have prevented a reliable acquisition of DOS data. These potential limits can be

addressed with a new interface from the WHDD electronics to the finger. In addition, the use of a venous occlusion to create a dynamic change in the metabolic and hemodynamic state of the joint could be useful for future work. There are also limits to this study. First, the recruitment of patients was incredibly difficult and a result only one patient was enrolled into this study. More patients are required to make a sufficient analysis of the fDOT and DOS technology. In conclusion, we demonstrate that fDOT has the potential to aid in monitoring the progression and treatment efficacy of RA that can help in management decisions for rheumatologists.

5 Using DOS for Intraoperative Monitoring During Vascular Surgery

In this chapter, I will provide details for a system design that can be used for intraoperative monitoring during vascular surgery to assist in improving the efficacy of arterial revascularization for patients suffering from PAD. Characterization of the device, including performance and measurement accuracy, and repeatability will be reported. To conclude, I will describe the initial results of a longitudinal study in which perfusion in the lower extremities of 20 subjects were measured before and after arterial revascularization using the designed.

5.1 Peripheral Arterial Disease

Peripheral arterial disease (PAD) is the narrowing of arteries due to plaque accumulation and in the vascular walls (atherosclerosis) in the lower extremities [172]. Plaque is made up of fat, cholesterol, calcium, fibrous tissue, and other substances in the blood. When plaque builds up in the body's arteries, the condition is called atherosclerosis. Over time, plaque can harden and narrow the arteries. This limits the flow of oxygen-rich blood to your organs and other parts of your body. While many people with PAD have mild or no symptoms, PAD typically manifests itself as claudication, which is defined as a cramping leg pain with ambulation to a set distance. As the disease progresses, this distance becomes progressively shorter, and in later stages the pain becomes severe and present even at rest [173]. The location of the pain depends on the location of the clogged or narrowed artery. The severity of claudication varies widely, from mild discomfort to debilitating pain. Severe claudication can make it hard to walk or do other types of physical activities.

PAD affects approximately 12 million individuals in the United States and is associated with significant morbidity and mortality [174]. Every year, PAD is responsible for over 2,750,000 office visits, 10% of which result in hospital admissions. Approximately 45,000 PAD patients die from

this disease annually [175]. It is estimated that >200 million people have PAD worldwide, with a spectrum of symptoms from none to severe [176].

Risk factors for developing PAD include age, smoking, hypertension, hyperlipidemia, hypercholesterolemia, and diabetes. Although PAD is characterized by a slow and low rate of local symptoms and complications, it is also characterized by ongoing atherogenesis in other vascular beds and a very high rate of mortality (approximately 25%-30% within 5 years for patients with symptomatic PAD) due mainly to stroke and myocardial infarction (MI) [172].

If left untreated, the disease eventually leads to critical limb ischemia, a condition in which the formation of foot wounds or ulceration occur and don't heal due to lack of perfusion. This subsequently can lead to infection of the wound and tissue loss (gangrene), and ultimately amputation. Furthermore, patients with PAD have an increased risk of stroke and myocardial infarction, and show a two-fold increase in the risk of death from cardiovascular disease [177].

5.2 Treatment of PAD

Patients with severe PAD will often require lower extremity percutaneous transluminal angioplasty or bypass surgery to fix the occluded blood to flow to the extremities. In angioplasty, an empty and collapsed balloon on a guide wire, known as a balloon catheter, is passed into the artery to narrowed locations and then inflated to a fixed size using water pressure. The balloon crushes the fatty deposits, opening up the blood vessel for improved flow; the balloon is then deflated and withdrawn.

Stents are small steel mesh tubes that can be placed inside an artery during an angioplasty procedure. Stents "prop" open arteries to keep blood flowing. A stent is then usually placed at the same location to ensure that the vessel remains open. If this technique is ineffective, a vascular bypass is conducted. This is very invasive, as the surgeon has to make a large cut and move the

muscles and tissue to reach the artery, then re-route it by taking a segment of another artery or using synthetic tubing.

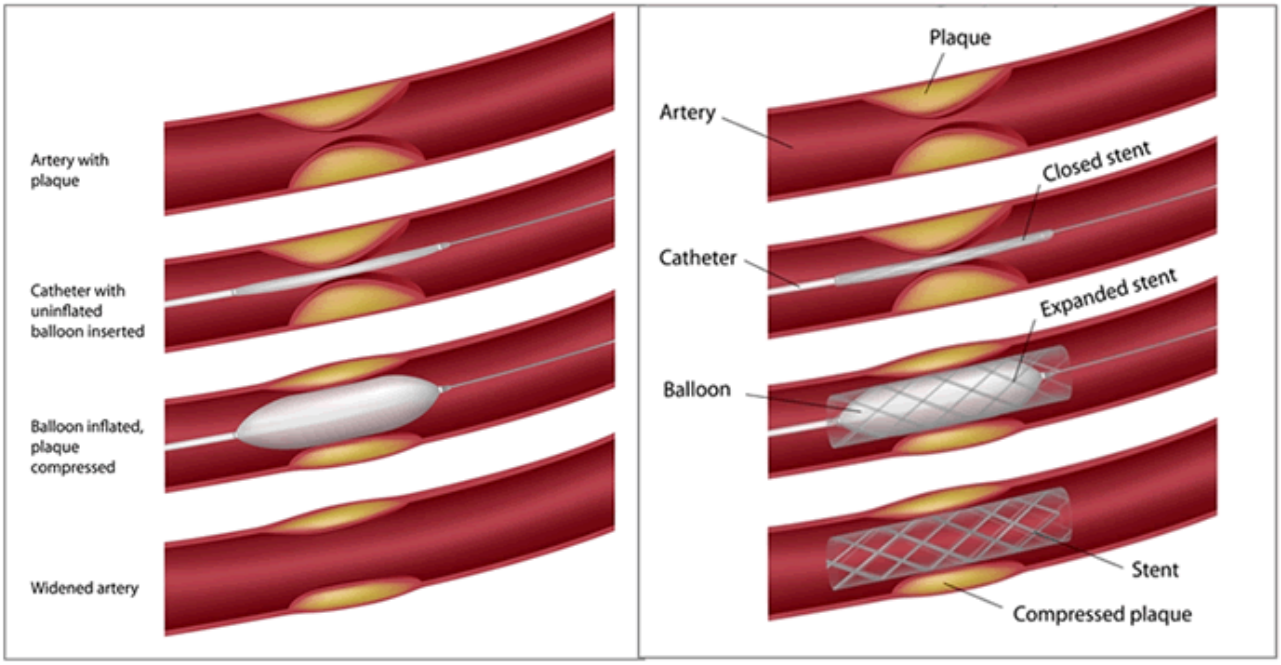

Figure 5.1 Diagrams of balloon angioplasty (left) and stent placement (right) in a stenotic artery

In addition to lifestyle changes such as smoking cessation and exercise programs, antiplatelet drugs (aspirin, clopidogrel), angiotensin-converting enzyme inhibitors, and statins are recommended for all persons with PAD. Lower extremity percutaneous transluminal angioplasty or bypass surgery is performed when advanced stages are reached and limb-threatening ischemia occurs. Once gangrene develops, amputation is necessary to prevent infected and dying tissues from causing

septicemia. Therefore, accurate and timely diagnosis of PAD is crucial in the prevention of further health consequences [8].

5.3 Current Diagnostic Techniques

5.3.1 Ankle brachial Index

The most widely accepted, objective definition of PAD is the ankle brachial index (ABI) [172]. The ABI is calculated by measuring the maximum systolic blood pressure at the ankle and dividing it by the systolic blood pressure in the brachial artery in the upper arm. In healthy individuals ABI values range between 0.9 and 1.2. Values less than 0.9 identify patients with some form of vascular occlusions or stenosis. Most patients with symptoms of claudication will have an ABI between 0.5 and 0.8 and those with more severe symptoms such as rest pain will generally have values less than 0.5.

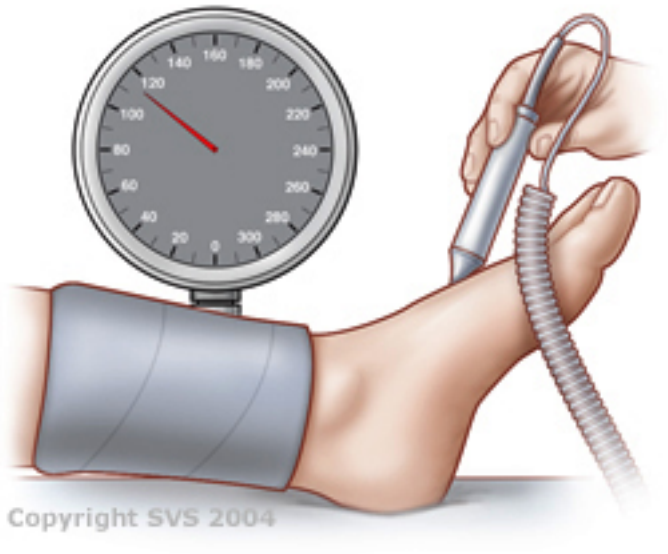

Figure 5.2 Ankle brachial index being measured on the dorsalis pedis artery of the foot.

Although the ABI is often useful in the diagnosis and determination of the severity of PAD, it has major shortcomings [178, 179]. The presence of distal emboli, micro-emboli and atherosclerotic plaques in the foot can lead to tissue breakdown, ulceration and amputation, even if the ABI is

close to 1. Furthermore, falsely elevated ABI readings occur in patients with medial wall calcification, which is a condition commonly seen in diabetic patients. In these cases, the ABI reflects the ability of the vessel wall to resist compression rather than being a true indicator of the blood flow and pressure within the vessel. In addition, diabetic patients with neuropathy showed that ABI's inability to detect arterial disease resulted in false-negative results in one third of the limbs [179]. Consequently, physicians rarely employ this test in diabetic patients. Considering that between 120 and 140 million people suffer from diabetes mellitus (DM) worldwide and that diabetic patients are at excess risk of developing PAD, the implications of the problem are enormous [180].

5.3.2 Pulse-volume recordings

Pulse-volume recordings (PVR) are conducted using segmental limb pressure cuffs along with the ABI measurement in an attempt to localize a stenosis or occlusion. Limb pressure cuffs are placed on the thigh, calf, ankle and the metatarsal region of the foot. These pressure cuffs are then inflated sequentially to 65mmHg and a plethysmographic tracing is recorded at the various levels (Figure

5.3). The pleth recording is typically performed using Doppler ultrasound but laser Doppler systems also exist to perform the same function [181, 182].

Figure 5.3 Example of a patient undergoing a PVR measurement

The shape of the tracing should consist of a systolic upstroke and a rapid down stroke with a prominent dichrotic notch during the downs stroke period. With increasing severity of PAD, the waveforms become more attenuated with wider slopes until eventually the waveforms are absent. Figure 5.4 below represents PVR waveform recordings conducted at a vascular lab. As one can see, the severity increases as the amplitude decreases and the shape of the waveform loses its higher frequency content.

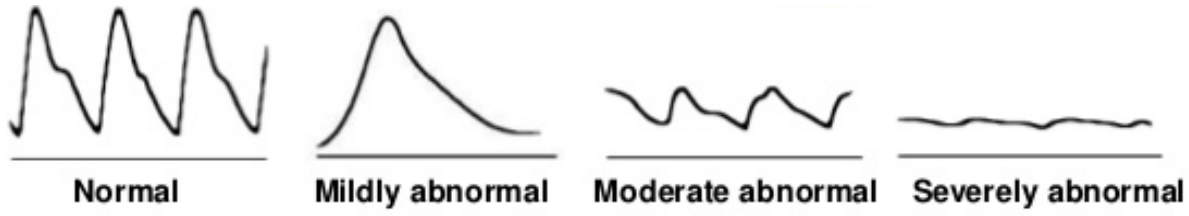

Figure 5.4 Example pleth signal from pulse volume recording (PVR). The PVR test has four categorical results.

5.3.3 Duplex ultrasound

Imaging methods are usually used as second line diagnostic tests, to confirm initial diagnostic results and to assess for a potential surgical intervention [182]. Typically, lower limb Duplex-ultrasound (DUS) examinations are initially performed first to determine the location of stenosis or occlusions in the legs. DUS is a combination of B-mode and Doppler ultrasound and is useful in detecting lesions along the lower extremities.Duplex Doppler ultrasound is another clinical tool used for functional assessment of blood flow in large vessels. Changes in a cross-sectional area of the vascular lumen can be determined by means of peak systolic velocity (PSV) at the site of a stenosis, the ratio of PSV at the site of the stenosis and its immediate normal vicinity, end diastolic velocity, and more subjective criteria such as number of phases in the Doppler waveform and degree of spectral broadening [183]. Although this technique is excellent for measuring flow in large vessels, it has difficulty in probing small vessels [e.g., diameter less than 100 μm] in the lower extremity muscles. Current non-invasive techniques for the evaluation of microvascular blood flow include Doppler optical coherence tomography [182] and laser Doppler.

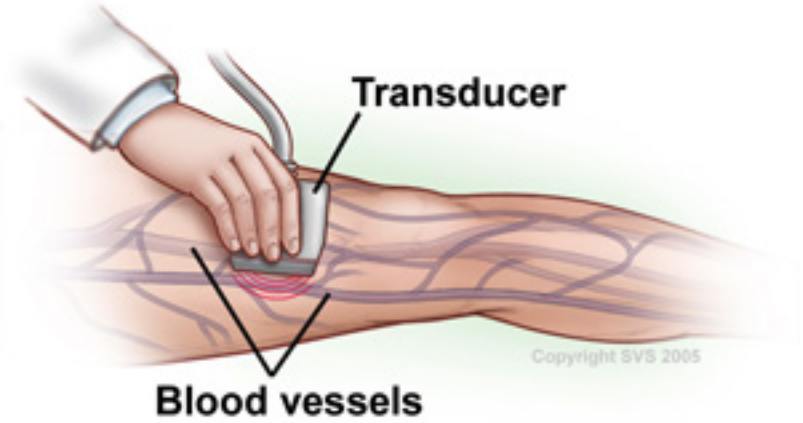

Figure 5.5 Duplex ultrasound scan being conducted along the lower extremities.

The imaging technician will look for occlusions and listen for bruits ("wooshing" sounds) resulting from blood flow through narrowed arteries. DUS is used to identify lesions within the leg (Figure 5.5), however the arteries below the knee are small, which makes the DUS assessment difficult. As the arteries decrease in size the results become heavily user dependent. Furthermore, identifying lesions does not provide direct information on the perfusion of the foot [184].

5.3.4 Angiography

The current gold standard in PAD diagnosis is called digital subtraction angiography (DSA) [185]. DSA provides images of the blood vessels in the lower extremities to detect a problem with blood flow. These images are used in the operating room to assess the precise location of one or more occlusions in the lower arteries. Vascular surgeons use this information to place stents or balloons

and continue using DSA during the angioplasty procedure to ensure proper placement and verify that blood flow through the artery is improved.

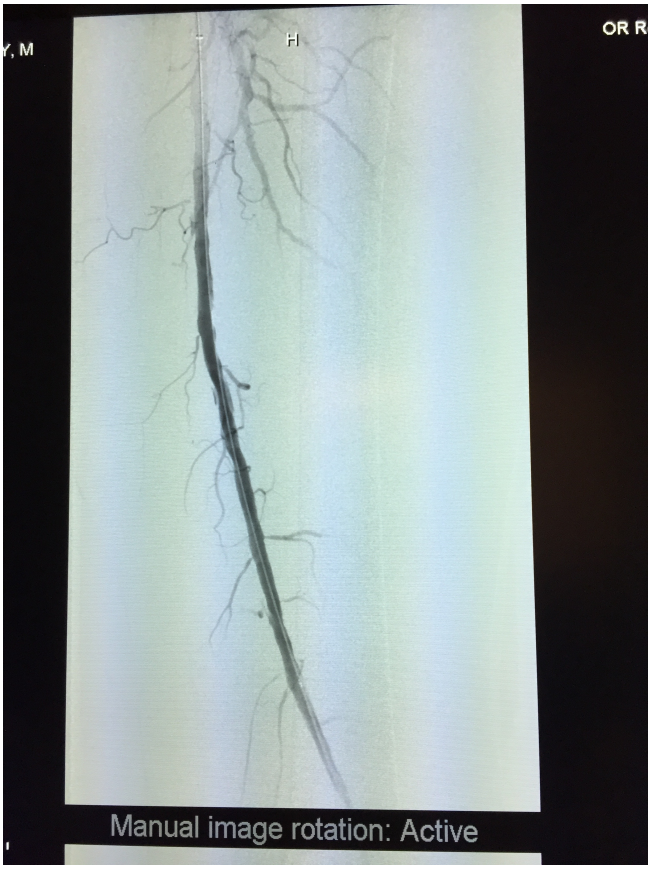

Figure 5.6 DSA image of the vasculature in thigh. The main vessel in this image is the femoral artery. The contrast dye used is passing through the femoral towards the tibial arteries.

The procedure involves inserting a catheter (a small, thin tube) into an artery patient (usually through the femoral artery) and passing it down to the blood vessels towards the foot. A contrast dye is injected through the catheter and X-ray images are taken to obtain an image of the vasculature in the lower extremities. DSA is conducted on all patients being considered for amputation to determine whether revascularization is an option. DSA is invasive and also requires

nephrotoxic contrast media. In addition, it also requires ionizing radiation, which limits DSA's frequency of use.

DSA has been used for intraoperative verification of bypass graft patency. Limitations of this technique include inability to measure flow dynamics, violation of graft integrity, risks of ionizing hazard, contrast injection, and arterial puncture.

5.4 Use of Diffuse Optical Imaging for Diagnosis of PAD

Monitoring techniques to directly quantify tissue hemodynamic and metabolic responses to the revascularization in local ischemic muscles of a lower extremity would describe a critical feature of treatment success and lead to a better understanding of the treatment mechanisms. Use of diffuse optical spectroscopy (DOS) to monitor PAD in the lower extremities during surgical interventions has the potential to objectively assess the success of arterial revascularization.

Optical imaging techniques has been used by many groups to evaluate muscle vascularization in the calf [186-190], even during surgical intervention of PAD [186]. Although results in [186] showed a significant improvement in relative blood flow (rBF) in the affected limb, measurements on the control side largely varied. Additionally, changes in Hb and HbO2 did not show significant changes.

To expand on this research, our group has made a significant effort to utilizing optical tomographic imaging to measure perfusion in the foot for PAD patients [191-195]. In our group's initial pilot study, we used vascular optical tomographic imaging (VOTI) on 40 individuals (20 healthy volunteers, 10 non- diabetic PAD patients, and 10 patients with PAD and diabetes) were presented to quantify VOTI's sensitivity and specificity at detecting PAD, its ability to assess the severity of the disease and localize the perfusion response in the foot. The VOTI system is a optical fiber

based system with a total of 34 fibers encompassed the foot, forming a coronal cross section at the mid-metatarsal level (Figure 5.7). These fibers shine light through the foot and capture the back-reflected and transmitted light. It was shown that the VOTI system was capable of quantifying the blood volume changes within the foot during the thigh cuff occlusion and outputting diagnostic parameters, such as change in hemoglobin concentration, enabling the assessment of foot perfusion. The study resulted in a statistically significant difference between the healthy cohort and both the non-diabetic and the diabetic PAD cohorts [194].

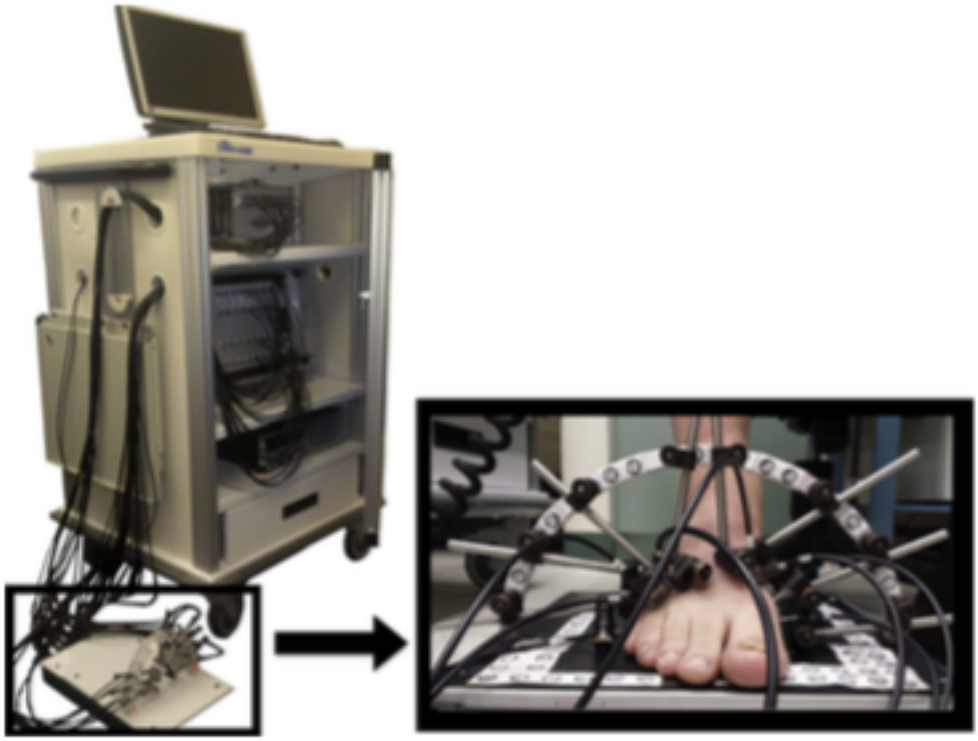

Figure 5.7 The VOTI system with its sandal shaped measuring probe provides cross sectional images of hemoglobin concentrations in the foot.

From these results, our group has looked to expand this work into monitoring of tissue perfusion during the angioplasty procedure. Unfortunately, the VOTI system was shown to be too large to be integrated into an operating room setting. In addition, the use of optical fibers from VOTI or

use of non-contact imaging [193] was intended to be used in a clinical exam room setting, where the patient is sitting down.

To make DOS measurements more appropriate for the OR setting, I present work towards creating a multi-channel DOS system based on the technology of the WHDD (Chapter 2) to monitor haemoglobin concentrations during surgical intervention. However in DOS, measurements are performed in a reflection-based geometry at isolated points on the surface of the tissue, which makes the technique heavily dependent on the location of the probe. Because of this, I have employed a system with four channels to capture vascular information at the foot where blood is supplied from various major arteries at or below the knee.

5.5 Vascular Optical Spectroscopic Measurement (VOSM) System Design for Intraoperative Use During Vascular Surgery

This section will provide a technical overview and characterization of a DOS device designed for intraoperative monitoring device during revascularization of arteries of the lower extremities, which I have named the vascular optical spectroscopic measurement or VOSM system. This design is a portable multi-channel DOS system that can be easily integrated in the OR. Previous studies that have used DOS for intraoperative use only used DOS on the calf muscle to measure improvement in tissue perfusion [186-190]. This placement however does not provide vascular information at the foot, where ulcers and gangrene is more prevalent. Placement of DOS probes on the foot may not be sensitive to revascularization to specific arteries due to the angiosome concept. Angiosomes are vascular territories are called angiosomes (Figure 5.8), and are defined

as five distinct zones in the lower legs as fed by the medial sural artery, lateral sural artery, posterior tibial artery (PTA), anterior tibial artery (ATA), and peroneal artery (PA).

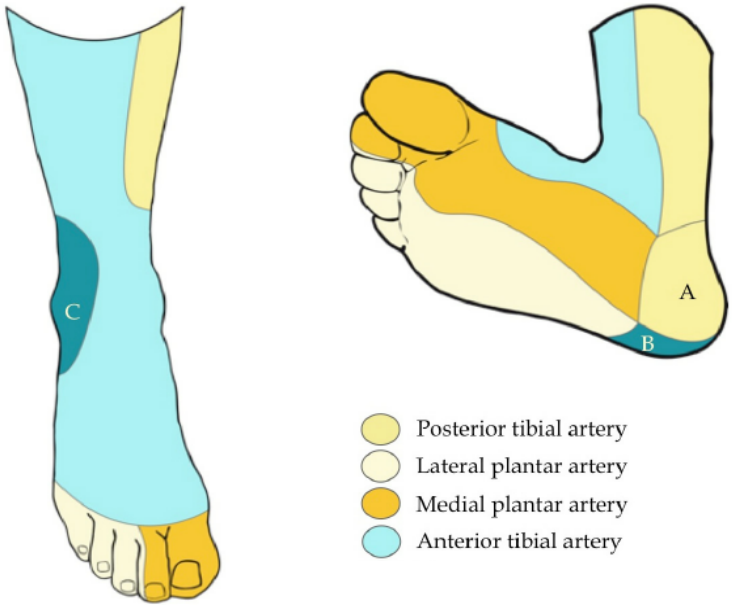

Figure 5.8 Diagram of different angiosomes in the lower extremity.

Because this angiosome concept can separate which ulcerations can affect specific zone, it has the potential to help surgeons choose whether a bypass or an endovascular procedure has the best chance of healing an existent ischemic ulcer. The design of the multi-channel system intends to provide perfusion measurement at various vascular territories that lie through the foot. By monitoring multiple angiosomes, our hope is to provide immediate feedback to the surgeon as to the efficacy of the revascularization to the ulcers.

5.5.1 Design Overview of the VOSM Device

A technical overview of the vascular optical spectroscopic measurement (VOSM) system is described here. This VOSM system will be an extension of the design from the handheld wireless probe from Chapter 1. In the first chapter, the WHDD contained a single channel device that could

only provide data for a single vascular volume. For the VOSM system, I have expanded the WHDD to 4 channels to monitor multiple angiosomes. A diagram of the system overview is shown in Figure 5.9.

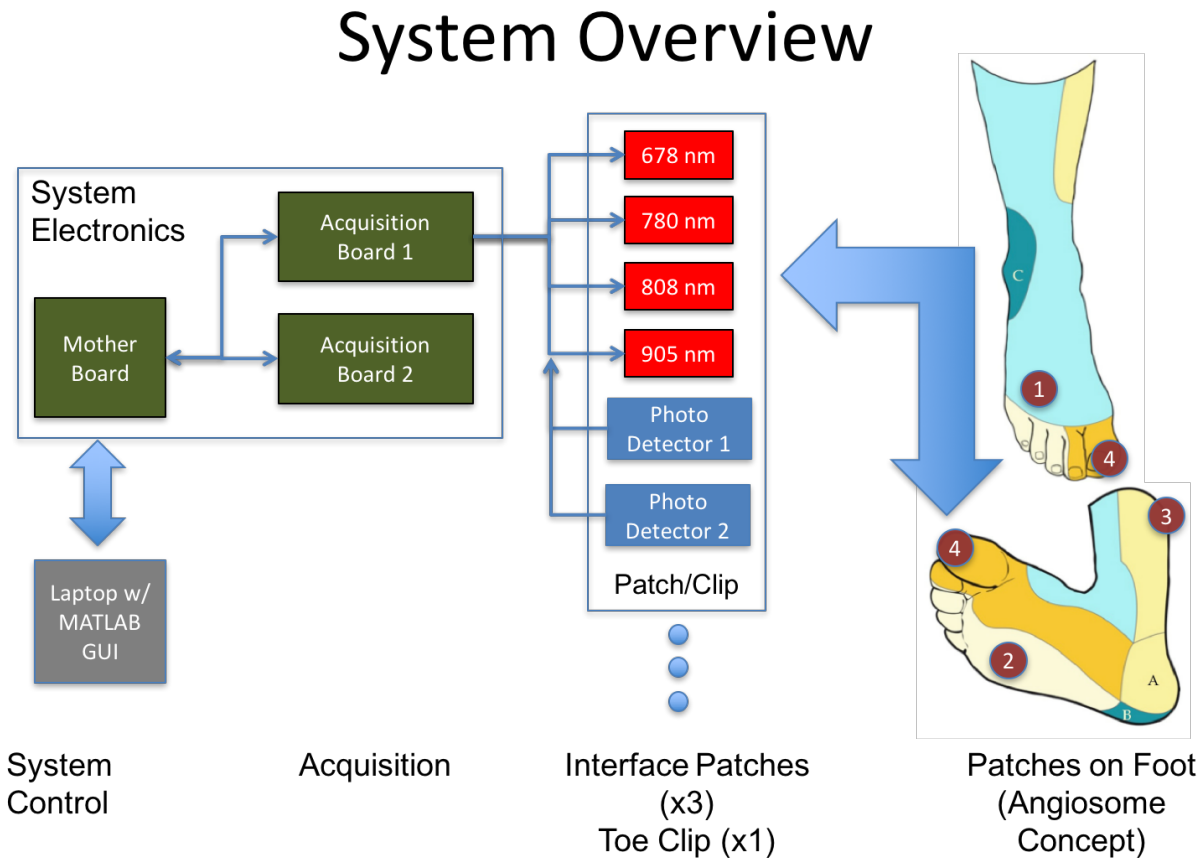

Figure 5.9 Outline of intraoperative system for vascular surgery. A PC controls the system via USB. The motherboard will relay an experiment profile to the multiple DOS channels. Each channel has an interface patch that is placed on the foot of the subject according to the angiosome concept.

The VOSM system consists of three main components. (1) a laptop with a MATLAB graphical user interface (GUI) that controls the VOSM system electronics. (2) The VOSM system that contains a central processing board, or motherboard to be used for communication to and from the GUI, and two acquisition boards that contain the lasing and detection circuitry to perform the DOS

measurements. Each of the electronics boards has connectors for USB connectivity to the PC, power, inter-board connectivity, and DOS measurement cabling. (3) The interface cabling and interface patches that are placed on the subject's foot. The cabling is made up of leads that power the laser diodes as wells as leads for detection of reflected light from the DOS measurements. Each of the four interface patches contains four laser sources and two photodetectors. A photo of the entire system is shown in Figure 5.10.

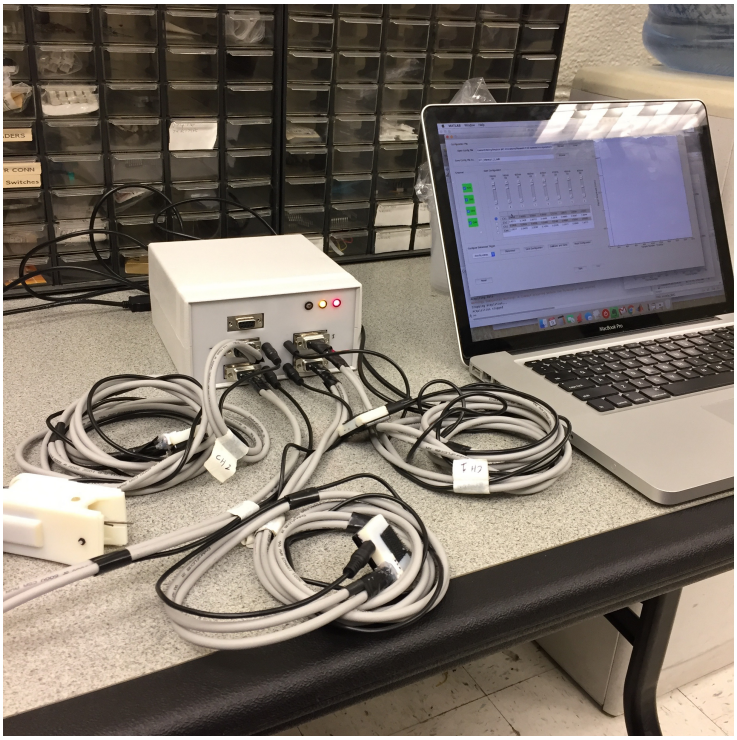

Figure 5.10 VOSM system for vascular measurements on the lower extremities. The VOSM system consists of a laptop with a MATLAB GUI that controls the VOSM hardware via RS-232. There are 4 DOS channels consisting of 3 patches and 1 toe clip.

The main system electronics consists of the motherboard and two acquisition boards that are stacked and screwed on top of one another using standoffs (Figure 5.11) and enclosed in a plastic enclosure (Figure 5.12).

Figure 5.11 VOSM system enclosure with system electronics. There are three electronics boards in the enclosure, with the motherboard on top (A), and two acquisition boards below (B, C). In addition, there is an expansion connector to control a legacy optical switch (D).

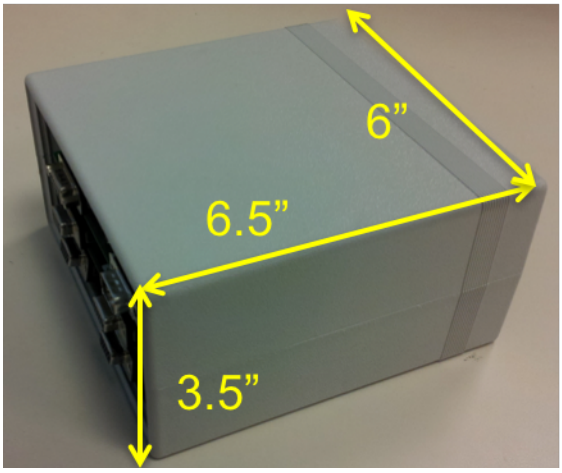

Figure 5.12 VOSM system enclosure and its physical dimensions.

5.5.2 Motherboard

The motherboard in the VOSM system is a central control board that processes measurement instructions to and from the PC/laptop and instructs the acquisition boards to perform single measurements (Figure 5.13). At the heart of the masterboard is a central microcontroller (PIC32MX695F512H, Microchip) to perform and communicate tasks. The microcontroller performs these tasks by utilizing its multiple UART ports to communicate with peripheral devices. One of the UART ports is converted to RS-232 for communication with the PC connected to the VOSM hardware. Through this port, the PC is able to send measurement instruction profiles and acquisition settings for the acquisition boards to the motherboard, while during acquisition of data, the motherboard bundles all of the measurement data from the acquisition boards to create a data packet containing one frame of data. A second UART port from the motherboard microcontroller communicates with the acquisition boards by sending information packets to the microcontrollers on one of the two acquisition boards. These information packets contain information about gain settings and a flag on whether to perform a measurement. When the acquisition board acquires a new frame of data, this data is sent back to the motherboard microcontroller on the same UART bus. A third UART port can be used for communcations with an optical switch used in another imaging system, for special experimentation purposes.

The communication between the PC and microcontroller is perform via RS-232. The UART bus on the motherboard microcontroller sends and receives information through RS-232 by using a converting chip that will take the 0V to +3.3V UART signal and converts it into the -5V to +5V

RS-232 signal. The structure of the data packets between the motherboard and the PC and the motherboard and the acquisition boards will be discussed further in section 5.5.6.

Although this current motherboard is set up to communicate with two acquisition boards, the motherboard allows for scalability, allowing up to 4 acquisition boards to be connected at one time. The firmware involved for this scaled addition is presently implemented.

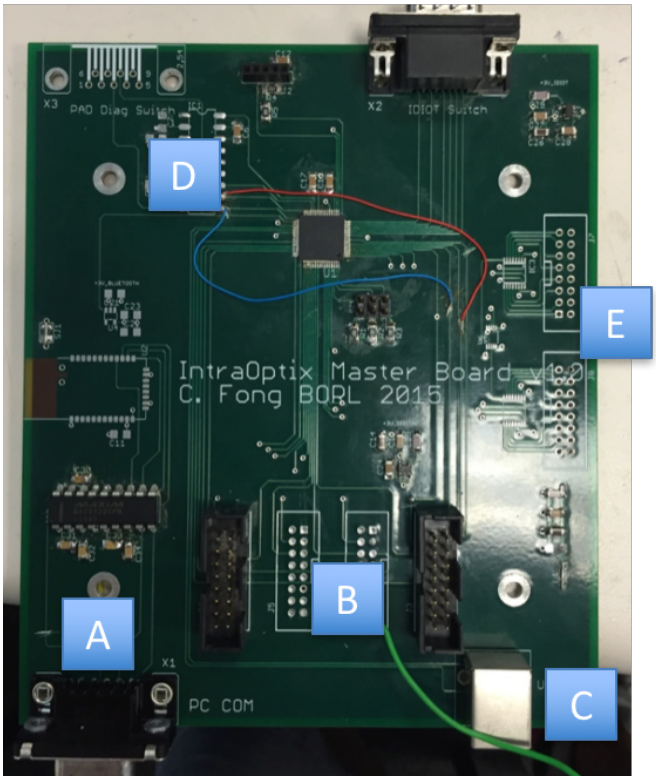

Figure 5.13 Photo of the master board used in the VOSM system. The board contains a RS-232 connection to a PC (A), connections to the two acquisition boards (B), a USB connector used power the VOSM system and for USB connectivity (C), digital I/O control for interboard communications (D), and optional expansion for data acquisition.

5.5.3 Acquisition Board

Along with the motherboard, there are two acquisition boards that are enclosed in the VOSM system. Each acquisition board consists of two DOS channels (which correspond to two DOS patch probes), connectors to the interface cables and patches, an ADC to sample the DOS measurements, and a microcontroller for DOS signal demodulation and communication between the acquisition board and motherboard. Figure 5.14 shows a diagram of an acquisition board, containing DOS channels 1/2 or channels 3/4 for the two respective acquisition boards.

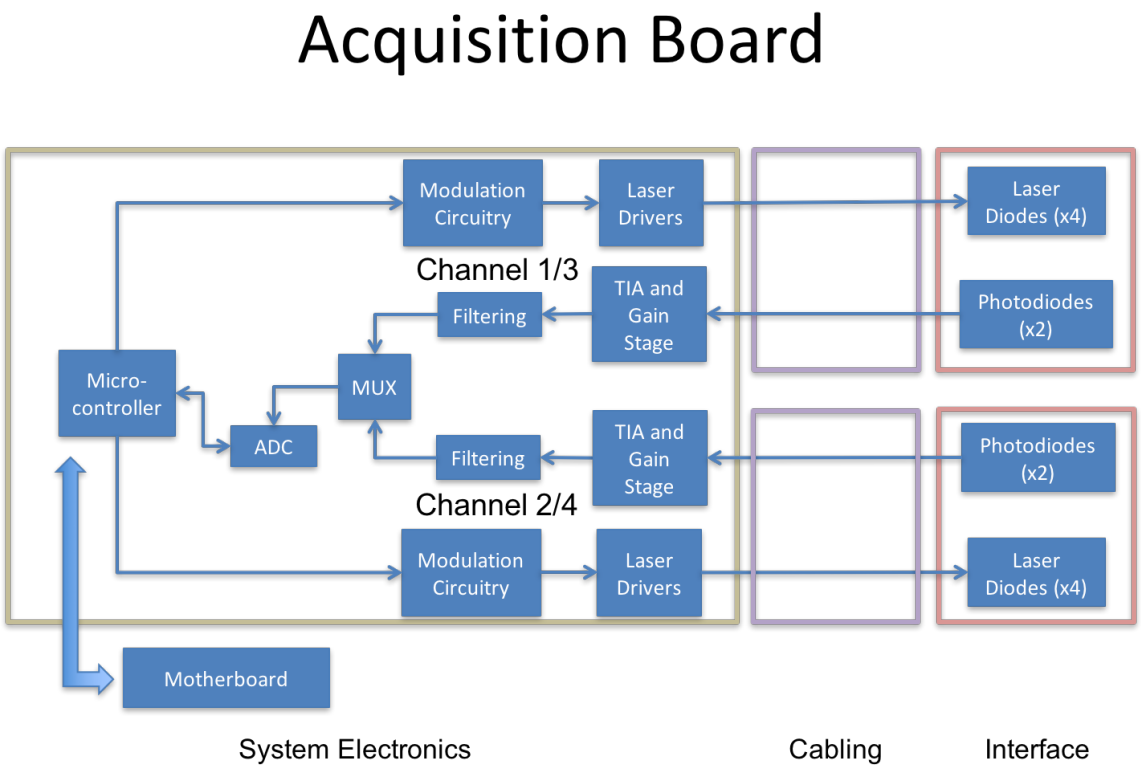

Figure 5.14 Diagram of an acquisition board used in the VOSM system. Each acquisition board contains two DOS channels and a microcontroller. The microcontroller accepts instructions from the motherboard and acquires data according to the gain settings and scanning profile. Modulation signals control the output power that the laser drivers provide to the laser diodes. Cabling from the laser driver to the interface supplies power to the lasers. Lasers emit light into tissue and photodetectors sense the reflected light. The current from the photodetectors is amplified and filtered for signal conditioning into the MUX. The resulting signal is sampled and processed for demodulation using our digital lock-in detection scheme.

Each DOS channel consists of sections for laser modulation and laser driving circuitry for source illumination, as well as current amplification, signal conditioning, and sampling for the detection electronics. Once the signal is properly conditioned, an analog multiplexer (MAX4518, Maxim) selects which detector channel should be sampled and the acquisition board's ADC (LTC1865L, Linear Technology). Addition processing of the detected signal is performed through the board microcontroller to compute the amplitude of the detected signal. Once an entire frame from the acquisition board is obtained, the data is sent back to the master board. The following subsections describe the functionality of the DOS channels in further depth. A photo of an acquisition board is shown in Figure 5.15.

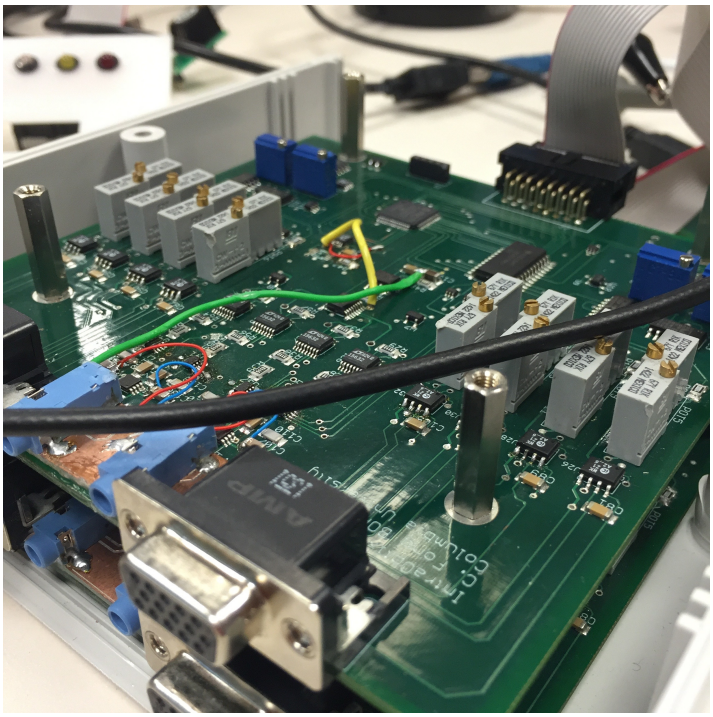

Figure 5.15 Photograph of one of the two acquisition boards in the VOSM system.

5.5.3.1 Light Illumination Unit

The input light is generated by 5 mW 5.6 mm-diameter laser diodes at wavelengths of 780 nm, 808 nm, 678 nm, and 904 nm (L780P010, L808P010, HL6748MG, L904P010, Thorlabs). The wavelengths are selected to provide a range of spectral information to reconstruct oxygenated hemoglobin ([HbO_2]), deoxygenated hemoglobin ([Hb]) and scattering while working within the limited selection of wavelengths available in this small package. The laser diodes are driven by the 15 V Laser Diode Driver (iC-WKN, iC Haus). Each wavelength has the ability to modulate the amplitude at a programmatically controllable frequency ranging from 1 to 5 KHz. The modulation signal is generated using a combination of a 1 kHz–33 MHz Oscillator (LTC6903, Linear Technology), a binary counter (M74HC4820, STMicroelectronics) and a SPI-controllable low-pass filter (LTC1569-6, Linear Technology) that was typically set to a 72kHz. This creates a 1k-5kHz sinusoidal signal that has a range from 0 to 3.3V. To control the output laser power on the laser driver, the sinusoid must be conditioned for a specific mean and amplitude. Therefore, an adjustable gain and offset amplifier stage was applied before the modulation set pin on the laser driver. The laser power of the driver is set by a POT resistor such that the laser output power is 5mW. The modulation of the input light provides several advantages including superior noise rejection (including ambient light) as well as the ability to illuminate the tissue simultaneously with multiple wavelengths.

5.5.3.2 Detection Unit

The light is absorbed and scattered as light passes through the sample to two silicon photodiodes (SiPD) (Hamamatsu S1337-33BR) on an interface adapter board that is placed on the foot of a

subject. The maximum source detector distance for the first PD (PD1) is 16mm and the 25mm for the PD2. Current from the two SiPD travels down a 3 foot cable and is converted to voltage using a single-supply transimpedance amplifier (Op-Amp: AD8606, Analog Devices) that utilizes a bandwidth-extension technique previously implemented in [57]. The gain for the TIA is fixed at 20k V/A for PD1 and 50k V/A for PD2 with a bandwidth of 74kHz and 30kHz respectively. The operational amplifier (op-amp) used for the TIA is specifically chosen for this application due to its low bias current and noise. The bias current of this device is ~1 pA which allows us to measure photodiode currents in the tens of picoamps. In addition, the AD8606 has excellent voltage noise performance of 6.5 nV/Hz$^{-1/2}$ and 0.01 pA/Hz$^{-1/2}$ which means that with a 20 kΩ resistor the noise generated from the op-amp is:

$$V_{op-amp,noise} = I_{noise}\mathrm{R} = \left(\frac{0.01pA}{\sqrt{Hz}}\right)\left(\sqrt{5.1kHz}\right)(50k\Omega) = 35.7nV \tag{5.1}$$

Whereas the thermal noise of the 50kΩ resistor is:

$$V_{thermal} = \sqrt{4kTRf} = \sqrt{(4)(1.38 * 10^{-23}m^2kgs^{-2}K^{-1})(298K)(20k\Omega)(5.1kHz)} = 1.3\mu V \tag{5.2}$$

The noise generated by the op-amp is still well below the thermal noise of the resistor. In both Eq. (5.1) and (5.2) the frequency used is 5.1 kHz which is the bandwidth of our acquired signal, as specified by the cutoff frequency of the low-pass anti-aliasing filter. Notice that in Eq. (5.2) it is important that temperature be controlled as it can lead to an unwanted increase in the thermal noise. Additionally, a 3-bit programmable gain amplifier (PGA) (LTC6910, Linear Technology) stage is used to optimize the signal to the scale range of the ADC which is 0 to 3.3V. These PGAs were selected because they are low noise that are easy to use and occupy very little PC board space. are

low noise digitally programmable gain amplifiers (PGAs) that are easy to use and occupy very little PC board space. The highest voltage noise performance of the PGA (Gain =1V/V) is 24 $nV/Hz^{-1/2}$ which means that 5.1kHz bandwidth the noise generated from the PGA is 54.2nV.

Following the TIA and PGA gain stages, the signal is filtered with a 4th order Butterworth anti-aliasing filter that removes high frequency components and whose primary purpose is to ensure there are no frequencies present above the Nyquist frequency prior to digitization. The signal is sampled by the ADC at 50 kSamples/s which establishes a Nyquist frequency of 25 kHz. As a result, we choose a cutoff frequency of 5.1 kHz and a Butterworth filter that has a flat passband for the 5 kHz signals, while also providing strong attenuation of any higher frequency noise at risk of aliasing into the passband. The 4th order Butterworth filter is implemented using a single filter chips (LTC1563-2IGN, Linear Technologies). The filter, in combination with a number of resistors, form an 4th order low-pass Butterworth filter with a 5.1kHz cutoff frequency that has <0.1% attenuation at our upper core frequency of 5 kHz, but still offers over 50 dB of noise suppression in our aliasing range.

Once the signal has been properly filtered for sampling, the resulting signal goes into a 4 by 1 analog multiplexer (MUX) (MAX4518, Maxim) that selects which detector to sample. A 4 by 1 MUX was selected because there are two detectors per DOS channel and there are 2 channels resulting in four total detectors per acquisition board. This Maxim MUX is a precision, low-voltage chip that is suitable for this application.

5.5.3.3 Data Sampling and Amplitude Detection

Finally transitioning from the analog domain to the digital domain, the signal is quantized using a 16-bit ADC (LTC1865, Linear Technology) that provides speeds up to 150kps. To do this we must

convert a continuous, smoothly varying signal, into a finite number of samples that adequately capture the shape of the signal. Resolution in both x (time) and y (amplitude) are both important. Resolution in time is determined by the sampling rate of the ADC, fs (or inversely, the sampling period Ts=1/fs), while the resolution of the amplitude is determined by the number of bits that the ADC can capture in its digital sample. More bits allow for more resolution in approximating the analog signal. The 16-bit ADC used in our design provides 2^{16}=65536 levels of quantization, and given that we have a supply range of 3.3V, the ADC provides a resolution of 50.4 μV. The ADC uses a successive approximation (SAR) architecture to sample the signal. For this architecture, the conversion starts with the internal D/A converter (DAC) set to midscale. The comparator determines whether the SHA output is greater or less than the DAC output, and the result (the most-significant bit (MSB) of the conversion) is stored in the successive-approximation register (SAR) as a 1 or a 0. The DAC is then set either to 1⁄4 scale or 3⁄4 scale (depending on the value of the MSB), and the comparator makes the decision for the second bit of the conversion. The result (1 or 0) is stored in the register, and the process continues until all of the bit values have been determined.

With the ADC sampling rate set to 50kHz for a 5kHz modulated signal, 100 samples are acquired to precisely acquire exactly 10 cycles. Using our digital lock-in detection scheme [58] that was discussed in section 2.2.3, this vector of data will be converted to represent the amplitude for one of the 8 source-detector pairs for a single channel/patch. A single frame of channel data is acquired

once all combinations of four lasers and two detectors are illuminated/sampled. Once the frame is collected, the data is formatted into a packet and is transmitted via UART to the motherboard.

5.5.4 Interfacing and Cabling

Each DOS channel interface contains 4 laser sources and 2 PDs that fit onto a single patch interface or toe clip. The condition of the feet of many PAD patient can largely vary, with some exhibiting a substantial amount of pain, ulceration, and/or gangrene. To this end, careful consideration was taken into account for cabling and interfacing of the DOS channels to the foot to prevent further discomfort while undergoing the DOS measurements. The ideal patch interface design must be non-intrusive, lightweight, and durable. In addition, the interface would ideally have a disposable adhesive contact to easily stick the interface patches to the various angiosomes of the foot. The cabling requires 15 leads in order to operate and must be have good electrical isolation to prevent noise. Although these attributes for the interface would be ideal, many compromises were made

for the initial prototype for time consideration and potential redesigns of the opto-electrical components that may be costly to make for a custom designed interface.

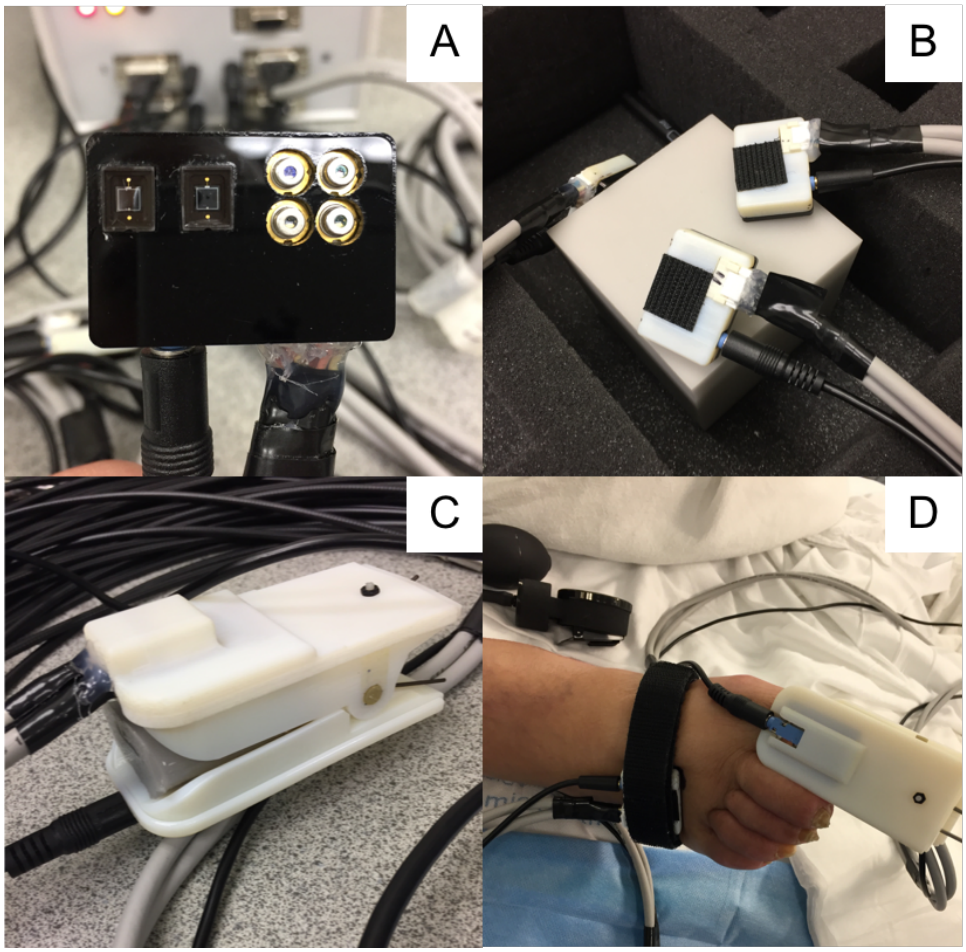

Figure 5.16 Front face of a patch interface, containing 4 laser sources and 2 photodetectors, with a laser cut cover made of acrylic (A). The back face of the patch interfaces shown with a phantom block interface used for calibration of our measurements (B). The toe clip shown with a silicone calibration bar in the toe chamber (C). Photo of a patch interface on a patient's foot, alongside the toe clip (D).

The initial patch interface design for the VOSM prototype was made on a low-profile PCB board that was enclosed in a 3D printed back casing and had its opto-electric components protected using laser cut acrylic (Figure 5.16A,B,D). The PCB design underwent several iterations to improve the form factor and the cross-talk between the laser sources and the photodetectors. To maximize the SNR of the acquisition, the interfacing DOS channels have the illumination and detector circuitry

isolated from each other. In addition, the enclosure of the patch interfaces was 3D printed to minimize the volume and to ensure a compact and tight fit for the PCB board. The patch interface probes contain 8 SD pairs from 4 laser source and 2 detectors. The illumination wavelengths, SD distances and other patch dimensions are shown in Figure 5.17. Although artery depth in the foot can be up to 3cm into the foot and the optimum SD distance to measure arterial changes would be 6cm, the largest SD distance in this design is 25mm while the smallest is 10mm. These SD distances were chosen by an experimental process, in which laser cut acrylic of varying sizes were made and placed on the feet of volunteers to determine placement and size constraints that would arise from imaging patients. Through this process, it was determined that a 25mm SD pair distance would be the largest distance possible before interface placement issues on the subject became problematic. This maximum SD pair distance was further justified by the reconstruction processing performed by Khalil et. al. [195], in which the fiber-based imaging system largely used a

combination of reflectance measurements of 1, 2, and 3 cm SD pair distances for the image reconstruction of optical properties.

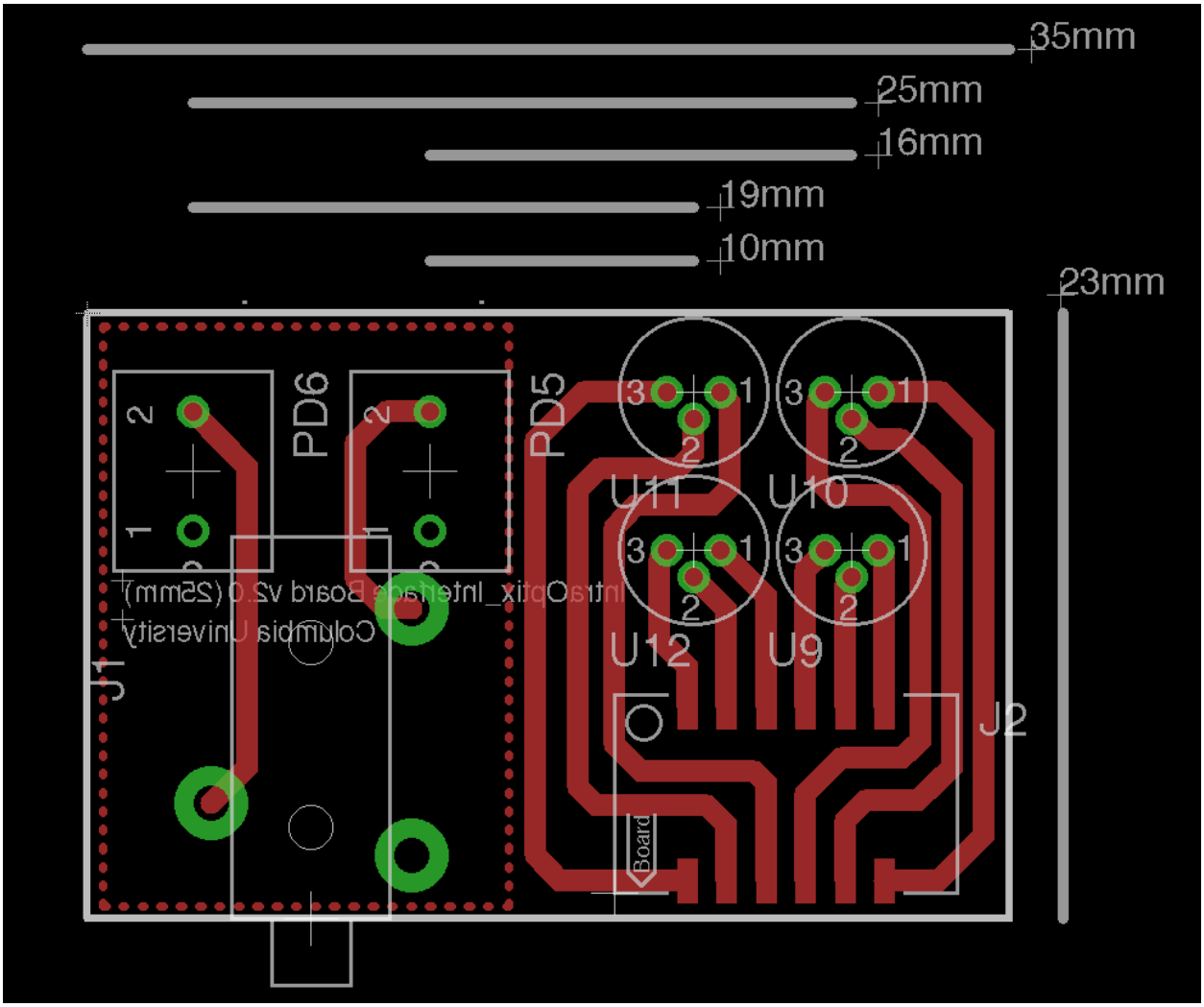

Figure 5.17 The top view of the PCB layout for the patch interface board. Lasing and detecting interfaces are facing into the page. Dimensions of the board and SD distances are shown.

The fourth channel for the VOSM system is a toe clip that fits on the big toe. This custom-made design was inspired by the numerous pulse-ox monitors that fit on the finger. The DOS topology differs from that of the patch design, as its measurement design is transmission based, where the 4 laser sources are placed on the plantar side of the toe and the two photodetectors are placed on the dorsal side. The toe clip is made up of four 3D printed parts, two clip parts that house the toe, and opto-electronics, two covers that protect and hold the PCB boards and connectors, screws, and

a self-adjusting spring to create a snug fit in the toe chamber (Figure 5.16C,D). The toe clip chamber distance from the illumination sources and the detectors is 17mm. The size of toe clip is 80mm x 27mm x 25mm. The Solidworks CAD model is shown in Figure 5.18

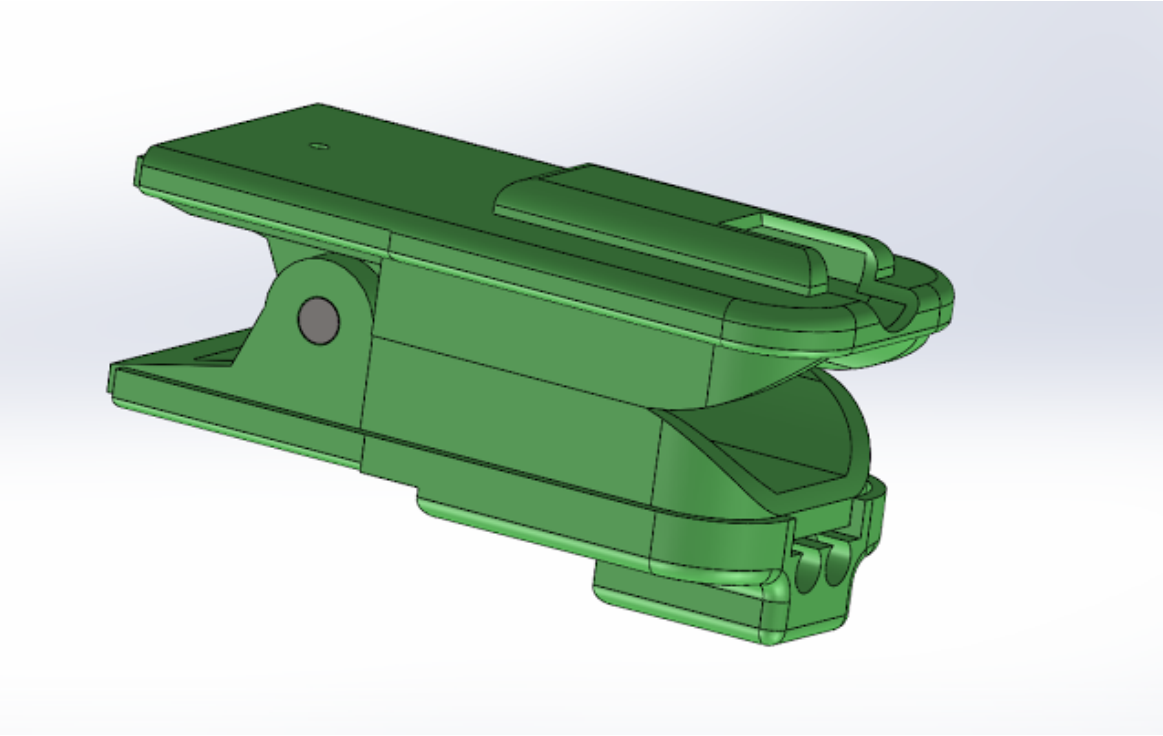

Figure 5.18 A CAD drawing of the toe clip design. The design consists of four 3D printed parts including the toe chamber and covers for the opto-electronic enclosures, a hinge to hold the chamber, and a spring to apply closing pressure onto the toe being measured.

In order to connect the opto-electronics, the two PDs require 3 leads while the four laser sources require a total of 12 leads from the main VOSM electronics to the interfacing. The Chapter 1, the WHDD interface was connected directly to the rest of the device, which is not feasible for this application. The interface must be connected to cabling from the main device to a small PCB board that will embody the laser and photodetector components. Previous iterations of the cabling consisted of a single cable solution, where all 15 leads were enclosed in the cable. Although a single cable solution is less cumbersome, the cross-talk between the illumination and detector leads dominated the actual measurements (Not shown). For the current VOSM system design, the

detector cable used is a shielded audio stereo cable, that contains two signal leads (Left and Right, corresponding to PD1 and PD2) and a ground lead. The custom-built illumination cable consists of two 6-lead cables, that make up the necessary 12 leads required to illuminate the 4 laser sources. The illumination cables are connected through a VGA connector at the VOSM system end and a micro rectangular connector (SM12B-ZPDSS-TF, ZPD Connectors) at the interface end (Figure 5.19).

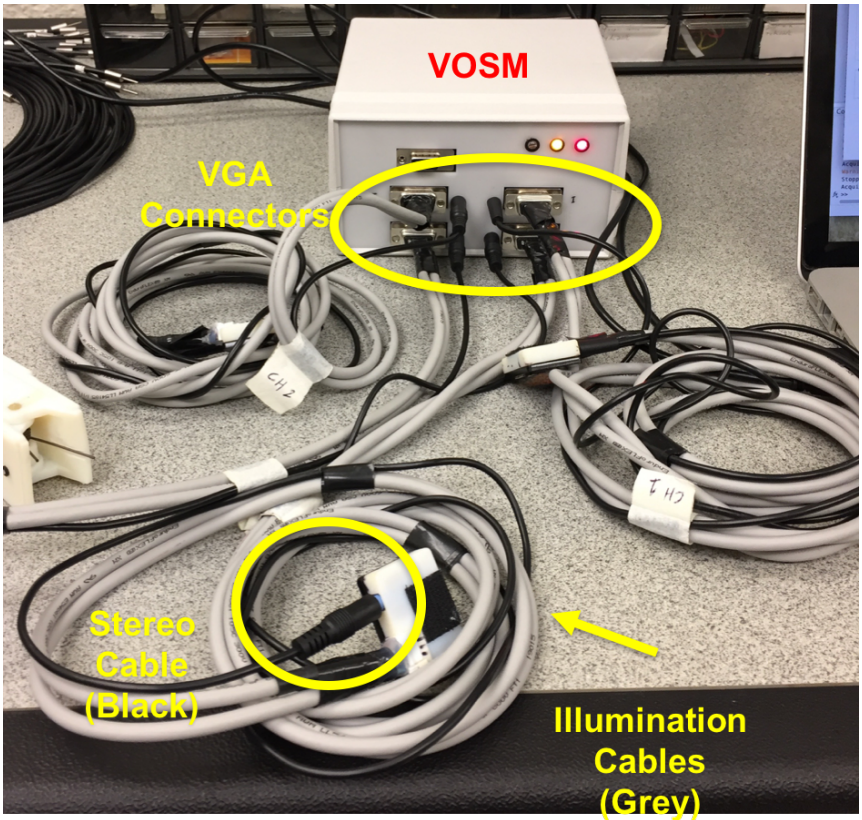

Figure 5.19 VOSM system with interface cabling. VGA connectors are used to connect the illumination leads to the main VOSM system electronics. A stereo cable is used for the detector leads. Dual cables consisting of 6 leads each are used to power the laser diode.

5.5.5 Graphical User Interface

A MATLAB based graphical user interface (GUI) was designed to control, collect, and display data streaming from the VOSM system (Figure 5.20). The GUI can connect to the VOSM system using a virtual COM port, in which a USB to RS-232 cable is used to send and receive data to the VOSM system. Similar to the GUI used for the WHDD described in Chapter 1, the Graphical User Interface Design Environment (GUIDE) module was used to create point-and-click control of software applications, eliminating the need to learn a language or type commands in order to run the application.

The GUI that was created has the ability to control the VOSM system using connect, stop, start, and calibration of gain, save the data to a specified location, load previous gain settings, and display incoming data from the multiple channels from VOSM in real time. The data received by the GUI is saved to a text file at a user specified location. The interface also has the ability to manually adjust and send individual gain settings to the device using sliders for each source detector pair by pressing the "Send Configuration" button. The DOS channels can be manipulated by selecting the corresponding radio buttons, and with 4 sources and 2 detectors, there are a total of 8 source-detector pairs that can have the gain adjusted for a given DOS channel.

The user can load previous gain information by clicking on the "Browse" button on the "Open Config. File" section and selecting a "*_config.txt" file and pressing the "Load" button. Once

loaded, the sliders for the gain configuration will update accordingly. The user must then press the "Send Configuration" button to send the loaded gain settings to the device.

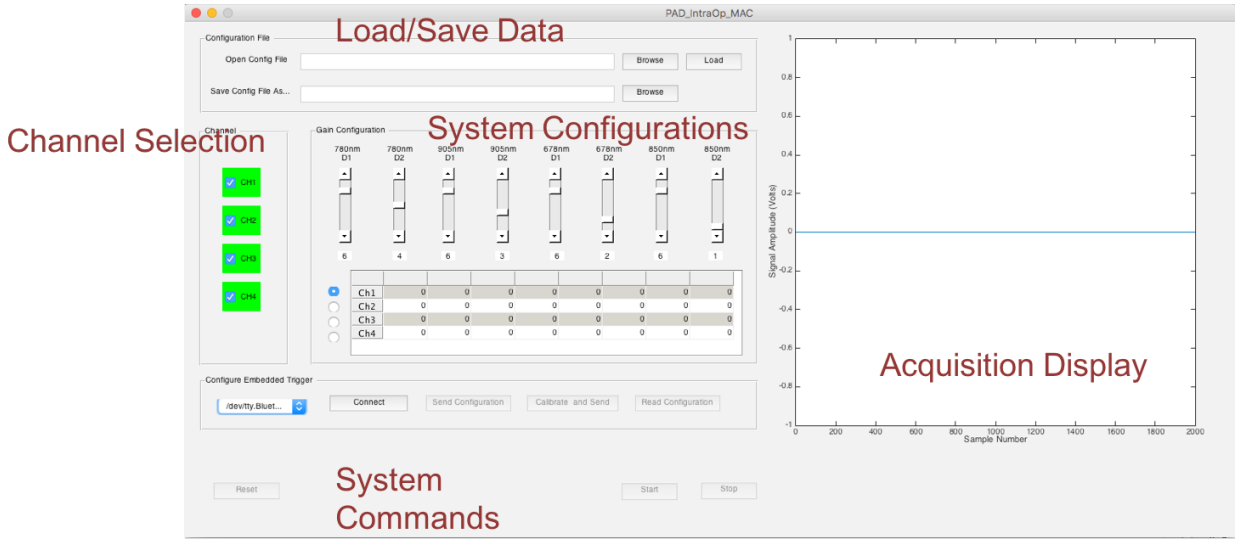

Figure 5.20 A screenshot of the GUI used to control the VOSM system. The user can select up to 4 channels for a measurement (Channel Selection). Data can be saved and a gain configuration profile can be loaded (Load/Save Data). Radio buttons can select the gain profiles of the corresponding DOS channel, sliders are used to control gain settings of individual SD pairs, and a table of the returned signal of all 32 possible SD pairs are displayed (System Configurations). Incoming data from a selected DOS channel is displayed (Acquisition Display).

Once the gain configuration is sent, the user can press the "Start" button to begin acquiring data. The start data will send a command to the device to begin imaging. Once the imaging is initiated, the VOSM will continually collect frames from the user selected DOS channels. Each frame of data is sent in a packet via USB/RS-232. Each packet contains a header with the packet size, the SD pair data with an adjustable size of significant digits of raw (voltage) data, and the gain of the SD pair. For each frame, the GUI parses the packet by computing the size of the packet from the header. The GUI then separates the data from the packet and writes the frame to the text file. In addition, the frame of data is displayed on the GUI screen for real-time visualization of the data acquisition. Although this GUI can be natively used with a Windows PC, this GUI has the ability

to be used with the Mac OSx operating system as well with the installation of the Prolific PL2303 USB to RS232 driver (PL2303_MacOSX_1.6.1_20160309.pkg).

5.5.6 Data Flow and Commands

A diagram of the flow of commands and data is shown in Figure 5.21.

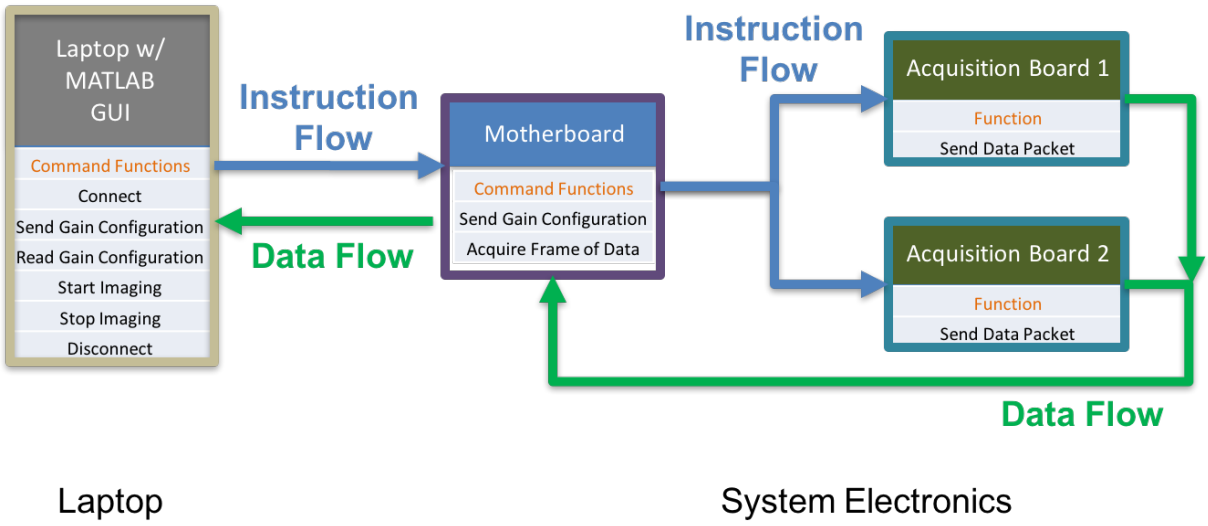

Figure 5.21 Diagram of the instruction and data flow between laptop containing the MATLAB GUI, the motherboard in the VOSM system hardware, and the two acquisition boards.

The VOSM instructional commands of ASCII strings are sent from the PC GUI to the main VOSM system to be processed there or are relayed to the appropriate acquisition board for further processing (Table 5.1). Each instruction packet begins with a 5-character header that contains the function command character (A, G, D, Y, S), 3 characters for the packet size (000-999), and an end of header character (!). The remaining packet contains channel and/or gain information for the

VOSM firmware. The commands that are executed by the motherboard are used to initialize all of the system electronics and to execute user feedback information such as LEDs lights.

GUI Commands to VOSM System Hardware				
Function	**Commands**	**Packet Size**	**Example**	**Note**
Connect	A	0	A000!	Initialize VOSM
Send Gain Configuration	G	#Ch * (#SD+1) * 2	G018!2 2 6 6 6 6 6 6	Gain for Ch 2, ready LED on
Read Gain Configuration	D	#Ch * 2	D004!2 3	Read Gain for Ch 2 and 3, ready LED on
Start Imaging	Y	#Ch * 2	Y004!2 3	Being Imaging on Ch 2 and 3, imaging LED on
Stop Imaging	S	0	S000!	Stop all imaging, ready LED on
Disconnect	A	0	A000!	Initialize VOSM, ready LED off

Table 5.1 Command functions and packets sent from the GUI to the VOSM system hardware to control the device.

All instruction packets are parsed in with the firmware of motherboard processor. The "channel number" info contained in the instruction packets is relayed to the proper acquisition board. For example, packets containing channel 1 and 2 information will be sent to acquisition board 1 to manipulate DOS channel 1 and 2, while packets containing information for channel 3 and 4 will be sent to acquisition board 2. Commands processed by the acquisition boards are only related to setting gain bit information and obtaining data from a specific DOS channel only (Table 5.2).

Commands from Motherboard to Acquisition Boards				
Function	**Commands**	**Packet Size**	**Example**	**Note**
Send Gain Configuration	G	(ChNumber + #SD) * 2	G018!0 6 5 7 4 7 6 5 3	Send gain info to local channel 0
Acquire Frame of Data	D	ChNumber * 2	D002!1	Get data from local channel 1

Table 5.2 Command functions and packets sent from the motherboard to the one of the two acquisition boards to either relay gain settings for a local DOS channel, or obtain a frame of data from the local DOS channel.

For each command sent to an acquisition board, the associated local DOS channel for that command will send back to the motherboard 8 data value readings for each SD pair, which is a single frame of data. If a measurement profile includes all four channels, the motherboard will send 4 commands to the acquisition boards, and will receive back 1 frame of data (data packet) from each of the 4 DOS channels that the VOSM system contains. The motherboard will parse the data packets and will build a new data packet that is sent back to the PC. Since the RS-232 buffer is limited in size, the VOSM system will transmit the measurement data one DOS channel at a time sequentially. The structure of the data packet that the PC receives from a single DOS channel is shown in Table 5.3.

Data Packet from VOSM Hardware to PC	
Function	Data Packet
Commands	D
Packet Size	2 * (ChNumber + #SD) + (SigDigits (7) + 1) * #SD
Example	G087!2 1.11111 2.22222 3.33333 1.11111 2.22222 3.33333 1.11111 2.22222 6 5 7 4 7 6 5 3
Note	Data from DOS channel 2, with gain settings

Table 5.3 An example data packet from a single DOS channel

5.5.7 Reconstruction of Optical Properties

The measurement data collected from the VOSM system contains the reflectance information of the three patch channels, and the transmission information from the toe clip channel, all of which have units of volts. The voltage range of the DOS channels is 0 to 3.3V. Once the measurement data acquired, a DCT filter with a filter size of 200, which corresponds to the cutoff frequency of

the cuff occlusion protocol described later in this chapter. This filter will smooth the data, suppressing noise that may have been due to motion of the patient.

In addition to pre-processing of the measurement data, calibration measurements must be taken to reconstruct the voltage data into concentrations of [HbO_2], [Hb], and the reduced scattering coefficient us'. The calibration for the patch channels is performed by placing the interface patches onto the solid phantom cube described in section 3.5.4 (Figure 5.16B). With the calibration data acquired with the patch channels, the optical properties from each frame of the measurement data is reconstructed using the spatially resolved spectroscopy (SRS) constrained evolution strategy algorithm as described in section 2.2.6.

The transmission based toe clip data undergoes a separate reconstruction procedure, where the calibration measurement is performed by placing an in-house made solid phantom in the chamber of the toe clip and measuring it at the same gain settings as the measurement data. Next, the measurement and calibration data is applied to the modified Beer-Lambert law (mBLL) model to reconstruct the concentrations [HbO_2], [Hb], and the reduced scattering coefficient us'. The modified Beer–Lambert law (mBLL) [196-198], assumes (1) the absorption of the medium changes homogeneously, and (2) the scattering loss is constant [199]. The mBLL model is stated as:

$$A = ln\frac{I_{inc}}{I_{det}} = L\mu_a + G \tag{5.3}$$

where A is the attenuation (defined here as log base e), Iinc is the incident light intensity, Idet is the detected light intensity, L is the total mean path length of detected photons, μa is the absorption coefficient of the tissue and G is a geometry-dependent factor, which is independent of absorption and represents intensity loss caused by scattering. The differential form of the MBLL (dMBLL)

also holds for relatively small changes of attenuation, if G can be regarded constant, and the absorption changes homogeneously in the illuminated tissue volume:

$$\Delta A = ln\frac{I_{det,1}}{I_{det,2}} = L\Delta\mu_a \tag{5.4}$$

The latter is the weighted sum of the change in the concentration of tissue chromophores, mainly oxy- and deoxyhemoglobin:

$$\Delta\mu_a = \alpha_{HbO_2}\Delta c_{HbO_2} + \alpha_{Hb}\Delta c_{Hb} \tag{5.5}$$

where the α weights denote the specific (molar) absorption coefficients of the chromophores. When the changes of attenuation are measured at more than two wavelengths, concentration changes can be determined by linear least-squares fitting [198]. To obtain the tissue chromophore concentrations with our calibration based setup up, $I_{\text{det,1}}$ is equal to an experimental measurement frame while $I_{\text{det,2}}$ is equal to the median of the phantom measurements for each SD pair.

5.5.8 System Characterization

The VOSM system requirements consists of a small form factor and ease of interfacing to a foot for a patient with PAD. In addition, the system must be fast enough the observe vascular changes from an angioplasty during intraoperative use, or from a venous occlusion as performed in our group's diagnostic measurements [194, 195], and must have enough sensitivity and stability to

observe these changes. Here we discuss the characterization of the system with the following parameters: Speed, Sensitivity and Dynamic Range, Linearity, Stability, Size.

5.5.8.1 Speed

The speed of acquisition is an essential parameter for dynamic measurements. The temporal response of the VOSM system is limited by the communication speed of the data from the VOSM sytem to the PC and the digital lock-in detection scheme applied in microcontroller of the acquisition board. Since we measure the tissue perfusion of the foot from one or more DOS channels, the imaging rate also depends on the number DOS channels used in an experiment. Consequently, the fastest the system can measure with one DOS channel, consisting of 4 wavelengths and 2 detectors is (10.23 Hz). Or, with two DOS channels, VOSM can acquire data at 5.12 Hz). Finally, the slowest configuration is to use all 4 DOS channels, which operates at a framerate of 2.56Hz. For dynamic measurements applied by either angioplasty or induced venous occlusion by a pressure cuff, this framerate is more than adequate.

5.5.8.2 Sensitivity and Dynamic Range

The dark noise is the measured signal when no incident light is present, and thus represents the smallest measurement that can be reliably performed with the system. Figure 5.22 shows the dark noise measured for each gain setting with the standard deviation of the measurements across all detectors indicated by the error bars. By increasing amplification in the PGA stage, we do not see an increase of until a gain of 100. At the lower gain stages, we see noise levels below 100 μV, but as the gain increases we see increasing noise until at the highest gain stage of 100 (25.9MV/V) we have an RMS dark noise of 108 uV. Although the highest gain settings results in a much higher dark noise measurement compared to the lowest, the RMS dark noise only results in a noise of less

the 1% of the optimal return for a foot measurement, which is 2.8V. That is 108uV/2.8V = 0.003%, or 88dB of SNR.

The largest light signal that can be detected uses the full detector range for the lowest gain setting, which in this case is to detect a 3.3 V peak-to-peak voltage on the 20kV/V gain setting. Using these values, we can calculate the dynamic range of the system to be 89.7 dB.

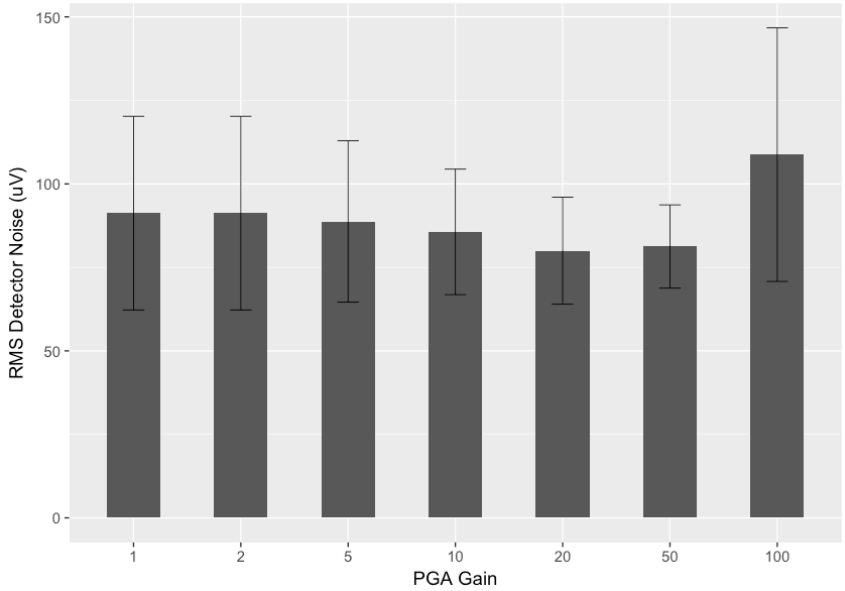

Figure 5.22 Plot of the root mean squared (RMS) dark noise for each detector gain setting. Error bars represent the standard deviation of all detectors.

5.5.8.3 Coefficient of Variation and Long Term Stability

The coefficient of variation (CoV), shown in Equation (5.6) is calculated here for a static block phantom used section 2.3.4 in with optical properties shown in Table 2.3 over a period of 5 minutes (800 frames) with the full number of sources and detectors.

$$\text{CoV} = \frac{\sigma}{\mu}, \text{SNR} = 20log_{10}\frac{1}{CoV} \tag{5.6}$$

Figure 5.23 shows the mean of the CoV calculated for all SD pairs at the given gain setting for each channel. At the highest gain setting (PGA Gain = 100) the CoV is as low as 0.24% for the ATA and LPA channels. For the PTA and MPA channels, the CoV is above 1% at PGA gain = 5

and at the highest gain setting it increases to approximately 10%. It is speculated that the MPA has a high CoV due to its transmission based topology. The SNR for each of these settings can be calculated according to equation (5.6) giving us an average SNR of 71.8 dB for the lowest gain setting and 33.8 dB for the highest gain setting.

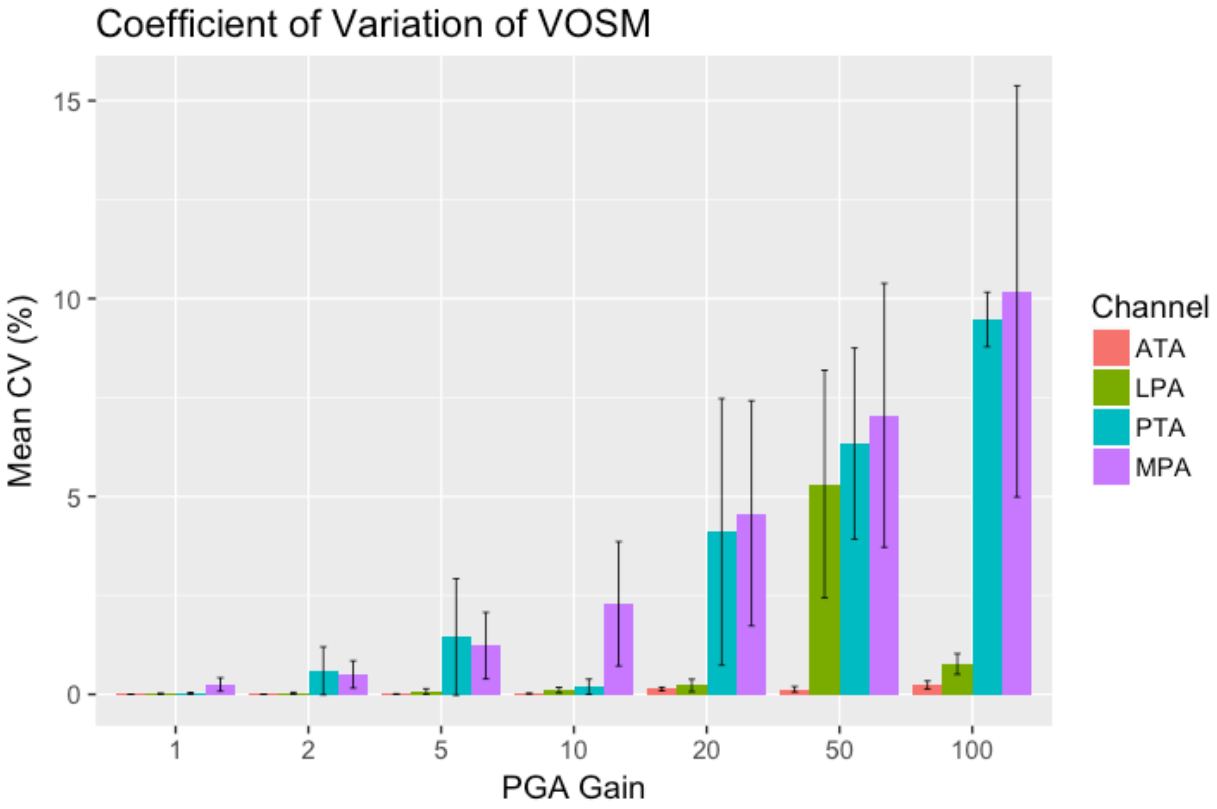

Figure 5.23 The mean CV of the source-detector pairs at each gain setting for each channel. Errors bars represent the standard deviation across source-detector pairs.

5.5.8.4 Linearity

System linearity was examined by measuring the detected voltage from the solid block phantom and the toe clip phantom simultaneously across all possible PGA chip gain settings (LTC6910-1, Linear Technology) for each channel. The linearity experiment was repeated four times in order to cover all gain settings. The PGA chips used in the detector channels are 3-bit controlled with gain settings (0, -1, -2, -5, -10, -20, -50, -100V/V). The results are plotted in Figure 5.24, where it

is demonstrated that a linear relationship across the gain settings is generally maintained. For the curves below, linearity with R-squared measures of R=0.973 (ATA), R=0.949 (LPA), R=0.936 (PTA), and R=0.859 (MPA). It is hypothesized that the MPA channel did not have as good a regression fit due to its transmission based topology compared to the reflection based channels.

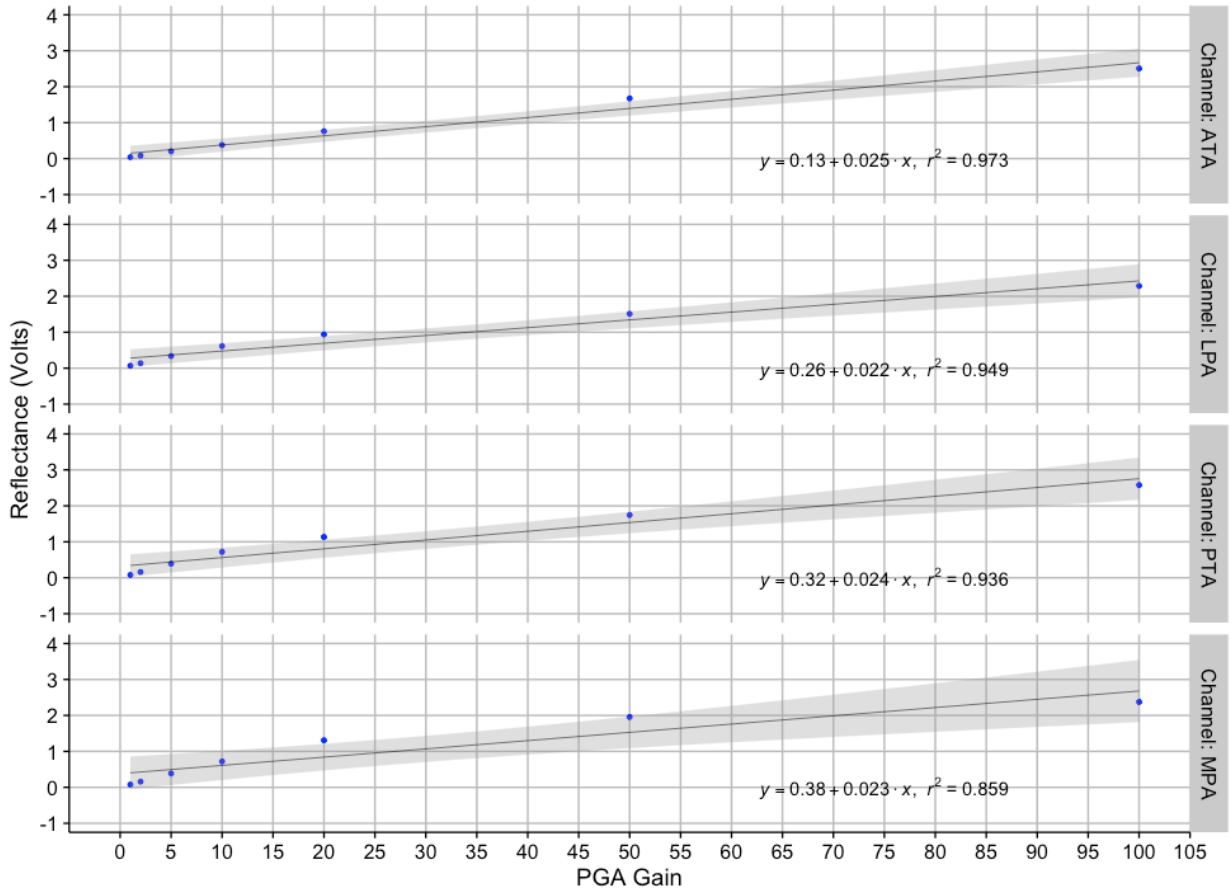

Figure 5.24 Linearity across all gain settings measured through an INO phantom block. Each facet represents the channels of the VOSM system.

5.5.8.5 Physical Dimensions

The VOSM electronic components and software interface described in the previous sections are combined into a single system that is easy to transport, as shown in Figure 5.10. The computer that contains the control GUI is currently a MacBook Pro 15" with a 2.3 GHz Intel Quad-Core i7 but the VOSM system can be easily controlled with most laptops containing MATLAB and a USB 2.0

port. All of the VOSM system electronics are completely encased by a 6.6" x 6" x 3.5" enclosure (1598ESGYPBK, Hammond Manufacturing). The VOSM system has four DOS interface channels, with each channel connected by 3 cables extending 3ft long. The interface patches that connect to the cables are 35mm x 25mm x 7mm in size while the dimensions of the toe clip is 80mm x 27mm x 25mm. Table 5.4 provides a summary of the dimensions of the VOSM system components.

VOSM System Dimensions (cm)			
	L	**W**	**H**
System Enclosure	16.8	15.2	8.9
Interface Patches	3.5	2.5	0.7
Toe Clip	8.0	2.7	2.5
Cabling	152.4		
Laptop	36.3	24.9	2.4

Table 5.4 Dimension of the VOSM system and its components

5.6 Monitoring of Peripheral Arterial Disease in the lower extremities after surgical intervention using Dynamic Diffuse Optical Spectroscopy

To investigate the performance of the VOSM system in a clinical setting, we gathered preliminary measurement data from 22 PAD subjects before and after surgical interventions aimed to improve tissue perfusion in the lower extremities. The goal of the study is to explore the use of dynamic imaging techniques to detect and characterize PAD. In a previous 40 patient study examining the dynamic response of blood parameters to a venous occlusion, our group had shown that DDOT can distinguish between healthy subjects and patients with PAD, even in the diabetic PAD patients with calcified incompressible arteries [194, 195]. Although it was a future consideration, we did not examine the longitudinal outcomes of patients that underwent treatment to improve PAD. Here we aim to use DOS to examine its ability to track the severity of PAD before, and up to 12 months

after a PAD patient has undergone surgical intervention to fix the occluded blood to flow to the extremities.

In this section, the initial results from a longitudinal study are presented to quantify VOSM's ability of monitoring the perfusion effects of surgical intervention for PAD patient, its ability to assess the severity of the disease based on the perfusion response in the foot.

5.6.1 Methods

5.6.1.1 Clinical Study

We have employed a 100-patient longitudinal study to monitor PAD patients at six time points over a one year period before and after surgical intervention of PAD, where currently 22 PAD patients are enrolled for this cross-sectional analysis. IRB approval was obtained from Columbia University Medical Center (CUMC) Investigational Review Board (Protocol# IRB- AAAK6702), and patients are recruited in the pre-operative area for vascular surgery at CUMC. Any patient undergoing surgical intervention are to be asked to enroll in the study. The inclusion/exclusion criteria do not have any restrictions based on race or gender. Recruitment of a greater proportion of minorities in keeping with the demographic makeup of patients seeking treatment at Columbia University Medical Center is anticipated. As this technique is still under investigation, the patients are not informed of any results that come from their VOSM monitoring.

Once a patient has been enrolled and has signed the appropriate consent forms, the patient will be monitored before undergoing surgery, immediately after the procedure, and during follow-up examinations 1 month, 3 months, 6 months, and 12 months after the surgery. Standard clinical measures, are performed during examinations prior to the intervention, and during follow-up examinations. Because this report is based on an early cross-section of the study, results from the

pre- and post-operative measurements, as well as the 1 month follow-up are the only timepoints examined.

5.6.1.2 Study Devices

We propose the use of dynamic diffuse optical spectroscopy (DDOS) to monitor PAD before and after surgical intervention through the VOSM system as described in section 5.5. The VOSM system uses DDOS, which is a non-invasive, non-ionizing, contrast-free, fast imaging modality that allows for the measurement of blood volume changes in the foot. With VOSM, up to four DDOS channels made up of small patches are placed onto the lower limb and foot, where light is shone onto the surface of the tissue of interest. The light will illuminate various positions on the surface of the lower limb and foot. The reflected light intensities are recorded and the measurements are further processed to display the temporal changes of concentrations of oxy [HbO2], deoxy [Hb] and total hemoglobin ([HbO2] + [Hb] = [HbT]), which is proportional to the total blood volume (BV) in that limb.

The VOSM system measurements are compared to the current standard for PAD measurements, the ankle-brachial index (ABI). ABI is used to monitor PAD within the lower extremities by taking the systolic blood pressure in the arm and dividing it by the systolic blood pressure in the foot. An ABI level that is less than 0.9 is indicative of affected vasculature, while a level above 0.9 and below 1.2 is considered normal. Falsely elevated ABI readings (>1.2) occur in patients with medial wall calcification, which is a condition commonly seen in diabetic patients.

In addition to the ABI measurements, pulse-volume recordings (PVR) are conducted using segmental limb pressure cuffs along with the ABI measurement in an attempt to localize a stenosis

or occlusion. The PVR waveforms obtained for each segment are categorized in four categories: Normal, mildly abnormal, moderately abnormal, and severely abnormal.

5.6.1.3 Angiosome Concept and DOS Channel Placement

The four DDOS channels will be placed in various regions in the lower extremities according to the angiosome theorem [200-211]. An angiosome is defined as a three-dimensional anatomic unit of tissue fed by a source artery. The angiosome concept was initially described in plastic and reconstructive surgery papers and was intended to provide the basis for a logical planning of incisions and flaps [200, 201]. Adjacent angiosomes are bordered by choke vessels, which link neighboring angiosomes to one another and demarcate the border of each angiosome. Stenosis in arteries can affect the entire limb, but the degree of effects can be localized. This concept of perfusion delineates vascular territories that are supplied by specific arteries. Tissue defects caused by PAD can be treated by targeting arteries according to the location of foot ulcers. The angiosome model for the revascularization of the foot was followed by several authors who confirmed its relevance for ulcer healing and consequent limb salvage [202-205, 208]. This model includes 5 angiosomes (Figure 5.25) that we have used as a guide for our placement of VOSM

system channels, to monitor revascularization in arteries of the lower extremity for patients suffering from PAD.

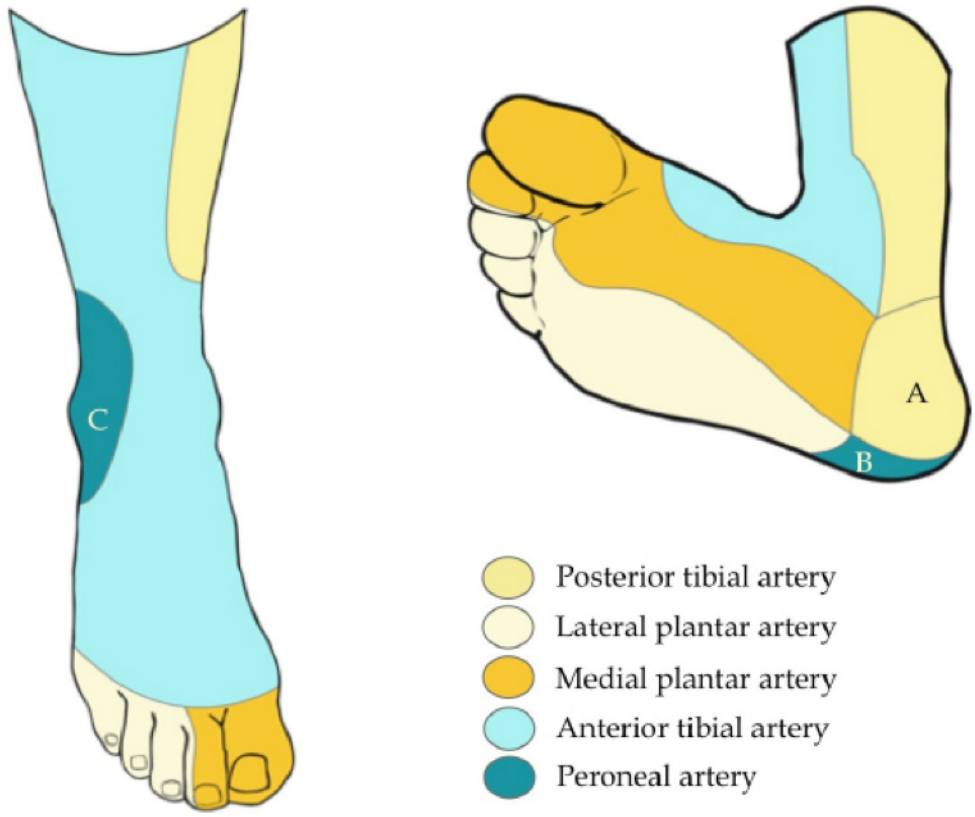

Figure 5.25 Diagram of the angiosome concept for the lower extremities [202]. Angiosomes are defined as three-dimensional anatomic units of tissue (from skin to bone) fed by a given source artery.

The VOSM system, which includes four DOS channels, were placed on four of the five angiosomes regions. The VOSM patch channels were placed on the regions that are supplied by the anterior tibial artery (ATA, dorsal side of foot), the lateral plantar artery (LPA, plantar side of foot), and the posterior tibial artery (PTA, calf muscle). In addition, the toe clip was placed on the

hallux, or commonly known as the big toe, to monitor the perfusion from the medial plantar artery (MPA). Example of the placement is shown in Figure 5.26

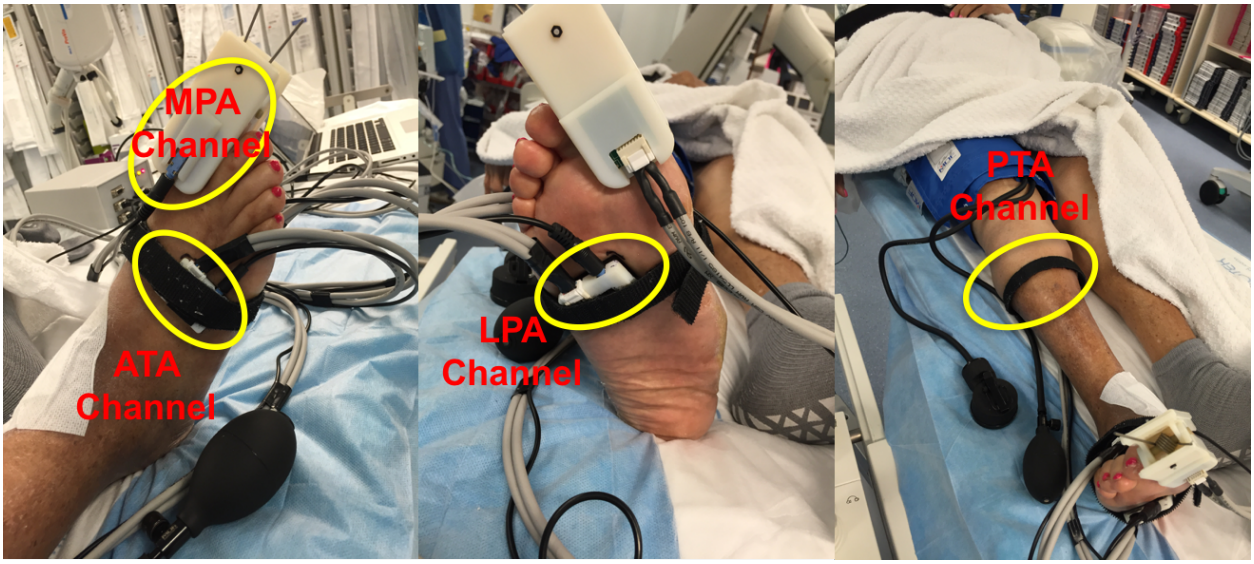

Figure 5.26 VOSM patch and toe clip placement on a PAD subject. Each channel monitors perfusion on an angiosome.

Although the PTA channel of the VOSM system is not located on the foot as the other channels are, we decided to place this patch on the calf for two reasons: (1) the tissue perfusion at the calf is still considered in the region of the angiosome associated with the PTA [212-218] and (2), many studies on exercise oxygenation use pulse oximetry or spectroscopic probes on the calf muscle. For these reasons, we examine the change in perfusion via the PTA from the calf location [219, 220].

One compromise we made to perfusion monitoring was the lack of a VOSM channel at the angiosome related to the peroneal artery. Although the angiosome concept states that a region is primarily associated with an artery, sufficient cross branching from other arteries may allow us to monitor the peroneal artery's effect on tissue perfusion. Thus, we believe that the four VOSM

channels measuring perfusion from 4 of the 5 angiosomes in the foot will provide sufficient information on the overall perfusion changes from the surgical intervention.

5.6.1.4 VOSM Imaging Protocol

A five stage dynamics imaging protocol was employed to measure the individuals with the VOSM system, who were lying flat on a surgical bed or adjustable exam chair while up to 4 of the VOSM channels were placed and strapped to the foot and calf using Velcro strips (Figure 5.27). To illicit a controlled vascular response a pressure cuff was applied to the thigh. The protocol consisted of (1) rest phase, (2) 60 mmHg thigh cuff occlusion phase, (3) release and recovery phase, (4) 100 mmHg thigh cuff occlusion phase, and (5) release and recovery phase. Initially, the patient was imaged at rest for 1 minute. Then in the second phase, a pressure cuff was inflated to 60 mmHg to induce venous occlusion for 1 minute. The thigh cuff prevented the blood from leaving the leg through the veins, while arteries continued to supply blood to the foot. This pressure caused the blood to pool in the leg, which absorbed the light as it propagated through the foot, decreasing the intensity of the detected signal. In the third phase, the pressure was released allowing for 1 minute of recovery time. In the fourth phase, the thigh cuff was reapplied at 100 mmHg for 1 minute, inducing a greater venous occlusion. Finally, the cuff was released and the patient was imaged for

1 minute. This protocol was selected because it focuses on arterial flow, while avoiding the arterial compression required by blood pressure based measurements.

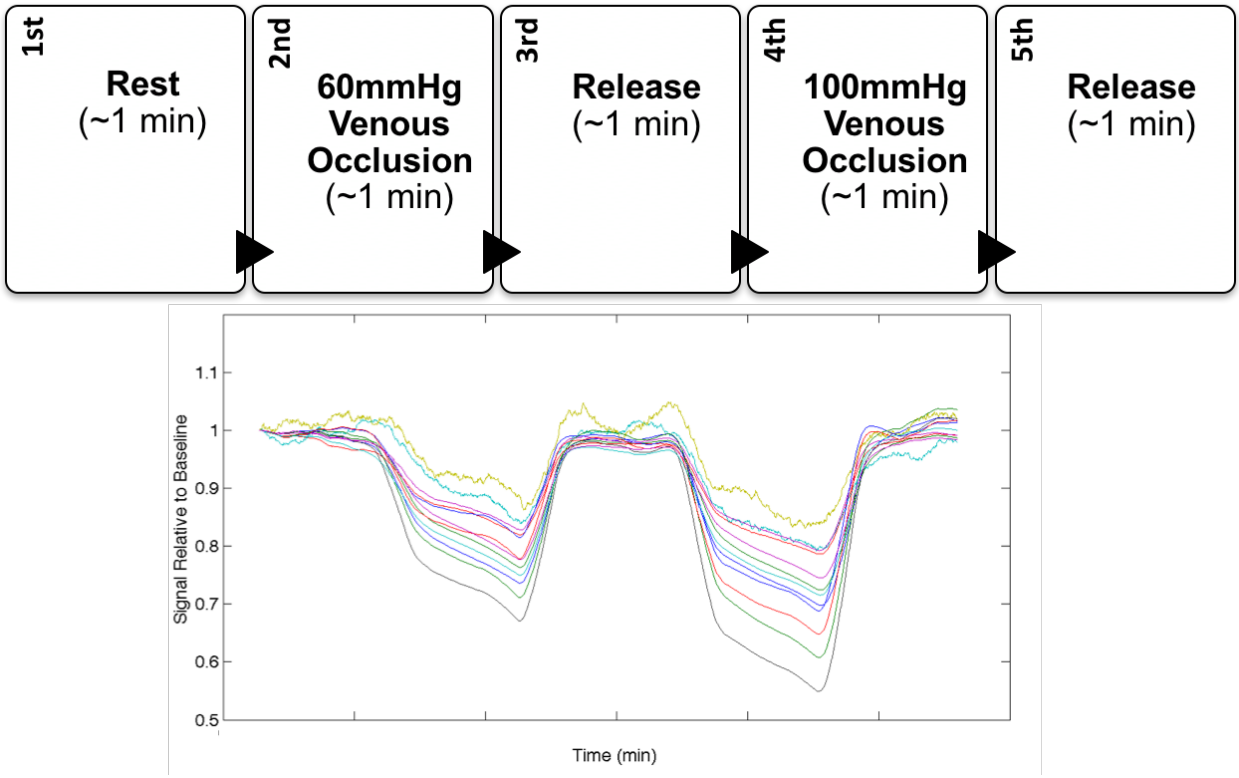

Figure 5.27 A five stage dynamics measurement protocol was employed to measure the individuals with the VOSM system. Diagram of the measurement protocol (TOP). Raw traces of the returned signal normalized to the first "rest" period.

5.6.1.5 Feature Extraction

VOSM can provide multiple measurements per second of these blood parameters, allowing for the observation of temporal variations in these parameters. For example, by applying a pressure cuff at 100mmHg around the thigh, we induce venous occlusion in the leg and can use the VOSM system to observe the blood pooling in the foot and then returning to rest state upon release of the thigh cuff. In order to quantify the temporal changes in [HbT] from blood pooling during a venous occlusion, we have developed 3 features (Figure 5.28) that can provide a measure of the status of

the vascularity. All features extracted are normalized measurements relative to the baseline (rest) phase. These are:

1. The percent change in [HbT] from the "rest" phase to the end of the occlusion phase. This feature will measure the overall all change of blood pooling due to the thigh cuff occlusion.
2. The rise time of the [HbT] curve during the venous occlusion, which is calculated as the time duration, in seconds, from 10% to 80% of the peak [HbT]. The rise time feature is a measure of how fast the blood pooling occurs to reach 80% of it maximum value.
3. The normalized pooling rate of [HbT] into the lower extremity, as defined as the amount of [HbT] that is pooled from the start of the venous occlusion to the point of the cuff release, normalized to the level of [HbT] at the cuff release. This measure of blood pooling will provide information of the amount of blood that was pooled over the occlusion interval. The area under the time traces is highly proportional to this measure.

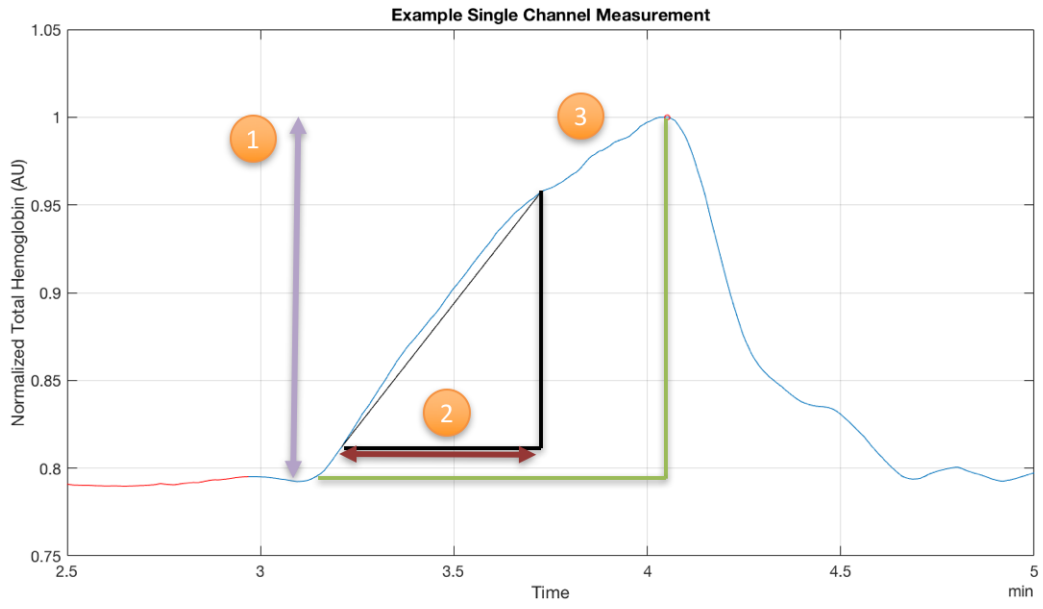

Figure 5.28 Normalized data of HbT during a venous occlusion on a patient. There are 3 features extracted from this time trace. (1) Percent change of HbT from baseline to cuff release. (2) Rise time, defined as the time

from 10% to 80% of the maximum HbT measured. (3) Normalized pooling rate, defined as the amount of HbT pooled during a venous occlusion, normalized to the peak HbT.

5.6.1.6 Surgical Interventions

Patients with severe and moderate PAD, as measured by ABI, PVR, and Duplex US, underwent exploratory angiograms in order to visualize the stenosis of the arteries in the lower extremities. During the angiogram imaging, patients that demonstrated clear stenosis immediately underwent surgical intervention. Procedures that were performed include angioplasty, stenting, atherectomy, or a combination of the three. If necessary, multiple lesions that were contained in the same or different arteries were treated at the discretion of the attending surgeon.

In order to perform our angiosome analysis, the arteries that were treated were grouped into zones that corresponded with one or multiple angiosomes, as was initially explained in section 5.6.1.3. The diagram in Figure 5.29 shows the major arteries that primarily affect perfusion to the foot.

Table 5.5 provides a list of arteries that may be treated, its corresponding "zone", and the angiosomes or VOSM channels that are hypothesized to be primarily affected by the treatment.

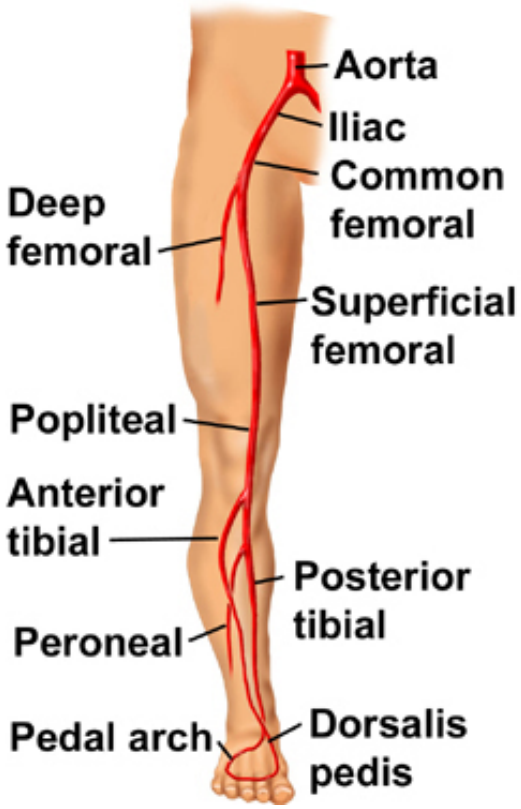

Figure 5.29 Diagram of major arteries in the leg. During revascularization, one or more arteries were treated in order to improve tissue perfusion in the foot. The arteries treated were grouped into zones, and each zone treated corresponded to one or more angiosomes that should observe a large improvement compared to other angiosome regions.

	Intervention Zones	
	Description	**Example Artery**
Zone 1:	Above Knee	Superficial Femoral Artery (SFA)
Zone 2:	Anterior of Leg/Foot	Anterior Tibial Artery (ATA)
Zone 3:	Posterior of leg, Dorsal of Foot	Posterior Tibial Artery (PTA)
Zone 4:	Lateral Side of Leg/Foot	Peroneal Artery (PERO)

Table 5.5 Designated intervention zones that separate major arteries that were treated for patients undergoing revascularization

5.6.1.7 Statistical Methods

The three features extracted from the VOSM time trace measurements were analyzed. In order to verify linear independence between features, principle component analysis was performed for dimensionality reduction. The data were in the form of mean and standard deviations unless otherwise stated. To quantify VOSM's ability to measure changes in tissue perfusion over time, comparisons between pre-op, post-op, and 1 month follow-ups (FUs) were made using a repeated measure analysis of variance (RM-ANOVA). Verification of the covariance structure between time points was performed by implementing a linear mixed effects regression model. The use of RM-ANOVA however, only tests the global hypothesis about any number of treatments whose effects are measured repeatedly in the same subjects. Since it is possible to observe each experimental subject before, after, and at multiple points after a single treatment, the paired t-test was used to identify the average change the treatment produces over time. To correct for multiple time-point comparisons, a Holm-Sidak p-value correction was applied. For a 95% confidence interval, and three measurements α_1=0.0167, α_2=0.025, α_3=0.05 were obtained as significance cutoffs. To quantify the repeatability of the system, a Bland and Altman diagram was created and the coefficient of repeatability was calculated.

Comparisons of VOSM parameters were compared to the gold standard measurements of ankle brachial index (ABI). The continuous variable ABI was analyzed between pre-op and FU measurements using the RM-ANOVA and post-analysis using the paired t–test, with α set to 0.05. Repeatability is a crucial measure of VOSM's efficacy in demonstrating that the procedure is objective. The test must produce consistent results among a control group with a single assessor (test-retest reliability). To establish test-retest reliability, it is necessary to show minimal variance in the interaction of the subject and the tasks (thereby indicating that there is no statistically significant effect in the replicate trials). An appropriate method to determine whether the data have

test-retest reliability is by the repeated measures analysis of variance (RM-ANOVA) based on the null hypothesis that no significant difference exists between replicates. This hypothesis was tested in the present study at an α level of 0.05 based on a 95% confidence interval to prove that the null hypothesis should be rejected and therefore that there is a statistically significant difference between replicates.

5.6.2 Results

5.6.2.1 Study Population

Twenty-two individuals were recruited for this IRB approved diagnostic pilot study in the Division of Vascular Surgery at New York Presbyterian Hospital - Columbia University. The inclusion/exclusion criteria did not have any restrictions based on race or gender. The physicians and researchers involved in the study recruited patients that were scheduled for exploratory angiograms. The patients enrolled in this study have access to all of the treatment, counselling and support services offered through the CUMC Division of Vascular Surgery.

The patients recruited were 59% male and 41% female, with a mean age of 74.4 +/- 13.5 years. The mean weight of the patients was 175.2 +/- 39.9 lbs. Of the patients recruited, 7.4% were current

smokers and 80% were diabetics. The ethnic make-up was 5% Hispanic, 45% Non-Hispanic White, 9% Black, and 9% Asian (Figure 5.30).

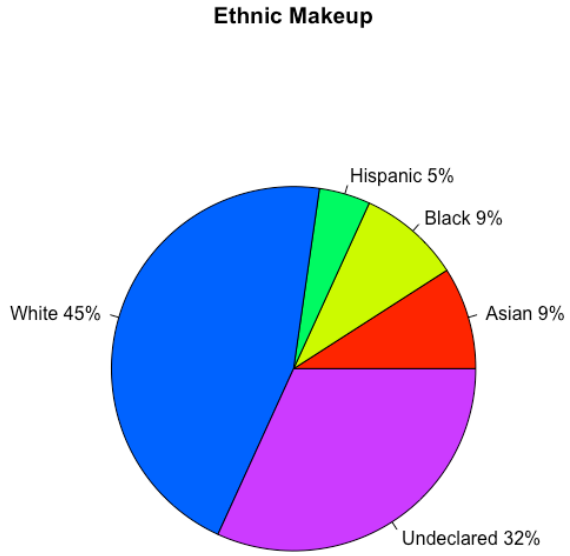

Figure 5.30 Ethnic makeup of the PAD monitoring study.

Patients with severe PAD will often require surgical intervention to fix the occluded blood to flow to the extremities. This pilot study attempts to measure tissue perfusion in the lower extremities affected vasculature from these patients to monitor improvement or disease progression. To correlate vascular improvements according to angiosome regions, we also collected information regarding the arteries that were treated during surgical intervention (Figure 5.31). This analysis

was only completed on PAD patients to see how the VOSM readings correlate with current techniques.

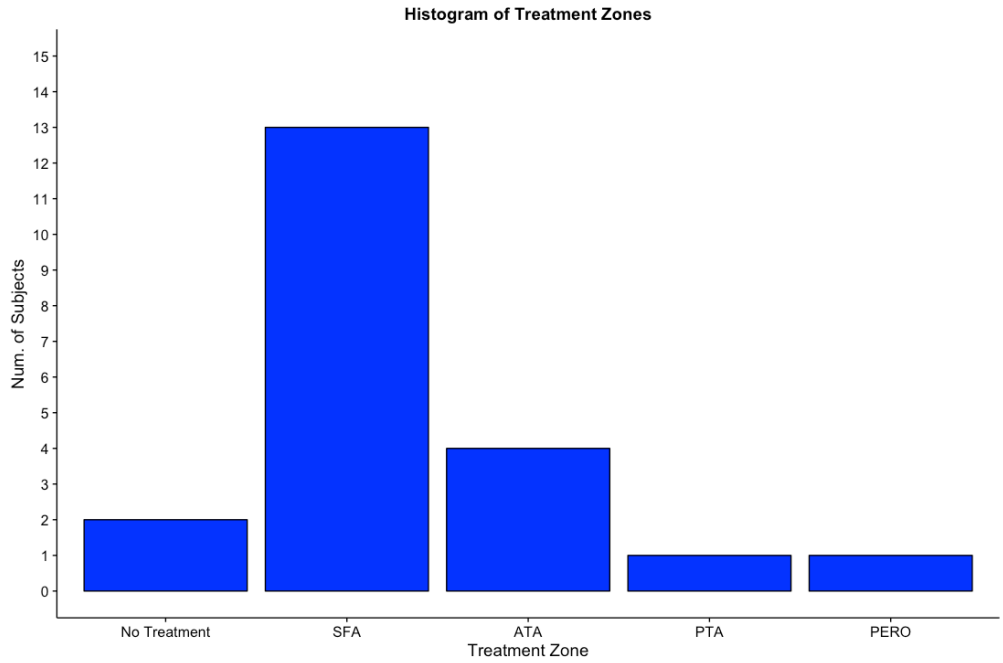

Figure 5.31 Number of subjects separated by their "treatment zones" as described in section 5.6.1.3. Treatment zones SFA is related to the arteries above the knee (SFA, Illiac, Popliteal), ATA is for the anterior tibial artery, PTA is the posterior tibial artery, and PERO is the peroneal artery.

5.6.2.2 Example Case Study

We present a case study to demonstrate the efficacy of detecting PAD within the lower extremities with the VOSM system. Two patients were selected: a PAD patient with diabetes and a PAD patient without diabetes. The physician recommended that the subjects undergo a diagnostic angiogram with the potential of intervention based on a combination of the patients' ABI readings, segmental ultrasound waveforms, physical symptoms and medical history. The patients were

enrolled just prior to their procedure and the imaging protocol was performed before and after the procedure, as well as one month after intervention.

Example Case 1: Diabetic PAD

Using the traditional ABI measurement, it is possible to discern between the healthy control and the PAD patient, however the diabetic PAD patient is not distinguishable. Diabetic patients often have incompressible arteries due to calcifications which result in elevated ABI readings and leads to false negative diagnoses. This patient, denoted as PAD02, was enrolled as a 59-year-old white male, who is an active smoker and was diagnosed with severe PAD prior to intervention. The VOSM imaging protocol was performed and the time trace of HbT was acquired (Figure 5.32 blue trace). The LPA showed a curve similar to that of a healthy subject, but the ATA and PTA channels demonstrated a slower pooling and rise time of HbT.

During the diagnostic angiogram, it was observed that the patient had three major plaque lesions at his popliteal, peroneal, and the posterior tibial artery (PTA), all of which underwent angioplasty intervention to improve tissue perfusion in the lower right extremity. After the procedure, the VOSM measurement was taken again and an improved % change in HbT, rise time and pooling rate was observed (Figure 5.33).

Measurements were taken at 1 and 6 months after the procedure, at which time gold standard ABI measurements were taken (ABI=1.01 and 1.18 respectively). However, VOSM measurements demonstrated a 14% decrease in perfusion after one month, and further decreased at 6 months (Not shown). Furthermore, this patient was unable to complete the study, as he underwent a second angioplasty before the 1 year of VOSM measurements.

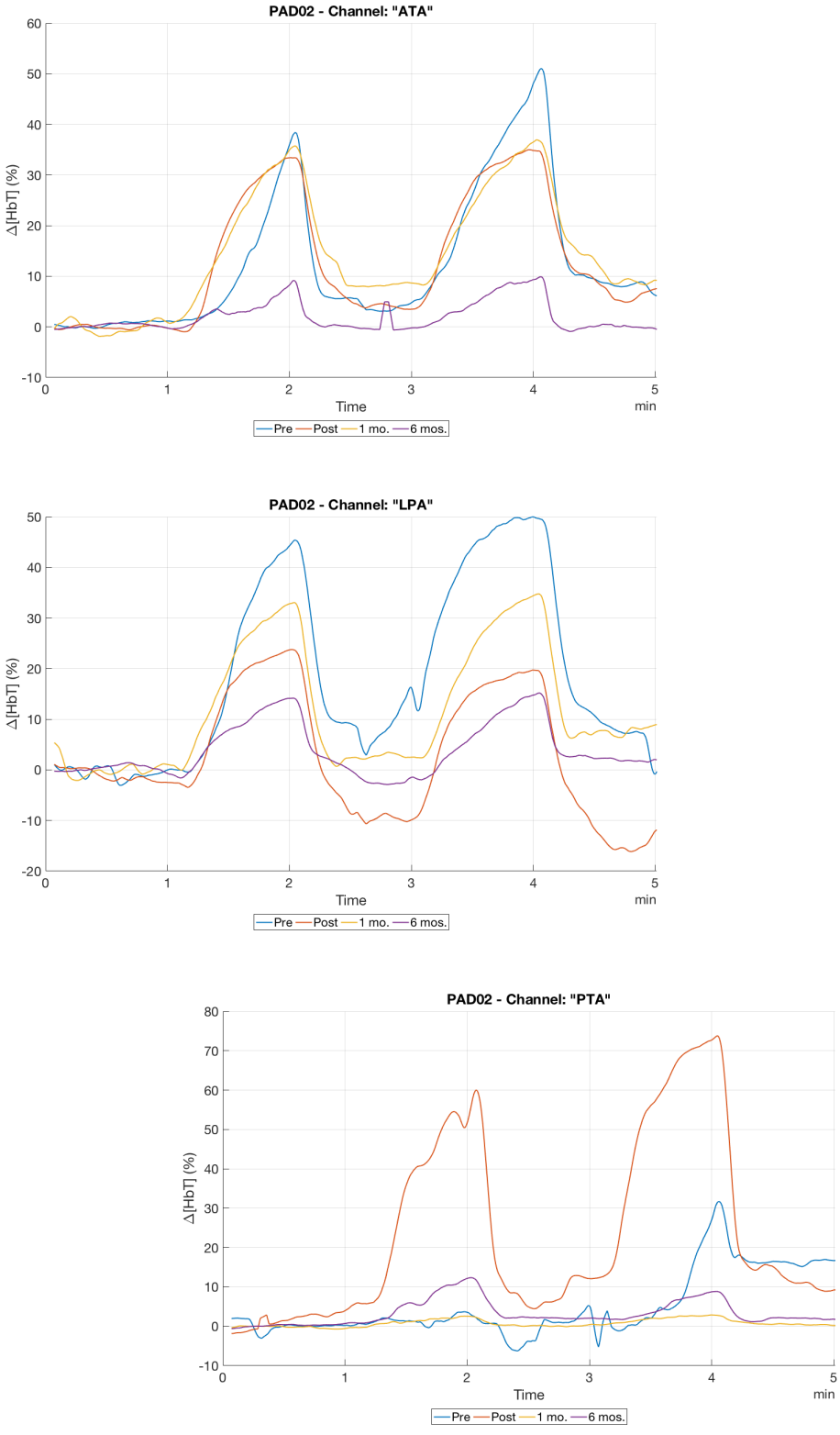

Figure 5.32 HbT(%) measurement data from a diabetic PAD patient before and up to 6 months after intervention.

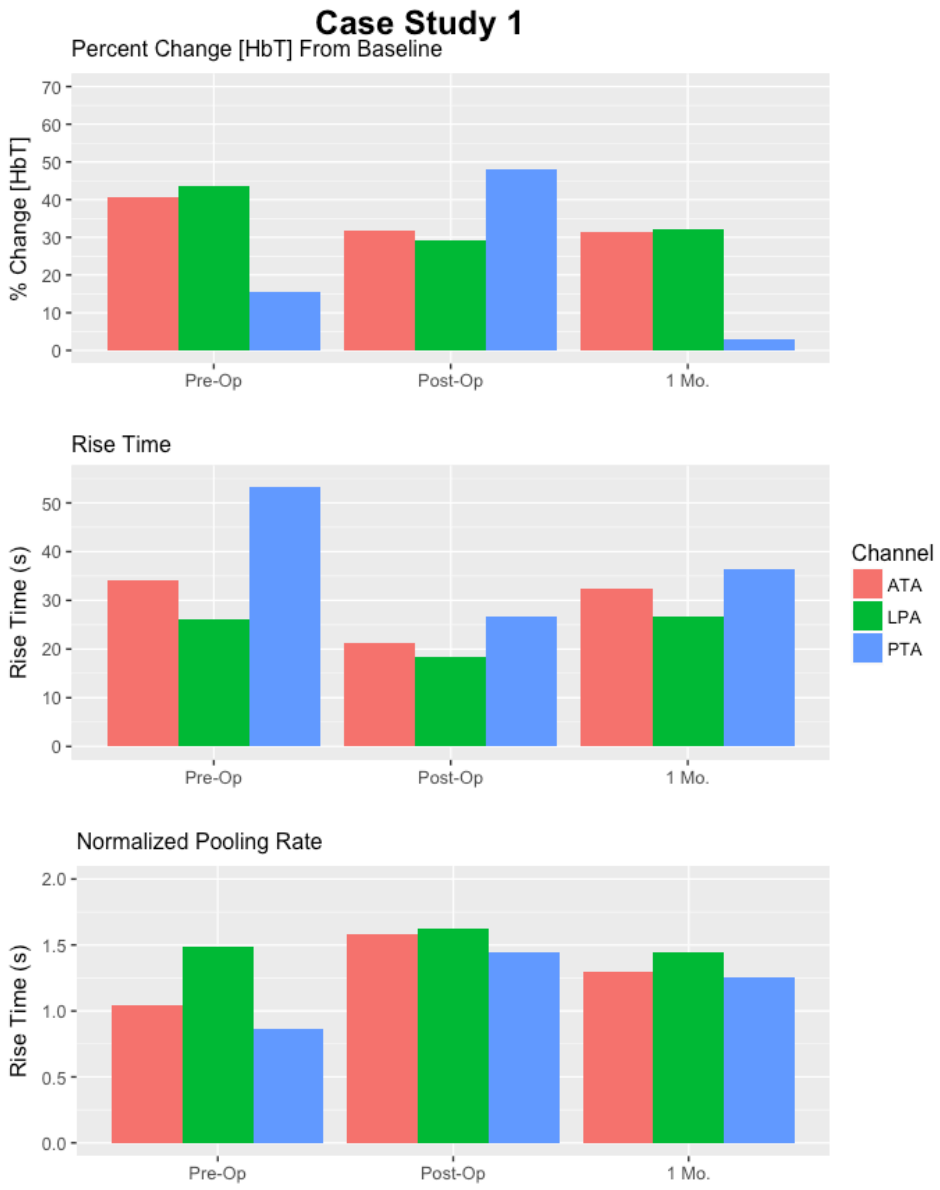

Figure 5.33 Feature results from the first three measurement points for PAD02, our diabetic PAD patient case.

This indicates that although the ABI measurements showed a normal reading, VOSM was able to detect a decrease in perfusion related to stenosis in the arteries.

Example Case 2: Non-Diabetic PAD

In this example, we demonstrate that VOSM has the ability to track ABI measurements with patients without diabetes. Here, we present an 89-year-old Asian male, who was diagnosed with

moderate PAD prior to intervention. The VOSM imaging protocol was performed and the time trace of HbT was acquired (Figure 5.34 blue trace). All curves at intervention were indicative of a subject with PAD, particularly the PTA and MPA channels, as the response of pooling was about 20 seconds later than that of the LPA channel. The patient underwent an angioplasty of the right peroneal, which should create an increase in perfusion primarily in the LPA and PTA channel.

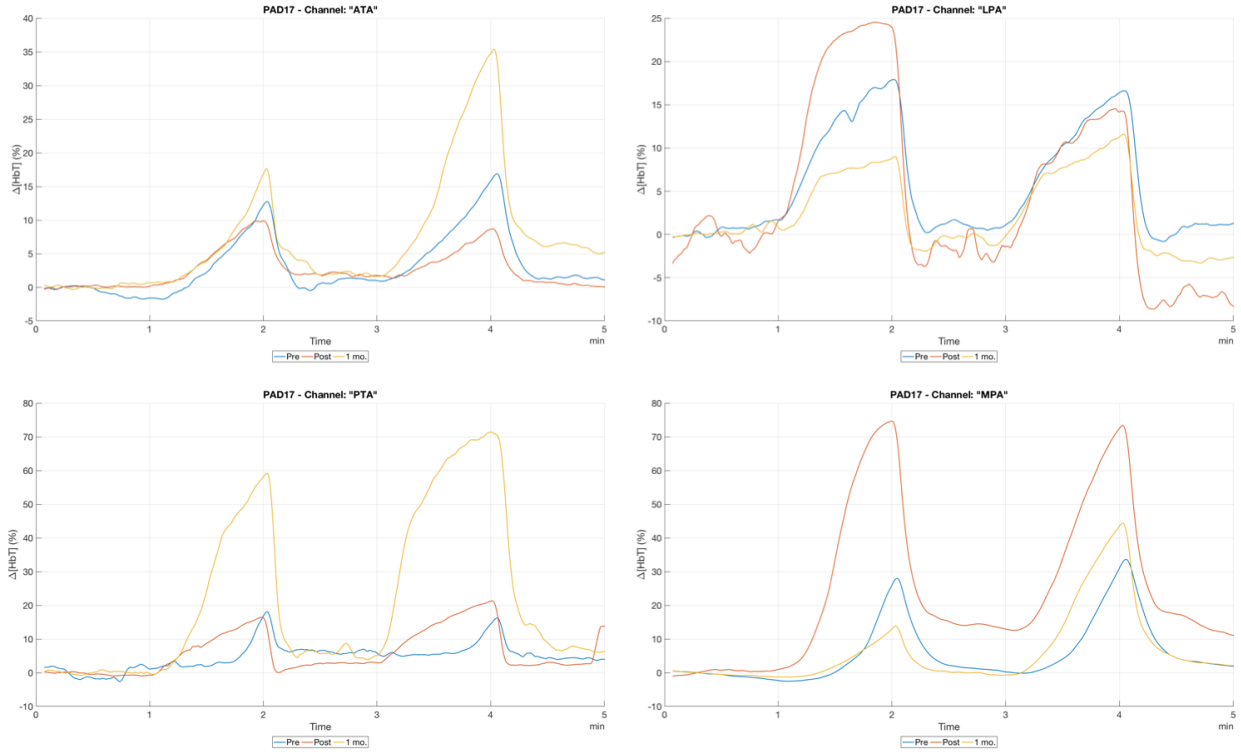

Figure 5.34 Time traces of HbT for PAD17, a non-diabetic PAD subject with moderate PAD at the time of the procedure.

Using the extracted features form the time traces, it was determined that there was an increase in perfusion immediately after intervention for all channel, but at measurements taken at the 1 month follow-up indicated that there was still improvement in two channels, but a decrease in perfusion in the ATA and LPA channels. ABI measurements showed that the patient went from a moderate

to a mild level of PAD severity 1 month after intervention. These results illustrate that the VOSM may be able to detect mild changes of severity to PAD, as also indicated with ABI measurements.

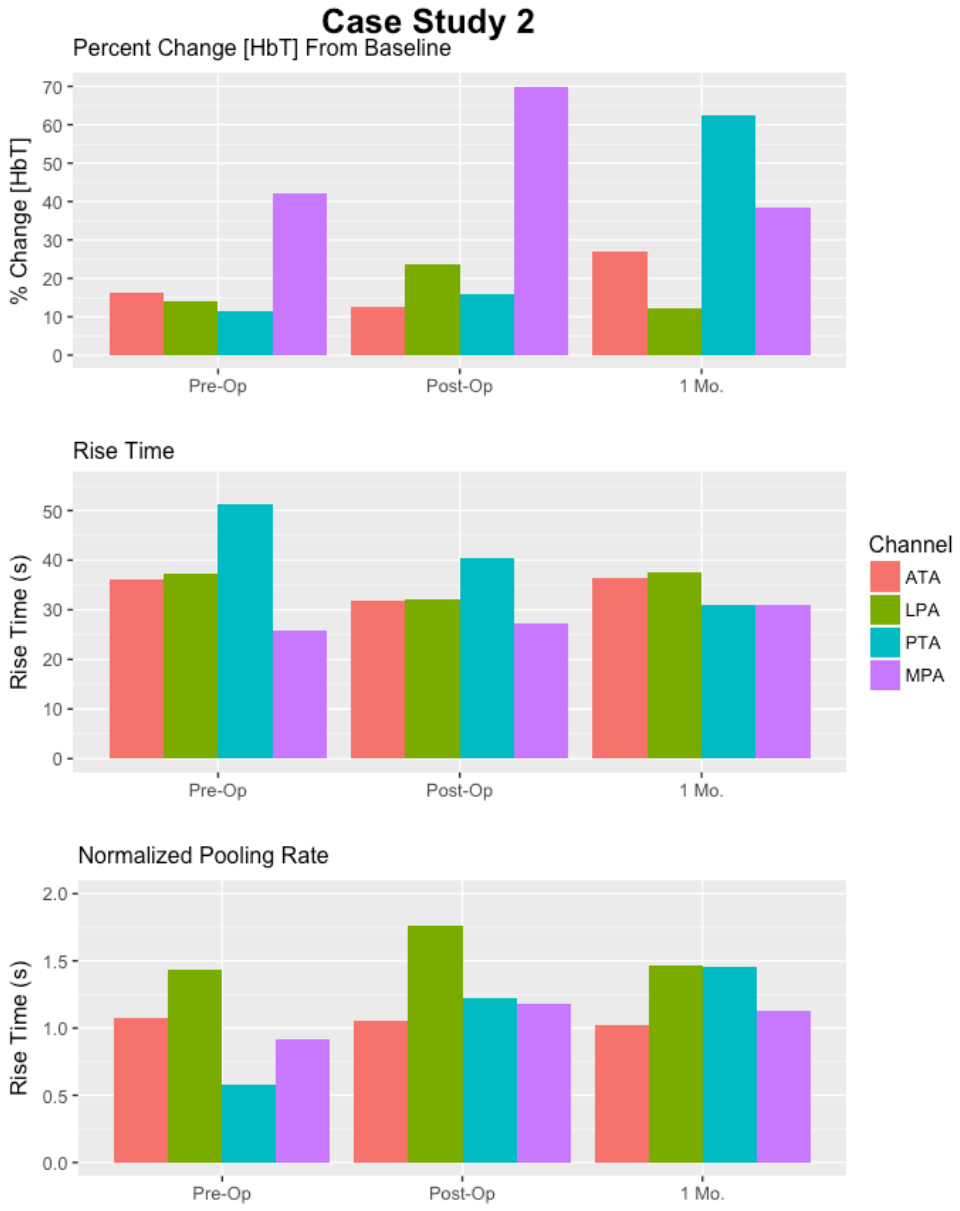

Figure 5.35 Feature results from the first three measurement points for PAD17, our non-diabetic PAD patient case.

It is important to note that with 29% of PAD patient over the age of 50 being also diabetic, it is important that the diagnostic measures be accurate for these patients, as they make a up a large sum of the PAD population.

5.6.2.3 ABI Measurements

ABI readings were collected from medical records of the patient enrolled in the study before and at 1-month after revascularization. In total, 9 ABI measurements taken prior to patient revascularization and 11 measurements were made at their 1-month follow-up. The PAD patients prior to intervention had an average ABI of 0.88 +/- 0.14 indicating moderate disease, while measurements made during the 1-month follow up had an average ABI of 0.95 +/- 0.36, which could be misinterpreted as healthy vasculature, as 80% of the subjects were diabetic. Although arterial calcifications render the arteries incompressible and falsely elevate the ABI readings, a statistical significance ($p=0.013$) is observed between the pre-operative and 1-month follow-up

ABI readings. In general, this is indicative of an improvement of vascular flow to the lower extremities.

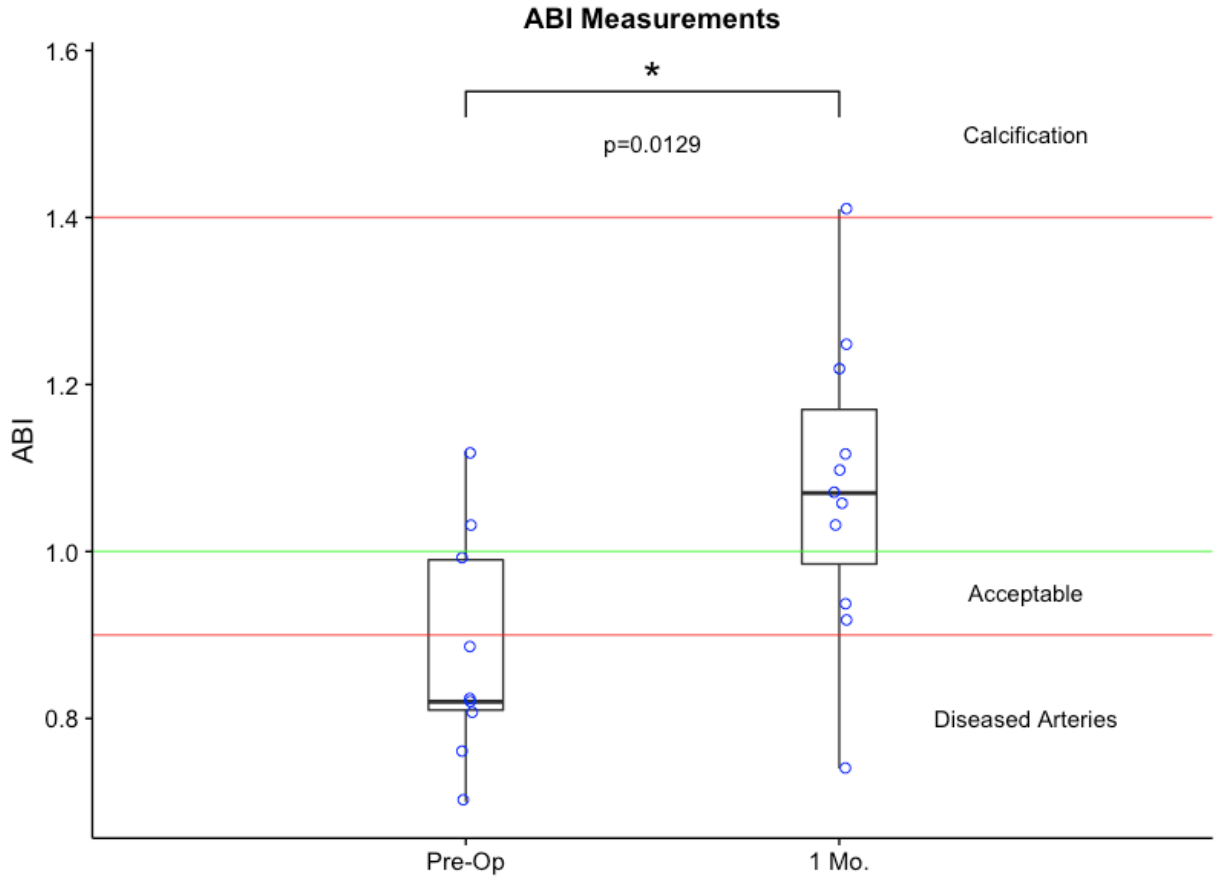

Figure 5.36 Comparison of ABI measurements taken from subjects before and 1-month after revascularization. A statistically significant change in the ABI was observed (p=0.0129)

5.6.2.4 VOSM Measurements up to 1-Month After Intervention

The three features extracted from the time traces were analyzed (Percent change, HbT Rise time, and normalized pooling rate) and boxplots were created for each feature and thigh cuff pressure associated with the measurement (Figure 5.37, Figure 5.38, Figure 5.39, and Figure 5.40). The boxplots show a general trend that the percentage change feature increases between the pre- and post-operative measurements and then decreases after one month. This pre-, post-op, and 1 month

measurement trend is also observed for the pooling rate. Conversely, the rise time of HbT between pre- and post-operative measurements decreases, and then again increases between post-op and 1-month follow up measurements. The basis of these results indicate that features indicate that there is an increase in perfusion after the intervention but generally shows a decrease in perfusion 1-month after the intervention.

To quantify these observations, a RM-ANOVA test was used for each VOSM channel to compute global difference between optical vascular measures. With 3 features, 2 thigh cuff pressures, and 4 VOSM channels, there were a total of 24 RM-ANOVA tests that were performed. Table 5.6 shows the p-values computed from the hypothesis testing, where the null hypothesis is rejected if the p-value is below 0.05. A rejection of the null hypothesis indicates that a significant difference is present in at least one of the repeated measures. From these results, it is shown that rise time provides a strong measure for vascular differences in the ATA and LPA channels. The Pooling rate feature also demonstrates significant changes with the LPA channel for both thigh cuff pressures. In addition, the percent change feature shows no significant differences between measurements for any channel or thigh cuff pressures. Furthermore, there are no differences between measurements with PTA and MPA channels for any of the features, which may indicate that there is a lack of sensitivity at these physical locations.

	Repeated Measures ANOVA (p-values)					
	% Change		Rise Time		Pooling Rate	
Channel	60mmHg	100mmHg	60mmHg	100mmHg	60mmHg	100mmHg
ATA Channel	0.401	0.106	0.040	0.005	0.063	0.156
LPA Channel	0.053	0.116	0.001	0.000	0.006	0.012
PTA Channel	0.984	0.945	0.274	0.337	0.168	0.666
MPA Channel	0.351	0.435	0.213	0.274	0.144	0.257

Table 5.6 Computed p-values from the repeated-measure ANOVA tests. The null hypothesis was rejected if the p-value was computed to be less than 0.05.

Despite the lack of global significance in these 24 groups using the RM-ANOVA, post-hoc testing was performed to quantify specific changes between measurement pairs. Within subject comparisons were made between pre-, post-operative, and 1 month follow-up measurements using a paired t-test. Difference in measurements in the ATA Channel (Figure 5.37) show that the there is a significant difference between the pre- and post-operative measurements for all features and thigh cuff pressures. Furthermore, there are no other significant differences between any other group, which signifies that the patient may be worsening one month after revascularization, albeit it is to a lesser degree than the vascular state as measured pre-operation.

There are many observations that can be made from these pair-wise comparisons. The most notable difference is that out of 24 channel/feature/cuff pressure combinations, with a total of 72 measurement comparisons, there were 13 significant differences observed, with 11 of those calculations observed between pre- and post-operative measurements, and the other 2 calculations observed between post-operative and 1-month follow measurements. This trend may indicate that although the patient improves after intervention, tissue perfusion in the lower extremities may worsen after only 1 month.

The ATA channel shows significant differences between the pre- and post-operative measurements across all features and cuff pressures, while the LPA channel also has differences between pre- and post-operative measurements, expect in the percent change category at 100mmHg. As indicated by the RM-ANOVA results, comparison made within the PTA and MPA channels were largely insignificant, with only the MPA channel showing a change between pre- and post-operative VOSM measurements for the 60mmHg normalized pooling rate feature. There are no significant differences between groups from the PTA channel, which may indicate that there is not

enough sensitivity from the calf location. In addition, there is only two significantly different comparisons outside of the pre- and post-operative measurements, which are between post-operative and 1-month follow ups (LPA-percent change-60mmHg thigh cuff pressure, and the MPA-rise time-100mmHg).

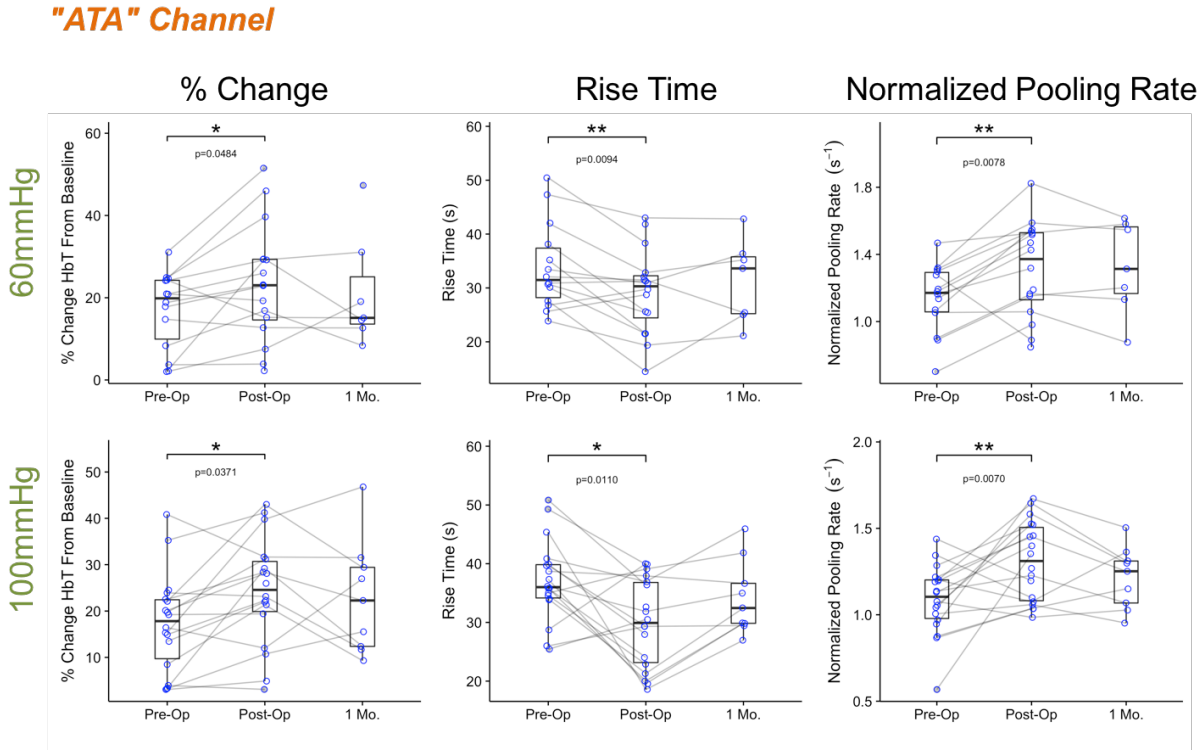

Figure 5.37 Comparisons between pre-op, post-op, and 1 month follow-up measurements from the ATA patch channel using a paired t-test. Calculations were made against all three features (Percent change, HbT Rise Time, and the Normalized Pooling Rate), and for both thigh cuff pressures (60 and 100mmHg).

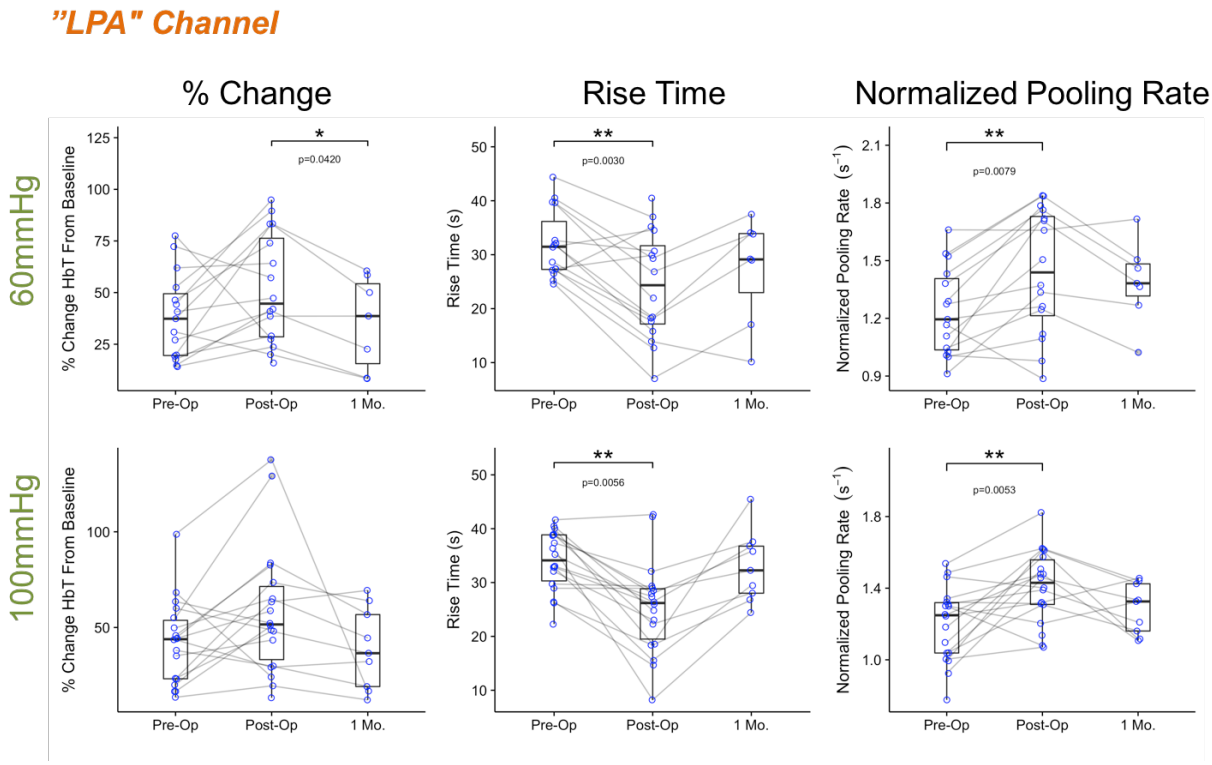

Figure 5.38 Comparisons between pre-op, post-op, and 1 month follow-up measurements from the LPA patch channel using a paired t-test. Calculations were made against all three features (Percent change, HbT Rise Time, and the Normalized Pooling Rate), and for both thigh cuff pressures (60 and 100mmHg).

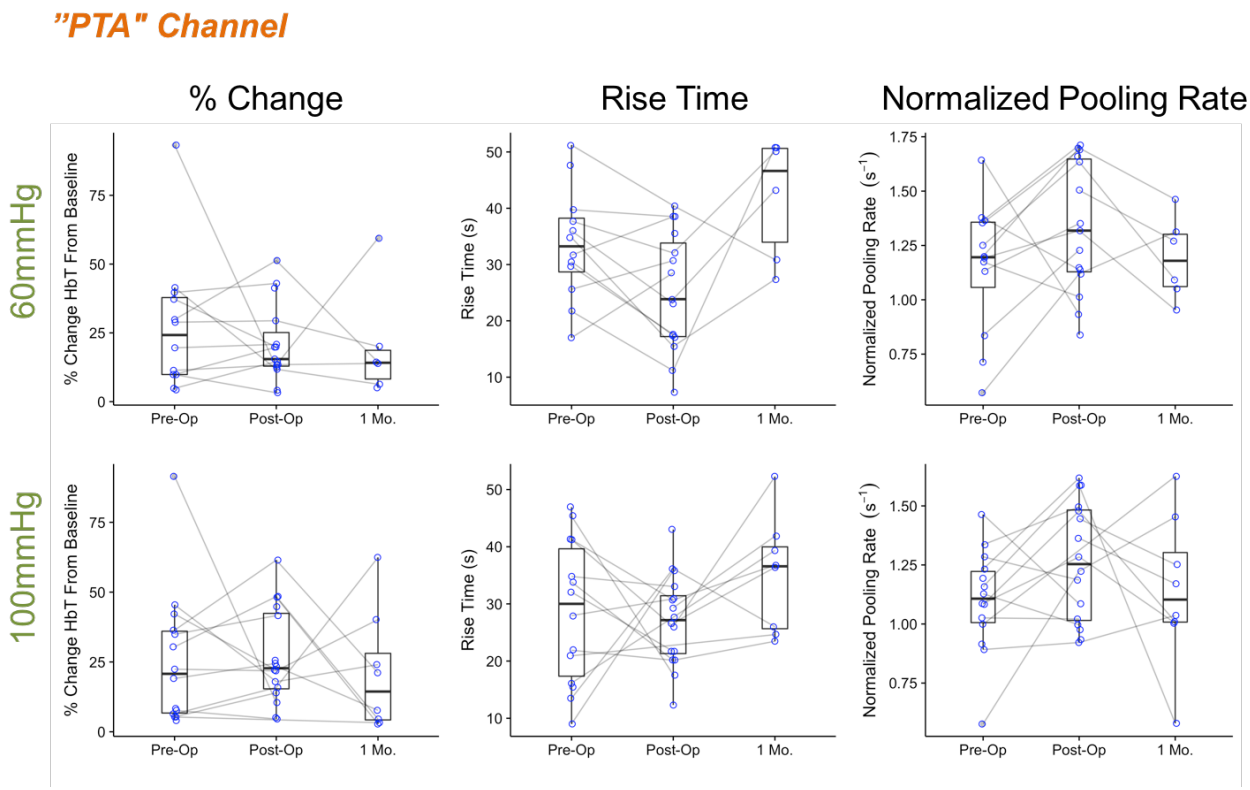

Figure 5.39 Comparisons between pre-op, post-op, and 1 month follow-up measurements from the PTA patch channel using a paired t-test. Calculations were made against all three features (Percent change, HbT Rise Time, and the Normalized Pooling Rate), and for both thigh cuff pressures (60 and 100mmHg).

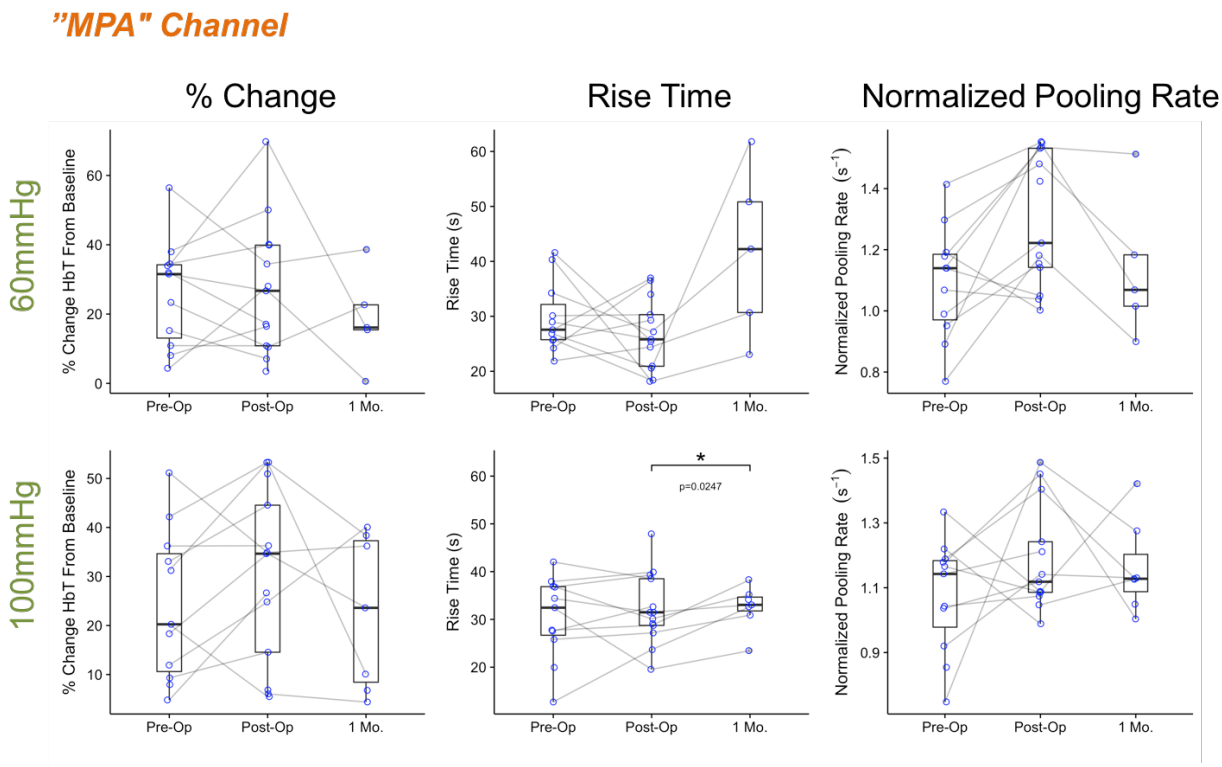

Figure 5.40 Comparisons between pre-op, post-op, and 1 month follow-up measurements from the MPA toe clip channel using a paired t-test. Calculations were made against all three features (Percent change, HbT Rise Time, and the Normalized Pooling Rate), and for both thigh cuff pressures (60 and 100mmHg).

Table 5.7 provides a list of the Holm-Sidak adjusted p-values of the multiple comparisons. Based on these p-values from the 3 features and 2 cuff pressures, it can be deduced that the rise time feature at 60mmHg provides the highest sensitivity in measuring changes in perfusion across repeated measurements. It should be emphasized that the PTA and MPA channels did not observe statistical significance in the RM-ANOVA test and as such the significant changes in paired t-test from the MPA channel may be a result of a type I error.

ATA Channel	60mmHg			100mmHg		
	HbT % change	HbT Rise time	Pooling Rate Norm	HbT % change	HbT Rise time	Pooling Rate Norm
Pre - Post	0.049	0.007	0.021	0.037	0.011	0.023
Pre - 1 Mo.	0.682	0.139	0.266	0.476	0.171	0.239
Post - 1 Mo.	0.682	0.355	0.842	0.476	0.011	0.488

LPA Channel	60mmHg			100mmHg		
	HbT % change	HbT Rise time	Pooling Rate Norm	HbT % change	HbT Rise time	Pooling Rate Norm
Pre - Post	0.102	0.002	0.003	0.135	0.006	0.009
Pre - 1 Mo.	0.481	0.130	0.237	0.979	0.145	0.180
Post - 1 Mo.	0.042	0.058	0.237	0.247	0.006	0.090

PTA Channel	60mmHg			100mmHg		
	HbT % change	HbT Rise time	Pooling Rate Norm	HbT % change	HbT Rise time	Pooling Rate Norm
Pre - Post	1.000	0.150	0.348	1.000	0.761	1.000
Pre - 1 Mo.	1.000	0.774	0.571	1.000	0.261	1.000
Post - 1 Mo.	1.000	0.230	0.143	1.000	0.261	0.597

MPA Channel	60mmHg			100mmHg		
	HbT % change	HbT Rise time	Pooling Rate Norm	HbT % change	HbT Rise time	Pooling Rate Norm
Pre - Post	0.739	0.658	0.033	0.416	0.877	0.747
Pre - 1 Mo.	0.219	0.658	0.906	0.888	0.750	0.747
Post - 1 Mo.	0.739	0.418	0.181	0.627	0.025	0.747

Table 5.7 Computed Holm-Sidak adjusted p-values comparing repeated measures for all channel, feature, and thigh cuff pressure combinations.

Within the ATA and LPA channels, there were features that showed statistically significant differences, largely between pre- and post-operative measurements. Although establishing the general trend of the effect from the surgical intervention is important, quantifying the percentage change of the features between time points is also important, as the inter-measurement reliability

may affect the overall outcome of the VOSM measurements. Figure 5.41 and Figure 5.42 show the vascular response according to the VOSM features from pre- and post-intervention and post-intervention vs. 1 month follow-ups. The features show an 18 to 50% increase perfusion based on these features from before and after intervention, with the LPA channel demonstrating a larger change in response compared to the ATA channel. Furthermore, these results show that the perfusion decreases again after 1 month. The magnitude of these changes range from 8 to 38%, with the normalized pooling rate showing the minimal amount of change at -8%.

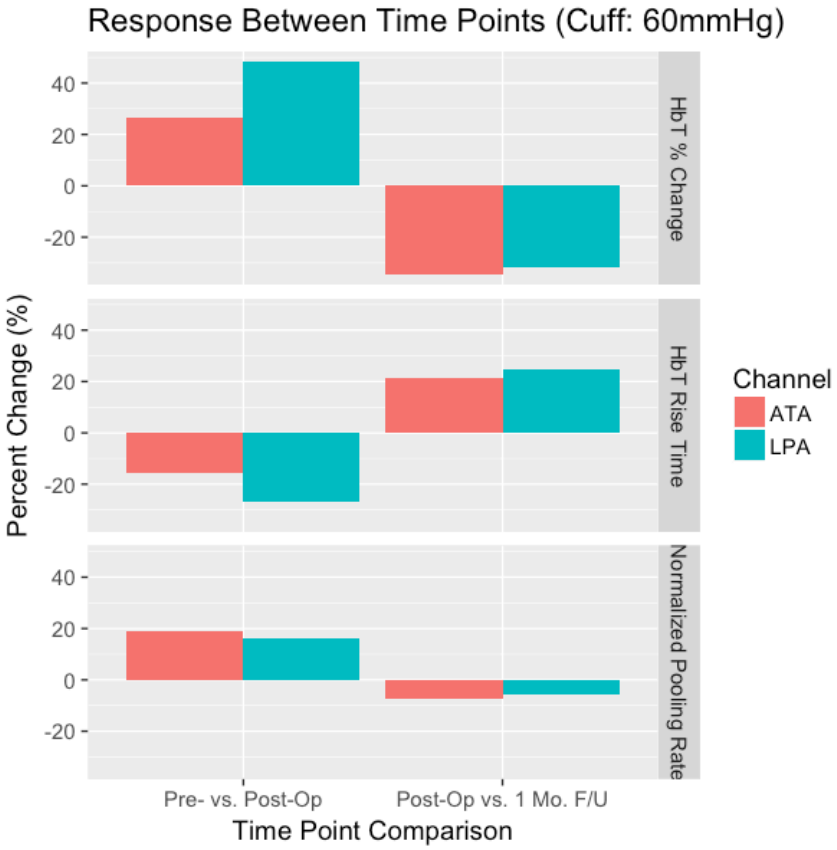

Figure 5.41 Percent change in response between time points (Pre- vs. Post-intervention and Post-Intervention vs. 1 Month F/U) from the VOSM features used to measure perfusion. Data displayed is from cuff measurements made at 60mmHg.

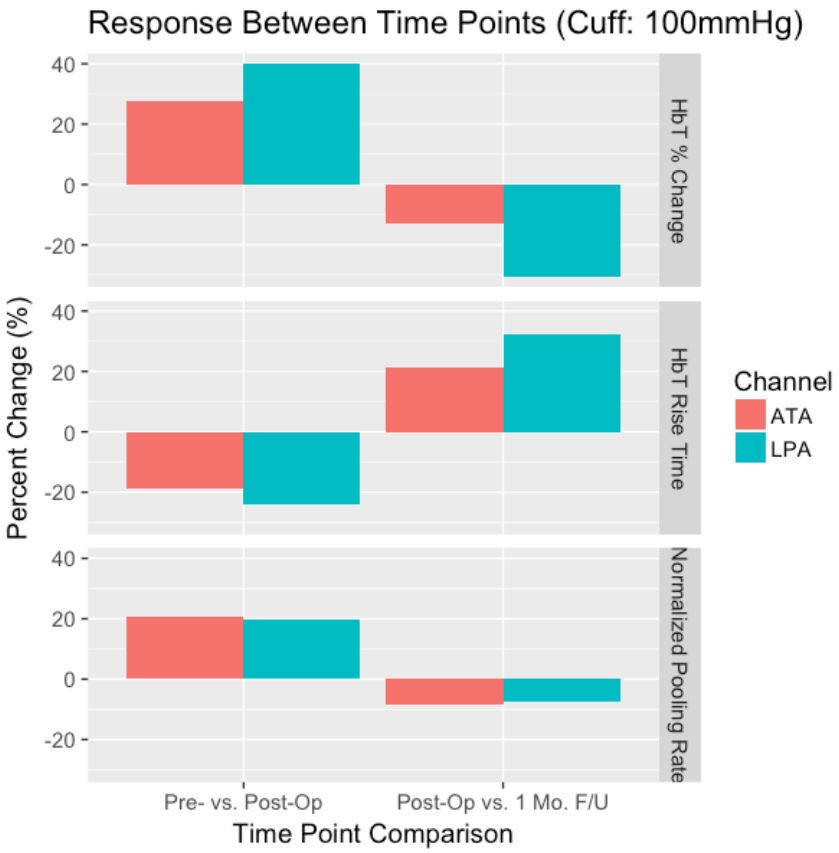

Figure 5.42 Percent change in response between time points (Pre- vs. Post-intervention and Post-Intervention vs. 1 Month F/U) from the VOSM features used to measure perfusion. Data displayed is from cuff measurements made at 100mmHg.

5.6.2.5 Angiosome Analysis

Angiosome theory is a topic of great interest in vascular surgery. The primary use of the four VOSM channel patches is to localize perfusion changes to these angiosome according to the artery or arteries treated during surgical intervention. The four angiosomes captured from the lower extremities include regions that are supplied by the anterior tibial artery (ATA, dorsal side of foot), the lateral plantar artery (LPA, plantar side of foot), and the posterior tibial artery (PTA, calf muscle). In addition, the toe clip was placed on the hallux, or commonly known as the big toe, to monitor the perfusion from the medial plantar artery (MPA). Due to the vast number of arteries in

the lower extremity, treatment locations were divided into zones for which angiosomes are expected to observe a change (Table 5.5).

In order to quantify the interaction between the treated artery and the perfusion response of the angiosome, the VOSM measurements were separated by each defined treatment zone. For example, surgical treatment to the ATA (Zone 2) is expected to primarily improve perfusion in the dorsal region of the foot, and should be measured as such by the ATA VOSM channel. However, the treatment of the femoral artery, which supplies blood to all of the angiosome regions, is expected to improve perfusion to all angiosome regions and all VOSM channel measurements should observe this change.

Vascular changes to the angiosome regions according to the treatment locations were quantified by using the paired t-test to analyze the differences in the feature data before and after the surgical intervention. Since the differences in vascular results between pre-op and 1 month VOSM measurements are not statistically significant (Section 5.6.2.2), measurements taken at 1 month were not included in this analysis. Furthermore, because the differences in the pre- and post-operation data are maximized, the sensitivity of vascular response from the angiosomes according to the treatment locations are also maximized. Significant changes in perfusion after revascularization according the treatment zones were evaluated using a p-value < 0.05 for thigh cuff pressures at 60mmHg (**Error! Reference source not found.**) and at 100mmHg (**Error! ference source not found.**). The significant changes between angiosome and treatment zone are

highlighted in yellow, while NA values denotes that a comparison measure was not possible due to the small number of the patients that underwent treatment at that location.

HbT perc change	SFA	ATA	PTA	PERO
ATA- Cuff:60mmHg	0.009	0.978	NA	NA
LPA- Cuff:60mmHg	0.087	0.994	NA	NA
PTA- Cuff:60mmHg	0.588	NA	NA	NA
MPA- Cuff:60mmHg	0.857	NA	NA	NA

HbT Rise time	SFA	ATA	PTA	PERO
ATA- Cuff:60mmHg	0.03	0.174	NA	NA
LPA- Cuff:60mmHg	0.029	0.311	NA	NA
PTA- Cuff:60mmHg	0.502	NA	NA	NA
MPA- Cuff:60mmHg	0.6	NA	NA	NA

Norm. Pooling Rate	SFA	ATA	PTA	PERO
ATA- Cuff:60mmHg	0.088	0.046	NA	NA
LPA- Cuff:60mmHg	0.086	0.107	NA	NA
PTA- Cuff:60mmHg	0.615	NA	NA	NA
MPA- Cuff:60mmHg	0.456	NA	NA	NA

Table 5.8 Calculated p-values between pre- and post-operative VOSM channel measurements according to the subject's defined treatment zone. These measurements are only made for cuff occlusions at 60mmHg

HbT perc change	SFA	ATA	PTA	PERO
ATA- Cuff:100mmHg	0.026	0.012	NA	NA
LPA- Cuff:100mmHg	0.086	0.923	NA	NA
PTA- Cuff:100mmHg	0.924	NA	NA	NA
MPA- Cuff:100mmHg	0.121	NA	NA	NA

HbT Rise time	SFA	ATA	PTA	PERO
ATA- Cuff:100mmHg	0.002	0.323	NA	NA
LPA- Cuff:100mmHg	0.005	0.184	NA	NA
PTA- Cuff:100mmHg	0.743	NA	NA	NA
MPA- Cuff:100mmHg	1	NA	NA	NA

Norm. Pooling Rate	SFA	ATA	PTA	PERO
ATA- Cuff:100mmHg	0.02	0.058	NA	NA
LPA- Cuff:100mmHg	0.126	0.21	NA	NA
PTA- Cuff:100mmHg	0.114	NA	NA	NA
MPA- Cuff:100mmHg	0.502	NA	NA	NA

Table 5.9 Calculated p-values between pre- and post-operative VOSM channel measurements according to the subject's defined treatment zone. These measurements are only made for cuff occlusions at 100mmHg

As these tables show, the number of treatment measurements in zone 3 and 4 are too low to make a quantitative comparison using the paired t-test. Also, due to poor signal quality at the PTA and MPA channels, a paired t-test for the Zone 2 (ATA) could not be computed. For treatment above the knee (SFA, Popliteal, Iliac), measurements taken at the PTA and MPA are not significant ($P>0.114$). Finally, there are more significant differences in the angiosome-to-treatment zone comparisons with the cuff measurement at 100mmHg than 60mmHg. This may signify that a cuff pressure at 100mmHg provides a more sensitive measurement to changes.

5.6.2.6 Repeatability

To assess the reliability of VOSM, the imaging protocol described in section 5.6.1.4 is performed in two trials during each patient visit, and the 3 features that are extracted from the VOSM time traces are compared from the initial and repeated reading. To quantify the differences between the features of the repeated measures, a Bland-Altman diagram was created to visualize the mean and

difference of the repeated measure of the percent change, rise time, and pooling rate features (Figure 5.40).

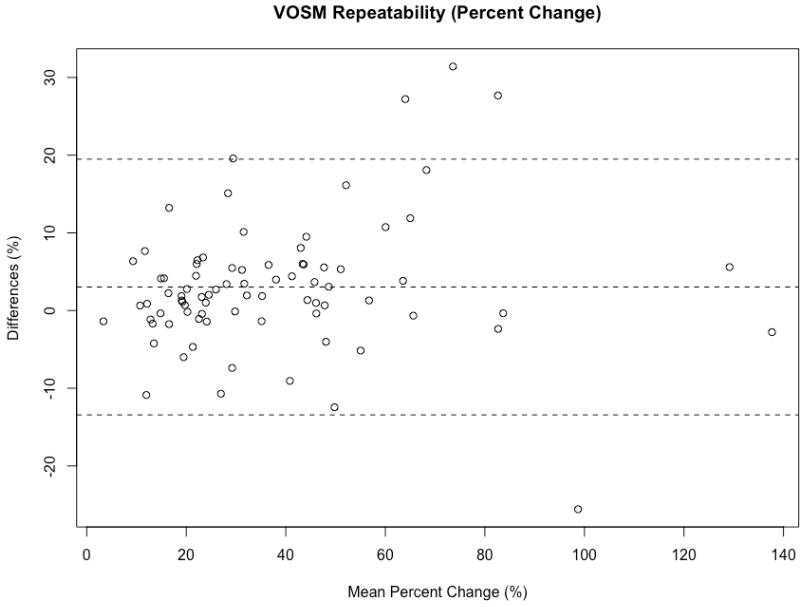

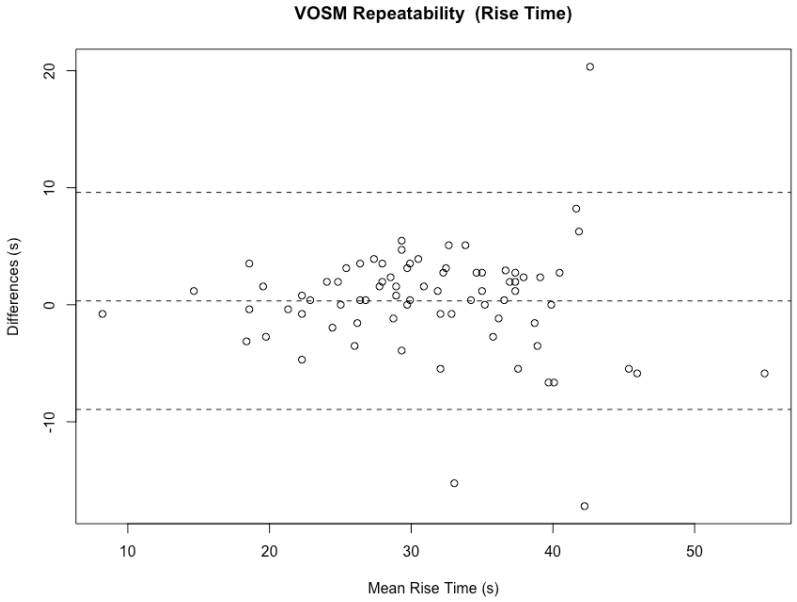

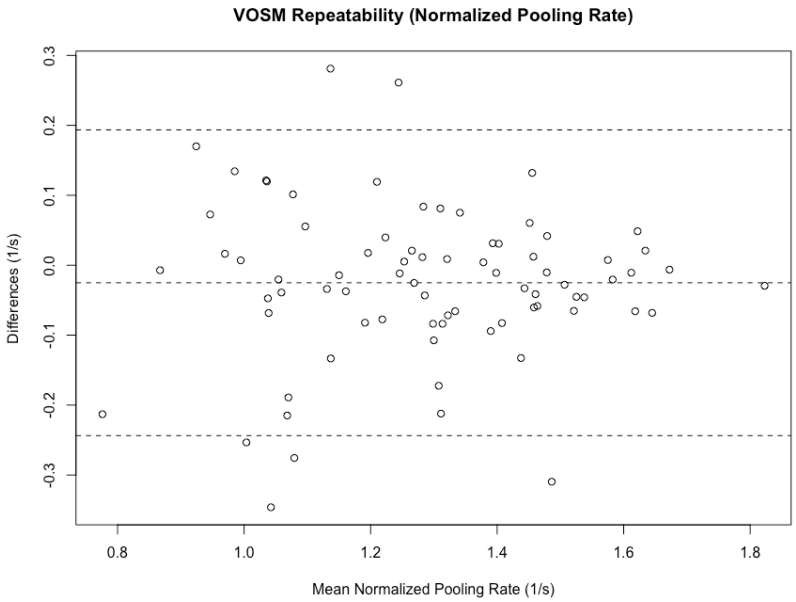

Figure 5.43 Bland-Altman plots demonstrating the reliability of the VOSM system through three of the extracted features. TOP: percent change of HbT from the baseline measurement, MIDDLE: Rise time of the pooling from 10% to 80% of the maximum HbT, BOTTOM: Normalized pooling rate of HbT.

These figures demonstrate that the repeated measures have a mean variation of 18.1% for "Percent change HbT", 9.9% for "Rise time", and 7.1% for "Normalized pooling rate". However, computing the mean of the difference of the repeated measurements is heavily weighted on potential outliers that may occur due to physical factors such as motion artifacts during acquisition, ulcerations at the toe, or physiological changes that may be caused by repeated thigh cuff occlusions. To substantiate the weight of the outliers on the repeatability measurements, a boxplot of the percent variation from the initial and repeated reading for all VOSM channels are shown in Figure 5.44. Here it is shown that there are outliers that reach up to 54% variation between initial and repeated measure (Percent change HbT). Despite the range of variations from repeatable measures, 70.5% of the instances fall below the mean difference in repeated measures for the normalized pooling rate and 61% for the rise time feature. By using boxplots, the median of the difference is shown to be lower than the mean variation (HbT % Change = 11.2%, "Rise time" =

7.7%, “Normalized pooling” = 4.2%). The mean and median differences in repeated measures in summarized in Table 5.10.

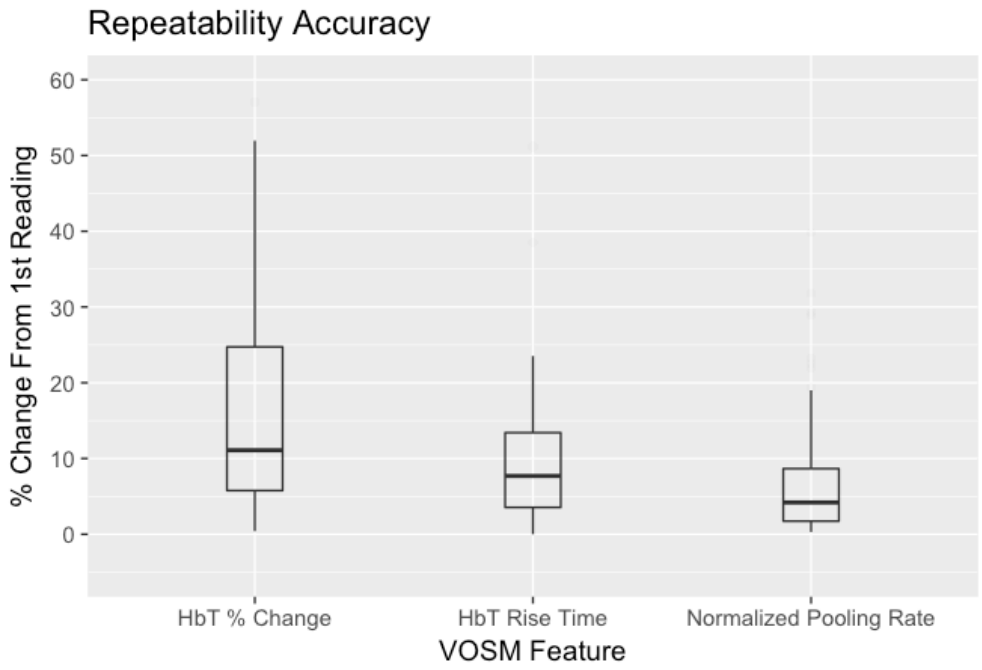

Figure 5.44 Boxplot the percent change from initial and repeated measurements for all measurements from all channels.

In addition to computing the percent change between the repeated measures, an RM-ANOVA test was performed for each of the three features. Using this metric, the null hypothesis is desired, as it demonstrates there is no significant difference between the first and second measurement. The p-values from the RM-ANOVA are shown in Table 5.10. These results show that the “Rise time” and “Normalized pooling rate” have no significant differences between the first and second measurement. However, the “Percent change in HbT” feature has a $p<0.05$, signifying that the first and second measurements is significant. This suggests that the percent change feature may not be a reliable feature for tracking

	VOSM Feature		
	% Change HbT	Rise Time	Normalized Pooling Rate
Mean Variation	18.1%	9.9%	7.1%
Median Variation	11.2%	7.7%	4.2%

RM-ANOVA p-Values	0.002	0.545	0.051

Table 5.10 Summary of the repeatability error from the 3 VOSM features.

5.7 Discussion

The VOSM system is a non-invasive, non-ionizing, contrast-free imaging modality that uses diffuse optical spectroscopy (DOS) in which red and near-infrared light to is used to measure changes in blood perfusion in tissue. The DOS technology has been applied to image PAD in the foot. Using our imaging protocol to simulate hemodynamic changes in the lower extremities, optical changes due to blood pooling is observed. For large vessel disease, the plaque buildup increases the resistance and reduces compliance of the vessels. This leads to a reduction in the blood pooling into the foot, resulting in lower pooling rate of [HbT]. In small vessel disease, the same effect can be caused by arterial stenosis.

In order to quantify the level of perfusion in the lower extremeties, multiple features were extracted from these VOSM time traces as described in our imaging protocol (Percent change HbT, HbT Rise Time, and Normalized Pooling Rate). Based on these features, VOSM shows statistically significant differences in blood perfusion in PAD patients before and after surgical intervention to improve affected vasculature in the foot.

Measurements to quantify repeatability were taken at each imaging session with VOSM. During each session, the imaging protocol was performed twice and were compared to each other with respect to channel and thigh cuff pressure. It was found that the rise time and normalized pooling rate feature were repeatable within 7 and 5% respectively. There were outliers that were observed for these repeatability measurements, which caused the mean variance to increase. It is believed that the high level of variance in for these measurements are due to physiological changes in the

leg after multiple thigh cuff occlusions, motion artifacts, or patch placement was moved out of the a region with high vasculature.

Measurements of perfusion were made at four separate points on the leg, with two of the channels (ATA, LPA channels) demonstrating the most sensitivity between pre- and post-operative measurements, based on statistically significant differences between the measurements. The most sensitive feature extracted from the VOSM times traces to monitor increase of blood pooling during the cuff occlusion is from the HbT rise time feature at a thigh cuff pressure of 100mmHg (RM-ANOVA $p<0.001$). The normalize pooling rate was also determined to be a suitable measure of blood perfusion in the foot, but did not demonstrate a statistically significant difference between measures for the ATA channel. This analysis was also completed for 60 mmHg thigh cuff occlusions, which was not as effective as the 100mmHg pressure. We suspect this is because of 60 mmHg may not be a sufficient cuff pressure to produce a full venous occlusion. In addition, the PTA and MPA channels on the VOSM system did not demonstrate statistically significant changes between measurements based on the RM-ANOVA. This may indicate that the position of these channels should be adjusted in order to acquire more sensitive measurements on these arteries.

VOSM measurements performed one month after surgical interventions displayed an increase in the HbT rise time, and did not have any statistically significant changes with the pre-operative measurement for any of the feature and thigh cuff combinations. This suggests that the blood perfusion after only one month is worsening and further treatment may be required to maintain proper perfusion to the foot otherwise risk of ulceration, gangrene, or amputation may be

imminent. For example, of the 22 subjects enrolled, there have been 3 that have required a second intervention before completing the 12 months of monitoring as described in our study protocol. Conversely, the ground truth measure of ABI taken one month after intervention suggests otherwise, as these diagnostics demonstrated an improvement at the 1 month mark ($p=0.013$), suggesting that perfusion is improved compared to pre-operative measurements. Unfortunately, this cross-sectional analysis cannot provide insight into when and if the gold standard measurements indicate additional intervention is needed. Furthermore, our continuation of the study is necessary in providing insight as to if the VOSM measurements provide an earlier indication into changes in tissues perfusion as compared with ABI measurements.

There is currently no gold standard for assessing angiosome perfusion, making statistical analysis on tissue perfusion in the various angiosome regions difficult. Future studies involving animal models or angiographic foot analysis in patients with distal arterial disease may help to validate angiosome analysis using VOTI. Although more data is required for an in-depth angiosome analysis, it was shown in this analysis that the VOSM ATA channel could show the most sensitive measurements for cases in which the AT artery was treated. These results suggest that the use of the VOSM system may aid in treatment planning, where a physician can intervene to improve perfusion to the most compromised areas of the foot. Unfortunately, there were only 1 case each for treatment of peroneal and the PT artery, and our angiosome analysis could not be done for these cases.

VOSM provides a direct measurement of the perfusion to multiple angiosome regions, serving as a measure of the effects of the lesions or stenosis on the foot. The DOS technology that VOSM utilizes can be used to non-invasively monitor patients with PAD, without needing to inject contrast into the patient's bloodstream. These cross-sectional results of this 100-patient study

indicate that a physician can effectively monitor patients with PAD independently of arterial calcifications using VOSM, despite the ABI measurements not being accurate. Future studies will involve greater enrollment to account for multivariate risk factors including smoking, age, hypertension, weight, and demographics to understand their effects on tissue perfusion as measured using the VOSM system.

6 Conclusion and Future Directions

This dissertation investigates the ability and clinical functionality of DOS as a compact system to monitor various diseases such as infantile hemangiomas (IH), rheumatoid arthritis (RA), and peripheral artery disease (PAD). We began by creating a second-generation handheld wireless probe, so that it would easy to use in the clinic and capable of accommodating the various tissue types and sizes observed in the clinic. Upon completing the new probe, we began a 15-patient pilot study to show that the WHDD was capable of monitoring the stages of IH to provide a proof concept that DOS technology could provide a quantitative measure to assess the highly vascular IH lesions.

In order to verify the accessibility of the WHDD system, we hoped to demonstrate that its sensitivity to vascular changes could be applied to measuring optical changes of the finger joint with patients suffering from RA that are undergoing treatment therapy. In a case study, ehe optical measurements from the WHDD were compared optical changes from our proven fDOT system and a sensitivity analysis was performed. Unfortunately, the sensitivity of the WHDD could not match that of the fDOT system from this single case. I believe that an improvement to the optical interfacing to the finger joint would make for more reliable measurements. In addition, the ability of fDOT to make accurate measurements of reduced scattering in comparison to the continuous wave topology of the WHDD system increases the sensitivity of monitoring RA. I suggest if a smaller form factor device is created for monitoring RA, future work must incorporate these two attributes.

Finally, in our study investigating the use of DOS to monitor blood perfusion in the foot in PAD patients before and up to a year after surgical intervention, a portable system was designed based on the hardware designs from the WHDD system. This system, called vascular optical

spectroscopic measurement (VOSM) system, has four DOS channels capable of making vascular measurements on the lower extremities of PAD patients. We demonstrated that the VOSM system is capable of displaying the increase in blood pooling associated with the intervention. We have also provided evidence that tissue perfusion vastly decreases only a month after the intervention, despite what the reading from the gold standard measures of ABI and PVR indicate. The cross-sectional analysis performed suggests a correlation between the location of the arteries treated and tissue perfusion improvement within the associated angiosome region. This feature may be able to guide vascular surgeons in how to approach revascularization for their patients. Future work for this project includes the completion of the 100-patient clinical study to perform a complete analysis. Furthermore, improvements should be made on the system's interfacing such that usability in a clinical setting is not an issue.

DOS has plenty of applications within the vascular realm. In the future, we hope to see DOS in a small form factor such as the WHP used by physicians to assess diseases. Furthermore, DOS can be used in 3rd world nations where technology is scarce or standard technology is too expensive for monitoring diseases such as breast cancer.

References

[1] T. Durduran, R. Choe, W. B. Baker, and A. G. Yodh, "Diffuse optics for tissue monitoring and tomography," *Reports on Progress in Physics,* vol. 73, no. 7, p. 076701, 2010.

[2] G. Strangman, D. A. Boas, and J. P. Sutton, "Non-invasive neuroimaging using near-infrared light," *Biological Psychiatry,* vol. 52, no. 7, pp. 679-693, 10/1/ 2002.

[3] V. Ntziachristos, A. H. Hielscher, A. G. Yodh, and B. Chance, "Diffuse optical tomography of highly heterogeneous media," (in Eng), *IEEE Trans Med Imaging,* vol. 20, no. 6, pp. 470-8, Jun 2001.

[4] B. W. Pogue, M. S. Patterson, H. Jiang, and K. D. Paulsen, "Initial assessment of a simple system for frequency domain diffuse optical tomography," (in Eng), *Phys Med Biol,* vol. 40, no. 10, pp. 1709-29, Oct 1995.

[5] H. Zhao, F. Gao, Y. Tanikawa, K. Homma, Y. Onodera, and Y. Yamada, "Anatomical and Functional Images of in vitro and in vivo Tissues by NIR Time-domain Diffuse Optical Tomography," *JSME International Journal Series C Mechanical Systems, Machine Elements and Manufacturing,* vol. 45, no. 4, pp. 1033-1039, 2002.

[6] A. H. Hielscher *et al.*, "Near-infrared diffuse optical tomography," (in Eng), *Dis Markers,* vol. 18, no. 5-6, pp. 313-37, 2002.

[7] C. Zhu and Q. Liu, "Review of Monte Carlo modeling of light transport in tissues," (in Eng), *J Biomed Opt,* vol. 18, no. 5, p. 50902, May 2013.

[8] D. A. Boas *et al.*, "Imaging the body with diffuse optical tomography," *IEEE Signal Processing Magazine,* vol. 18, no. 6, pp. 57-75, 2001.

[9] Z. Xiaowei, C. Ling, T. Chun-Yu, T. B. Penney, and C. Nanguang, "Theoretical investigation of near-infrared light path in multi-layer brain models for three DOT systems," in *2012 Photonics Global Conference (PGC)*, 2012, pp. 1-5.

[10] R. A. Simon and C. S. John, "Optical tomography: forward and inverse problems," *Inverse Problems,* vol. 25, no. 12, p. 123010, 2009.

[11] W. M. Star, "Diffusion Theory of Light Transport," in *Optical-Thermal Response of Laser-Irradiated Tissue*, A. J. Welch and M. J. C. Van Gemert, Eds. Boston, MA: Springer US, 1995, pp. 131-206.

[12] B. J. Tromberg, B. W. Pogue, K. D. Paulsen, A. G. Yodh, D. A. Boas, and A. E. Cerussi, "Assessing the future of diffuse optical imaging technologies for breast cancer management," (in Eng), *Med Phys,* vol. 35, no. 6, pp. 2443-51, Jun 2008.

[13] N. Shah, A. E. Cerussi, D. Jakubowski, D. Hsiang, J. Butler, and B. J. Tromberg, "Spatial variations in optical and physiological properties of healthy breast tissue," (in Eng), *J Biomed Opt,* vol. 9, no. 3, pp. 534-40, May-Jun 2004.

[14] Z. J. Lin *et al.*, "Interleaved imaging of cerebral hemodynamics and blood flow index to monitor ischemic stroke and treatment in rat by volumetric diffuse optical tomography," (in Eng), *Neuroimage,* vol. 85 Pt 1, pp. 566-82, Jan 15 2014.

[15] M. L. Flexman *et al.*, "Monitoring early tumor response to drug therapy with diffuse optical tomography," (in Eng), *J Biomed Opt,* vol. 17, no. 1, p. 016014, Jan 2012.

[16] R. C. Mesquita *et al.*, "Direct measurement of tissue blood flow and metabolism with diffuse optics," (in Eng), *Philos Trans A Math Phys Eng Sci,* vol. 369, no. 1955, pp. 4390-406, Nov 28 2011.

[17] B. Montcel, R. Chabrier, and P. Poulet, "Detection of cortical activation with time-resolved diffuse optical methods," (in Eng), *Appl Opt,* vol. 44, no. 10, pp. 1942-7, Apr 1 2005.

[18] A. Liebert *et al.*, "Bed-side assessment of cerebral perfusion in stroke patients based on optical monitoring of a dye bolus by time-resolved diffuse reflectance," (in Eng), *Neuroimage,* vol. 24, no. 2, pp. 426-35, Jan 15 2005.

[19] Y. Kang, J. Lee, K. Kwon, and C. Choi, "Application of novel dynamic optical imaging for evaluation of peripheral tissue perfusion," (in Eng), *Int J Cardiol,* vol. 145, no. 3, pp. e99-101, Dec 3 2010.

[20] A. H. Hielscher *et al.*, "Sagittal laser optical tomography for imaging of rheumatoid finger joints," (in eng), *Phys Med Biol,* vol. 49, no. 7, pp. 1147-63, Apr 07 2004.

[21] C. H. Schmitz, M. Löcker, J. M. Lasker, A. H. Hielscher, and R. L. Barbour, "Instrumentation for fast functional optical tomography," *Review of Scientific Instruments,* vol. 73, no. 2, pp. 429-439, 2002.

[22] F. E. W. Schmidt, M. E. Fry, E. M. C. Hillman, J. C. Hebden, and D. T. Delpy, "A 32-channel time-resolved instrument for medical optical tomography," *Review of Scientific Instruments,* vol. 71, no. 1, pp. 256-265, 2000/01/01 1999.

[23] S. Keren, O. Gheysens, C. S. Levin, and S. S. Gambhir, "A comparison between a time domain and continuous wave small animal optical imaging system," (in eng), *IEEE Trans Med Imaging,* vol. 27, no. 1, pp. 58-63, Jan 2008.

[24] S. Fantini, M.-A. Franceschini, J. S. Maier, S. A. Walker, B. B. Barbieri, and E. Gratton, "Frequency-domain multichannel optical detector for noninvasive tissue spectroscopy and oximetry," *Optical Engineering,* vol. 34, no. 1, pp. 32-42, 1995.

[25] B. Pogue, M. Testorf, T. McBride, U. Osterberg, and K. Paulsen, "Instrumentation and design of a frequency-domain diffuse optical tomography imager for breast cancer detection," (in eng), *Opt Express,* vol. 1, no. 13, pp. 391-403, Dec 22 1997.

[26] F. Leblond, S. C. Davis, P. A. Valdes, and B. W. Pogue, "Pre-clinical whole-body fluorescence imaging: Review of instruments, methods and applications," (in eng), *J Photochem Photobiol B,* vol. 98, no. 1, pp. 77-94, Jan 21 2010.

[27] B. J. Tromberg *et al.*, "Imaging in breast cancer: diffuse optics in breast cancer: detecting tumors in pre-menopausal women and monitoring neoadjuvant chemotherapy," (in Eng), *Breast Cancer Res,* vol. 7, no. 6, pp. 279-85, 2005.

[28] S. Srinivasan *et al.*, "Near-infrared characterization of breast tumors in vivo using spectrally-constrained reconstruction," (in Eng), *Technol Cancer Res Treat,* vol. 4, no. 5, pp. 513-26, Oct 2005.

[29] X. Intes, "Time-domain optical mammography SoftScan: initial results," (in Eng), *Acad Radiol,* vol. 12, no. 8, pp. 934-47, Aug 2005.

[30] B. J. Tromberg, "Optical scanning and breast cancer," (in Eng), *Acad Radiol,* vol. 12, no. 8, pp. 923-4, Aug 2005.

[31] P. Vaupel, A. Mayer, and M. Hockel, "Tumor hypoxia and malignant progression," (in Eng), *Methods Enzymol,* vol. 381, pp. 335-54, 2004.

[32] A. Rice and C. M. Quinn, "Angiogenesis, thrombospondin, and ductal carcinoma in situ of the breast," (in Eng), *J Clin Pathol,* vol. 55, no. 8, pp. 569-74, Aug 2002.

[33] B. W. Murphy *et al.*, "Toward the discrimination of early melanoma from common and dysplastic nevus using fiber optic diffuse reflectance spectroscopy," *Journal of Biomedical Optics,* vol. 10, no. 6, pp. 064020-064020-9, 2005.

[34] P. J. Speicher *et al.*, "Hypoxia in Melanoma: Using Optical Spectroscopy and EF5 to Assess Tumor Oxygenation Before and During Regional Chemotherapy for Melanoma," *Annals of Surgical Oncology,* journal article vol. 21, no. 5, pp. 1435-1440, 2014.

[35] G. Zonios, A. Dimou, I. Bassukas, D. Galaris, A. Tsolakidis, and E. Kaxiras, "Melanin absorption spectroscopy: new method for noninvasive skin investigation and melanoma detection," *Journal of Biomedical Optics,* vol. 13, no. 1, pp. 014017-014017-8, 2008.

[36] Y. N. Bhambhani, "Muscle Oxygenation Trends During Dynamic Exercise Measured by Near Infrared Spectroscopy," *Canadian Journal of Applied Physiology,* vol. 29, no. 4, pp. 504-523, 2004/08/01 2004.

[37] R. Boushel, H. Langberg, S. Green, D. Skovgaard, J. Bülow, and M. Kjær, "Blood flow and oxygenation in peritendinous tissue and calf muscle during dynamic exercise in humans," *The Journal of Physiology,* vol. 524, no. 1, pp. 305-313, 2000.

[38] V. Quaresima *et al.*, "Calf and shin muscle oxygenation patterns and femoral artery blood flow during dynamic plantar flexion exercise in humans," *European Journal of Applied Physiology,* journal article vol. 84, no. 5, pp. 387-394, 2001.

[39] Y. Xu, N. Iftimia, H. Jiang, L. Key, and M. Bolster, "Imaging of in vitro and in vivo bones and joints with continuous-wave diffuse optical tomography," (in Eng), *Opt Express,* vol. 8, no. 7, pp. 447-51, Mar 26 2001.

[40] A. H. Hielscher *et al.*, "Frequency-domain optical tomographic imaging of arthritic finger joints," (in Eng), *IEEE Trans Med Imaging,* vol. 30, no. 10, pp. 1725-36, Oct 2011.

[41] S. K. Piper *et al.*, "A wearable multi-channel fNIRS system for brain imaging in freely moving subjects," *NeuroImage,* vol. 85, Part 1, pp. 64-71, 1/15/ 2014.

[42] J. R. Kuo, M. H. Chang, C. C. Wang, C. C. Chio, J. J. Wang, and B. S. Lin, "Wireless near-infrared spectroscopy system for determining brain hemoglobin levels in laboratory animals," (in Eng), *J Neurosci Methods,* vol. 214, no. 2, pp. 204-9, Apr 15 2013.

[43] T. Muehlemann, N. Reefmann, B. Wechsler, M. Wolf, and L. Gygax, "In vivo functional near-infrared spectroscopy measures mood-modulated cerebral responses to a positive emotional stimulus in sheep," (in Eng), *Neuroimage,* vol. 54, no. 2, pp. 1625-33, Jan 15 2011.

[44] H. Atsumori *et al.*, "Development of wearable optical topography system for mapping the prefrontal cortex activation," (in Eng), *Rev Sci Instrum,* vol. 80, no. 4, p. 043704, Apr 2009.

[45] T. Muehlemann, D. Haensse, and M. Wolf, "Wireless miniaturized in-vivo near infrared imaging," (in Eng), *Opt Express,* vol. 16, no. 14, pp. 10323-30, Jul 7 2008.

[46] L. Wang *et al.*, "Wireless Spectroscopic Compact Photonic Explorer for Diagnostic Optical Imaging," *Biomedical Microdevices,* journal article vol. 7, no. 2, pp. 111-115, 2005.

[47] M. Kfouri *et al.*, "Toward a Miniaturized Wireless Fluorescence-Based Diagnostic Imaging System," *IEEE Journal of Selected Topics in Quantum Electronics,* vol. 14, no. 1, pp. 226-234, 2008.

[48] Y.-J. Jung, M. Roman, J. Carrasquilla, S. J. Erickson, and A. Godavarty, "Portable wide-field hand-held NIR scanner," 2013, vol. 8572, pp. 85720A-85720A-9.

[49] S. Rodriguez, H. Kaliada, G. Clark, Y. jung, and A. Godavarty, "In-vivo Breast Imaging Using An Ultra-Portable Hand-Held Near-Infrared Optical Scanner (NIROS)," in *Biomedical Optics 2014*, Miami, Florida, 2014, p. BM3A.66: Optical Society of America.

[50] C. J. Cheng, S. Y. Wu, W. C. Huang, H. W. Hou, and W. C. Fang, "A wireless near-infrared imaging system design for breast tumor detection," in *2014 IEEE International Conference on Consumer Electronics (ICCE)*, 2014, pp. 228-231.

[51] T. Watanabe, R. Sekine, T. Mizuno, and M. Miwa, "Development of Portable, Wireless and Smartphone Controllable Near-Infrared Spectroscopy System," (in eng), *Adv Exp Med Biol,* vol. 923, pp. 385-92, 2016.

[52] A. J. Das, A. Wahi, I. Kothari, and R. Raskar, "Ultra-portable, wireless smartphone spectrometer for rapid, non-destructive testing of fruit ripeness," *Scientific Reports,* Article vol. 6, p. 32504, 09/08/online 2016.

[53] Z. J. Smith *et al.*, "Cell-Phone-Based Platform for Biomedical Device Development and Education Applications," *PLOS ONE,* vol. 6, no. 3, p. e17150, 2011.

[54] G. Hu, Q. Zhang, V. Ivkovic, and G. E. Strangman, "Ambulatory diffuse optical tomography and multimodality physiological monitoring system for muscle and exercise applications," (in eng), *J Biomed Opt,* vol. 21, no. 9, p. 091314, Sep 2016.

[55] M. L. Flexman, H. K. Kim, R. Stoll, M. A. Khalil, C. J. Fong, and A. H. Hielscher, "A wireless handheld probe with spectrally constrained evolution strategies for diffuse optical imaging of tissue," *Review of Scientific Instruments,* vol. 83, no. 3, pp. 033108-8, 03/00/ 2012.

[56] C. Mansouri, J.-P. L'Huillier, N. Kashou, and A. Humeau, "Depth sensitivity analysis of functional near-infrared spectroscopy measurement using three-dimensional Monte Carlo modelling-based magnetic resonance imaging," (in English), *Lasers in Medical Science,* vol. 25, no. 3, pp. 431-438, 2010/05/01 2010.

[57] J. M. Lasker, J. M. Masciotti, M. Schoenecker, C. H. Schmitz, and A. H. Hielscher, "Digital-signal-processor-based dynamic imaging system for optical tomography," *Review of Scientific Instruments,* vol. 78, no. 8, pp. -, 2007.

[58] J. M. Masciotti, J. M. Lasker, and A. H. Hielscher, "Digital Lock-In Detection for Discriminating Multiple Modulation Frequencies With High Accuracy and Computational Efficiency," *Instrumentation and Measurement, IEEE Transactions on,* vol. 57, no. 1, pp. 182-189, 2008.

[59] T. J. Farrell, M. S. Patterson, and B. Wilson, "A diffusion theory model of spatially resolved, steady-state diffuse reflectance for the noninvasive determination of tissue optical properties in vivo," *Medical Physics,* vol. 19, no. 4, pp. 879-888, 07/00/ 1992.

[60] M. Keijzer, W. M. Star, and P. R. M. Storchi, "Optical diffusion in layered media," *Appl. Opt.,* vol. 27, no. 9, pp. 1820-1824, 05/01 1988.

[61] S. L. Jacques, "Optical properties of biological tissues: a review," (in eng), *Phys Med Biol,* vol. 58, no. 11, pp. R37-61, Jun 07 2013.

[62] B. A. Drolet, N. B. Esterly, and I. J. Frieden, "Hemangiomas in Children," *New England Journal of Medicine,* vol. 341, no. 3, pp. 173-181, 1999.

[63] T. S. Chen, L. F. Eichenfield, and S. F. Friedlander, "Infantile Hemangiomas: An Update on Pathogenesis and Therapy," *Pediatrics,* vol. 131, no. 1, pp. 99-108, January 1, 2013 2013.

[64] C. Léauté-Labrèze, S. Prey, and K. Ezzedine, "Infantile haemangioma: Part I. Pathophysiology, epidemiology, clinical features, life cycle and associated structural abnormalities," *Journal of the European Academy of Dermatology and Venereology,* vol. 25, no. 11, pp. 1245-1253, 2011.

[65] M. E. Kleinman *et al.*, "Hypoxia-Induced Mediators of Stem/Progenitor Cell Trafficking Are Increased in Children With Hemangioma," *Arteriosclerosis, Thrombosis, and Vascular Biology,* vol. 27, no. 12, pp. 2664-2670, December 1, 2007 2007.

[66] F. I. J. Drolet Ba, "Characteristics of infantile hemangiomas as clues to pathogenesis: Does hypoxia connect the dots?," *Archives of Dermatology,* vol. 146, no. 11, pp. 1295-1299, 2010.

[67] C. G. Bauland, M. A. M. van Steensel, P. M. Steijlen, P. N. M. A. Rieu, and P. H. M. Spauwen, "The Pathogenesis of Hemangiomas: A Review," *Plastic and Reconstructive Surgery,* vol. 117, no. 2, pp. 29e-35e 10.1097/01.prs.0000197134.72984.cb, 2006.

[68] A. N. Haggstrom *et al.*, "Prospective Study of Infantile Hemangiomas: Clinical Characteristics Predicting Complications and Treatment," *Pediatrics,* vol. 118, no. 3, pp. 882-887, September 2006 2006.

[69] T. Binzoni, A. Vogel, A. H. Gandjbakhche, and R. Marchesini, "Detection limits of multi-spectral optical imaging under the skin surface," *Physics in Medicine and Biology,* vol. 53, no. 3, p. 617, 2008.

[70] J. J. Dixon, D. James, P. J. Fleming, and C. T. C. Kennedy, "A novel method for estimating the volume of capillary haemangioma to determine response to treatment," *Clinical and Experimental Dermatology,* vol. 22, no. 1, pp. 20-22, 1997.

[71] A. N. Haggstrom, J. L. Beaumont, J. Lai, and et al., "Measuring the severity of infantile hemangiomas: Instrument development and reliability," *Archives of Dermatology,* vol. 148, no. 2, pp. 197-202, 2012.

[72] P. A. McGrath, C. E. Seifert, K. N. Speechley, J. C. Booth, L. Stitt, and M. C. Gibson, "A new analogue scale for assessing children's pain: an initial validation study," (in eng), *Pain,* vol. 64, no. 3, pp. 435-43, Mar 1996.

[73] M. M. Tollefson and I. J. Frieden, "Early Growth of Infantile Hemangiomas: What Parents' Photographs Tell Us," *Pediatrics,* vol. 130, no. 2, pp. e314-e320, August 1, 2012 2012.

[74] M. M. Tollefson and I. J. Frieden, "Early growth of infantile hemangiomas: what parents' photographs tell us," (in eng), *Pediatrics,* vol. 130, no. 2, pp. e314-20, Aug 2012.

[75] M. W. Tsang, M. C. Garzon, and I. J. Frieden, "How to Measure a Growing Hemangioma and Assess Response to Therapy," *Pediatric Dermatology,* vol. 23, no. 2, pp. 187-190, 2006.

[76] A. L. Bruckner and I. J. Frieden, "Hemangiomas of infancy," *Journal of the American Academy of Dermatology,* vol. 48, no. 4, pp. 477-496, 4// 2003.

[77] L. C. Chang *et al.*, "Growth Characteristics of Infantile Hemangiomas: Implications for Management," *Pediatrics,* vol. 122, no. 2, pp. 360-367, August 2008 2008.

[78] I. J. Frieden, "Infantile Hemangioma Research: Looking Backward and Forward," *J Invest Dermatol,* vol. 131, no. 12, pp. 2345-2348, 2011.

[79] C. Lauren and M. C. Garzon, "Treatment of Infantile Hemangiomas," (in English), *Pediatric Annals,* vol. 41, no. 8, pp. 1-7, 2012.

[80] B. A. Drolet *et al.*, "Prospective Study of Spinal Anomalies in Children with Infantile Hemangiomas of the Lumbosacral Skin," *The Journal of Pediatrics,* vol. 157, no. 5, pp. 789-794, 11// 2010.

[81] F. Thoumazet, C. Léauté-Labrèze, J. Colin, and B. Mortemousque, "Efficacy of systemic propranolol for severe infantile haemangioma of the orbit and eyelid: a case study of eight patients," *British Journal of Ophthalmology,* vol. 96, no. 3, pp. 370-374, March 1, 2012 2012.

[82] H. Moukaddam, J. Pollak, and A. Haims, "MRI characteristics and classification of peripheral vascular malformations and tumors," (in English), *Skeletal Radiology,* vol. 38, no. 6, pp. 535-547, 2009/06/01 2009.

[83] G. Gorincour, V. Kokta, F. Rypens, L. Garel, J. Powell, and J. Dubois, "Imaging characteristics of two subtypes of congenital hemangiomas: rapidly involuting congenital hemangiomas and non-

involuting congenital hemangiomas," (in English), *Pediatric Radiology,* vol. 35, no. 12, pp. 1178-1185, 2005/12/01 2005.

[84] J. A. Mohammed, A. Balma-Mena, A. Chakkittakandiyil, F. Matea, and E. Pope, "Infrared thermography to assess proliferation and involution of infantile hemangiomas: a prospective cohort study," (in eng), *JAMA Dermatol,* vol. 150, no. 9, pp. 964-9, Sep 2014.

[85] K. König *et al.*, "Clinical optical coherence tomography combined with multiphoton tomography of patients with skin diseases," *Journal of Biophotonics,* vol. 2, no. 6-7, pp. 389-397, 2009.

[86] I. Kuzmina, I. Diebele, J. Spigulis, L. Valeine, A. Berzina, and A. Abelite, "Contact and contactless diffuse reflectance spectroscopy: potential for recovery monitoring of vascular lesions after intense pulsed light treatment," *Journal of Biomedical Optics,* vol. 16, no. 4, pp. 040505-040505, 2011.

[87] A. Kokolakis *et al.*, "Prehistological evaluation of benign and malignant pigmented skin lesions with optical computed tomography," *Journal of Biomedical Optics,* vol. 17, no. 6, pp. 066004-1, 2012.

[88] I. Kuzmina *et al.*, "Towards noncontact skin melanoma selection by multispectral imaging analysis," *Journal of Biomedical Optics,* vol. 16, no. 6, pp. 060502-060502, 2011.

[89] M. Sury, "Brain monitoring in children," (in eng), *Anesthesiol Clin,* vol. 32, no. 1, pp. 115-32, Mar 2014.

[90] M. Ferrari and V. Quaresima, "A brief review on the history of human functional near-infrared spectroscopy (fNIRS) development and fields of application," (in eng), *Neuroimage,* vol. 63, no. 2, pp. 921-35, Nov 01 2012.

[91] R. Salonia, M. J. Bell, P. M. Kochanek, and R. P. Berger, "The utility of near infrared spectroscopy in detecting intracranial hemorrhage in children," (in eng), *J Neurotrauma,* vol. 29, no. 6, pp. 1047-53, Apr 10 2012.

[92] J. C. Hebden, "Advances in optical imaging of the newborn infant brain," (in eng), *Psychophysiology,* vol. 40, no. 4, pp. 501-10, Jul 2003.

[93] L. Lim *et al.*, "Clinical study of noninvasive in vivo melanoma and nonmelanoma skin cancers using multimodal spectral diagnosis," (in eng), *J Biomed Opt,* vol. 19, no. 11, p. 117003, 2014.

[94] I. Kuzmina, I. Diebele, J. Spigulis, L. Valeine, A. Berzina, and A. Abelite, "Contact and contactless diffuse reflectance spectroscopy: potential for recovery monitoring of vascular lesions after intense pulsed light treatment," (in eng), *J Biomed Opt,* vol. 16, no. 4, p. 040505, Apr 2011.

[95] S. H. Tseng, P. Bargo, A. Durkin, and N. Kollias, "Chromophore concentrations, absorption and scattering properties of human skin in-vivo," (in eng), *Opt Express,* vol. 17, no. 17, pp. 14599-617, Aug 17 2009.

[96] R. B. Saager, D. J. Cuccia, S. Saggese, K. M. Kelly, and A. J. Durkin, "A light emitting diode (LED) based spatial frequency domain imaging system for optimization of photodynamic therapy of nonmelanoma skin cancer: quantitative reflectance imaging," (in eng), *Lasers Surg Med,* vol. 45, no. 4, pp. 207-15, Apr 2013.

[97] C. A. Patil, H. Kirshnamoorthi, D. L. Ellis, T. G. van Leeuwen, and A. Mahadevan-Jansen, "A clinical instrument for combined raman spectroscopy-optical coherence tomography of skin cancers," (in eng), *Lasers Surg Med,* vol. 43, no. 2, pp. 143-51, Feb 2011.

[98] C. R. Simpson, M. Kohl, M. Essenpreis, and M. Cope, "Near-infrared optical properties of ex vivo human skin and subcutaneous tissues measured using the Monte Carlo inversion technique," (in eng), *Phys Med Biol,* vol. 43, no. 9, pp. 2465-78, Sep 1998.

[99] M. Sharma, E. Marple, J. Reichenberg, and J. W. Tunnell, "Design and characterization of a novel multimodal fiber-optic probe and spectroscopy system for skin cancer applications," (in eng), *Rev Sci Instrum,* vol. 85, no. 8, p. 083101, Aug 2014.

[100] D. H. Darrow *et al.*, "Diagnosis and Management of Infantile Hemangioma," *Pediatrics,* vol. 136, no. 4, pp. e1060-e1104, 2015-10-01 00:00:00 2015.

[101] A. Li, J. Liu, W. Tanamai, R. Kwong, A. E. Cerussi, and B. J. Tromberg, "Assessing the spatial extent of breast tumor intrinsic optical contrast using ultrasound and diffuse optical spectroscopy," *Journal of Biomedical Optics,* vol. 13, no. 3, pp. 030504-030504-3, 2008.

[102] Q. Zhu, T. Durduran, V. Ntziachristos, M. Holboke, and A. G. Yodh, "Imager that combines near-infrared diffusive light and ultrasound," *Optics Letters,* vol. 24, no. 15, pp. 1050-1052, 1999/08/01 1999.

[103] Q. Zhu, N. Chen, and S. H. Kurtzman, "Imaging tumor angiogenesis by use of combined near-infrared diffusive light and ultrasound," *Optics Letters,* vol. 28, no. 5, pp. 337-339, 2003/03/01 2003.

[104] M. Lualdi, A. Colombo, M. Carrara, L. Scienza, S. Tomatis, and R. Marchesini, "Optical devices used for image analysis of pigmented skin lesions: a proposal for quality assurance protocol using tissue-like phantoms," *Physics in Medicine and Biology,* vol. 51, no. 23, p. N429, 2006.

[105] P. Urso, M. Lualdi, A. Colombo, M. Carrara, S. Tomatis, and R. Marchesini, "Skin and cutaneous melanocytic lesion simulation in biomedical optics with multilayered phantoms," *Physics in Medicine and Biology,* vol. 52, no. 10, p. N229, 2007.

[106] S. Del Bianco *et al.*, "Liquid phantom for investigating light propagation through layered diffusive media," *Optics Express,* vol. 12, no. 10, pp. 2102-2111, 2004/05/17 2004.

[107] S.-H. Tseng, C. K. Hayakawa, J. Spanier, and A. J. Durkin, "Determination of Optical Properties of Superficial Volumes of Layered Tissue Phantoms," *IEEE transactions on bio-medical engineering,* vol. 55, no. 1, pp. 335-339, 2008.

[108] M. Lualdi, A. Colombo, A. Mari, S. Tomatis, and R. Marchesini, "Development of simulated pigmented lesions in an optical skin-tissue phantom: Experimental measurements in the visible and near infrared," *Journal of Laser Applications,* vol. 14, no. 2, pp. 122-127, 2002.

[109] S. D. Bianco *et al.*, "Liquid phantom for investigating light propagation through layered diffusive media," *Optics Express,* vol. 12, no. 10, pp. 2102-2111, 2004/05/17 2004.

[110] Q. Zhu *et al.*, "Ultrasound-Guided Optical Tomographic Imaging of Malignant and Benign Breast Lesions: Initial Clinical Results of 19 Cases," *Neoplasia,* vol. 5, no. 5, pp. 379-388, 9// 2003.

[111] S. C. Kanick *et al.*, "Integration of single-fiber reflectance spectroscopy into ultrasound-guided endoscopic lung cancer staging of mediastinal lymph nodes," *Journal of Biomedical Optics,* vol. 15, no. 1, pp. 017004-017004-8, 2010.

[112] M. Guven, B. Yazici, X. Intes, and B. Chance, "Diffuse optical tomography with a priori anatomical information," (in eng), *Phys Med Biol,* vol. 50, no. 12, pp. 2837-58, Jun 21 2005.

[113] C. R. Stevens, D. R. Blake, P. Merry, P. A. Revell, and J. R. Levick, "A comparative study by morphometry of the microvasculature in normal and rheumatoid synovium," (in eng), *Arthritis Rheum,* vol. 34, no. 12, pp. 1508-13, Dec 1991.

[114] P. C. Taylor and B. Sivakumar, "Hypoxia and angiogenesis in rheumatoid arthritis," (in eng), *Curr Opin Rheumatol,* vol. 17, no. 3, pp. 293-8, May 2005.

[115] D. L. Scott, F. Wolfe, and T. W. J. Huizinga, "Rheumatoid arthritis," *The Lancet,* vol. 376, no. 9746, pp. 1094-1108.

[116] T. Pincus, "The underestimated long term medical and economic consequences of rheumatoid arthritis," (in eng), *Drugs,* vol. 50 Suppl 1, pp. 1-14, 1995.

[117] N. J. Cooper, "Economic burden of rheumatoid arthritis: a systematic review," (in eng), *Rheumatology (Oxford),* vol. 39, no. 1, pp. 28-33, Jan 2000.

[118] E. D. Harris, Jr., "Rheumatoid arthritis. Pathophysiology and implications for therapy," (in eng), *N Engl J Med,* vol. 322, no. 18, pp. 1277-89, May 03 1990.

[119] C. G. Helmick *et al.*, "Estimates of the prevalence of arthritis and other rheumatic conditions in the United States. Part I," (in eng), *Arthritis Rheum,* vol. 58, no. 1, pp. 15-25, Jan 2008.

[120] V. Morris, "Primer on the Rheumatic Diseases, 12th edn. Edited by J. H. Klippel with associate editors L. L. Crawford, J. H. Stone and C. M. Weyland. £49.24. Arthritis Foundation, Atlanta, GA, USA, 2001. 700 pages. ISBN 0-91-242329-3," *Rheumatology,* vol. 41, no. 6, p. 715, June 1, 2002 2002.

[121] V. Majithia and S. A. Geraci, "Rheumatoid arthritis: diagnosis and management," (in eng), *Am J Med,* vol. 120, no. 11, pp. 936-9, Nov 2007.

[122] O. Steinbrocker, C. H. Traeger, and R. C. Batterman, "Therapeutic criteria in rheumatoid arthritis," (in eng), *J Am Med Assoc,* vol. 140, no. 8, pp. 659-62, Jun 25 1949.

[123] F. A. Cooles and J. D. Isaacs, "Pathophysiology of rheumatoid arthritis," (in eng), *Curr Opin Rheumatol,* vol. 23, no. 3, pp. 233-40, May 2011.

[124] H. D. El-Gabalawy and P. E. Lipsky, "Why do we not have a cure for rheumatoid arthritis?," *Arthritis Research & Therapy,* journal article vol. 4, no. 3, p. S297, 2002.

[125] L. B. van de Putte and P. L. van Riel, "Rheumatoid arthritis--changing theories and treatment modalities," (in eng), *Acta Orthop Scand Suppl,* vol. 266, pp. 10-3, Oct 1995.

[126] J. T. Sharp *et al.*, "How many joints in the hands and wrists should be included in a score of radiologic abnormalities used to assess rheumatoid arthritis?," (in eng), *Arthritis Rheum,* vol. 28, no. 12, pp. 1326-35, Dec 1985.

[127] D. van der Heijde, "How to read radiographs according to the Sharp/van der Heijde method," (in eng), *J Rheumatol,* vol. 27, no. 1, pp. 261-3, Jan 2000.

[128] M. Backhaus *et al.*, "Arthritis of the finger joints: a comprehensive approach comparing conventional radiography, scintigraphy, ultrasound, and contrast-enhanced magnetic resonance imaging," (in eng), *Arthritis Rheum,* vol. 42, no. 6, pp. 1232-45, Jun 1999.

[129] A. L. Tan, R. J. Wakefield, P. G. Conaghan, P. Emery, and D. McGonagle, "Imaging of the musculoskeletal system: magnetic resonance imaging, ultrasonography and computed tomography," (in eng), *Best Pract Res Clin Rheumatol,* vol. 17, no. 3, pp. 513-28, Jun 2003.

[130] M. Ostergaard, M. Stoltenberg, P. Lovgreen-Nielsen, B. Volck, C. H. Jensen, and I. Lorenzen, "Magnetic resonance imaging-determined synovial membrane and joint effusion volumes in rheumatoid arthritis and osteoarthritis: comparison with the macroscopic and microscopic appearance of the synovium," (in eng), *Arthritis Rheum,* vol. 40, no. 10, pp. 1856-67, Oct 1997.

[131] F. M. McQueen, "Magnetic resonance imaging in early inflammatory arthritis: what is its role?," *Rheumatology,* vol. 39, no. 7, pp. 700-706, July 1, 2000 2000.

[132] C. Schirmer *et al.*, "Diagnostic quality and scoring of synovitis, tenosynovitis and erosions in low-field MRI of patients with rheumatoid arthritis: a comparison with conventional MRI," (in eng), *Ann Rheum Dis,* vol. 66, no. 4, pp. 522-9, Apr 2007.

[133] L. Terslev *et al.*, "Doppler ultrasound and magnetic resonance imaging of synovial inflammation of the hand in rheumatoid arthritis: A comparative study," *Arthritis & Rheumatism,* vol. 48, no. 9, pp. 2434-2441, 2003.

[134] P. J. Lund, A. Heikal, M. J. Maricic, E. A. Krupinski, and C. S. Williams, "Ultrasonographic imaging of the hand and wrist in rheumatoid arthritis," (in eng), *Skeletal Radiol,* vol. 24, no. 8, pp. 591-6, Nov 1995.

[135] M. Hau *et al.*, "Evaluation of pannus and vascularization of the metacarpophalangeal and proximal interphalangeal joints in rheumatoid arthritis by high-resolution ultrasound (multidimensional linear array)," (in eng), *Arthritis Rheum,* vol. 42, no. 11, pp. 2303-8, Nov 1999.

[136] M. Szkudlarek, M. Court-Payen, S. Jacobsen, M. Klarlund, H. S. Thomsen, and M. Ostergaard, "Interobserver agreement in ultrasonography of the finger and toe joints in rheumatoid arthritis," (in eng), *Arthritis Rheum,* vol. 48, no. 4, pp. 955-62, Apr 2003.

[137] D. Aletaha and J. Smolen, "The Simplified Disease Activity Index (SDAI) and the Clinical Disease Activity Index (CDAI): a review of their usefulness and validity in rheumatoid arthritis," (in eng), *Clin Exp Rheumatol,* vol. 23, no. 5 Suppl 39, pp. S100-8, Sep-Oct 2005.

[138] J. F. Fries, P. Spitz, R. G. Kraines, and H. R. Holman, "Measurement of patient outcome in arthritis," (in eng), *Arthritis Rheum,* vol. 23, no. 2, pp. 137-45, Feb 1980.

[139] J. E. Ware, Jr., S. D. Keller, H. T. Hatoum, and S. X. Kong, "The SF-36 Arthritis-Specific Health Index (ASHI): I. Development and cross-validation of scoring algorithms," (in eng), *Med Care,* vol. 37, no. 5 Suppl, pp. Ms40-50, May 1999.

[140] V. Prapavat, R. Schuetz, W. Runge, J. Beuthan, and G. J. Mueller, "Evaluation of scattered light distributions of cw-transillumination for functional diagnostic of rheumatic disorders in interphalangeal joints," 1995, vol. 2626, pp. 121-129.

[141] V. Prapavat, W. Runge, J. Mans, A. Krause, J. Beuthan, and G. Muller, "[The development of a finger joint phantom for the optical simulation of early inflammatory rheumatic changes]," (in ger), *Biomed Tech (Berl),* vol. 42, no. 11, pp. 319-26, Nov 1997. Entwicklung eines Fingergelenkphantoms zur optischen Simulation fruher entzundlich-rheumatischer Veranderungen.

[142] V. Prapavat, J. Mans, R. Schuetz, G. Regling, J. Beuthan, and G. J. Mueller, "In-vivo investigations on the detection of chronical polyarthritis (c.P.) using a cw-transillumination method at interphalangeal joints," 1995, vol. 2626, pp. 360-366.

[143] L. D. Montejo *et al.*, "Comparison of Classification Methods for Detection of Rheumatoid Arthritis with Optical Tomography," in *Biomedical Optics and 3-D Imaging*, Miami, Florida, 2010, p. BWF2: Optical Society of America.

[144] C. D. Klose, A. D. Klose, U. Netz, J. Beuthan, and A. H. Hielscher, "Multiparameter classifications of optical tomographic images," (in eng), *J Biomed Opt,* vol. 13, no. 5, p. 050503, Sep-Oct 2008.

[145] A. H. Hielscher *et al.*, "Frequency-Domain Optical Tomography of Arthritic Joints," in *Biomedical Optics and 3-D Imaging*, Miami, Florida, 2010, p. BSuD87: Optical Society of America.

[146] U. J. Netz, J. Beuthan, and A. H. Hielscher, "Multipixel system for gigahertz frequency-domain optical imaging of finger joints," *Review of Scientific Instruments,* vol. 79, no. 3, pp. -, 2008.

[147] S. G. Werner *et al.*, "Inflammation assessment in patients with arthritis using a novel in vivo fluorescence optical imaging technology," (in eng), *Ann Rheum Dis,* vol. 71, no. 4, pp. 504-10, Apr 2012.

[148] W. T. Chen, U. Mahmood, R. Weissleder, and C. H. Tung, "Arthritis imaging using a near-infrared fluorescence folate-targeted probe," (in eng), *Arthritis Res Ther,* vol. 7, no. 2, pp. R310-7, 2005.

[149] T. Fischer *et al.*, "Detection of rheumatoid arthritis using non-specific contrast enhanced fluorescence imaging," (in eng), *Acad Radiol,* vol. 17, no. 3, pp. 375-81, Mar 2010.

[150] A. K. Scheel *et al.*, "First clinical evaluation of sagittal laser optical tomography for detection of synovitis in arthritic finger joints," (in eng), *Ann Rheum Dis,* vol. 64, no. 2, pp. 239-45, Feb 2005.

[151] J. M. Lasker, C. J. Fong, D. T. Ginat, E. Dwyer, and A. H. Hielscher, "Dynamic optical imaging of vascular and metabolic reactivity in rheumatoid joints," *Journal of Biomedical Optics,* vol. 12, no. 5, pp. 052001-052001-13, 2007.

[152] J. B. Fishkin, E. Gratton, M. J. vandeVen, and W. W. Mantulin, "Diffusion of intensity-modulated near-infrared light in turbid media," 1991, vol. 1431, pp. 122-135.

[153] K. Hyun Keol and H. H. Andreas, "A PDE-constrained SQP algorithm for optical tomography based on the frequency-domain equation of radiative transfer," *Inverse Problems,* vol. 25, no. 1, p. 015010, 2009.

[154] H. K. Kim and A. Charette, "A sensitivity function-based conjugate gradient method for optical tomography with the frequency-domain equation of radiative transfer," *Journal of Quantitative Spectroscopy and Radiative Transfer,* vol. 104, no. 1, pp. 24-39, 3// 2007.

[155] K. Ren, G. Bal, and A. H. Hielscher, "Frequency Domain Optical Tomography Based on the Equation of Radiative Transfer," *SIAM Journal on Scientific Computing,* vol. 28, no. 4, pp. 1463-1489, 2006.

[156] A. D. Klose, U. Netz, J. Beuthan, and A. H. Hielscher, "Optical tomography using the time-independent equation of radiative transfer — Part 1: forward model," *Journal of Quantitative Spectroscopy and Radiative Transfer,* vol. 72, no. 5, pp. 691-713, 3/1/ 2002.

[157] B. E. van den Borne, B. A. Dijkmans, H. H. de Rooij, S. le Cessie, and C. L. Verweij, "Chloroquine and hydroxychloroquine equally affect tumor necrosis factor-alpha, interleukin 6, and interferon-gamma production by peripheral blood mononuclear cells," (in eng), *The Journal of rheumatology,* vol. 24, no. 1, pp. 55-60, 1997/01// 1997.

[158] D. Van Der Heijde, P. Van Riel, F. Gribnau, I. Nuver-Zwart, and L. Van De Putte, "EFFECTS OF HYDROXYCHLOROQUINE AND SULPHASALAZINE ON PROGRESSION OF JOINT DAMAGE IN RHEUMATOID ARTHRITIS," *The Lancet,* vol. 333, no. 8646, pp. 1036-1038, 1989/05/13 1989.

[159] M. A. J. van Rossum *et al.*, "Sulfasalazine in the treatment of juvenile chronic arthritis: A randomized, double-blind, placebo-controlled, multicenter study," *Arthritis & Rheumatism,* vol. 41, no. 5, pp. 808-816, 1998.

[160] R. F. van Vollenhoven *et al.*, "Addition of infliximab compared with addition of sulfasalazine and hydroxychloroquine to methotrexate in patients with early rheumatoid arthritis (Swefot trial): 1-year results of a randomised trial," *The Lancet,* vol. 374, no. 9688, pp. 459-466, //.

[161] J. R. O'Dell, "TRIPLE THERAPY WITH METHOTREXATE, SULFASALAZINE, AND HYDROXYCHLOROQUINE IN PATIENTS WITH RHEUMATOID ARTHRITIS," *Rheumatic Disease Clinics of North America,* vol. 24, no. 3, pp. 465-477, 8/1/ 1998.

[162] J. R. O'Dell *et al.*, "Treatment of Rheumatoid Arthritis with Methotrexate Alone, Sulfasalazine and Hydroxychloroquine, or a Combination of All Three Medications," *New England Journal of Medicine,* vol. 334, no. 20, pp. 1287-1291, 1996.

[163] L. Montejo, "Computational Methods For The Diagnosis of Rheumatoid Arthritis With Diffuse Optical Tomography," Ph.D., Biomedical Engineering, Columbia University, 2014.

[164] J. Jia, "Fast Radiative-Transfer-Equation-Based Image Reconstruction Algorithms for Non-Contact Diffuse Optical Tomography Systems," Biomedical Engineering, Columbia Unversity, Columbia University Academic Commons, 2015.

[165] L. D. Montejo, A. D. Klose, and A. H. Hielscher, "Implementation of the equation of radiative transfer on block-structured grids for modeling light propagation in tissue," (in eng), *Biomed Opt Express,* vol. 1, no. 3, pp. 861-878, Sep 14 2010.

[166] E. M. Paleolog, "Angiogenesis in rheumatoid arthritis," *Arthritis Research & Therapy,* vol. 4, no. 3, p. S81, 2002// 2002.

[167] J. Fukae *et al.*, "Change of synovial vascularity in a single finger joint assessed by power doppler sonography correlated with radiographic change in rheumatoid arthritis: Comparative study of a novel quantitative score with a semiquantitative score," *Arthritis Care & Research,* vol. 62, no. 5, pp. 657-663, 2010.

[168] J. Fukae *et al.*, "Positive synovial vascularity in patients with low disease activity indicates smouldering inflammation leading to joint damage in rheumatoid arthritis: time-integrated joint inflammation estimated by synovial vascularity in each finger joint," (in eng), *Rheumatology (Oxford),* vol. 52, no. 3, pp. 523-8, Mar 2013.

[169] M. A. Khalil *et al.*, "Detection of Peripheral Arterial Disease Within the Foot Using Vascular Optical Tomographic Imaging: A Clinical Pilot Study," (in eng), *Eur J Vasc Endovasc Surg,* vol. 49, no. 1, pp. 83-9, Jan 2015.

[170] M. A. Khalil *et al.*, "Dynamic diffuse optical tomography imaging of peripheral arterial disease," (in eng), *Biomed Opt Express,* vol. 3, no. 9, pp. 2288-98, Sep 01 2012.

[171] M. L. Flexman *et al.*, "Digital optical tomography system for dynamic breast imaging," (in eng), *J Biomed Opt,* vol. 16, no. 7, p. 076014, Jul 2011.

[172] G. J. Hankey, P. E. Norman, and J. W. Eikelboom, "Medical treatment of peripheral arterial disease," *JAMA,* vol. 295, no. 5, pp. 547-553, 2006.

[173] M. H. Criqui and V. Aboyans, "Epidemiology of Peripheral Artery Disease," *Circulation Research,* 10.1161/CIRCRESAHA.116.303849 vol. 116, no. 9, p. 1509, 2015.

[174] A. T. Hirsch, M. H. Criqui, D. Treat-Jacobson, and et al., "PEripheral arterial disease detection, awareness, and treatment in primary care," *JAMA,* vol. 286, no. 11, pp. 1317-1324, 2001.

[175] W. R. Hiatt, "Medical Treatment of Peripheral Arterial Disease and Claudication," *New England Journal of Medicine,* vol. 344, no. 21, pp. 1608-1621, 2001.

[176] F. G. R. Fowkes *et al.*, "Comparison of global estimates of prevalence and risk factors for peripheral artery disease in 2000 and 2010: a systematic review and analysis," *The Lancet,* vol. 382, no. 9901, pp. 1329-1340.

[177] L. Norgren, W. R. Hiatt, J. A. Dormandy, M. R. Nehler, K. A. Harris, and F. G. R. Fowkes, "Inter-Society Consensus for the Management of Peripheral Arterial Disease (TASC II)," *Journal of Vascular Surgery,* vol. 45, no. 1, pp. S5-S67.

[178] S. P. Glasser, "On arterial physiology, pathophysiology of vascular compliance, and cardiovascular disease," (in eng), *Heart Dis,* vol. 2, no. 5, pp. 375-9, Sep-Oct 2000.

[179] L. Norgren, W. R. Hiatt, J. A. Dormandy, M. R. Nehler, K. A. Harris, and F. G. Fowkes, "Inter-Society Consensus for the Management of Peripheral Arterial Disease (TASC II)," (in eng), *J Vasc Surg,* vol. 45 Suppl S, pp. S5-67, Jan 2007.

[180] E. B. Jude, I. Eleftheriadou, and N. Tentolouris, "Peripheral arterial disease in diabetes—a review," *Diabetic Medicine,* vol. 27, no. 1, pp. 4-14, 2010.

[181] A. Humeau-Heurtier, E. Guerreschi, P. Abraham, and G. Mahé, "Relevance of Laser Doppler and Laser Speckle Techniques for Assessing Vascular Function: State of the Art and Future Trends," *IEEE Transactions on Biomedical Engineering,* vol. 60, no. 3, pp. 659-666, 2013.

[182] M. Al-Qaisi, D. M. Nott, D. H. King, and M. Hamady, "Imaging of peripheral vascular disease," *Reports in Imaging,* pp. 1-10, // 2009.

[183] M. J. W. Koelemay, D. Den Hartog, M. H. Prins, J. G. Kromhout, D. A. Legemate, and M. J. H. M. Jacobs, "Diagnosis of arterial disease of the lower extremities with duplex ultrasonography," *British Journal of Surgery,* vol. 83, no. 3, pp. 404-409, 1996.

[184] A. Krnic, N. Vucic, and Z. Sucic, "Duplex scanning compared with intra-arterial angiography in diagnosing peripheral arterial disease: three analytical approaches," (in eng), *Vasa,* vol. 35, no. 2, pp. 86-91, May 2006.

[185] J. A. Lawrence, D. Kim, K. C. Kent, M. K. Stehling, M. P. Rosen, and V. Raptopoulos, "Lower extremity spiral CT angiography versus catheter angiography," *Radiology,* vol. 194, no. 3, pp. 903-908, 1995/03/01 1995.

[186] G. Yu, Y. Shang, Y. Zhao, R. Cheng, L. Dong, and S. P. Saha, "Intraoperative evaluation of revascularization effect on ischemic muscle hemodynamics using near-infrared diffuse optical spectroscopies," *Journal of Biomedical Optics,* vol. 16, no. 2, pp. 027004-027004-11, 2011.

[187] S. M. Toomay and B. L. Dolmatch, "CT Angiography of Lower Extremity Vascular Bypass Grafts," *Techniques in Vascular and Interventional Radiology,* vol. 9, no. 4, pp. 172-179, 12// 2006.

[188] R. P. E. Boezeman, J. C. Kelder, F. G. J. Waanders, and J. P. P. M. de Vries, "Continuous Surveillance of Lower Limb Perfusion During Aortic Surgery With Near-Infrared Spectroscopy: A Pilot Study," *Vascular and Endovascular Surgery,* vol. 45, no. 5, pp. 407-411, July 1, 2011 2011.

[189] D. Perry, M. Bharara, D. G. Armstrong, and J. Mills, "Intraoperative Fluorescence Vascular Angiography: During Tibial Bypass," *Journal of Diabetes Science and Technology,* vol. 6, no. 1, pp. 204-208, January 1, 2012 2012.

[190] C. Casavola, L. A. Paunescu, S. Fantini, M. A. Franceschini, P. M. Lugarà, and E. Gratton, "Application of near-infrared tissue oxymetry to the diagnosis of peripheral vascular disease," *Clinical Hemorheology and Microcirculation,* vol. 21, no. 3, pp. 389-393, 01/01/ 1999.

[191] J. W. Hoi, H. Kim, and A. H. Hielscher, "A Non-Contact Fiber-Less Diffuse Optical Tomographic System for Dynamic Imaging of the Feet with Peripheral Artery Disease," in *Biomedical Optics 2016*, Fort Lauderdale, Florida, 2016, p. JW3A.15: Optical Society of America.

[192] A. Marone *et al.*, "Effects of Posture and Heart Rate Changes on Optical Tomographic Imaging of the Peripheral Arteries," in *Biomedical Optics 2016*, Fort Lauderdale, Florida, 2016, p. OTh2C.5: Optical Society of America.

[193] J. W. Hoi *et al.*, "Non-contact continuous-wave diffuse optical tomographic system to capture vascular dynamics in the foot," 2015, vol. 9313, pp. 931312-931312-5.

[194] M. A. Khalil *et al.*, "Detection of Peripheral Arterial Disease Within the Foot Using Vascular Optical Tomographic Imaging: A Clinical Pilot Study," *European Journal of Vascular and Endovascular Surgery,* vol. 49, no. 1, pp. 83-89, 1// 2015.

[195] M. A. Khalil *et al.*, "Dynamic diffuse optical tomography imaging of peripheral arterial disease," *Biomedical Optics Express,* vol. 3, no. 9, pp. 2288-2298, 2012/09/01 2012.

[196] W. B. Baker, A. B. Parthasarathy, D. R. Busch, R. C. Mesquita, J. H. Greenberg, and A. G. Yodh, "Modified Beer-Lambert law for blood flow," (in eng), *Biomed Opt Express,* vol. 5, no. 11, pp. 4053-75, Nov 01 2014.

[197] T. Durduran, R. Choe, W. B. Baker, and A. G. Yodh, "Diffuse Optics for Tissue Monitoring and Tomography," (in eng), *Rep Prog Phys,* vol. 73, no. 7, Jul 2010.

[198] L. Kocsis, P. Herman, and A. Eke, "The modified Beer-Lambert law revisited," (in eng), *Phys Med Biol,* vol. 51, no. 5, pp. N91-8, Mar 07 2006.

[199] H. Obrig and A. Villringer, "Beyond the visible--imaging the human brain with light," (in eng), *J Cereb Blood Flow Metab,* vol. 23, no. 1, pp. 1-18, Jan 2003.

[200] G. I. Taylor and W. R. Pan, "Angiosomes of the leg: anatomic study and clinical implications," (in eng), *Plast Reconstr Surg,* vol. 102, no. 3, pp. 599-616; discussion 617-8, Sep 1998.

[201] G. I. Taylor and J. H. Palmer, "The vascular territories (angiosomes) of the body: experimental study and clinical applications," (in eng), *Br J Plast Surg,* vol. 40, no. 2, pp. 113-41, Mar 1987.

[202] J. F. Daniel Brandão, Armando Mansilha and António Guedes Vaz, "Below the Knee Techniques: Now and Then, Angioplasty, Various Techniques and Challenges in Treatment of Congenital and Acquired Vascular Stenoses," in *InTech*, D. T. F. (Ed.), Ed., 2012.

[203] V. Alexandrescu *et al.*, "A reliable approach to diabetic neuroischemic foot wounds: below-the-knee angiosome-oriented angioplasty," (in eng), *J Endovasc Ther,* vol. 18, no. 3, pp. 376-87, Jun 2011.

[204] R. F. Neville, C. E. Attinger, E. J. Bulan, I. Ducic, M. Thomassen, and A. N. Sidawy, "Revascularization of a specific angiosome for limb salvage: does the target artery matter?," (in eng), *Ann Vasc Surg,* vol. 23, no. 3, pp. 367-73, May-Jun 2009.

[205] V.-A. Alexandrescu *et al.*, "Selective Primary Angioplasty following an Angiosome Model of Reperfusion in the Treatment of Wagner 1–4 Diabetic Foot Lesions: Practice in a Multidisciplinary Diabetic Limb Service," *Journal of Endovascular Therapy,* vol. 15, no. 5, pp. 580-593, 2008/10/01 2008.

[206] C. E. Attinger, K. K. Evans, E. Bulan, P. Blume, and P. Cooper, "Angiosomes of the foot and ankle and clinical implications for limb salvage: reconstruction, incisions, and revascularization," (in eng), *Plast Reconstr Surg,* vol. 117, no. 7 Suppl, pp. 261s-293s, Jun 2006.

[207] T. Nagase *et al.*, "Variations of plantar thermographic patterns in normal controls and non-ulcer diabetic patients: Novel classification using angiosome concept," *Journal of Plastic, Reconstructive & Aesthetic Surgery,* vol. 64, no. 7, pp. 860-866, 7// 2011.

[208] O. Iida *et al.*, "Importance of the angiosome concept for endovascular therapy in patients with critical limb ischemia," *Catheterization and Cardiovascular Interventions,* vol. 75, no. 6, pp. 830-836, 2010.

[209] N. Azuma, H. Uchida, T. Kokubo, A. Koya, N. Akasaka, and T. Sasajima, "Factors Influencing Wound Healing of Critical Ischaemic Foot after Bypass Surgery: Is the Angiosome Important in Selecting Bypass Target Artery?," *European Journal of Vascular and Endovascular Surgery,* vol. 43, no. 3, pp. 322-328, 3// 2012.

[210] C. E. Attinger, K. K. Evans, E. Bulan, P. Blume, and P. Cooper, "Angiosomes of the Foot and Ankle and Clinical Implications for Limb Salvage: Reconstruction, Incisions, and Revascularization," *Plastic and Reconstructive Surgery,* vol. 117, no. 7S, pp. 261S-293S, 2006.

[211] V. Alexandrescu and G. Hubermont, "The challenging topic of diabetic foot revascularization: does the angiosome-guided angioplasty may improve outcome," (in eng), *The Journal of cardiovascular surgery,* vol. 53, no. 1, pp. 3-12, 2012/02// 2012.

[212] C. Casavola, L. A. Paunescu, S. Fantini, M. A. Franceschini, P. M. Lugara, and E. Gratton, "Application of near-infrared tissue oxymetry to the diagnosis of peripheral vascular disease," (in eng), *Clin Hemorheol Microcirc,* vol. 21, no. 3-4, pp. 389-93, 1999.

[213] G. Yu, Y. Shang, Y. Zhao, R. Cheng, L. Dong, and S. P. Saha, "Intraoperative evaluation of revascularization effect on ischemic muscle hemodynamics using near-infrared diffuse optical spectroscopies," (in eng), *J Biomed Opt,* vol. 16, no. 2, p. 027004, Feb 2011.

[214] L. Balacumaraswami and D. P. Taggart, "Intraoperative imaging techniques to assess coronary artery bypass graft patency," (in eng), *Ann Thorac Surg,* vol. 83, no. 6, pp. 2251-7, Jun 2007.

[215] N. V. Solenkova, R. Umakanthan, M. Leacche, and J. G. Byrne, "Intraoperative Imaging in Cardiac Surgery," in *Intraoperative Imaging and Image-Guided Therapy*, F. A. Jolesz, Ed. New York, NY: Springer New York, 2014, pp. 685-690.

[216] A. J. Comerota, R. C. Throm, P. Kelly, and M. Jaff, "Tissue (muscle) oxygen saturation (StO2): a new measure of symptomatic lower-extremity arterial disease," (in eng), *J Vasc Surg,* vol. 38, no. 4, pp. 724-9, Oct 2003.

[217] A. W. Gardner, D. E. Parker, N. Webb, P. S. Montgomery, K. J. Scott, and S. M. Blevins, "Calf muscle hemoglobin oxygen saturation characteristics and exercise performance in patients with intermittent claudication," (in eng), *J Vasc Surg,* vol. 48, no. 3, pp. 644-9, Sep 2008.

[218] M. Vardi and A. Nini, "Near-infrared Spectroscopy for Evaluation of Peripheral Vascular Disease. A Systematic Review of Literature," *European Journal of Vascular and Endovascular Surgery,* vol. 35, no. 1, pp. 68-74, 1// 2008.

[219] T. Dermont, L. Morizot, M. Bouhaddi, and A. Menetrier, "Changes in Tissue Oxygen Saturation in Response to Different Calf Compression Sleeves," (in eng), *J Sports Med (Hindawi Publ Corp),* vol. 2015, p. 857904, 2015.

[220] T. Komiyama, A. Onozuka, T. Miyata, and H. Shigematsu, "Oxygen saturation measurement of calf muscle during exercise in intermittent claudication," (in eng), *Eur J Vasc Endovasc Surg,* vol. 23, no. 5, pp. 388-92, May 2002.

Appendix A

Guide to processing and reconstructing 3D optical property maps of finger joints for monitoring treatment of rheumatoid arthritis.

First, follow all post processing procedures as described in the TOPOscan manual.

When creating a surface mesh, be sure that the element size length is <1mm

http://geuz.org/gmsh/doc/texinfo/gmsh.html#Specifying-mesh-element-sizes

Mesh creation (Gmsh):

- File > Open > .stl file
- Geometry > Elementary entitites > Add > Volume
- Select volume > (popup) Create new .geo file > 'e'
- Mesh > 3D
- Geometry > Edit File
- Edit file in TextWrangler.
    - Add 'Mesh.CharacteristicLengthFactor = 0.01;' to beginning of file. Higher the number, the larger the elements.
    - Add 'Mesh.CharacteristicLengthExtendFromBoundary = x;' to change density at surface boundary (<1 more dense at surface, >1 more dense in the center)
    - Save File.
- Geometry > Reload
- Mesh > 3D
- Tools > Statistics
- Nodes on surfaces + Nodes in volumes = Total Nodes (Max nodes for reconstruction is 10,000 - shoot for 8,000)
- Tetrahedra = Number of elements
- Other
    - Save Model Options - saves a .opt file with all the options

Find marker locations

- Using meshlab, use the PickPoints tool and click on select point (Right click).
- Select a point and the coordinates will appear in the pop-up window.
- Save the point as a .pp file
- If FVM algorithm needs to be reconstructed, use: g++ -o GID2FVM GID2FVM.cpp

How data is preprocessed:

- 16 (usually) images are taken within a modulation cycle, at one source position.
- To calibrate images

    - "beamspot" files are produced from experiment or an old one is called
        - These 16 images are demodulated to find phase and amplitude of the beam spot
        - After demodulated, a 45x45 pixel AOI is taken at the beam spot
        - Phase value is averaged over that area - call this **phase of system**
    - A calibration file is loaded
        - This file contains data from a diffused image of a sheet of paper binned at the specified parameter
        - Demodulated as well
    - Calibration amplitude
        - Calibration file * max(beam spot amplitude) / Calibration file amplitude at beam spot location
    - Calibration phase
        - Calibration file - Calibration file amplitude at beam spot location + phase of system
    - Calibration intensity (DC)
        - Same method as calibration amplitude
- Raw finger data is demodulated into its amplitude in phase
    - Demodulation steps
        - 16 images at 1 pixel will look like a sinusoid
        - These vectors are multiplied by
            - hac=(2/Np)*(cos(2*pi*Nc*(0:Np-1)/Np)+sqrt(-1)*sin(2*pi*Nc*(0:Np-1)/Np));
            - hdc=(1/Np)*ones(1,Np);
        - This results in a complex number (abs- amplitude, angle(M)*180/pi+180)
    - Resulting calibrated images
        - Amplitude
            - 1/F*(Ameasure/Acal)
            - F = 9.437
        - Similarly with intensity (DC)
        - Phase
            - PHImeasure-PHIcalibrate
            - However if PHI<0 then add 360 to it
            - PHI will be between 0 and 360

To change a batch file:
chmod a+x Filename.sh

Appendix B

Publications Resulting from This Work

PATENTS

- A.H. Hielscher, Y. Li, A. Bur, M. Flexman, J. Masciotti, **C.J. Fong**, Systems and methods for dynamic imaging of tissue using digital optical tomography, 20100292569 (2010).
- A.H. Hielscher, and **C.J. Fong**, Imaging interfaces for full finger and full hand optical tomography, 20150150458 (2015).
- A.H. Hielscher, and **C.J. Fong**, Dynamic diffuse optical spectroscopic measurement system for monitoring blood perfusion, (Application filed - 2016).

JOURNAL PAPERS

- **C.J. Fong**, J.W. Hoi, L. Geller, H.K. Kim, J. Wu, M. Garzon, A.H. Hielscher, "Assessment of Infantile Hemangiomas Using a Handheld Wireless Diffuse Optical Spectroscopic Device," Pediatr. Dermato., 34, 3, (2017).
- M.L. Flexman, H.K. Kim, R. Stoll, M.A. Khalil, **C.J. Fong**, A.H. Hielscher, "A wireless handheld probe with spectrally constrained evolution strategies for diffuse optical imaging of tissue," Rev. Sci. Instrum. 83, 033108 (2012).
- M.L. Flexman, M.A. Khalil, R. Al Abdi, H.K. Kim, **C.J. Fong**, E. Desperito, D.L. Hershman, R.L. Barbour, A.H. Hielscher "Digital optical tomography system for dynamic breast imaging," Journal of Biomedical Optics 16(7), 076014 (2011).

CONFERENCE PROCEEDINGS

- **C.J. Fong**, J.W. Hoi, H.K. Kim, L. Geller, N. Antonov, M.L. Flexman, M. Garzon, A.H. Hielscher, "Infantile Hemangiomas Assessment with a Handheld Wireless Near-

Infrared Spectroscopic Device," Biomedical Optics OSA Technical Digest, Miami USA, (2014).

- **C.J. Fong**, L. Geller, J.W. Hoi, M.L. Flexman, C. Lauren, H.K. Kim, M. Garzon, A.H. Hielscher, "A Near-Infrared Spectroscopic Handheld Wireless Device for Assessing Infantile Hemangiomas," Britton Chance Centennial Symposium on Metabolic Imaging and Spectroscopy, Philadelphia, PA. (2013)
- **C.J. Fong**, M.L. Flexman, J.W. Hoi, L. Geller, M. Garzon, H.K. Kim, A.H. Hielscher, "A handheld wireless device for diffuse optical spectroscopic assessment of infantile hemangiomas ", Proc. of SPIE 8578 (2013).
- M.L. Flexman, M.A. Khalil, **C. J. Fong**, R.M. Al Abdi, R.L. Barbour, B. Reig, D. Hershman, E. Desperito, A.H. Hielscher, "Optical tomographic imaging of the hemodynamic response to a breath hold in breast cancer patients," Proc. SPIE 7896, 78962J (2011).
- Y. Li, A. M. Bur, **C.J. Fong**, M.L. Flexman, R.A. Abdi, R.L. Barbour, A.H. Hielscher, "Design of a Digital Optical Tomography System for Dynamic Breast Imaging," Biomedical Optics OSA Technical Digest, BSuB5 (2010).